

#### **Archive ouverte UNIGE**

https://archive-ouverte.unige.ch

Thèse 2024

**Open Access** 

This version of the publication is provided by the author(s) and made available in accordance with the copyright holder(s).

The most massive stars at cosmic dawn. Formation and evolution of firstgeneration massive and supermassive stars: rotation, variable accretion rates, chemical feedback

Nandal, Devesh

#### How to cite

NANDAL, Devesh. The most massive stars at cosmic dawn. Formation and evolution of first-generation massive and supermassive stars: rotation, variable accretion rates, chemical feedback. Doctoral Thesis, 2024. doi: 10.13097/archive-ouverte/unige:182547

This publication URL: <a href="https://archive-ouverte.unige.ch/unige:182547">https://archive-ouverte.unige.ch/unige:182547</a>
Publication DOI: <a href="https://archive-ouverte/unige:182547">10.13097/archive-ouverte/unige:182547</a>

© The author(s). This work is licensed under a Creative Commons Attribution (CC BY 4.0) <a href="https://creativecommons.org/licenses/by/4.0">https://creativecommons.org/licenses/by/4.0</a>

## The most massive stars at cosmic dawn

Formation and evolution of first-generation massive and supermassive stars: rotation, variable accretion rates, chemical feedback

#### **THÈSE**

présentée à la Faculté des sciences de l'Université de Genève pour obtenir le grade de Docteur és sciences, mention Astronomie et Astrophysique

par

**Devesh NANDAL** 

de

Hisar (India)

Thèse No

GENÈVE

Observatoire Astronomique de l'Université de Genève



# DOCTORAT ÈS SCIENCES, MENTION ASTRONOMIE ET ASTROPHYSIQUE

### Thèse de Monsieur Devesh NANDAL

intitulée :

«The most Massive Stars at Cosmic Dawn
Formation and Evolution of First-Generation Massive and Supermassive Stars: Rotation,
Variable Accretion Rates, Chemical Feedback»

La Faculté des sciences, sur le préavis de

Monsieur G. MEYNET, professeur ordinaire et directeur de thèse Département d'Astronomie

Madame S. EKSTRÖM, docteure et codirectrice de thèse Département d'Astronomie

Monsieur L. MAYER, professeur Institute for Computational Science, University of Zurich, Zurich

Monsieur T. E., WOODS, docteur Department of Physics and Astronomy, University of Manitoba, Winnipeg, Canada

Monsieur J. REGAN, docteur Faculty of Sciences & Engineering, Hamilton Institute, Maynooth University, Maynooth, Ireland

Monsieur M. DESSAUGES, docteur Département d'Astronomie

autorise l'impression de la présente thèse, sans exprimer d'opinion sur les propositions qui y sont énoncées.

Genève, le 26 février 2024

Thèse - 5804 -

Le Décanat

N.B. - La thèse doit porter la déclaration précédente et remplir les conditions énumérées dans les "Informations relatives aux thèses de doctorat à l'Université de Genève".

To my parents

To Virginia

## Acknowledgements

To pierce the dawn amidst an unrelenting storm to ride the night when drenched in scorn to beckon the formless in a sundered swarm One needs to be dauntless, one needs to be reborn

So thought the spirit, and it sang in a hushful tone lighter then louder, the song echoed in the beyond harking fellow wanderers, who stopped, then marched along But steadfast was the spirit, with wings it bore on its own

Flew and flew it did, and it sang and sang alone
In a void of deafening silence, there was no hovel or home
and then one day of days, it heard a familiar tone
the name was not his own, but of the dreams it planted in loam

Spirit silently scuttered and sang to the source of sound who welcomed the weary spirit, with a heart that was unbound the sage of sky and sight, sat calm in his sanctified ground and offered a shelter to the spirit, in his hearth of lost and found

The sanctuary of spirited sage, was shelved with knowledge profound and there delved a mage of mists, her sight could splinter any sound the spirit asked for their blessing, their wisdom, their jubilant crown sages smiled and smirked, for they never did frown

Days would pass, and years would glide erudition did flow and the spirit grew wide but such are the ways of learned and light to be drenched in darkness, in a never ending plight

The strength to endure and the will to stride in a turbulent sea, that washes all pride is the duty of a spirit, said the makers of its might who etched their honour, their valor in it's sight

endured and flourished, did the spirit of time

and walked the plains and the mountains it would climb with its fellow spirits, that would sing and chime for one of them knew, its struggle and its kind

> atop a hill, beneath the shimmering will the spirit entwined and a melody was singed in the ledgers of bind, forever in time the spirit was the one, forged in prime

> the sky grew clearer, the dawn grew nearer spirit of the song, flew higher and clearer storm turned to sizzle, fog turned to mirror the spirit has sundered, the profaned thunder

My dream of pursuing this PhD would not have been possible without the unfailing support and love of my parents, Dr. Sumer Singh Nandal and Dr. Shakuntla Nandal. They carried me in their lofty arms to any dream I pointed at. The sacrifices they made in the life has led to me the places I am at today. Despite being away from them for all these years, I felt them very close to my heart. Their strength and wisdom empowered me through this PhD. I am what I am becoming...what I hope to become is like them!

I would like to thank Prof. Georges Meynet for giving me the opportunity to pursue a PhD under his supervision. I had the privilege of learning physics through countless of interactions with him. He was always available to speak with me, no matter the time and place. He was there to celebrate my victories and to share my difficulties. This support went beyond his role as my supervisor as he helped me to navigate through my personal challenges. If I have succeeded to become a better human being in the last four years, it is primarily due to him.

My co-supervisor Dr. Sylvia Ekström is the reason why I chose this PhD. She is kind and caring, and has always taken care of me during the last four years. She taught me the computational aspect of my degree and I always knew there is no theoretical model I cannot compute, since I have her on my side. She cared for me outside my work life; I spent countless of evening with her and her husband Mr. Javier G. Nombela. She and her husband are my new found family in Switzerland.

My friend Dr. Gaël Buldgen has taught me how important it is to have a loyal friend in one's life. We spent countless of hours speaking about astrophysics, training in the gym and spending time travelling around Switzerland. He was always there when I went through difficult times and picked me up when I was exhausted. We come from two different worlds, but here in Switzerland and beyond, we are like brothers.

I would also like to thank all the members of my stellar group for their help during my degree. I had a great time speaking with each and every one of you. A special thanks to Camilla Pezzotti for being my friend. You are the coolest and the funniest person I have ever met!

The greatest thing to happen to me during this PhD was to meet my girlfriend Dr. Virginia Thompson. She supported me through all the difficult times and always put me needs before hers. My last year of PhD was extremely busy and she took time to find things we could do together. Our time together has been the best memory of my PhD. I am extremely lucky to beat such astronomical odds and find the best partner in the whole Universe.

#### **Abstract**

This thesis presents an investigation into the formation and evolution of the universe's earliest and most massive stars, emphasizing Population III stars, including Supermassive Stars (SMS) with masses exceeding 100,000 solar masses. Utilising the enhanced Geneva Stellar Evolution Code (GENEC), the study offers insights into the chemical impacts, and ultimate fates of these stars.

The research commences with an analysis of massive stars with solar and near-solar metallicity. It uncovers how rotational modifications in GENEC impact the evolutionary paths of massive stars, particularly those between 15 and 60 solar masses. Various approaches to incorporating rotation in stellar models have been examined. In non-magnetic models, the level of chemical mixing varies based on the chosen diffusion coefficients, yet the angular velocity distribution remains consistent. Conversely, magnetic models yield much flatter internal angular velocity profiles. At the end of their evolutionary cycle, the magnetic models predict a core angular momentum significantly lower than the predictions by non-magnetic models.

The thesis then shifts to exploring massive, fast-rotating stars at low and zero metallicities. These stars are identified as key contributors to the chemical enrichment of the interstellar medium, especially in nitrogen enrichment of high-redshift galaxies like GN-z11 and CEERS-1019. The research demonstrates that fast-rotating Population III stars closely reproduce observed abundance ratios, such as nitrogen to oxygen, which are not replicated by stars with higher metallicities. Further, the study investigates accreting, non-rotating extremely massive stars, delving into their chemical influence and revealing the significant role of accretion rates in their evolution. A critical accretion rate is identified, marking the transition of these stars into the red supergiant phase and influencing their lifespan, surface helium enrichment, and physical properties.

A major focus is on SMS within the atomically cooled halo regime. The research explores their evolution, internal structures, and potential to form black holes. The thesis reveals that SMS at specific accretion rates can reach the general relativistic instability during core hydrogen burning, leading to direct collapse into black holes.

In addition to these findings, the thesis outlines future research directions, including the study of Population III and very metal-poor stars with different rotational mixing physics, the implementation of rotation and accretion in SMS models, and the exploration of internal magnetic fields instabilities and WIMP annihilation in SMS evolution. The potential observational traces of SMS, particularly through the James Webb Space Telescope data, are also identified as a key area for future study.

#### Resumé

Cette thèse de doctorat présente une investigation de la formation et de l'évolution des premières et des plus massives étoiles de l'univers, mettant l'accent sur les étoiles de Population III et les étoiles supermassives. Grâce à l'utilisation d'une version améliorée du code d'évolution stellaire de Genève (GENEC), cette étude renseigne sur l'impact chimique et les phases ultimes de l'évolution de ces étoiles.

Le travail de recherche commence par une analyse des étoiles massives à métallicité solaire et presque solaire. Cette première étude explore comment les changements des effets de rotation dans GENEC influencent l'évolution des étoiles massives, plus particulièrement entre 15 et 60 masses solaires. Diverses façons d'inclure la rotation sont examinées. Dans les modèles sans champs magnétiques, le degré de mélange chimique varie selon les choix de coefficients de diffusion, bien que la distribution de vitesse angulaire dans l'étoile reste semblable. À l'opposé, les modèles magnétiques présentent des profils de rotation internes beaucoup plus plats. À la fin de leur évolution, les modèles magnétiques prédictent une quantité de moment angulaire dans le cœur bien plus petite que les prédictions des modèles dits "non-magnétiques".

La thèse se tourne alors vers l'exploration des étoiles massives en rotation rapide à métallicité faible et nulle. Ces étoiles sont vues comme des contributeurs clés à l'enrichissement chimique du milieu interstellaire, particulièrement l'enrichissement en azote dans les galaxies à haut-redshift GN-z11 et CEERS-1019. L'étude démontre que des étoiles de population III en rotation rapide peuvent reproduire les ratios d'abondance observés pour l'azote et l'oxygène, qui ne peuvent être reproduits par des étoiles de plus haute métallicité. Ensuite, l'étude s'intéresse au cas d'étoiles en phase d'accrétion, sans rotation, de masses plus extrêmes, et se plonge dans leur impact chimique, révélant le rôle crucial des taux d'accrétion agissant durant leur évolution. Un taux d'accrétion critique est identifié, marquant la transition de ces étoiles vers la phase de supergéante rouge et influençant leur durée de vie, leur enrichissement d'hélium en surface ainsi que leurs propriétés physiques.

Une attention majeure est apportée aux étoiles supermassives dans des BOB. L'étude explore leur évolution, leurs propriétés de structure interne et leur potentiel pour former des trous noirs. La thèse révèle que pour certains taux d'accrétion de matière, ces étoiles peuvent atteindre une instabilité de relativité générale durant leur phase de combustion central d'hydrogène, menant à leur effondrement en trous noirs.

En plus de ces découvertes, cette thèse décrit plusieurs directions futures de recherches, incluant l'étude des étoiles de population III et de très faible métallicité suivant diverses prescriptions physiques de mélange rotationnel, l'

# Contents

A	cknov	wledge	ments	iii
1	Intr	oductio	on	1
2	Fror	n Sing	ularity to Stardust	3
	2.1	The p	rimordial Universe	3
		2.1.1	Einstein Equations	3
		2.1.2	Robertson-Walker Metric	4
		2.1.3	Calculation of the Ricci Tensor and Scalar	5
		2.1.4	Energy-Momentum Tensor for a Perfect Fluid	6
		2.1.5	Friedman Equations	7
		2.1.6	Big bang nucleosynthesis	8
		2.1.7	Observed primordial abundances	10
	2.2	Evolu	tion of the Cosmic Fluid	12
	2.3	The B	irth of the First Stars	13
	2.4	Gravi	tational Instability	13
	2.5	Thern	nodynamic implications	14
		2.5.1	Instability in Rotating Systems	15
		2.5.2	Critical mass for halos	16
		2.5.3	Cosmic PopIII star formation rate density	17
		2.5.4	PopIII formation pathways	17
		2.5.5	Primordial stellar models	19
		2.5.6	Disc fragmentation	20
		2.5.7	IMF for PopIII stars	22
		2.5.8	Magnetic fields	23

		2.5.9	Radiative fields	26
		2.5.10	Streaming Velocities	26
		2.5.11	Dark matter annihilation	27
	2.6	Super	massive stars	28
		2.6.1	Classical description	31
		2.6.2	Formation and evolution of accreting SMSs	38
		2.6.3	Evolution of accreting SMSs	40
		2.6.4	Swelling of SMSs due to accretion	41
		2.6.5	Accretion in SMSs	44
3	Imp	roveme	ents to the Geneva stellar evolution code	49
	3.1		tion of massive stars using the Geneva code	49
		3.1.1	Rotating main sequence models	
	3.2	Nume	rical convergence of massive star models in GENEC	
		3.2.1	Introduction and Purpose	
		3.2.2	Core Functionalities	
		3.2.3	Conclusion	64
	3.3	Hydog	gen burning plateau in accreting stars	65
		3.3.1	Problem Summary	65
		3.3.2	Key Observations	65
	3.4	Enhan	cements to Accretion Handling in GENEC Models	71
		3.4.1	Problem Identification	71
		3.4.2	Solution Implementation	71
		3.4.3	Results	71
	3.5	Imple	mentation of Variable Accretion Rate in GENEC	72
		3.5.1	Motivation	72
		3.5.2	Mass dependent Accretion law	72
		3.5.3	Integration of Variable Accretion Rates from Cosmological Simulations	72
	3.6	Incorp	oration of metals and isotopes Accretion in Metal-enriched Environments	<b>7</b> 3
		3.6.1	Streamlined Computational Tools for Supermassive Star Analysis	74
	3.7	Concl	usion	74
4	Mas	ssive sta	ars: Impact of rotational prescriptions	76
	4.1	Backg	round literature	77
	4.2	Additi	ional physics	78

		4.2.1	Hydrostatic effects due to rotation	79
		4.2.2	Angular Momentum Advection Equations	79
		4.2.3	Hydrodynamical Instabilities in Radiative Zones Due to Rotation	80
		4.2.4	Understanding Shear Diffusion Coefficients: A Deep Dive into Stabilizing	
			Effects and Transport Processes	81
		4.2.5	Magnetic models	83
		4.2.6	The present numerical experiments compared to other works	86
		4.2.7	A Deep Dive into Stellar Model Parameters	87
	4.3	The N	on-Magnetic 15 $M_{\odot}$ Stellar Models and Their Diffusion Coefficients $\ \ \ldots \ \ \ldots$	91
		4.3.1	Summary on the Vertical Shear Diffusion Coefficient $D_{ m shear}$	92
		4.3.2	Analysis on the Horizontal Shear Diffusion Coefficient $D_{\mathrm{h}}$	93
		4.3.3	Tracks and lifetimes	95
		4.3.4	Internal and Surface Rotations, Surface Abundances	96
		4.3.5	He-burning lifetimes and blue-red supergiant ratios	98
		4.3.6	Difference of the Structure at the End of the Core He-Burning Phase	99
		4.3.7	Analysis and Interpretation of the 60 $M_{\odot}$ Stellar Models $\ \ldots \ \ldots \ \ldots$	100
		4.3.8	Surface Velocities and Abundances in 60 $M_{\odot}$ Stellar Models $\ \ldots \ \ldots \ \ldots$	103
		4.3.9	Post-MS Evolution of 60 $M_{\odot}$ Stellar Models	107
		4.3.10	Magnetic Models	107
		4.3.11	The 60 $M_{\odot}$ Model	110
		4.3.12	Additional prescriptions E and F $\ldots \ldots \ldots \ldots \ldots \ldots$	111
		4.3.13	Discussion and Conclusions	114
5	Che	mical s	ignatures of PopIII massive stars in the early Universe	117
	5.1	Introd	uction	118
	5.2	Stellar	models and enrichment	119
		5.2.1	Integrated Abundance Ratios	120
	5.3	Result	s	125
		5.3.1	Mechanism of Transport of Chemical Species	125
		5.3.2	Post-Main Sequence Evolution and Chemical Transport	125
		5.3.3	Ejected Material Composition from Individual Stars	126
		5.3.4	Abundance Ratios in Stellar Population Ejecta After Dilution	131
	5.4	Discus	ssion	136
		5.4.1	Standard versus Fast Rotating Main Sequence Stars	136

		5.4.2	Ejection above Remnant versus CO Core	6
	5.5	Concl	usion	6
6	Extr	emely	Massive stars: Formation and evolution 14	.0
	6.1	Litera	ture review	1
	6.2	Detail	ed Examination of Our Accreting Star Models	2
		6.2.1	Core Physical Components	2
		6.2.2	Assumption of constant Accretion Rates	:3
		6.2.3	Implications and Forward-Look	4
	6.3	Evolu	tion of Extremely Massive Accreting Pop III Stars	8
		6.3.1	Pre-main-sequence phase	8
		6.3.2	Core hydrogen burning	8
		6.3.3	Core helium burning	9
		6.3.4	Late Evolutionary stages	9
	6.4	Influe	nce of Massive Pop III Stars	C
		6.4.1	Chemical Feedback	1
		6.4.2	Mechanical and Radiative Feedback	2
		6.4.3	Comparison with Previous Work	3
	6.5	Impac	et of Varying Metallicity	4
	6.6	Concl	usion	5
7	Vari	iable ac	cretion rate and preMS	7
	7.1	Litera	ture review	8
	7.2	Accre	tion in Geneva Stellar evolution code	2
		7.2.1	The stellar accretion rates	2
		7.2.2	Using the stellar accretion rates as input	2
	7.3	Evolu	tion of accreting massive PopIII stars	3
	7.4	Detail	ed Analysis of Pre-Main Sequence Evolution	8
		7.4.1	Setting the Stage: Initial Conditions	8
		7.4.2	Evolutionary Trajectories on the Hertzsprung-Russell Diagram 16	8
		7.4.3	Core hydrogen burning evolution	9
		7.4.4	Helium Burning	′1
	7.5	Discus	ssion	7
		7.5.1	Determining the Critical Accretion Rate	7
		7.5.2	Luminosity wave and <sub>crit</sub>	9

		7.5.3	Variable accretion rates and model comparisons	180
		7.5.4	Impact of accretion on physical parameters	180
		7.5.5	Kelvin-Helmholtz timescale versus accretion timescale	181
	7.6	Concl	usion	182
8	Che	mical s	signatures of PopIII supermassive stars	185
	8.1	Introd	luction	185
	8.2	Litera	ture review	186
	8.3	Metho	ods	187
		8.3.1	Cosmological Context	187
		8.3.2	Massive PopIII Star (Nitrogen) Enrichment	189
		8.3.3	Extrapolation to Galactic Scale	191
	8.4	Result	ts	193
		8.4.1	Transport of Chemical Species in Massive Pop III Stars	193
		8.4.2	Integrated Abundances	194
		8.4.3	Impact of Dilution Factor	198
		8.4.4	Massive PopIII Stars as Efficient Nitrogen Enrichers and Progenitors of High-	
			z N-loud Quasars	199
	8.5	Discus	ssion	199
		8.5.1	Mass Ranges	199
	8.6	Impac	ct of evolutionary stages on the integrated abundances	200
		8.6.1	Predicted Abundances	200
		8.6.2	Mass Ranges	201
		8.6.3	Predicted Abundances	201
		8.6.4	Comparison with Previous Studies	202
	8.7	Concl	usion	203
9	Sup	ermass	sive stars and general relativistic instability: impact on upper mass limit and	d
	lum	inosity		206
	9.1	Litera	ture review on accreting models	208
	9.2	The m	nodels	210
		9.2.1	Linear adiabatic radial pulsation stability	212
	9.3	Evolu	tion in the HR diagram	214
	9.4	Some	properties of Pop III supermassive stars	215
		941	Internal structures	215

		9.4.2	Chemical structure	216
		9.4.3	Maximum luminosity	216
	9.5	The up	oper mass limit of stars	217
		9.5.1	The nuclear limit	218
		9.5.2	The pair creation limit	220
		9.5.3	The GR limit	220
	9.6	Effects	of changing the metallicity	225
		9.6.1	For classical accretion rates	225
		9.6.2	For high accretion rates	226
	9.7	Conclu	usions	227
10	A 4.4	itional	avouls.	230
10			ate of Betelgeuse inferred from its pulsations	
	10.1		Literature review	
			Global Parameters	
			Observed Pulsation Periods	
	10 <b>2</b>		S	
	10.2			
			Stellar Evolution Models	
			Rotation and Mixing	
			Pulsation Analysis	
	10.2		Convection in equilibrium	
	10.3		S	
			Periods of Excited Radial Pulsations	
			Synthesis of Semi-Periodic Variation	
			Discussion	
		10.3.4	Conclusion	255
11	Con	clusion	s and future perspectives	257
		11.0.1	Future perspectives	261
		11.0.2	Impact of the Physics of Rotation on Primary Nitrogen Production	261
R۵	feren	ces		269



## Introduction

In the nascent stages of the universe, characterized by a striking uniformity, the cosmic microwave background radiation provides evidence of a universe governed by homogeneity and isotropy. This initial state, fundamental to cosmological models, set the stage for the complex structures and processes that followed. A crucial transition in this early universe was the formation of the first stars, which initiated the diversification of stellar populations and the enrichment of the interstellar medium.

This thesis investigates Population III (Pop III) stars with main emphasis on supermassive stars (SMS), formed from primordial, metal-free gas. These stars played a critical role in cosmic evolution, enriching the universe with heavy elements and paving the way for subsequent generations of stars, including Population II (Pop II) and Population I (Pop I) stars. The latter, like our Sun, are metal-rich and predominantly found in spiral galaxies' disk regions. (elaborate on the motivation of the thesis. STAREX, SMBH seeds)

Pop III stars, while not directly observed, are understood through indirect evidence, such as observations of extremely metal-poor (EMP) stars and data from high-redshift galaxies. This research contributes to the evolving understanding of these early stars, challenging the notion of their solitary formation and instead suggesting the prevalence of fragmentation and the emergence of multi-stellar systems. This paradigm shift is supported by the influence of factors such as radiative feedback, magnetic fields, and dark matter annihilation, which add layers of complexity to the process of primordial star formation.

Chapter 2 sets the stage with an extensive literature review on early universe star formation. It examines the fundamental processes such as accretion, feedback mechanisms, rotation, internal magnetic fields, and mass loss, crucial for understanding stellar evolution. Chapter 3 introduces the Geneva stellar evolution code (GENEC), highlighting significant enhancements that underpin

this research. In Chapter 4, the focus shifts to the evolution of standard massive stars in the 15 to 60 solar mass range. This analysis, extending to solar-like stars, explores the effects of rotation and magnetic fields on their evolutionary paths. Massive stars models, especially fast rotating ones are used to explain the chemical signature of high redshift galaxies like GN-z11 and CEERS 1019 in Chapter 5

Chapter 6 discusses the impact of accretion on star evolution and the resultant chemical feedback. The narrative then progresses to Chapter 7, where the spotlight is on variable accretion rates obtained from cosmological simulations of mini-halos. This variability is key to understanding the critical accretion rate that determines the fate of protostars as either blue or red supergiants. Chapter 8 examines how chemical yields from these stellar models align with observations from high-redshift galaxies like GN-z11 and CEERS 1019, observed by the James Webb Space Telescope (JWST).

In Chapter 9, the focus shifts to supermassive stars, specifically those in the mass range of 80,000 to 800,000 solar masses. This chapter delves into the general relativistic instability that leads to their direct collapse into black holes. Chapter 9 explores the dark collapse phenomenon, where accreting objects bypass traditional stellar formation, directly transitioning into black holes before core hydrogen burning. The thesis concludes in Chapter 11, summarizing the findings and envisioning future research directions in this dynamic field.

Through this comprehensive exploration, the thesis aims to provide a deeper understanding of the complex processes shaping massive and supermassive stars. It seeks to bridge gaps in our knowledge of early cosmic history, shedding light on the formation and evolution of these massive celestial bodies and their profound impact on the universe.

Chapter 2

## From Singularity to Stardust

With eyes cast skyward and minds full of wonder, our ancestors embarked on a journey to decode the origin of our Universe. As we evolved, so did our inquiries, culminating in a profound question about the beginning of all things. This collective endeavor, blending observational insights with mathematical rigor, gave rise to the big bang theory. The big bang model proposes our universe birthed from an infinitely dense and hot singularity roughly 13.8 billion years ago. This cataclysmic event heralded the inception of space, time, matter, and energy, guiding the universe's continued growth and transformation.

### 2.1 The primordial Universe

In our quest to grasp the Big Bang model and the genesis of the cosmos, we must start at the beginning (Weinberg 1972). The Friedman equations are crucial. They explain the universe's expansion from an almost inconceivably hot, dense state to its present vastness and complexity (Peebles 1993; Bullock & Boylan-Kolchin 2017). This section will derive these equations within General Relativity's framework. This theory is our best understanding of gravitation to date. The objective is to reconstruct the universe's evolution, starting from the very fabric of space and time during the Planck epoch.

#### 2.1.1 Einstein Equations

At the heart of our cosmic origin story lie the Einstein field equations, which articulate the relationship between the geometry of spacetime and the energy content of the universe. They are elegantly expressed as:

$$R_{\mu\nu} - \frac{1}{2}g_{\mu\nu}R - \Lambda g_{\mu\nu} = 8\pi G T_{\mu\nu}$$
 (2.1)

In equation 2.1,  $R_{\mu\nu}$  denotes the Ricci curvature tensor, capturing the degree to which spacetime is curved by matter at each point. The metric tensor,  $g_{\mu\nu}$ , describes the fundamental geometric structure of spacetime itself. The Ricci scalar R is a scalar quantity representing the trace of the Ricci tensor, summarizing the curvature of spacetime caused by all mass and energy present. The cosmological constant, denoted by  $\Lambda$ , encapsulates the energy density of empty space, or dark energy, and its inclusion reflects the accelerated expansion of the universe. The term  $8\pi G$  incorporates Newton's gravitational constant, G, which mediates the strength of gravitational interaction, and  $T_{\mu\nu}$ , the energy-momentum tensor, represents the distribution of matter and energy in spacetime. It is detailed further as:

$$T_{\mu\nu} = (\rho + p)u_{\mu}u_{\nu} - pg_{\mu\nu} \tag{2.2}$$

Here,  $\rho$  represents the energy density, and p is the pressure exerted by the matter content. The term  $u_{\mu}$  is the four-velocity, depicting the velocity of matter moving through spacetime, which, together with  $g_{\mu\nu}$ , models the influence of matter on the universe's expansion.

#### 2.1.2 Robertson-Walker Metric

The Einstein tensor  $G_{\mu\nu}$  is paired with the Ricci tensor and scalar to formulate the geometry of spacetime. For a cosmological model, we apply a specific metric that captures the universe's homogeneous and isotropic nature. This metric is known as the Robertson-Walker metric and is represented as:

$$ds^{2} = dt^{2} - a^{2}(t) \left[ \frac{dr^{2}}{1 - \frac{r^{2}}{K^{2}}} + r^{2}d\theta^{2} + r^{2}\sin^{2}\theta d\phi^{2} \right]$$
 (2.3)

Equation 2.3 describes a universe devoid of preferred locations or directions, reflecting the cosmological principle. The absence of cross-terms between space and time in this metric signifies the isotropy of the universe. Furthermore, the metric's spherical symmetry corresponds to its homogeneity. The scale factor a(t) is a function of time alone, signifying the change in relative distances within the universe as it expands or contracts over time. The curvature parameter K in the Robertson-Walker metric is pivotal. It is tied to the curvature radius of the universe's spatial hypersurface. When  $K^{-2}=0$ , the metric simplifies to the flat Euclidean space. For  $K^{-2}>0$ , the universe is closed and finite, whereas  $K^{-2}<0$  characterizes an open and infinite universe.

#### 2.1.3 Calculation of the Ricci Tensor and Scalar

To specialize the Einstein equations for a homogeneous and isotropic universe, we must calculate the Ricci tensor and scalar. This process begins with the Christoffel symbols derived from the Robertson-Walker metric:

$$\Gamma_{ji}^{l} = \frac{1}{2}g^{lm}(\partial_{j}g_{mi} + \partial_{i}g_{mj} - \partial_{m}g_{ji})$$
(2.4)

With the Christoffel symbols determined, we proceed to calculate the Riemann tensor. It is described by the equation:

$$R_{kji}^{l} = \partial_{j} \Gamma_{ki}^{l} - \partial_{i} \Gamma_{kj}^{l} + \Gamma_{ki}^{m} \Gamma_{mj}^{l} - \Gamma_{kj}^{m} \Gamma_{mi}^{l}$$

$$(2.5)$$

Equation 2.4 expresses the Christoffel symbols, which are necessary for constructing the Ricci tensor and scalar that describe the curvature of spacetime influenced by matter and energy. The Robertson-Walker metric's structure ensures that most Christoffel symbols are symmetric or vanish. The non-zero terms are crucial and are given by:

$$\begin{split} \Gamma^t_{rr} &= -\frac{\dot{a}}{1 - \frac{r^2}{K^2}}, \\ \Gamma^t_{\theta\theta} &= r^2 \dot{a}, \\ \Gamma^t_{\phi\phi} &= r^2 \dot{a} \sin^2 \theta, \\ \Gamma^r_{rt} &= \Gamma^r_{tr} = \Gamma^\theta_{\theta t} = \Gamma^\phi_{\phi t} = \frac{\dot{a}}{a}, \\ \Gamma^r_{rr} &= \frac{r}{K^2 (1 - \frac{r^2}{K^2})}, \\ \Gamma^\theta_{\theta r} &= \Gamma^\phi_{\phi r} = \frac{1}{r}, \\ \Gamma^\phi_{\phi\theta} &= \Gamma^\phi_{\theta\phi} = \theta. \end{split}$$

Our focus narrows to the Riemann tensor components with matching top and middle bottom indices. These are sufficient for constructing the Ricci tensor  $R_{im}$ . The significant components of the Ricci tensor that are non-zero are encapsulated by:

$$R_{tt} = -3\frac{\ddot{a}}{a} \tag{2.6}$$

Equation 2.6 is pivotal as it relates directly to the universe's expansion rate, informing us about its dynamic state. The Ricci tensor for the Robertson-Walker metric, which is diagonal, has the following non-zero components:

$$R_{rr} = \frac{\dot{a}^2}{a^2} + \frac{2\ddot{a}}{a} + \frac{2}{K^2(1 - \frac{r^2}{K^2})},\tag{2.7}$$

$$R_{\theta\theta} = r^2 \left( \frac{\dot{a}^2}{a^2} + \frac{2\ddot{a}}{a} \right) + \frac{2r^2}{K^2},$$
 (2.8)

$$R_{\phi\phi} = r^2 \sin^2 \theta \left( \frac{\dot{a}^2}{a^2} + \frac{2\ddot{a}}{a} \right) + \frac{2r^2 \sin^2 \theta}{K^2}.$$
 (2.9)

These components confirm the Ricci tensor's diagonal nature. To summarize, we can state the  $R_{tt}$  component as:

$$R_{tt} = -3\frac{\ddot{a}}{a} \tag{2.10}$$

Furthermore, we can express the Ricci tensor in a more general form:

$$R_{ii} = -g_{ii} \left( \frac{\ddot{a}}{a^3} + \frac{2\dot{a}^2}{a^4} + \frac{2K}{a^2} \right) \tag{2.11}$$

Finally, the Ricci scalar, which is the trace of the Ricci tensor, is given by:

$$R = g^{ik}R_{ik} = -6\left(\frac{\ddot{a}}{a} + \frac{\dot{a}^2}{a^2} + \frac{K}{a^2}\right)$$
 (2.12)

The Ricci scalar encapsulates the overall curvature of spacetime, taking into account both the expansion rate and the spatial curvature of the universe.

#### 2.1.4 Energy-Momentum Tensor for a Perfect Fluid

A perfect fluid, by definition, is isotropic and appears uniform in every direction. This means that in comoving coordinates, its macroscopic speed has no privileged direction and is described solely by its temporal component,  $u^{\alpha} = (1, 0, 0, 0)$ .

The relation  $(u^{\alpha})^2 = g_{\alpha\beta}u^{\alpha}u^{\beta} = c^2 = 1$  implies that  $g_{tt}(u^t)^2 = c^2$ , hence  $u^t = 1$ .

Considering the expression for the energy-momentum tensor  $T_{\mu\nu}$  for a perfect fluid, we find that it is diagonal, with its components being:

$$T_{tt} = \rho g_{tt} \tag{2.13}$$

and

$$T_{ii} = -pg_{ii} (2.14)$$

Our derivation suggests that the universe is filled with a perfect fluid, which aligns with the cosmological principle stating that the universe is homogeneous and isotropic on large scales.

#### 2.1.5 Friedman Equations

With the groundwork laid in preceding sections, we now have all the necessary components to fulfill our objective within the Einstein framework. We proceed by integrating these elements into Einstein's equations. The equations that deviate from zero are those with matching indices, reflecting our metric's diagonal character. We commence with the temporal component:

$$R_{tt} - \frac{1}{2}Rg_{tt} - \Lambda g_{tt} = 8\pi G\rho u_t u_t \tag{2.15}$$

This equation encapsulates the energy density of the universe in its temporal aspect, revealing the relationship between spacetime curvature and matter-energy content. After synthesizing the preceding components, we obtain the Friedmann equation:

$$\left(\frac{\dot{a}(t)}{a(t)}\right)^2 = \frac{8\pi G}{3}\rho(t) + \frac{\Lambda}{3} - \frac{1}{K^2 a^2(t)}$$
 (2.16)

This equation, known as the first Friedman equation, encapsulates the expansion rate of the universe in terms of the scale factor a(t), the energy density  $\rho(t)$ , the cosmological constant  $\Lambda$ , and the curvature parameter K. We now turn to the spatial components of the Einstein field equations. For each spatial component, we find the same expression:

$$-\frac{\dot{a}^2}{a^2} - \frac{2\ddot{a}}{a} - \frac{2}{K^2 a^2} + \Lambda = -8\pi Gp \tag{2.17}$$

By manipulating equations 2.16 and 2.17, we deduce a second independent equation that avoids the  $(\dot{a}/a)^2$  term:

$$\frac{\ddot{a}(t)}{a(t)} = -\frac{4\pi G}{3}(\rho(t) + 3p) + \frac{\Lambda}{3}$$
 (2.18)

Equation 2.18, the second Friedman equation, describes the acceleration of the universe's expansion, linking it to the matter content and the cosmological constant. In conclusion, the Friedman equations, 2.16 and 2.18, are the two independent equations that are used to describe the universe's dynamics under general relativity.

The Friedman equations serve as the mathematical underpinning that describes how the universe expands from its initial hot, dense state. As the universe expands, the Friedman equations dictate that the temperature of the universe decreases. This cooling allows the universe to transition from a state where no atoms could exist to one where nuclei and then atoms could form.

#### 2.1.6 Big bang nucleosynthesis

The very first nuclear reactions in the early epoch only occurs when the Universe begins its transition from its fully radiation dominated state into a partial one. Consisting of a dense mix of photons, electron-positron pairs (e<sup>-</sup>,e<sup>+</sup>), trace amounts of nucleons and neutrinos ( $\nu_i$ ,  $i=e,\mu,\tau$ ), the nuclear reactions commences over the Fermi length (1 f =  $10^{-15}$ m) and generates energies in scale of MeV. With the exception of nucleons, all other fundamental particles have comparable densities due to relativistic effects at temperatures around  $10^{12}$ K. Despite these particles being separated over large distances, the rate of reaction is extremely rapid which leads to numerous collisions as the universe continues to expand. This leads to a rapid establishment of equilibrium and the quick erasure of any deviations from this state. The process of big bang nucleosynthesis (BBN) begins and the important milestones are indicated below:

• 10 millisecond: This earliest stage of BBN is dominated by rapid collisions which sets the weak interactions in equilibrium. The neutron-proton ratio stays in equilibrium, give by n/p =  $\exp(-\Delta m/T)$ , where  $\Delta m = 1.293$  MeV signifies the neutron-proton mass difference. The charged current weak interactions facilitate

$$p + e^- \leftrightarrow n + \nu_e,$$

$$n + e^+ \leftrightarrow p + \overline{\nu}_e;$$

whereas beta and inverse beta decay lead to

$$n \to p + e^- + \overline{\nu}_e$$
.

Additionally, all neutrino species are also in equilibrium with respect to electrons and positron;  $e^+ + e^- \leftrightarrow \nu_i + \overline{\nu}_i$ .

- 0.1 second: This stages is marked by a drop in temperature to  $3\times10^{10}$ K and the slowing down of the rate of reaction for neutral current weak interactions with respect to the expansion rate of the Universe. The heavier species of neutrinos  $(\nu_{\mu}, \nu_{\tau})$  fully decouple but  $\nu_{e}$  continue to interact via charged-current interactions. No new neutrino pairs are produced after this stage, the existing pairs either annihilate or expand with the Universe. The n-p ratio is still intact and at equilibrium.
- **1 second**: At this juncture, the universe cools to approximately 10<sup>10</sup>K. The diminishing rate of charged-current weak interactions fails to sustain n-p equilibrium. A significant factor is

the neutron's greater mass compared to the proton, leading to a unidirectional bias in reactions. This bias results in neutrons converting into protons more frequently than the reverse. Consequently, the n-p ratio stabilizes once the temperature reaches  $T_*$ . The equilibrium ratio is expressed by the Boltzmann equation:

$$\frac{n}{p} \approx \frac{n}{p_*} = \exp\left(\frac{-\Delta m}{T_*}\right) \approx \frac{1}{6},$$
 (2.19)

where equation above illustrates the stabilization of the neutron-to-proton ratio to approximately 1/6. This ratio emerges due to the cooling of the universe reducing the effectiveness of charged-current weak interactions that maintain neutron-proton equilibrium. As the universe expands and cools, these interactions can no longer keep pace, leading to a freeze-out of the n/p ratio at  $T_*$ . The higher mass of neutrons compared to protons predisposes them to decay into protons, especially as the temperature drops below a critical threshold, marking the point at which this ratio stabilizes. This critical temperature,  $T_*$ , reflects the energy scale at which weak interactions cease to efficiently convert protons back into neutrons, with the specific ratio of 1/6 governed by the Boltzmann factor,  $\exp(-\Delta m/T_*)$ , indicative of the balance between the universe's cooling rate and neutron decay dynamics.

Post this stage, neutron density declines exponentially, governed by:

$$n_n(t) = n_n(t_*) \exp\left(-\frac{t - t_*}{\tau_n}\right)$$
(2.20)

with  $\tau_n$ , the neutron lifetime, approximated at 885.7 seconds. Concurrently, protons and neutrons engage in interactions such as  $p+n \to {}^2{\rm H} + \gamma$ , leading to deuterium formation. However, this stage is also marked by the deuterium bottleneck. The intense photon activity during this period continuously disrupts deuterium atoms, delaying further nucleosynthesis.

- 10 seconds: The temperature has now dropped to  $3\times10^9$ K and the energy density of the Universe has decreased beyond the point where it is no longer energetically favourable for two photons to produce electron-positron pairs. The reaction  $e^- + e^+ \rightarrow 2\gamma$  is out of equilibrium and only photons are produced.
- **100 seconds**: As the Universe cools below 10<sup>9</sup>K, it reaches a state conducive to deuterium survival against photodissociation. Deuterium, comprising a proton and a neutron, becomes the first stable nucleus to facilitate nucleosynthesis:

$$d + n \to^3 H + \gamma \tag{2.21}$$

$$d + d \to^3 H + p \tag{2.22}$$

$$d+p \to^3 He + \gamma \tag{2.23}$$

$$d+d \to^3 He + n \tag{2.24}$$

$$^{3}H \rightarrow ^{3}He + e^{-} + \bar{\nu}_{e}$$
 (2.25)

$$^{3}He + n \rightarrow ^{3}H + p \tag{2.26}$$

$$^{3}H + p \rightarrow^{4} He + \gamma \tag{2.27}$$

$$^{3}H + d \rightarrow^{4} He + n \tag{2.28}$$

$$^{3}He + n \rightarrow ^{4}He + \gamma \tag{2.29}$$

$$^{3}He + d \rightarrow^{4} He + p \tag{2.30}$$

$$^{3}He + ^{3}He \rightarrow ^{4}He + 2p$$
 (2.31)

These reactions conspicuously bypass stable nuclei at mass numbers 5 and 8, leading to a natural bottleneck in element formation. The reduced kinetic energy of particles due to cooling makes it more difficult to cross the Coulomb barrier and impedes nuclear fusion. This energy decrease hinders particles from overcoming the electrostatic repulsion in heavier nuclei, effectively stalling nucleosynthesis beyond helium. Approaching 1000 seconds, this marks the cessation of Big Bang Nucleosynthesis. While studies like Iocco et al. (2007) indicate sporadic formation of elements like carbon, nitrogen, and oxygen (approximately 1 in  $10^{16}$  hydrogen atoms), elements beyond  $A \ge 12$  remain largely unproduced during this epoch.

#### 2.1.7 Observed primordial abundances

The decoupling of each species of neutrinos ( $\nu_i$ ,  $i=e,\mu,\tau$ ) marks the event where the standard model can accurately describe the following cosmological evolution. The abundances of various elements from BBN can be seen in the left and right panels of Figure 2.1. If the total abundance produced from Big Bang nucleosynthesis is assumed to be one, the plots depict that the majority of the early Universe's content consists of protons. Neutrons begin their exponential decay around 200 seconds, whereas helium nuclei become the second most abundant species. Deuterium ranks third and helium-3 fourth, with these elements maintaining constant levels until the onset of stellar nucleosynthesis, which occurs much later. Figure 2.1 shows the relationship between abundances and time. However, these abundances primarily depend on the baryon-to-photon ratio,  $\eta_{10}$ , given

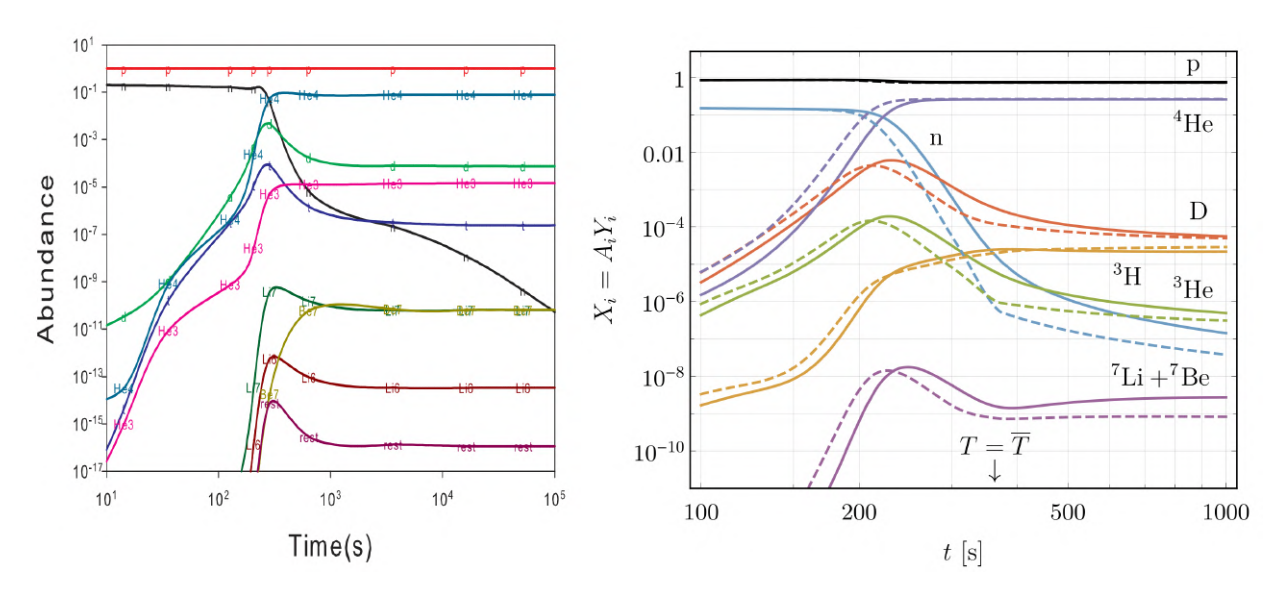


Figure 2.1: Production of primordial elements during the big bang nucleosynthesis. *Left panel:* The buildup of deuterium and helium isotopes following the first ten seconds after Big Bang as described by Mishra & Basu (2011). *Right panel:* A similar plot as the left panel but with updated values from recent observations as shown by Cuesta et al. (2023). The lines with the updated values of  $\eta_{10}$  are compared to previous values shown in dotted lines. Such observations are obtained from recent determination of the parameter  $\eta_{10}$  by WMAP (see text in 2.1.7 for more details)carried out over the decades have allowed us to better constrain the abundances of the big bang.

by:  $\eta_{10} = 10^{10} (n_b/n_\gamma) = 274 \Omega_b h^2 \tag{2.32}$ 

where  $\eta_{10}$  is the scaled baryon-to-photon ratio,  $n_b$  is the baryon number density,  $n_\gamma$  is the photon number density,  $\Omega_b$  is the baryon density parameter defined as the ratio of baryonic density ( $\rho_b$ ) to the critical density ( $\rho_{crit}$ ), and h is the dimensionless Hubble parameter. The critical density  $\rho_{crit}$  is given by  $\rho_{crit} = 3H_0^2/8\pi G$ , where  $H_0$  is the Hubble constant and G is the gravitational constant. The value of  $\eta_{10}$  has been refined through various theoretical and observational efforts, including the significant contribution from the Wilkinson Microwave Anisotropy Probe (WMAP), leading to an updated value of  $6.0914 \pm 0.0438$  (Planck Collaboration et al. 2016). Based on this value, a higher  $\eta_{10}$  correlates with a faster ignition of deuterium and  $^3He$ , as well as a subsequent reduction in their primordial abundances after 200 seconds, as illustrated in the right panel of Figure 2.1. As the abundance of neutrons decreases after 250 seconds, and the number of neutrino families increases, this directly influences the abundance of  $^4He$ , which rises at around 240 seconds and stabilizes thereafter. The mass fraction of  $^4He$ , denoted as  $Y_p$ , the primordial value from the BBN, can be estimated based on the neutron-to-proton ratio:

$$Y_p = 2\left(1 + \frac{n_p}{n_n}\right)^{-1} {(2.33)}$$

Table 2.1: Yields at CMB-WMAP baryonic density ( $\eta_{10} = 6.0914 \pm 0.0438$ ) adapted from Singh et al. (2023). The numerical values for elements is given in mass fraction ratios.

	2012	2014	2015	2016	2019	2023	Observations
$^4He$	0.2479	$0.2482 \pm 0.0003$	$0.2484 \pm 0.0002$	0.2470	$0.2467 \pm 0.0003$	$0.2461 \pm 0.0002$	$0.2449 \pm 0.0040$
$D/H \times 10^{-5}$	2.563	$2.64^{+0.08}_{-0.07}$	$2.45{\pm}0.05$	2.579	$2.623 \pm 0.031$	$2.620 \pm 0.031$	$2.53{\pm}0.04$
$^{3}He/H \times 10^{-5}$	1.058	$1.05\pm0.03$	$1.07\pm0.03$	0.9996	$1.067\pm0.005$	$1.066\pm0.005$	$1.1 \pm 0.2$
$^{7}Li/H \times 10^{-10}$	5.019	$4.94^{+0.40}_{-0.38}$	$5.61 \pm 0.26$	4.648	$4.447{\pm}0.067$	$4.421 \pm 0.066$	$1.58 \pm -0.28$

Here,  $n_p$  and  $n_n$  represent the number of protons and neutrons, respectively. As the  $\eta_{10}$  value shifts from low to high,  ${}^3He$  facilitates the production of  ${}^7Li$  and  ${}^7Be$  via  $\alpha-\gamma$  reactions. Table 9.2 illustrates the abundance of primordial elements over the last decade, with theoretical models closely mirroring observational data. Following the establishment of primordial element abundances in BBN, the Universe continues to evolve and cool, leading to the formation of regions with local over-densities, crucial for the next stage of its evolution.

#### 2.2 Evolution of the Cosmic Fluid

Observations from the Cosmic Background Radiation (CMB) indicate that the Universe began with an isotropic and near-homogeneous initial density distribution, as described in detail by Klessen & Glover (2023). Spatial fluctuations from this near-perfect distribution are given by  $\delta(x) = \rho(x)/\rho - 1$ , with a magnitude of approximately  $10^{-5}$  on large scales relative to the average background density,  $\rho$ . In a purely baryonic universe the fluctuations would still grow but pressure effects would delay the collapse compared to a  $\Lambda$ CDM universe. However, in a Universe containing dark matter, as postulated by the ACDM model, these fluctuations can grow due to self-gravity. The evolution of such fluctuations ( $\delta$ ) is governed by the Jeans equation, which in the context of an expanding Universe is given by the equation 2.34. In this context, the expanding Universe refers to the continuous growth in size, as indicated by the Hubble parameter (H) in the Jeans equation. The assumption of zero pressure implies the neglect of internal pressure gradients within the cosmic fluid, focusing solely on gravitational effects. This simplification is crucial for studying the growth of large-scale structures where gravity is the dominant force. The modified Jeans criterion in an expanding Universe accounts for the 'drag' effect of expansion on structure growth. This approach is key to understanding the early stages of cosmic structure formation, where density fluctuations begin to evolve into galaxies and other large-scale structures. The equation is given by:

$$\frac{\partial^2 \delta}{\partial t^2} + 2H \frac{\partial \delta}{\partial t} = 4\pi G \rho \delta \tag{2.34}$$

Here,  $\delta$  is the density contrast,  $\frac{\partial}{\partial t}$  denotes a time derivative, H is the Hubble parameter describing the rate of expansion of the Universe, G is the gravitational constant, and  $\rho$  is the average matter density. The  $\Lambda$ CDM model characterizes the initial density fluctuations as a random Gaussian field. The intrinsic properties of this field are elucidated by exploring its power spectrum. Recent studies of these density fluctuations, such as those by the Planck Collaboration Planck Collaboration et al. (2020), have provided precise estimates of the Universe's physical properties up to a redshift of  $z\approx 1000$ . It is now clear that small over-densities and under-densities in the matter distribution of the universe evolve over time, forming the seeds for cosmic structure formation.

#### 2.3 The Birth of the First Stars

A significant aspect of the Big Bang Nucleosynthesis (BBN) is the formation of light elements. The heaviest stable nuclide produced is  ${}^{7}Li$ , while the lightest is hydrogen ( ${}^{1}H$ ), with deuterium ( ${}^{2}H$ ) being a heavier isotope of hydrogen. For neutral hydrogen atoms to form, recombination of protons and electrons is required, a process that becomes possible once the Universe cools down, approximately 380,000 years after the Big Bang. This period is known as the "Dark Age" of the Universe, which persisted until the first generation of stars began to form (Rees 1984).

The earliest stars in the Universe emerged in regions where the cosmic medium met two key conditions. First, the medium must decouple from the cosmic expansion and begin contracting under the influence of dark matter's gravity, forming dark matter halos. Second, the gas within these halos must cool and undergo rapid collapse, leading to an increase in the baryon-to-dark matter ratio and achieving stellar densities. Notably, halos with virial temperatures ( $T_{\rm vir}$ ) exceeding 8,000 K initially cool via Lyman- $\alpha$  emission from atomic hydrogen. In contrast, lower mass halos with temperatures below  $T_{8000}$  cool via molecular hydrogen ( $H_2$ ). These smaller halos are often termed "minihalos". According to the  $\Lambda$ CDM model, gravitational structures form hierarchically, with smaller structures emerging first. This indicates that minihalos are likely the primary sites for the formation of Population III stars.

### 2.4 Gravitational Instability

While dark matter can be treated as a fluid devoid of pressure and with zero temperature, the same cannot be said for the baryonic component of the Universe. On larger scales, dark matter's gravitational effects prevail. However, as we consider smaller scales, the role of gas pressure in baryonic matter becomes increasingly significant. Employing the classical Jeans stability analysis,

a threshold mass scale,  $M_J$ , is determined. Above this scale, gravity dominates and leads to collapse, while below it, gas pressure prevents such a collapse. The Jeans Mass for an isothermal gas sphere, primarily considering the baryonic mass density, is given by:

$$M_J = \frac{5\pi^2}{6} \left(\frac{1}{G}\right)^{3/2} \left(\frac{c_s^2}{\mu m_H}\right)^{3/2} \simeq 50\mu_0^2 \left(\frac{n}{1 \text{ cm}^{-3}}\right)^{-1/2} \left(\frac{T}{1K}\right)^{3/2},\tag{2.35}$$

where n represents the number density of hydrogen nuclei,  $c_s$  the speed of sound, G the gravitational constant,  $m_H$  the mass of a hydrogen atom, T the temperature, and  $M_J$  the Jeans Mass. The gas composition dictates the weighting factor  $\mu=(1+4x)$ , where x represents the Helium to Hydrogen ratio by count. For primarily primordial gas,  $x\approx 0.079$  and  $\mu\approx 1.32$ .

Considering the role of turbulence and magnetic fields, the effective sound speed,  $c_{s, eff}$ , is used. This adjustment to the classical sound speed accounts for the velocity dispersion due to turbulence,  $\sigma$ , and the Alfvén velocity from magnetic fields,  $v_A = \frac{B}{\sqrt{8\pi\rho}}$ , leading to:

$$c_{s,\text{eff}} = \left(c_s^2 + \sigma^2 + \frac{1}{2}v_A^2\right)^{\frac{1}{2}}.$$
 (2.36)

An increase in  $c_{s,eff}$  implies a higher threshold for gravitational collapse, thereby affecting the Jeans Mass and the accretion rate. This relationship provides a more nuanced understanding of star formation and structure formation in astrophysical contexts.

When studying a collapsing sphere, its potential accretion rate in relation to the Jeans mass and its free-fall time  $t_{ff}$  can be given by:

$$\dot{M} = \frac{M_J}{t_{ff}} \approx \frac{M_J}{\sqrt{\frac{3\pi}{32G\rho}}},\tag{2.37}$$

where  $\rho$  refers to the total density. This equation indicates how the accretion rate is influenced by the Jeans Mass, which varies based on the effective sound speed and other physical conditions.

### 2.5 Thermodynamic implications

Another crucial aspect that governs the transition of the Universe to large scale cosmological structures is thermodynamics. The behavior is most effectively captured by the state equation, which correlates thermodynamic parameters such as pressure, density, temperature, and internal energy. This is essential to transform the hydrodynamic equations into a coherent and solvable structure. For clarity, consider the scenario where the gas adheres to an efficient polytropic state

equation:

$$p \propto \rho^{\gamma_{\text{eff}}},$$
 (2.38)

with the index given by

$$\gamma_{\text{eff}} = 1 + \frac{d \ln T}{d \ln \rho}.\tag{2.39}$$

Here,  $\gamma_{\text{eff}}$  signifies the balance struck between different heating and cooling processes (as observed in studies by Klessen & Glover (2016)). Building on Equation 2.35, it's deduced:

$$M_J \propto \rho^{1.5\gamma_{\rm eff}-2}$$
. (2.40)

When  $\gamma_{\rm eff}>\frac{4}{3}$ , the increasing Jeans mass during contraction eventually aligns with the system's mass, which comprises both dark matter and baryons. Consequently, the exerted pressure halts further gravitational contraction. Specifically, for an adiabatic gas where  $\gamma_{\rm eff}=\frac{5}{3}$ , this equilibrium is attained well before achieving stellar densities. To facilitate star formation, it's pivotal for the gas to dissipate energy throughout its collapse, ensuring  $\gamma_{\rm eff}$  stays beneath this threshold. A pivotal factor is the cooling time, which can be gauged against the free-fall timescale:

$$\tau_{\text{cool}} = \frac{1}{\gamma - 1} \frac{n_{\text{tot}} k_b T}{\Lambda(T, n)},\tag{2.41}$$

In this context,  $n_{\text{tot}}$  denotes the total number density of all particles within a given volume, encompassing various types of particles such as atoms, ions, and electrons. The Boltzmann constant is represented by  $k_b$ , and T stands for the temperature of the gas. The symbol  $\Lambda$  is used to denote the cooling rate, which is a measure of how quickly the gas loses its thermal energy per unit time. The interplay between the cooling time ( $\tau_{\text{cool}}$ ) and the free-fall time ( $\tau_{\text{ff}}$ ) dictates the gas dynamics. If  $\tau_{\text{cool}}$  is less than  $\tau_{\text{ff}}$ , the gas cools rapidly, leading to a scenario where it collapses almost as if in free fall. This rapid cooling reduces pressure support, allowing gravity to dominate. On the other hand, if  $\tau_{\text{ff}}$  is shorter than  $\tau_{\text{cool}}$ , the gas retains significant pressure support and the star quickly reaches the hydrostatic equilibrium. This slows down the contraction process, causing the gas to evolve more slowly, over a period roughly equal to  $\tau_{\text{cool}}$ . Such a scenario leads to a quasi-static evolution of the gas.

#### 2.5.1 Instability in Rotating Systems

For systems sustained by rotation, gravitational instability criteria differ due to shearing stabilization. This phenomenon, especially prevalent in ultra-thin disks, was extensively analyzed by

Toomre (1964). The resulting instability condition is given by Toomre's criterion:

$$Q = \frac{kc_s}{\pi G\Sigma} < 1. {(2.42)}$$

Here, Q is the Toomre parameter, k the epicyclic frequency,  $c_s$  the speed of sound, G the gravitational constant, and  $\Sigma$  the surface density. In systems exhibiting Keplerian rotation, k equates to the rotational frequency  $\Omega$ , as discussed by Kratter & Lodato (2016).

This criterion has been adapted for thicker disks with varied components. Elmegreen (2002) and Romeo & Falstad (2013) introduced essential adjustment factors to account for these complexities. Disk fragmentation can result from two primary processes. Gammie (2001) posited that if a disk's cooling duration,  $\tau_{\rm cool}$ , is longer than its orbital period,  $\tau_{\rm orbit} = 1/\Omega$ , it may become unstable. Additionally, if external gas accretion onto the disk exceeds its own inward mass transport, this leads to an increase in  $\Sigma$  beyond the stability threshold, destabilizing the disk. Such scenarios are frequently observed in Pop III accretion disks, which are early Universe systems with a unique composition and dynamics.

#### 2.5.2 Critical mass for halos

Studies on the evolution of density perturbations in an expanding Universe, such as those by Barkana & Loeb (2001), demonstrate that notable baryonic density peaks can form only in halos possessing a mass greater than a certain critical value. This is represented by:

$$M_{\text{crit}} \approx 5 \times 10^3 M_{\odot} \left(\frac{\Omega_m h^2}{0.143}\right)^{-1/2} \left(\frac{\Omega_b h^2}{0.022}\right)^{-3/5} \left(\frac{1+z}{10}\right)^{3/2}$$
 (2.43)

This critical mass is closely related to the Jeans mass (referenced in Equation 2.35), characterized by a density (accounting for DM) approximating the Universe's average and a temperature that diminishes adiabatically with the Universe's expansion. This is valid for  $z \leq 100$  when the gas decouples thermally from the CMB due to Compton scattering. While having a baryonic density peak is essential for the emergence of Pop III stars, it is not the sole requirement. The gas also needs the capability to cool as shown by the relation of  $\gamma_{eff}$  and  $\tau_{cool}$  in equation 2.41. If the effective adiabatic index,  $\gamma_{eff}$ , exceeds the value of  $\frac{4}{3}$ , the Jeans mass during the contraction phase will grow and may eventually match the total mass of the system. Under these circumstances, pressure counterbalances gravitational forces, halting further collapse. This scenario unfolds rapidly for an adiabatic gas with  $\gamma_{eff} = \frac{5}{3}$ , occurring well before the gas reaches stellar densities. For star formation to proceed, the gas must effectively lose energy during collapse, ensuring that  $\gamma_{eff}$  stays

below this pivotal threshold, this necessitates a significantly greater critical mass. For example, Glover (2013) proposed a value based on a rudimentary model examining the gas dynamics in a high-redshift minihalo:

$$M_{\rm crit} \approx 1.4 \times 10^6 M_{\odot} \left(\frac{\Omega_m h^2}{0.143}\right)^{-1/2} \left(\frac{\mu}{1.32}\right)^{-3/2} \left(\frac{1+z}{10}\right)^{-3/2}$$
 (2.44)

The chemical weight factor,  $\mu$ , mentioned in this context, is elaborated upon in Equation 2.35. It must be noted that the two equations 2.43 and 2.44 are simplified models that do not fully capture the Universe's evolving conditions or various physical processes. Detailed nuances are better represented in numerical simulations and complex models, like those by Tseliakhovich et al. (2011). Conclusively, there is significant uncertainty regarding the exact value of  $M_{\rm crit}$ , with varying conclusions from different simulations due to resolution and incorporated processes. A comparison between different studies for  $M_{\rm crit}$  is done in the work by Klessen & Glover (2023) and is illustrated in Figure 2.5.2.

#### 2.5.3 Cosmic PopIII star formation rate density

Within the  $\Lambda$ CDM model, Pop III star formation initiates at redshifts of  $z{\geq}30$  in exceptional high-sigma fluctuations. The rate escalates as an increasing number of halos undergo collapse, peaking at redshifts  $z\approx15{\text -}20$ . While the combined rate of star formation across the entire Universe continues to rise (as observed by Madau et al. (2014)), the specific rate at which metal-free Pop III stars are formed begins to decline. This decline is attributed to the dwindling regions in the Universe untouched by supernova (SN) ejecta from massive stars, marking the segue to the emergence of slightly metal-enriched Pop II stars. Figure 2.3 is taken from Klessen & Glover (2023) and illustrates varying models for the star formation rate density (SFRD) relative to redshift. It highlights the present uncertainties surrounding the inception and progression of high-redshift star formation, as derived from both numerical simulations and semianalytical models.

#### 2.5.4 PopIII formation pathways

Diving into the dynamics of halo gas collapse and star formation, a pivotal element is the gas's cooling capacity. Interestingly, the fundamental cooling mechanisms within gas void of metallicity hinges on hydrogen, either molecular or atomic.

At high temperatures, collisions elevate hydrogen to excited electronic states. These states, when de-excited, release Lyman series photons. This phenomenon, commonly labeled as Lyman—cooling, reaches its maximum efficiency at temperatures close to 10<sup>4</sup> K. However, for tempera-

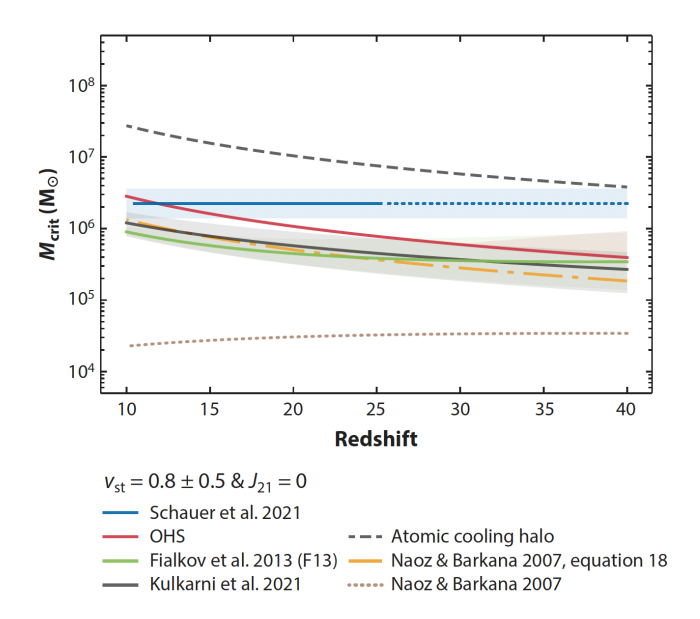


Figure 2.2: This figure is taken from Schauer et al. (2021a). This figure illustrates the critical mass  $(M_{\rm crit})$  necessary for cosmic fluid fluctuations to undergo gravitational collapse, featuring models from various studies including the impact of streaming velocities  $(V_{\rm st})$ . Streaming velocities refer to the relative motion between dark matter and baryonic matter, affecting the growth of cosmic structures. The parameter  $J_{21}$  represents the intensity of the ultraviolet background radiation field, measured in units of  $10^{-21}$  ergs/s/cm²/Hz/sr, which influences the ionization and heating of intergalactic gas. Data from Schauer et al. (2021a) and are highlighted, with the fit from Schauer et al. (2021) extrapolated for redshifts z < 25. The extrapolated part corresponds to blue solid line. The shaded areas in the graph represent variations due to different streaming velocities, with  $V_{\rm st}$  set to  $0.8 \pm 0.5$  and  $J_{21}$  set to 0, indicating models that do not consider external UV radiation fields. The comparison is made between models without streaming velocity effects, and those accounting for it, alongside critical masses for halos capable of atomic cooling. Additional significant studies contributing to this field are referenced in the figure's legend.

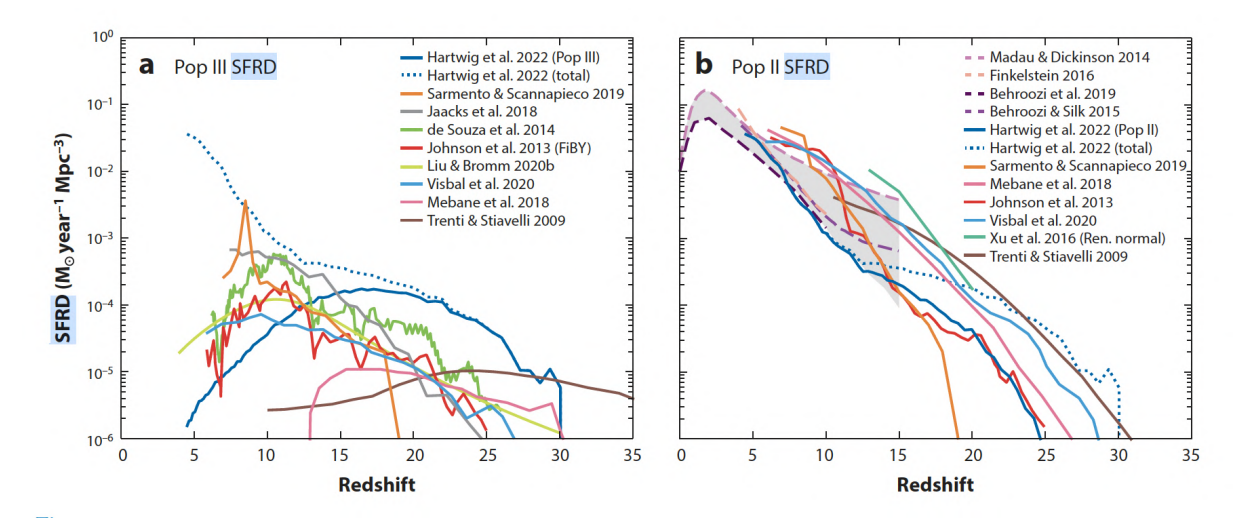


Figure 2.3: Star formation rate density (SFRD) taken from various studies for PopIII and PopII stars at z > 5 done over the past year as shown in the work by Klessen & Glover (2023).

tures to plunge further, molecular hydrogen  $(H_2)$  steps into the picture. The peculiarities of  $H_2$ , its lightweight nature combined with its non-existent dipole moment, restrict its cooling capability at extremely low temperatures. The lowest energy radiative transition of H2, the  $J=2 \rightarrow 0$  transition in its vibrational ground state, corresponds to approximately 512 K. Despite this, the thermal Maxwell-Boltzmann velocity distribution's high-velocity end allows cooling slightly below this temperature, to nearly 200K, as highlighted by Greif (2015). Such a phenomenon is termed as the Pop III.1 formation route.

Surprisingly, the temperature can plummet further with the intervention of deuterated hydrogen (HD) cooling (Nagakura & Omukai 2005). HD's unique non-zero dipole moment ensures its lowest energy transition between J=1 and J=0 rotational levels occurs at a very low temperature of 128 K. This Pop III.2 formation pathway becomes especially pertinent in regions with heightened fractional ionization. At sparse densities,  $H_2$  can primarily form through:

(a) A two-step reaction using an  $H^-$  ion as an intermediary:

$$H + e^- \to H^- + \gamma \tag{2.45}$$

$$H^- + H \to H_2 + e^-$$
 (2.46)

(b) A pathway with  $H_2^+$  as the intermediary molecule:

$$H + H^+ \to H_2^+ + \gamma$$
 (2.47)

$$H_2^+ + H \to H_2 + H^+$$
 (2.48)

Both mechanisms require the gas to be slightly ionized, with the molecular fraction typically around  $10^{-3}$ . At much higher densities, exceeding  $10^9$  cm<sup>-3</sup>, tri-body reactions become important:

$$H + H + H \to H_2 + H$$
 (2.49)

As a result, atomic hydrogen converts to  $H_2$  at particle densities near  $10^{11}$  cm<sup>-3</sup>. Yet, when the collapse intensifies and temperatures exceed 2,000 K at densities above  $10^{13}$  cm<sup>-3</sup>,  $H_2$  molecules undergo collisional dissociation, reverting the gas to an atomic state.

# 2.5.5 Primordial stellar models

With the establishment of gas cooling and heating mechanisms and the corresponding chemical reaction network described in previous section, it is possible to follow the initial collapse phase

from the cosmic mean up to the formation of the first hydrostatic core. To explore this phase further, seminal work by Clark et al. (2011) provides valuable insights and is shown in Figure 2.4. Using the data provided in this work, we can obtain a rough estimate of the in-fall rate of matter onto the center of halo. This in-fall of matter is referred to as the accretion rate and is:

$$\dot{M} = \zeta \left(\frac{M_j}{\tau_{ff}}\right) \propto \left(\frac{c_s^3}{G}\right)$$
 (2.50)

Here,  $M_J$  is the Jeans mass is approximately  $50~\rm M_\odot$  and is given by  $M_J \approx 50 M_\odot \mu^{-2} n^{-1/2} T^{3/2}$ . Remember that this is much less than a typical  $M_J$  of  $3000~\rm M_\odot$ . In this equation,  $\mu$  is the mean molecular weight, T is the temperature in Kelvin usually around  $6000\rm K$ , n is the number of particles per cubic centimeter, usually between 1-10. Additionally,  $c_s$  is the sound speed in a medium and given by  $c_s = \sqrt{\frac{\gamma k_B T}{\mu m_H}}$ , free fall time is given by  $\tau_{ff} \approx 52 Myr$ . The value of  $\zeta$  depends on the relation between the gas mass and  $M_J$  and is described in detail in studies by Larson (1969); Yoshida et al. (2007). Work by Haemmerlé et al. (2018) show that for a gas temperature of around 1500 K, the accretion rate,  $\dot{M} \approx 2 \times 10^{-3}~\rm M_\odot yr^{-1}$  and the dominant cooling mechanism is molecular (H<sub>2</sub>) hydrogen.

# 2.5.6 Disc fragmentation

Understanding the processes underlying the formation and fragmentation of disks is fundamental to the dynamics of primordial star formation. The turn of the millennium marked the availability of the first 3D simulations that were instrumental in tracing the initial cooling and collapse phases of gas within high-redshift minihalos (Bromm et al. 1999, 2002; Abel et al. 2002; Nakamura & Umemura 2001). Despite their three-dimensional modeling, these simulations were geared towards halos that presented an inherent spherical symmetry, an approximation deemed suitable due to the round nature of these halos.

These pioneering simulations faced computational constraints when reaching hydrogen number densities of  $n \approx 10^{16} \, \mathrm{cm}^{-3}$ . At this density, the central hydrostatic object amassed a mass of about  $\approx 10^{-3} M_{\odot}$ . Notably, the material exhibited minimal angular momentum upon reaching the center, leading to a pressure-supported disk-like structure.

Crucially, the supposition from these early works suggested the convergence of all the infalling mass into one high-mass star. This stood in contrast to patterns observed in contemporary star formation, where fragmentation was ubiquitous, and massive stars frequently resided within clusters (Lada & Lada 2003).

A decade later, simulations with enhanced resolutions began to shed more light. Greif et al.

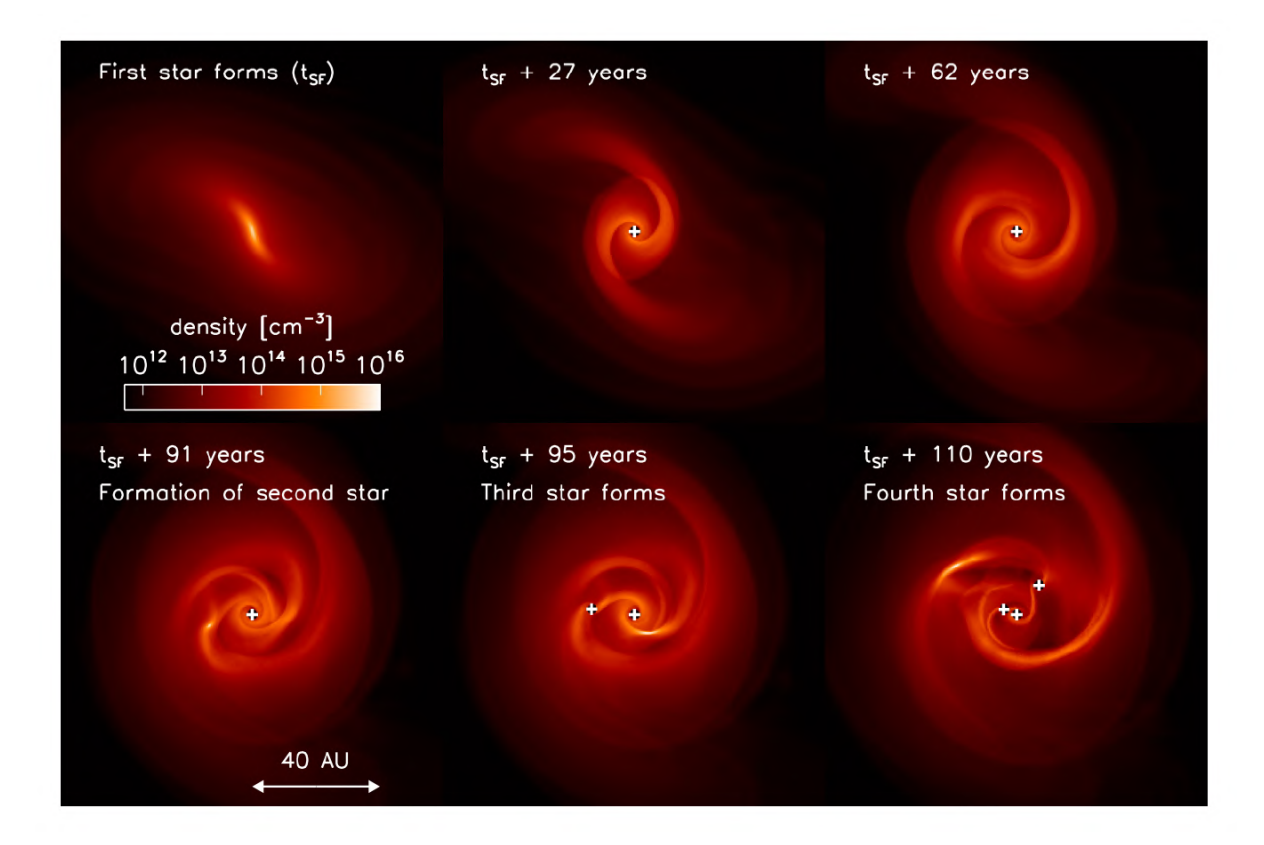


Figure 2.4: In a 120 AU zone around the initial protostar, density evolution reveals the protostellar disk's formation and subsequent fragmentation. The notable two-arm spiral arises from disk gravitational instability, with gravitational torques driving the main angular momentum transfer, enabling material accretion onto the protostar. As mass influx from the falling envelope continues, the disk's instability causes the spiral arms to become self-gravitating, leading to fragmentation and the creation of a multiple system. Taken from Clark et al. (2011).

(2011) visually detailed star-forming halos across varied scales. The gas virialized, underwent a runaway collapse in the central 10 pc, and subsequently formed a molecular core of about 200 AU. Notably, while halo parameters were consistent on expansive scales, smaller scales showed differentiation attributed to each halo's distinct dynamical properties. The gas collapse induced turbulence, introducing stochasticity in the structural appearance of central regions. Minor initial fluctuations, when amplified during nonlinear collapse, could lead to divergent evolutionary trajectories. Greif et al. (2011) found that HD cooling was selective, influencing fragmentation behaviors and emphasizing the significance of initial conditions.

With advancements in simulation capabilities, studies delved into the dynamics of the accretion disk. Here, the susceptibility of primordial accretion disks to fragmentation became apparent. Such findings, as discussed by Machida et al. (2008a) and Turk et al. (2009), suggested the formation of a varied stellar cluster, rather than a singular high-mass star.

A key factor inducing fragmentation was the disk's inefficacy in translocating the incoming

material due to gravitational or magnetoviscous torque limitations. This gave rise to significant spiral arms which, failing in inward material translocation, would collapse, intensifying fragmentation. Clark et al. (2011) demonstrated the emergence of multiple protostars within a short span post the formation of the initial accretion disk.

In the broader perspective of the early Universe, regions dominated by molecular hydrogen cooling showed different fragmentation scales compared to those influenced predominantly by atomic cooling. As inferred from the cooling and fragmentation thresholds, the molecular regions seemed to favor fragmentation at relatively lower densities of  $n \approx 10^8 - 10^{10} \, \mathrm{cm}^{-3}$ , whereas the atomic regions showed fragmentation at much higher densities, closer to  $n \approx 10^{16} \, \mathrm{cm}^{-3}$ . This stark contrast hints at the role of thermal processes and their interplay with gravitational dynamics in influencing fragmentation scales.

### 2.5.7 IMF for PopIII stars

Primordial accretion disks frequently fragment, presenting challenges in understanding the fate of these fragments. Three potential outcomes emerge: fragments can grow into a star or substellar object, be absorbed by the central star, or merge with another fragment. These outcomes raise questions about what sets the final mass of surviving fragments. There are three primary scenarios. Firstly, the system could exhaust its available mass, leaving behind sizable stars, which has implications for their detectability at high redshifts. Second, stellar feedback might deplete material, halting further accretion. This outcome varies greatly, with available simulations producing diverse results. Lastly, dynamical interactions could eject a fragment from the disk, typically resulting in the formation of low-mass objects. Some of these could exist even today, possibly identifiable through stellar archeological surveys.

As material gravitates toward the disk's center, protostars situated at the furthest edges of the disc will consume some of the in falling matter, thereby decreasing the amount of gas available for the central object. This phenomenon significantly diminishes the growth rate of mass at smaller radii, possibly causing the primary central object to starve, as evidenced by Girichidis et al. (2011). In simple binary systems observed today, stars generally have comparable masses mainly due to observational bias. Yet, the complex processes characterizing Population III star formation, including erratic events such as ejections, mergers, and accretion by the primary star, indicate a wide range of possible stellar masses.

Various studies, such as those by Greif et al. (2012) and Stacy & Bromm (2013) indicate that about two-thirds of fragments vanish rapidly, leaving one-third persisting. However, these numbers warrant cautious interpretation. The simulations don't fully encapsulate disk evolution, and

the highest-resolution models cover the least duration. Some considered "ejected" protostars might return and be subsequently accreted. Notwithstanding these complexities, a rough estimate suggests a 1:2 ratio between survivors and mergers. Furthermore, Susa (2019) proposed that the total fragment count increases over time.

Stacy & Bromm (2013) further show the behavior of the most tightly bound pairs in these systems. They discovered a binary fraction of about 35%, with significant semimajor axes and a broad range of orbital periods. Armed with this knowledge, researchers have the tools to simulate extensive ensembles of Pop III binary systems, employing specialized N-body simulations or semianalytic models, as demonstrated by Santoliquido et al. (2021); Liu et al. (2021).

The subsequent stellar mass distribution of Pop III stars remains an area of intense debate. Known as the initial mass function (IMF), the stochastic nature of the fragmenting processes contributes to an expansive range of stellar masses. Every model to date suggests possible masses ranging from the substellar domain to several hundred solar masses. High-resolution models without stellar feedback, such as those by Prole et al. (2022), reveal variations in the resulting mass spectrum due to resolution differences.

In summary, understanding the IMF of primordial stars remains a challenge. Existing models exhibit individual limitations. Some cannot achieve the required resolution, some don't cover the necessary time frame, and others may not incorporate all pertinent physical processes. As observed in the mentioned studies, models considering stellar feedback generally predict lower stellar masses. Resolution differences and the covered time span in simulations significantly influence outcomes, especially concerning disk fragmentation and the resulting stellar mass predictions. The overall findings emphasize the necessity for further high-resolution, long-duration simulations that encompass all critical physical processes to provide clarity on the IMF of primordial stars. Now we will explore the impact of various physical ingredients affecting the birth of the first stars in model detail.

# 2.5.8 Magnetic fields

Magnetic fields, present across a multitude of scales in today's universe have profound implications (Beck 1996). They are central to star formation, influencing interstellar media dynamics, and potentially contributing to the evolution and formation of supermassive black holes (SMBHs).

Our grasp of these fields, particularly at high redshifts, is somewhat limited. Theoretical models suggest diverse mechanisms for their emergence. One of the initial concepts is the battery processes, theorized by Biermann in 1950 (Biermann 1950). This process suggests that magnetic fields can sprout from thermoelectric effects in plasmas. The Weibel instability, as explored by

Medvedev & Silva (2004) and Lazar et al. (2009), offers another mechanism, where fields arise from anisotropic temperature or density variations in plasmas. A third proposal, by Schlickeiser & Shukla (2003), considers the role of thermal plasma fluctuations in generating magnetic fields. Beyond these theories, cosmological perspectives exist, emphasizing phase transitions during inflationary periods of the universe, as posited by several researchers like Sigl et al. (1997) and Grasso & Rubinstein (2001).

Despite the various genesis theories, fields resulting from these mechanisms are often deemed dynamically negligible due to their presumed weakness. Many early astrophysical models, especially those centered on SMBH formation, overlooked magnetohydrodynamic influences. However, the significance of the small-scale turbulent dynamo in this context is gaining recognition. Amplification rates align with the eddy-turnover time on certain scales and are influenced by the Prandtl numbers, as shown by Kazantsev (1968) and Subramanian & Barrow (1998). The Prandtl number (Pr) and magnetic Prandtl number (Pm) are dimensionless quantities in fluid dynamics and magnetohydrodynamics, respectively, that compare different diffusion rates. The Prandtl number is given by

$$Pr = \frac{\nu}{\alpha},\tag{2.51}$$

where  $\nu$  is the kinematic viscosity and  $\alpha$  is the thermal diffusivity. It measures the ratio of momentum diffusion to thermal diffusion. The magnetic Prandtl number, defined as

$$Pm = \frac{\nu}{\eta},\tag{2.52}$$

where  $\eta$  is the magnetic diffusivity, compares the momentum diffusion to magnetic field diffusion. These numbers are critical in the study of turbulent dynamos, where they influence the amplification and structure of magnetic fields in protostellar environments. This rapid amplification leads to a complex magnetic field configuration, with dominant fluctuations on the minutest scales. As the fields evolve, backreactions moderate their growth, eventually reaching saturation after a few large-scale eddy-turnover durations, a phenomenon supported by research from Schober et al. (2015). An example of such a dynamo for a collapsing primordial halo is depicted in Figure 2.5. The emerging magnetic field layout exhibits intricate complexity. The system's energy density is predominantly influenced by fluctuations on the minutest scales available. When backreactions gain prominence, the amplification rate diminishes, culminating in saturation after several large-scale eddy turnover periods.

When considering the protostellar environment, these magnetic fields take on multifaceted roles. They adeptly redistribute angular momentum in star-forming gases, thereby influencing

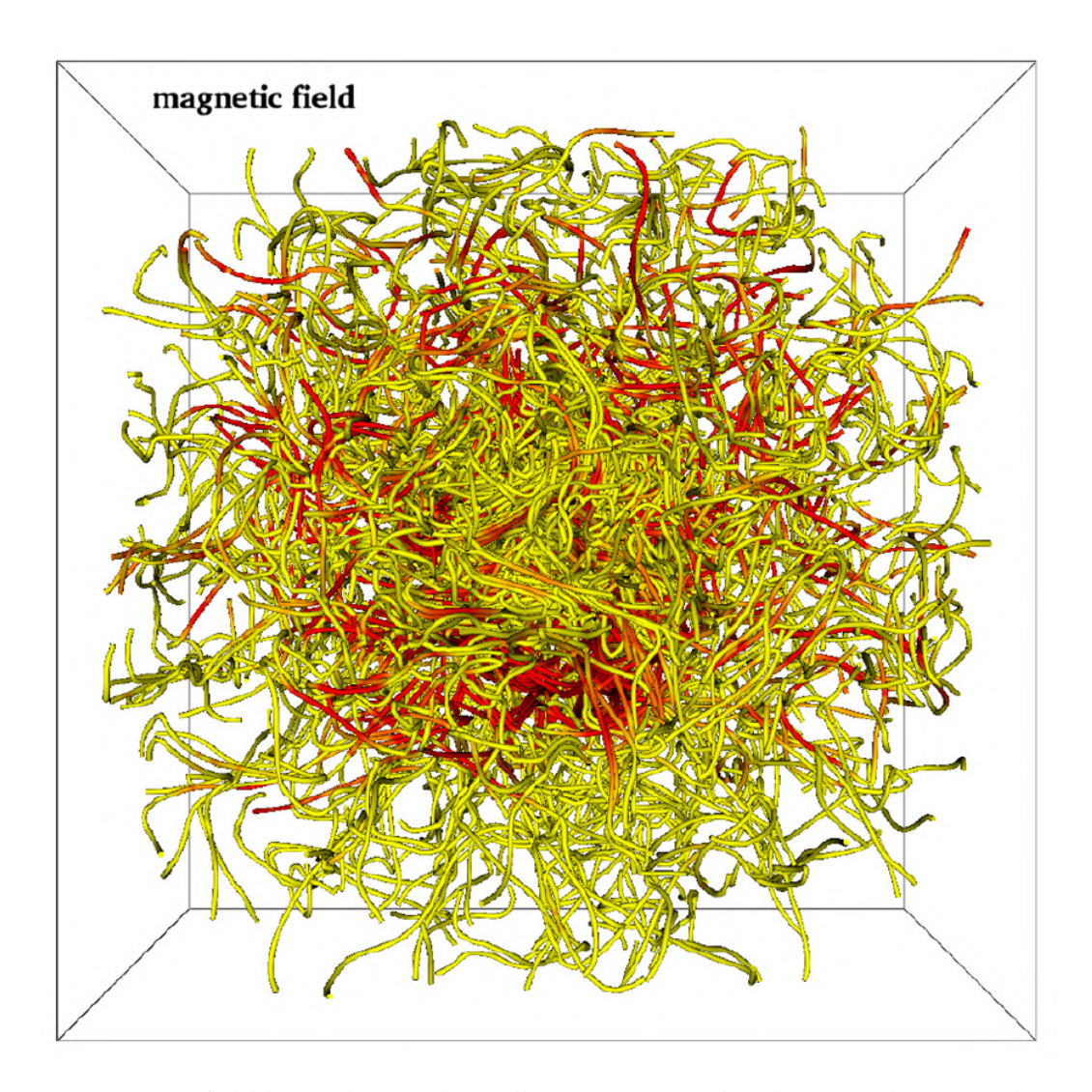


Figure 2.5: Magnetic field lines, depicted in yellow  $(0.5 \,\mu\text{G})$  and red  $(1 \,\mu\text{G})$ , showcase the intricate magnetic field configuration at the core of a collapsing primordial halo, an outcome of the small-scale dynamo. This visualization is based on the work of Federrath et al. (2011) and is taken from Woods et al. (2019).

the nascent structures of stars and potentially even affecting the initial mass function of stars in Pop III clusters. Research by Machida et al. (2008b) and Machida & Doi (2013) further underscores this. Additionally, magnetic fields propel protostellar jets and outflows, a mechanism crucial for stellar birth as shown by Machida et al. (2006). A pivotal implication, particularly in the context of SMBH formation, is the fields' capability to curb fragmentation in protostellar accretion disks. This suppression may pave the way for SMBH formation via direct collapse, a hypothesis supported by findings from Turk (2011) and Peters et al. (2014). Yet, simulating these interactions offers challenges. Initial magnetic field conditions, whether homogeneous or tangled, drastically affect subsequent developments. The specific topology of these fields in primordial environments, whether smooth or turbulent, impacts their evolutionary trajectory, and subsequently, their in-

fluences on cosmic structures. Conclusively, the intricate interplay between magnetic fields and cosmic entities, be it gases, stars or SMBHs, remains a domain demanding rigorous exploration.

#### 2.5.9 Radiative fields

As PopIII stars progress to the hydrogen-burning main sequence, their accretion continues, a phenomenon highlighted by Zinnecker & Yorke (2007); Yorke & Bodenheimer (2008); Maeder (2009). For accretion rates below  $10^{-3}M_{\odot}$ , these stars remain compact and hot, emitting a significant amount of ionizing photons. When accretion rates exceed  $10^{-2}M_{\odot}$ , their evolution differs. Studies by Hosokawa et al. (2016) and Umeda et al. (2016) suggest that these stars become larger with lower surface temperatures. In the right conditions, this might lead to the emergence of supermassive stars.

Modern star formation models, such as those by Yorke & Sonnhalter (2002) and Kuiper et al. (2010), indicate that protostellar accretion disks quickly become gravitationally unstable. Material moves inward in these disks, and radiation finds pathways to escape. Keto (2007) emphasized that the dynamical evolution of disk material, not radiative feedback, controls the accretion process. Protostellar disks around Pop III stars are hotter and less efficient at cooling than present-day disks, primarily due to the absence of metals and dust. The applicability of current models to the primordial context is unclear.

Simulations by researchers like Hirano et al. (2014a) suggest that radiative feedback can hinder stellar growth, giving masses ranging from a few tens to about 1000  $M_{\odot}$ . Yet, three-dimensional models, such as those by Stacy et al. (2012), show extensive disk fragmentation. The challenge remains in accurately modeling the dynamics and feedback mechanisms of Pop III stars.

# 2.5.10 Streaming Velocities

Streaming velocities describe the speed differences between baryonic matter and dark matter, first identified at a redshift around  $z \approx 1000$ . Prior to the recombination epoch, baryons and photons were tightly coupled, producing acoustic oscillations between baryons and dark matter, as described by Sunyaev & Zeldovich (1970). This interaction established relative velocities-differential speeds between baryonic and dark matter up to 30 km/s at a redshift  $z \approx 1000$ , along with coherence lengths, or scales of uniform velocity, spanning tens to hundreds of mega parsecs (Mpc) (Silk 1986; Tseliakhovich & Hirata 2010a). As the universe evolved, these velocities decreased linearly with the redshift. By  $z \approx 30$ , they had lessened to approximately 1 km/s, which coincides with the virial velocities-equilibrium speeds for gravitational binding of the first halos poised for cooling

and collapse. These streaming velocities, significant for their kinetic energy, could significantly alter gas dynamics and early star formation within these halos (Greif et al. 2011; Fialkov et al. 2012).

Numerical simulations offer insights into the implications of these velocities. For instance, they suggest that the kinetic energy introduced by the streaming velocity could limit baryon overdensity in lower-mass halos, postponing the advent of cooling. This might push up the critical mass needed for collapse, influencing patterns like the 21 cm emission (Visbal et al. 2012). Additionally, streaming velocities have been postulated to potentially create conducive conditions for the genesis of supermassive black holes (SMBHs) by inhibiting fragmentation and the birth of standard Population III stars (Tanaka & Li 2014). While such velocities may suppress H2 formation, leading to a reduction in cooling, the swift emergence of H2 once collapse commences indicates the persistence of traditional star formation modes. Thus, despite the impacts of streaming velocities, external irradiation still appears vital for the direct collapse-driven formation of SMBHs, a perspective further endorsed by Schauer et al. (2017).

#### 2.5.11 Dark matter annihilation

The enigmatic nature of dark matter, despite its crucial role in cosmic evolution and structure formation, remains a mystery. Many hypotheses, rooted in theories like supersymmetry, propose that dark matter might consist of weakly interacting massive particles (WIMPs). These particles, anticipated to be the lightest supersymmetric entities, align with the characteristics required for dark matter as by design (Jungman et al. 1996; Bertone et al. 2005). As baryonic matter collapses at the heart of early primordial halos, it might drag dark matter particles with it, leading to a phenomenon called 'adiabatic contraction' (Blumenthal et al. 1986). This could amplify the central dark matter density manifoldly. Given that the annihilation rate of dark matter grows exponentially with its density, this could result in an energy and ionization rate high enough to affect the gas dynamics significantly. Such processes, as suggested by the likes of Spolyar et al. (2008) and Freese et al. (2009), have the potential to offset the cooling effects of molecular hydrogen (H<sub>2</sub>). The outcome could be a halt in the gravitational collapse, resulting in the formation of unique entities termed 'dark stars'. Unlike traditional stars, these massive bodies, spanning several astronomical units, might be powered by dark matter annihilation rather than nuclear fusion, ensuring their stability over extended periods.

However, several complexities surround this notion. One intriguing aspect of this scenario is the interaction between dark matter annihilation-induced heating and molecular hydrogen ( $H_2$ ) formation. Increased heating from dark matter annihilation can lead to more frequent collisions

among hydrogen atoms, potentially enhancing the formation of  $H_2$ . This is because the elevated kinetic energy increases the likelihood of producing  $H^-$  ions, a precursor in  $H_2$  formation. Consequently, a higher concentration of  $H_2$  can lead to more effective cooling, as  $H_2$  efficiently radiates away heat through photon emission. This complex interplay between heating and cooling could thus influence the collapse and star formation processes within primordial gas clouds (Ripamonti et al. 2009). Another significant contention is the assumption of a perfect synergy between dark matter and gas collapse. Realistic conditions, as showcased in simulations by Stacy et al. (2012, 2014), indicate a potential misalignment, diminishing the effectiveness of annihilation energy for forming dark stars. Nevertheless, there's a possibility that dark matter annihilation may reshape the dynamics within the halo's accretion disk, potentially curbing disk fragmentation. Such influences could modify the attributes of metal-free stars, leaning them towards greater masses. However, as evident in the studies conducted thus far, our understanding of the intricacies of this process remains in its infancy. As a result, making definitive conclusions about its impact on the IMF of Pop III stars is premature.

# 2.6 Supermassive stars

The universe, with its vast expanse, is home to enigmatic celestial entities, among which supermassive black holes (SMBHs) stand prominent. These SMBHs, often observed with masses surpassing  $10^9~{\rm M}_{\odot}$ , are especially intriguing due to their presence at high redshifts (z >6), (Mortlock et al. 2011; Bañados et al. 2018). Their formation and existence, especially at such early cosmic times, challenge our understanding and require reevaluation of the accretion rates and seed formation mechanisms. The potential formation pathways leading to SMBHs were foundationally discussed by Rees (1978). The Rees diagram, shown in Figure 2.6 postulated several progenitors, including the likes of supermassive stars (SMSs), dense stellar clusters, and other compact entities. Originally, SMSs were thought to be the culprits behind the emissions in active galactic nuclei. However, with time and further investigations, it was discerned that SMBHs during their accretion phase are the true powerhouses (Rees 1984).

Despite these insights, the exact mechanisms and pathways leading to the formation of SMBHs remain elusive. The presence of these massive entities during the universe's infancy, particularly within 800 million years post-Big Bang, is perplexing. The duration required for a black hole to expand through Eddington-limited accretion, transitioning from an initial mass  $M_i$  to a concluding mass  $M_f$ , can be represented by the equation:

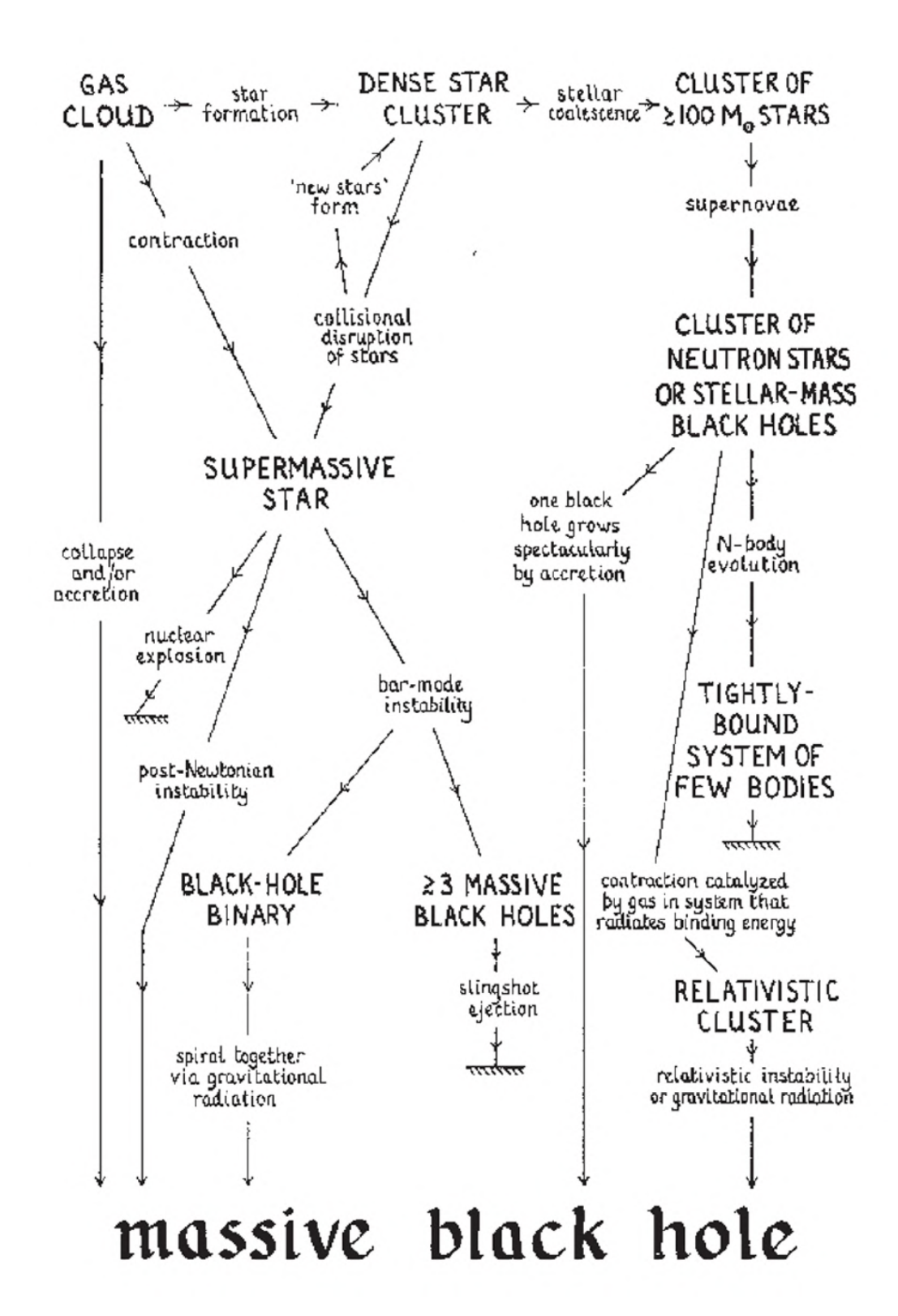


Figure 2.6: The diagram by Rees (1978) illustrates the potential formation routes for supermassive black holes.

$$\tau = \frac{0.4 \times \epsilon}{f_{\rm Edd} \times (1 - \epsilon)} \ln \left(\frac{\dot{M}_f}{\dot{M}_i}\right) \text{Gyr}, \tag{2.53}$$

where  $\epsilon$  stands for the accretion efficiency, which is generally about 0.1 when accreting via a slender disk (Shakura 1973). Meanwhile,  $f_{\rm Edd}$  denotes the duty cycle. A comprehensive discussion on this can be found in Inayoshi et al. (2020). To cultivate a supermassive black hole (SMBH) with a mass of  $10^9 M_{\odot}$  at z=7, initiating from a seed mass of  $10^2 M_{\odot}$ , an estimated duration of approximately 0.8 Gyr is essential. This timeframe surpasses the Universe's age at the mentioned redshift, even under the improbable premise of maintaining  $f_{Edd} = 1$ . Any reduction in  $f_{Edd}$  would amplify this mismatch. Theoretically, surpassing the Eddington limit in accretion rate is feasible if the accretion flow diverges substantially from a spherically symmetrical structure, directing material to the black hole in a pronounced filamentary manner. Alternately, this can also occur if the accretion disk is radiatively ineffective or if the encircling envelope emits in an anisotropic manner (Mayer et al. 2010a). Nonetheless they concluded that the deduced short quasar duty cycles mandate accretion rates significantly surpassing the Eddington limit during their active accretion phases. Short duty cycles seems implausible, leading to the favored hypothesis for SMBH formation at high redshifts: commencing with bulkier seeds, essentially elevating  $M_i$  to a considerably higher value. Constructing such a massive initial object necessitates extremely high accretion rates, demanding remarkably unique environmental prerequisites. It's evident that the encompassing halo must possess a significant mass to house an ample gas volume. To form a seed with a mass of  $10^5 M_{\odot}$ , a halo with a mass of about  $10^7 M_{\odot}$  is needed, unless an unrealistically large fraction of gas is assumed to contribute to the forming black hole. Ten million solar masses significantly exceeds the critical halo mass necessary for Population III star formation, suggesting that gravitational collapse and subsequent star formation might be delayed in such scenarios (because such massive halos are produced by merging of the initially less massive halos). A potential solution for forming supermassive black holes in the early universe is to consider the formation of supermassive stars as a pathway. Models of single supermassive stars have been shown to reach masses upwards of  $10^5$  M<sub> $\odot$ </sub> in the works by Hosokawa et al. (2012); Woods et al. (2017); Haemmerlé et al. (2018). Such objects if formed early enough (200 Myrs after the Big Bang) can collapse in to a black hole and accrete below the Eddington value and reach the masses we observe today. This implies such massive halos are not always needed to produce SMBHs. SMSs are postulated to have played a significant role, given their size and the environment they emerged within. One theory, the direct collapse (DC) model, proposes that supermassive stars (SMSs) attained their massive sizes through rapid mass accretion, particularly in atomic cooling primordial haloes (Bromm & Loeb 2003). Notably, while extensive research has been conducted on the evolution and final fates of these SMSs (Hoyle & Tayler 1964; Unno 1971; Fricke 1973; Fuller et al. 1986), there remains a significant gap in understanding their initial formation processes. The traditional 'monolithic' model

assumes that a SMS initially existed in a stable nuclear burning phase, and research has primarily focused on tracking its evolution from this point. In other words, monolithic implies an agnostic approach on the formation scenario of SMS.

However, delving deeper into the actual formation mechanisms of SMSs is pivotal, particularly when one considers the complexities of star formation. For instance, the stellar radiative feedback against the accruing mass is a potential inhibitor in forming sizable stars. Existing research, such as that by McKee & Ostriker (2007), suggests that in typical primordial star formations, where star sizes average around  $100~{\rm M}_{\odot}$ , the UV feedback from the star itself might be powerful enough to disrupt further mass accretion (Hosokawa et al. 2011; Sugimura et al. 2020). This understanding, when applied to the DC model, implies a challenge: a heightened UV feedback could potentially halt the formation of SMSs altogether. A more nuanced comprehension of accreting SMSs from inception is thus essential, not just to gauge the strength of the UV feedback but also to understand their eventual destiny, be it stable existence or eventual collapse into a black hole. In conclusion, our endeavor to decode the mysteries of SMBHs remains ongoing. The intertwining tales of SMBHs, their potential SMS progenitors, and the challenging conditions of the early universe offer a rich tapestry for further exploration and discovery.

# 2.6.1 Classical description

The very first description of SMS was done in the context of radiation dominated stars in the early 70s following the work by Chandrasekhar (1964a). This section covers the estimation of physical parameters such as mass, radius and density of SMS. The roadmap for this section is as follows:

- Fundamental Physics of SMS: Exploration of the unique characteristics of SMS, particularly
  their reliance on radiation pressure, and the mathematical relationships between pressure
  and density.
- Equations Governing SMS: Presentation of the equations that define the internal dynamics of SMS, including expressions for matter (gas) pressure, radiation pressure, and the critical ratio of matter to radiation pressure ( $\beta$ ).
- Mass and Radius Calculations: Derivation of the mass and radius of SMS, linking these
  macroscopic properties to the microscopic physics governed by quantum mechanics and
  general relativity.

- **Stability Analysis:** Examination of the star's vibrational modes and the application of a stability theorem, focusing on the transition from stability to instability at specific densities.
- Theoretical Implications and Limitations: Discussion of the theoretical implications of these
  findings, especially the potential energy release during star contraction and the limits set by
  Newtonian and relativistic dynamics.

We will now begin with the mathematical developments.

#### **Fundamental Physics of SMS**

Unlike conventional stars sustained by matter pressure, supermassive stars stand against gravity primarily through radiation pressure. Assuming a state of convective equilibrium and uniform chemical composition, the star behaves as a polytrope with an index  $\gamma=4/3$  (implying that star is unstable), where the pressure p is related to the density  $\rho$  by:

## **Equations Governing SMS**

$$p = K\rho^{4/3} \tag{2.54}$$

The radiation pressure  $p_r$  adheres to the Stefan-Boltzmann law:

$$p_r = \frac{\pi^2 (kT)^4}{45\hbar^3 c^3} \tag{2.55}$$

Matching pressure with radiation pressure, we find the temperature inside such a star follows:

$$kT = \left(\frac{45\hbar^3 c^3}{\pi^2} K\right)^{1/4} \rho^{1/3} \tag{2.56}$$

The pressure of matter within supermassive stars,  $p_m$ , adheres to the ideal gas law, expressed as:

$$p_m = \rho \frac{kT}{\hat{m}} \tag{2.57}$$

Here,  $\hat{m}$  is the mean mass of the constituent gas particles. Consequently, the ratio of matter to radiation pressure is captured by the parameter  $\beta$ :

$$\beta = \frac{p_m}{p_r} = \frac{45\hbar^3}{2\hat{m}\pi^2} \left(\frac{\rho}{(kT)^3}\right) = \frac{1}{\hat{m}} \left(\frac{45\hbar^3}{\pi^2 K^3}\right)^{1/4}$$
 (2.58)

This ratio,  $\beta$ , remains constant throughout the star and can replace K in defining the equation of state. Thus, we can rewrite K as:

$$K = \left(\frac{45\hbar^3}{\hat{m}^4 \pi^2 \beta^4}\right)^{1/3} \tag{2.59}$$

#### Mass and Radius Calculations

The mass M of a supermassive star, in the context of a polytrope with  $\gamma = 4/3$ , is then derived from the polytropic relation:

$$M = 4\pi (2.01824) \left(\frac{K}{\pi G}\right)^{3/2} \tag{2.60}$$

Employing the above definition of K, the mass formula refines to:

$$M = \frac{12\sqrt{5}}{\pi^{3/2}} \left(\frac{2.01824}{\hat{m}}\right) \left(\frac{\hbar^3}{\hat{m}^2 c^3}\right)^{3/2} \beta^{-2}$$
 (2.61)

From this, we infer the mass of the star in terms of the fundamental constants, the mean mass of the particles, and the  $\beta$  parameter. For ionized hydrogen at temperatures between  $10^5 K$  and  $10^{10} K$ , the mean mass of the gas particles, denoted by  $\hat{m}$ , is approximately the mass of the proton divided by two. This leads to a scenario where the radiation pressure can significantly exceed gas pressure. If we define the mass of such a supermassive star to be M, where we assume the radiation pressure to dominate the gas pressure by a factor of ten, we get  $M \geq 7200 M_{\odot}$ . While no definitive observation of such supermassive stars exists, they are postulated to be potential sites for the production of energy via gravitational collapse. The radius R of a supermassive star, modeled as a Newtonian polytrope with  $\gamma \approx \frac{4}{3}$ , can be expressed in terms of the central density  $\rho(0)$  as follows:

$$R = \left(\frac{K}{\pi G}\right)^{1/2} \rho(0)^{-1/3} \tag{2.62}$$

We can use this to obtain the relation to radius:

$$R = \left(\frac{45}{\pi^5}\right)^{1/6} (6.89685) \left(\frac{\hbar}{\hat{m}c}\right)^{1/2} \left(\frac{k}{\hat{m}\beta^4}\right)^{1/3} \rho(0)^{-1/3}$$
 (2.63)

This relation illustrates how the macroscopic properties of a supermassive star are intricately linked to the microscopic physics governed by quantum mechanics and general relativity. The radius of supermassive stars is constrained by the assumption that the rest-mass energy is paramount compared to both radiant and thermal energies. This leads to a condition linking the density  $\rho$  to the star's temperature as dictated by the hydrostatic equilibrium, which can be written as:

$$\pi^2 \left(\frac{kT}{\hbar c}\right)^4 < \frac{15}{\hbar^3 c^3} \rho \tag{2.64}$$

Employing our previous definitions and expressions, this condition simplifies to:

$$\rho < \frac{\pi^2 \beta^4 \hat{m}^4}{1215\hbar^3} \tag{2.65}$$

The central density  $\rho(r=0)$  being the greatest, we can apply this as a condition at the center. Using equations (11.5.8) and (11.5.9) to express  $\beta$  and  $\rho(0)$  in terms of the mass M and radius R, we find:

$$\frac{MG}{R} < \frac{4}{3} \left( \frac{2.01824}{6.89685} \right) = 0.39 \tag{2.66}$$

This inequality implies that for a supermassive star with mass M to be stable, particularly for masses around  $10^4 M_{\odot}$ , the radius must exceed approximately  $4 \times 10^4$  km. While general relativity is not necessary to understand the structure of these stars, it becomes crucial when considering their stability, as the balance between stability and instability is delicate and influenced even by small relativistic effects.

#### **Stability Analysis**

The investigation into the stability of supermassive stars extends beyond the derivation of equilibrium conditions, such as those given by the equation of mass conservation shown in eq.2.67. While this equation describes how mass distribution varies with radius within the star, determining stability requires an examination of the star's vibrational modes.

$$M'(r) = 4\pi r^2 \rho(r) (2.67)$$

To ascertain stability, we analyze the frequencies  $\omega_n$  of all normal modes. A positive imaginary component in any frequency signifies an unstable mode, indicating that the star may be prone to collapse or dispersion. But before we proceed with this, it is important to explore a theorem that explores the stability of stars.

Stability Theorem A star, modeled as a perfect fluid with a constant chemical composition and entropy per nucleon, transitions from stability to instability through a particular radial normal mode. This transition occurs at a specific central density  $\rho(0)$  where the derivative of gravitational energy E and nucleon number N with respect to  $\rho(0)$  is zero:

$$\frac{\partial E(\rho(0); s, \ldots)}{\partial \rho(0)} = 0, \tag{2.68}$$

$$\frac{\partial N(\rho(0); s, \dots)}{\partial \rho(0)} = 0. \tag{2.69}$$

A radial normal mode is defined as an oscillation mode with density perturbation  $\delta \rho$  that depends only on radial position r and time t. During the pulsational cycle, nuclear reactions, viscosity, heat conduction, and radiative energy transfer remain nearly constant. To prove stability,

one must note the absence of dissipative forces, implying that the dynamical equations are timereversal-invariant. The squared frequencies  $\omega_n^2$  of the normal modes are real continuous functions of  $\rho(0)$ , analogous to an electrical circuit without resistors. A star is stable if all  $\omega_n^2>0$ , allowing for stable oscillation. Conversely, if any  $\omega_n^2 < 0$ , the star exhibits unstable modes, either exponentially damped or growing. Thus, the condition for stability is met when no mode frequency squared is negative. Consider a value of central density  $\rho(0)$  where the frequency of a particular oscillatory mode is nearly zero. The resulting slow transformation of the equilibrium state  $\rho(r)$ into an adjacent configuration  $\rho(r) + \delta \rho(r)$  ensures that the new state remains essentially an equilibrium configuration, unaffected by dissipative forces such as nuclear reactions, viscosity, heat conduction, or radiative transfer. These conditions imply that the new configuration maintains the same uniform chemical composition and entropy per nucleon, conserving the total energy Eand baryon number N of the system. Given that a non-zero  $\delta \rho(0)$  would result in a distribution of density perturbations  $\delta \rho(r)$  across the star, it is clear that at the point of transition from stability to instability, there will be neighboring equilibrium states characterized by different central densities, but with identical entropy and composition. In this context, it is crucial to observe that stability is not merely determined by the current state of the star, but also by its potential to transition into these neighboring configurations without significant changes in its physical properties.

The significance of this theorem lies in its utility for qualitative assessments of stellar stability. It offers a clear criterion for determining the stability of a star based on its central density  $\rho(0)$ . A star with a sufficiently small central density is stable, while one with a large central density is prone to instability. Thus, the theorem delineates the critical point at which a star transitions from stability to instability. The theorem's value is amplified when used as a guiding principle for qualitative analysis. It suggests that by reformulating the fundamental equations of stellar structure within a variational framework, we can enhance our understanding of the conditions under which stars remain stable or become unstable.

The Stability Theorem as described in Weinberg (1972), suggests that the transition from stability to instability in supermassive stars occurs at a central density  $\rho(0)$  where the internal energy E is stationary. The energy E can be approximated as follows:

$$E \approx \int_{0}^{R} 4\pi r^{2} e(r) dr + \int_{0}^{R} 4\pi G \mathcal{M}(r) e(r) dr - \int_{0}^{R} 4\pi G r \mathcal{M}(r) dr - \int_{0}^{R} 6\pi G^{2} \mathcal{M}^{2}(r) \rho(r) dr \quad (2.70)$$

where the internal energy density e is given by:

$$e = \frac{\pi^2 (kT)^4}{15\hbar^3} + \frac{\rho kT}{\Gamma - 1} = 3p_r \left[ 1 + \frac{\beta}{3(\Gamma - 1)} \right]$$
 (2.71)

Here,  $\Gamma$  is the specific heat ratio of the matter, and  $\beta$  is the ratio of matter to radiation pressure

defined by  $\beta = \frac{pm}{pr}$ . The total pressure is thus:

$$p = pr + pm = pr(1+\beta) \tag{2.72}$$

In the regime of small  $\beta$ , we express the energy density to pressure ratio. For ionized hydrogen, where  $\Gamma = 5/3$ , the internal energy density and pressure relations take the specific form:

$$e \approx 3p \left[ 1 - \frac{(3\Gamma - 4)}{3(\Gamma - 1)} \beta + \mathcal{O}(\beta^2) \right]$$
 (2.73)

We omit the minor  $\beta$  correction in the earlier term in eq. 2.70, as it is substantially smaller by a GM/R magnitude. Nevertheless, it remains essential in the primary term. Hence,

$$E \approx \left[1 - \frac{(3\Gamma - 4)}{3(\Gamma - 1)}\beta\right] \int_{0}^{R} 12\pi r^{2}\rho(r)dr + \int_{0}^{R} 12\pi G\mathcal{M}(r)\rho(r)dr - \int_{0}^{R} \frac{4\pi G\mathcal{M}(r)dr}{\int_{0}^{r} 6\pi G^{2}\mathcal{M}^{2}(r')\rho(r')dr'} - \cdots$$
(11.5.14)

Integration by parts reformulates the first integral as

$$\int_0^R 12\pi r^2 \rho(r)dr = \int_0^R \rho(r)d(4\pi r^3) = -\int_0^R 4\pi r^3 p'(r)dr$$
 (2.74)

Expanding p'(r) with the fundamental equation to first order in GM/R yields

$$-r^{2}p'(r) \approx G\mathcal{M}(r)\rho(r)\left[1 + \frac{p(r)}{\rho(r)} + \frac{4\pi r^{3}p(r)}{\mathcal{M}(r)} + \frac{2G\mathcal{M}(r)}{r}\right]$$
(2.75)

Thus, we approximate

$$\int_{0}^{R} 12\pi r^{2} \rho(r) dr \approx \int_{0}^{R} 4\pi G r \mathcal{M}(r) \rho(r) dr + \int_{0}^{R} 4\pi G r \mathcal{M}(r) p(r) dr + \int_{0}^{R} 16\pi G^{2} r^{4} \rho^{2}(r) p(r) dr + \int_{0}^{R} 8\pi G^{2} \rho(r) \mathcal{M}^{2}(r) dr$$
(2.76)

We maintain the  $\beta$ -correction in the leading term due to its size relative to the others. At first order in  $\beta$  and GM/R, the expression becomes

$$E \approx -\left[\frac{(3\Gamma - 4)}{3(\Gamma - 1)}\beta\right] \int_{0}^{R} 4\pi G r \mathcal{M}(r)\rho(r)dr + \int_{0}^{R} 16\pi G^{2}r^{4}\rho^{2}(r)p(r)dr + \int_{0}^{R} 2\pi G^{2}\mathcal{M}^{2}(r)\rho(r)dr$$
(2.77)

As all terms are small, evaluate them using densities  $\rho$ , pressures p, and mass distributions  $\mathcal{M}$ . Apply the Newtonian equation (see eq. 2.78 for each term. The final expression is detailed in equation (2.77). We approximate the pressure derivative term (with respect to radius) for a New-

tonian polytrope with  $\gamma = 4/3$  as

$$-r^2 p'(r) \approx G\mathcal{M}(r)\rho(r) \tag{2.78}$$

Specifically, the initial integral in Eq. (2.78) for  $\gamma = 4/3$  becomes

$$\int_0^R 4\pi G r \mathcal{M}(r) \rho(r) dr = -V = \frac{3GM^2}{2R}$$
(2.79)

Integration by parts transforms the third term into

$$\int_{0}^{R} 16\pi G^{2} r^{4} \rho^{2}(r) p(r) dr = \int_{0}^{R} 4\pi r^{2} p(r) d\mathcal{M}(r) 
= -\int_{0}^{R} 4\pi r^{2} p'(r) \mathcal{M}(r) dr - \int_{0}^{R} 8\pi G \rho(r) \mathcal{M}(r) dr 
= \int_{0}^{R} 4\pi G^{2} \mathcal{M}^{2}(r) \rho(r) dr - \int_{0}^{R} 8\pi G \rho(r) \mathcal{M}(r) dr$$
(2.80)

Now, equation (2.77) can be restated as

$$E \approx -\left[\frac{(3\Gamma - 4)}{2(\Gamma - 1)}\right] \beta \frac{GM^2}{R} + \int_0^R 8\pi G r \mathcal{M}(r) \rho(r) dr + \int_0^R 6\pi G^2 \mathcal{M}^2(r) \rho(r) dr$$
 (2.81)

For  $\gamma = 4/3$ , the last two integrals convert to the Lane-Emden function  $\theta(\xi)$  as follows:

$$\int_0^R 6\pi G^2 \mathcal{M}(r)\rho(r)dr = \frac{6K^{7/2}\rho(0)^{2/3}}{5\pi^{5/2}G^{3/2}} \int_0^{\xi_1} \xi^2 \theta(\xi)^3 d\xi$$
 (2.82)

$$\int_{0}^{R} 8\pi G \mathcal{M}(r) \rho(r) dr = \frac{8K^{7/2} \rho(0)^{2/3}}{\pi^{3/2} G^{3/2}} \int_{0}^{\xi_{1}} \xi^{3} \theta'(\xi) \theta(\xi)^{4} d\xi$$
 (2.83)

Express K and  $\rho(0)$  with M and R via the Lane-Emden solutions, obtaining

$$\frac{K^{7/2}\rho(0)^{2/3}}{G^{3/2}} = \frac{\sqrt{\pi}}{64\sqrt{2}} \left(\frac{GM^2}{R}\right)$$
 (2.84)

Numerical integration with the Lane-Emden function yields

$$\frac{1}{8\pi\xi_1^4|\theta'(\xi_1)|^3} \left[ \int_0^{\xi_1} \xi^3 \theta'(\xi) \theta(\xi)^4 d\xi + \frac{3}{4\pi} \int_0^{\xi_1} \xi^2 \theta(\xi)^3 d\xi \right] \approx 5.1$$
 (2.85)

Thus, combining all parts, we deduce

$$E \approx -\left[\frac{(3\Gamma - 4)}{2(\Gamma - 1)}\right] \beta \frac{GM^2}{R} + 5.1 \frac{G^2 M^3}{R^2}$$
 (2.86)

For large R, where general relativity effects are negligible, the star acts like a Newtonian polytrope with

$$\gamma = 1 + \frac{p}{e} \approx \frac{4}{3} + \frac{(3\Gamma - 4)}{9(\Gamma - 1)}\beta \approx \frac{4}{3}$$
(2.87)

Stability shifts to instability when R decreases past a threshold where

$$\frac{\partial E}{\partial R} = \frac{\partial E}{\partial \rho(0)} \frac{\partial \rho(0)}{\partial R} = 0 \tag{2.88}$$

Maintaining constant entropy per nucleon, with fixed  $\beta$  and M, we derive from equations (2.77) and (2.86) that the minimum radius for stability is

$$R_{\min} = \frac{20.4(\Gamma - 1)GM}{(3\Gamma - 4)\beta}$$
 (2.89)

The star's maximum potential energy release, as it contracts to  $R_{\min}$ , is given by

$$-E(R_{\min}) = \frac{(3\Gamma - 4)^2 \beta^2 M}{81.6(\Gamma - 1)^2}$$
 (2.90)

For example, a star with  $\beta=0.1$  would have  $M\approx7200M_{\odot}$ . For  $\Gamma=5/3$ , the minimum radius is  $1.45\times10^6$  km. The fraction of rest-mass energy releasable by a star assembly is 0.03%. The maximum MG/R value for  $\Gamma=5/3$  is  $0.0735\beta$ , well below the limit set by equation (2.86).

#### Theoretical Implications and Limitations

The interplay of Newtonian and relativistic dynamics in stellar structure is encapsulated by parameter  $\beta$ , dictating stability through energy and entropy considerations. For negligible  $\beta$ , stars resemble Newtonian polytropes with characteristic polytropic indices. The onset of instability is marked by the vanishing gradient of the star's energy with respect to its radius. This critical juncture, mathematically derived and linked to the Lane-Emden function, shows the threshold radius beyond which a star cannot sustain hydrostatic equilibrium. A star's contraction to this radius delineates the upper bound of potential energy liberation (if any energy above this limit is released, star become unstable), a concept shown by calculated rest-mass energy fractions and stability limits under theoretical constraints.

#### 2.6.2 Formation and evolution of accreting SMSs

SMSs were initially postulated as potential models for quasars, not as precursors to them Hoyle & Fowler (1963); Iben (1963); Fowler & Hoyle (1964). Initially, most analytic theories overlooked

the origins of SMSs, relying on assumptions of a singularly contracting cloud and neglecting how its formation might impact later stages. Given this context, most of the SMSs' properties can be analytically determined, fitting well as polytropes with an index of 3. Yet, these stars are highly susceptible to instability (Chandrasekhar 1939). It was later realized that even within the mild gravitational potential of SMSs, post-Newtonian adjustments to the state equation establish a strict mass ceiling of approximately  $10^5 M$ , beyond which the star would face dynamic collapse (Chandrasekhar 1964a). This understanding reignited interest in studying SMSs as potential progenitors to Super Massive Black Holes (SMBHs) (Rees 1984). Subsequent numerical analyses using the KEPLER code (a Henyey based code use to solve the equations of stellar structure Weaver et al. 1978; Woods et al. 2017)) hinted that for primordial SMSs, collapses invariably resulted in black hole formation, but with preceding stable hydrogen burning for smaller masses (Fuller et al. 1986). Modern suggestions hint at a specific mass bracket around 50,000 M where primordial, single-entity SMSs could experience a massive nuclear explosion without leaving a gravitationally tethered remnant (Chen et al. 2014). However, the validity of this hypothesis, especially given its narrow mass window, is still debated, particularly considering model assumptions and the integrated physics, as shown in the works by Nagele et al. (2022).

Conceptualizing a singular, supermassive contracting cloud, potentially through the amalgamation of a dense stellar cluster, as an SMS precursor seems improbable to exceed a few  $10^3 M$ (Latif et al. 2016; Mayer et al. 2010b). Within the atomic cooling halo paradigm, a supermassive proto-star expands at accretion rates between 0.1 and 10  $Myr^{-1}$ . This alters its structure profoundly, preventing it from attaining thermal equilibrium (Begelman 2010). As a consequence, intricate stellar evolutionary computations are essential to deduce its observable properties and ultimate fate (Hosokawa et al. 2012). Notably, while these stars still confront post-Newtonian instability and eventual collapse, simplistic polytropic models tend to undervalue the final mass (Woods et al. 2017). For static SMSs, the general characteristics are now widely understood (Haemmerlé et al. 2018). Incorporating rotation in these calculations highlights a growth bottleneck for SMSs; an exceptionally efficient angular momentum removal process must be present to prevent an accreting proto-star from reaching the mass-ejection limit before entering the SMS domain (Haemmerlé et al. 2018). The mechanisms underlying this remain elusive, mirroring challenges seen across massive star formation of all metallicity levels. The forthcoming sections delve into the latest advancements on these topics, also benchmarking stellar evolutionary computations from multiple groups.

## 2.6.3 Evolution of accreting SMSs

In discussions surrounding the nature of supermassive stars, our understanding often hinges on precise definitions based on the physics at play, rather than just on mass. The fundamental structure of massive stars provides a starting point. When dealing with a gravitationally bound sphere of ideal gas, hydrostatic equilibrium necessitates that central temperatures rise with increasing total masses. As a result, radiation is the primary contributor to the total pressure in more massive stars, making gas pressure a minor factor.

One can further approximate the total pressure by considering its relationship with density, denoted as  $\propto \rho^{4/3}$ . This observation is well-documented, with stars fitting the criteria of a polytrope with an index of 3. As these stars progress, nuclear burning stimulates convection throughout the star, leading to a uniform entropy profile. The significant point is that, under the conditions relevant for these massive, radiation-dominated stars, the adiabatic pressure gradient closely mirrors predictions made by Chandrasekhar (1939) and shown in the equations below.

$$\Gamma = \left(\frac{\partial \ln P}{\partial \ln \rho}\right)_{\text{ad}} = 1 + \frac{1}{n} \approx 1 + \frac{1}{3} + \frac{\beta}{6}$$
(2.91)

Here, n is the polytropic index. The softness of the equation of state makes the star quite susceptible to minor disturbances. For precise numerical modeling of these stars, general relativistic corrections to the stellar structure equations become indispensable. This shift towards considering post-Newtonian effects originated from insights provided by Hoyle & Fowler (1963) and Iben (1963). Their works highlighted the pivotal role these effects play in determining the trajectory of extremely massive stars that are quasi-statically contracting. A supermassive proto-star can evolve from a dense stellar cluster's disruption and subsequent collapse, as proposed by Begelman & Rees (1978). However, if such a star contracts and its central density surpasses a certain threshold before stabilization via nuclear burning, a dynamical collapse ensues.

Understanding the boundary between stars that survive until nuclear burning and those that collapse due to the electron-positron pair instability necessitates in-depth stellar evolution calculations. Early computational models dating back to the 1970s, like those by Appenzeller & Fricke (1972), attempted to detail the evolution and fate of supermassive stars. Fuller et al. (1986) undertook a comprehensive study that included nuclear burning treatments, post-Newtonian corrections, and hydrodynamics. Woods et al. (2019) posited that stars exceeding a mass threshold directly collapse into black holes, whereas less massive ones proceed to the hydrogen-burning main sequence.

Notably, the metallicity of these stars impacts their behavior. For supermassive stars formed

in primordial conditions without Carbon-Nitrogen-Oxygen (CNO) elements, they need to activate the triple-alpha reaction since the pp-chain alone doesn't suffice (as per Heger & Woosley (2010); Hillebrandt et al. (1987b,a). For metal-rich supermassive stars with abundant CNO, thermonuclear explosions are possible in certain scenarios, as discussed by Chen et al. (2014); Hirano et al. (2022).

However, the conditions leading to the formation of non-zero metallicity supermassive stars remain a topic of debate. While dense stellar clusters' fragmentation might not yield sufficiently massive objects, the merger of gas-rich proto-galaxies might. Yet, there's uncertainty about whether these resulting stars would have a structure resembling the monolithic polytropes previously described. What is clear, however, is that the evolution and fate of rapidly accreting supermassive protostars, which can be formed in atomically cooled halos under specific conditions, differ significantly, as explored by several researchers including Hosokawa et al. (2012); Umeda et al. (2016).

# 2.6.4 Swelling of SMSs due to accretion

In a seminal study by Hosokawa et al. (2012), they embarked on a numerical exploration of protostars, particularly examining their evolution as they accreted material at various constant rates. Their study encompassed a broad spectrum of rates, with some even exceeding  $10^{-2}M$  per year.

For a clearer understanding, consider the black curve in panel Fig. 2.6.4. This curve illustrates the scenario where the accretion rate, denoted as  $\dot{M}$ , is  $10^{-3}M_{\odot}/{\rm yr}$ . This rate, albeit on the lower side, is commonly used in typical primordial star formation simulation. An intriguing characteristic of this curve is the evident stellar contraction observable between 6  $M_{\odot}$  and 30  $M_{\odot}$ . This phase is famously recognized as the Kelvin-Helmholtz (KH) contraction stage. It is a critical period in a star's life cycle during which it sheds energy through radiation. Consequently, there's a pronounced surge in the star's effective temperature and its emissivity of ionizing photons. This uptick marks the initiation of UV feedback mechanisms acting against the accretion flows. Interestingly, the KH contraction serves as a precursor to this stellar UV feedback. As the stellar evolution advances, the central temperature exhibits a steady rise. It is post this phase, specifically when the stellar mass surpasses  $30~{\rm M}_{\odot}$ , that hydrogen burning kicks off. Subsequently, the star's radius begins to align with the mass-radius relationship characteristic of zero-age main-sequence (ZAMS) stars.

However, when one compares this evolution to scenarios with swifter accretion, stark contrasts emerge. A closer examination of panel (a) reveals that the span of the KH contraction phase narrows down notably in these cases. Specifically, for accretion rates of  $6 \times 10^{-3} M$  per year and 0.03 M per year, the pattern shifts from contraction to expansion. Remarkably, for the highest accretion

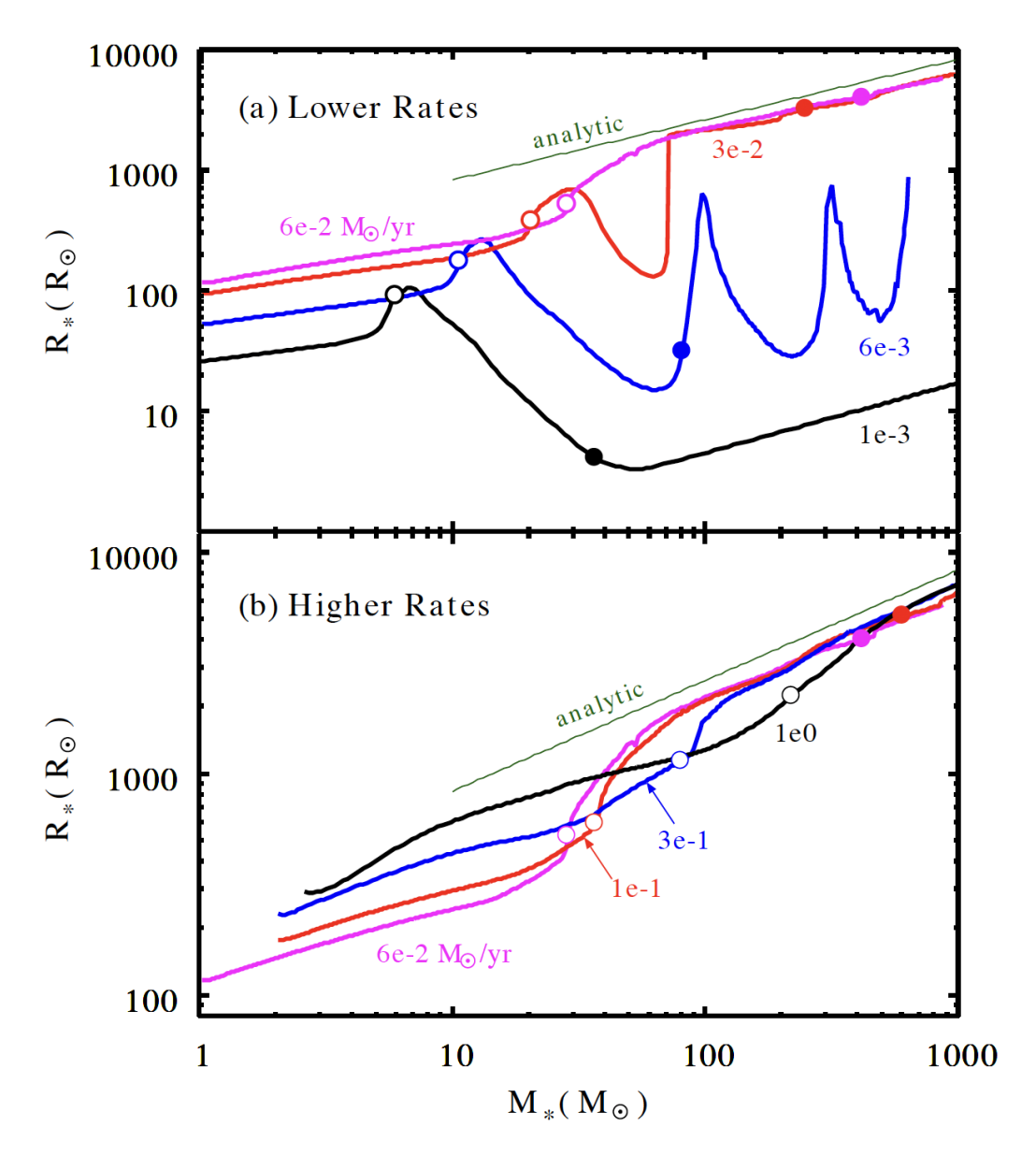


Figure 2.7: Hosokawa et al. (2012) studied the evolution of a star's radius in relation to varying accretion rates. In their findings, the top and bottom panels illustrate the changes at rates below and above  $6 \times 10^{-2} M$  per year, respectively. The graph showcases different lines, each representing specific accretion rates as detailed by their respective labels. An analytical mass-radius relationship is depicted by a slender green line. Points where hydrogen combustion begins near the core are marked with filled circles on these lines. Figure taken from Hosokawa et al. (2012)

rate studied, 0.06M per year, the contraction phase is entirely absent. In this scenario, as the star continually accrues gas, its radius exhibits a monotonous growth. This results in the star expanding to an impressive radius of roughly 7200 R, equivalent to nearly 30.5 astronomical units (AU), when its mass reaches around  $1000 \, \mathrm{M}_{\odot}$ .

Delving deeper, panel (b) elucidates the dynamics with even higher accretion rates, spanning from 0.06M per year to 1M per year. One observes captivating patterns, notably that the curves,

despite differing accretion rates, tend to mimic the same mass-radius relationship for stellar masses greater than approximately 300 M. This leads to an intriguing observation: for all the considered cases, when the stellar mass is around  $1000~M_{\odot}$ , the radius settles at about 30 AU.

The observed behaviors can be elucidated with an analytical approach. Beginning with the general expression for stellar luminosity and considering the Stefan-Boltzmann constant, for immensely massive stars, the luminosity approximates the Eddington value, described by

$$L_* = 4\pi R_*^2 T_{\text{eff}}^4 \tag{2.92}$$

$$L \approx L_{\rm Edd} \times M.$$
 (2.93)

here,

$$L_{\rm Edd} = \frac{4\pi G M m_p c}{\sigma_T} \tag{2.94}$$

where  $L_{\rm Edd}$  is the Eddington luminosity, G is the gravitational constant, M is the mass of the star,  $m_p$  is the mass of a proton, c is the speed of light, and  $\sigma_T$  is the Thomson scattering cross-section for the proton. In situations characterized by high accretion rates, a distinct phenomenon occurs. The outermost layer of the star swells because it consistently traps some heat emanating from its contracting core. This leads to the effective temperature plummeting to values around a few thousand Kelvin. In this temperature range, the  $H^-$  bound-free absorption predominantly influences the opacity. Given the intense temperature-dependency of the  $H^-$  opacity, the effective temperature stabilizes at a near-constant value. Incorporating the aforementioned equation for luminosity and an effective temperature of approximately 5000 K, we can derive the mass-radius relation expressed by the equation

$$R \approx 2.6 \times 10^3 R_{\odot} \times \sqrt{\frac{M_*}{100 M_{\odot}}} \tag{2.95}$$

Significantly, this equation, as portrayed by the thin green lines in Figure 2.6.4, is independent of the accretion rate. The constant value of  $2.6 \times 10^3$  accounts for the values of luminosities and the opacity in equation 2.95. This independence provides a coherent explanation for the convergence of the different lines in Figure 2.6.4 into a unified mass-radius relationship.

In essence, the comprehensive study by Hosokawa et al. (2012) sheds light on the intricate interplay between accretion rates and the subsequent evolutionary trajectories of protostars. Their findings underscore the significance of understanding the dynamism of these celestial bodies, elucidating how diverse accretion rates can sculpt their life cycles in profoundly different ways.

#### 2.6.5 Accretion in SMSs

As regions within molecular clouds collapse, they not only begin rotating but also form an accretion disk around the proto-star. This disk, a flat, circular structure of gas, dust, and other materials, arises due to the conservation of angular momentum and differential gravitational forces across the cloud. As material within the accretion disk spirals inward due to viscous forces, the fluid element traveling radially inward toward the star experiences a loss of angular momentum. Contrary to what might be assumed, a decrease in angular momentum does not necessarily lead to a reduction in tangential velocity. As the radius diminishes, the velocity V increases, since  $\frac{V^2}{r} = \sqrt{\frac{GM}{R}}$ , where G is the gravitational constant, M is the mass of the star, and R is the radial distance from the star's center. This process is governed by the relationship  $L = r \times m \times v$ , where r decreases while v increases, ensuring angular momentum conservation. It's important to note that for matter to be accreted from the disk onto the star, angular momentum must be transferred outward, likely through viscous mechanisms.

The specific angular momentum of the accreting matter is also critical. If the accreting matter had a tangential velocity opposite to the star's rotation, it could potentially slow down the star's rotation. However, such a scenario is unlikely since the initial rotation typically affects the entire protostellar cloud uniformly. Therefore, the accretion process tends to increase both the mass and angular momentum of the star, affecting its rotation rate and internal dynamics. The accretion process, therefore, not only increases the rotation rate of the star but also affects its angular momentum, particularly when the infalling material has significant tangential velocities. Such changes in rotation rate and angular momentum, dependent on the mass and specific angular momentum of the accreted material, have profound implications for stellar evolution. The angular momentum introduced by accreting matter influences the internal dynamics of the star, impacting convection and differential rotation. These internal changes, combined with the intrinsic rotation from the star's formation and the additional angular momentum from accretion, are crucial in determining the star's evolutionary path. Initially, we explore the scenario of non-rotating SMSs to understand these effects in a simplified context.

# Non-rotating SMSs

In understanding the formation and development of supermassive stars (SMSs), recent theories differ from traditional ones. Instead of a singular massive cloud's contraction, it's posited that SMSs form at high accretion rates, from roughly  $0.01 - 10.0 \, \mathrm{M}_{\odot} \, \mathrm{yr}^{-1}$ , based on a small central seed. Such accretion aligns the star's growth to supermassive sizes with its nuclear-burning timeline,

impacting the protostar's progression. The accretion timescale can be represented by

$$t_{acc} = \frac{M*}{\dot{M}},\tag{2.96}$$

which, in the star's early stages, is shorter than the Kelvin Helmholtz time,

$$t_{KH} = \frac{GM_*^2}{R_*L},\tag{2.97}$$

where L is the luminosity generated by the star, and  $R_*$  is its radius. This suggests the star expands before reaching the main sequence, as detailed by Omukai & Palla (2001).

Regarding SMS internal configurations, Begelman (2010) introduced modifications to the standard polytropic models, proposing mass-dependent equations of state termed 'hylotropes'. In the hylotropic model, the pressure P within a supermassive star is described by the equation:

$$P = A\rho^{4/3}M^{\alpha} \tag{2.98}$$

where P is the pressure, A is a constant,  $\rho$  is the density, M is the mass of the star, and  $\alpha$  is a parameter analogous to the polytropic index n in classical polytropic models. The findings suggest a growing SMS layer might not relax within its nuclear-burning time. As a result, main-sequence stars would deviate from an n=3 polytrope, having a nuclear-burning convective core surrounded by a high-entropy envelope. Hosokawa et al. (2012) indicates that a SMS's effective temperature stabilizes around 5,000 K, corresponding to the Hayashi limit for such stars. This stability arises due to the temperature sensitivity of H $^-$  absorption, the primary opacity source, which limits further cooling. A relationship between an SMS's radius and its mass can be expressed by

$$R_* \approx 2.3 \times 10^3 R_{\odot} \frac{M}{100 M_{\odot}}^{1/2},$$
 (2.99)

aligning with results from Hosokawa et al. (2012). Further evolution suggests that the radius expands with mass until reaching about  $\approx 10^4 M$ . Beyond this, reduced outer envelope gas density decreases the H<sup>-</sup> absorption's efficiency, causing slight SMS contraction.

Variability in accretion rates, especially via gravitationally unstable disks, can lead to disk fragmentation. Resulting "clumps" can merge with central SMSs during rapid accretion bursts. As Sakurai et al. (2015) demonstrated, between these bursts, the SMS's outer envelope undergoes thermal relaxation and contracts, increasing the SMS's effective temperature and generating ionizing photons. Rapidly accreting SMSs differ from monolithic ones in structure. Monolithic SMS

refers to a supermassive star that has formed and grown in a steady and uninterrupted manner, without the complexities of fragmentation or clump mergers. This growth pattern suggests a smoother accretion process and a more uniform internal structure, as opposed to SMSs that have undergone variable accretion rates and possible disk fragmentation. Their lower densities might prevent collapse at greater masses than traditionally anticipated. A monolithic SMS encounters post-Newtonian instability when its core density reaches a specific value. However, using hydrodynamics and post-Newtonian modifications to stellar structure equations, the onset of collapse in SMSs becomes complex. For an SMS accreting at  $10M\ yr^{-1}$ , collapse is delayed beyond when the polytropic criterion is met within the core, only occurring after reaching  $\approx 330,000M_{\odot}$ . Studies on the SMS's accretion history are essential to predict the final mass at collapse for massive black hole seeds. For non-rotating SMSs accreting zero-metallicity gas, the final mass at collapse can be expressed as

$$M_{\text{SMS,final}} \approx 0.83 \log_{10} \left( \frac{\dot{M}}{M_{\odot} \text{yr}^{-1}} \right) + 2.48 \times 10^5 M_{\odot}$$
 (2.100)

This enables the characterization of the initial seed masses of the quasars, though limited to nonrotating stars. Additionally, it's theorized that such a rapidly accreting protostar wouldn't only accumulate mass but would also amass angular momentum, leading to exceptionally high surface spin velocities.

#### **Rotating SMSs**

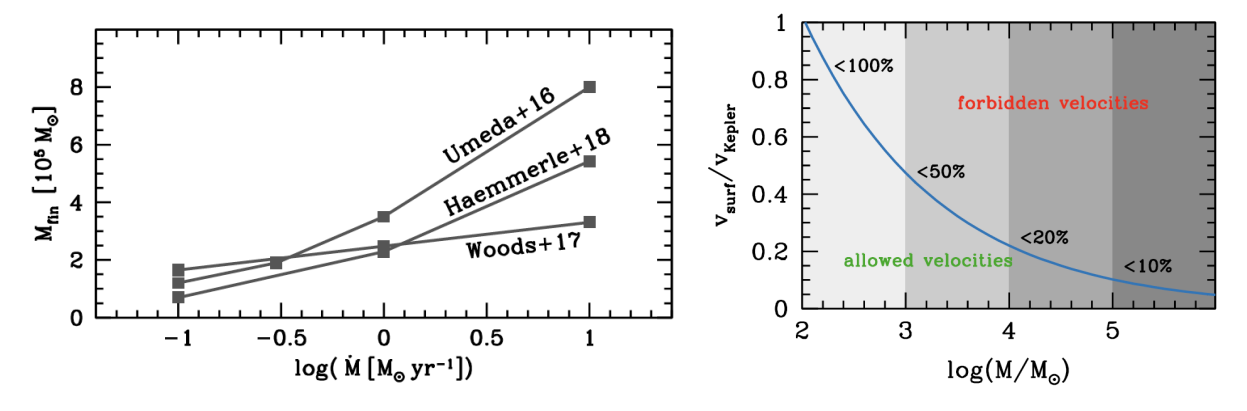


Figure 2.8: Final mass and rotational velocities of SMSs. *Left panel:* Mass thresholds for General Relativistic (GR) stability in accreting Supermassive Stars (SMSs) based on a constant accretion rate, as presented by Umeda et al. (2016), Woods et al. (2017), and Haemmerlé et al. (2018). *Right panel:* Criteria from the  $\beta$ -limit determining the surface rotational speeds of SMSs, as cited in Haemmerlé et al. (2018).

A key challenge that emerges during the stellar formation process of supermassive stars is the issue of angular momentum. When interstellar material undergoes contraction to attain stellar

densities, centrifugal forces, intensify unless a mechanism exists to extract angular momentum. This phenomenon has been previously explored by Spitzer (1978) and Bodenheimer (1995). SMS formation, in particular, encounters this impediment owing to an interplay of factors: dominant radiation pressure, a lack of substantial magnetic fields, and rapid evolutionary trajectories. This, according to Lee & Yoon (2016), Omukai (2007), and Haemmerlé et al. (2017), raises formidable challenges. Sugimura et al. (2018) notably pointed out the subsequent implications of this challenge on the growth trajectories of supermassive black holes (SMBHs) post their formation.

Conversely, the benefits of rotation manifest in the potential generation of gravitational waves (GWs) and ultra-long gamma-ray bursts (ULGRBs) when SMSs are on the brink of collapse. Both the disruption of spherical symmetry and the birth of collimated jets are rooted in the rotational dynamics of these stars. Historically, the impact of rotation on SMSs has predominantly been examined under the purview of monolithic models. These models, albeit illustrative, often neglect the accretion process. A common assumption within these studies, such as those by Bisnovatyi-Kogan et al. (1967), and Baumgarte & Shapiro (1999b), is the solid-body rotation where the star achieves Keplerian surface velocity. The genesis of this assumption can be traced back to the prevalence of convection in such models. Based on the law of angular momentum conservation, these stars, as they undergo contraction, are predicted to lose mass from their equatorial regions. This phenomenon is termed the mass-shedding limit. One of the pivotal revelations from these studies is the ability of stars, particularly those in the mass range of  $10^8 - 10^9$  solar masses, to harness rotation for stabilization against the effects of general relativity (GR). Elaborating on the insights, Baumgarte & Shapiro (1999a) deduced consistent rotational properties for monolithic SMSs nearing collapse. Drawing from these foundational monolithic models, researchers such as Saijo et al. (2002), and Shibata et al. (2016) modeled the terminal collapse of SMSs. The consensus gravitates towards the formation of a black hole that engulfs around 90-95% of the stellar mass with an approximate spin parameter hovering around 0.7.

Contrastingly, when one accounts for accretion rates nearing  $0.1~M_{\odot}yr^{-1}$ , a divergent picture emerges regarding the rotational attributes of SMSs, deviating from monolithic model predictions. This divergence is substantiated by two pivotal reasons as outlined by Haemmerlé et al. (2018), and Haemmerlé et al. (2019). First, accretion acts as a stabilizer for the star, inhibiting the solid-body rotation and leading to differential rotation instead. Consequently, the core exhibits rotational frequencies that are exponentially faster, approximately  $10^4-10^5$  times, than the surface. Second, for an accreting SMS to metamorphose into a supermassive hydrostatic entity, a precondition is that its surface consistently rotates at speeds below 10-20% of the Keplerian velocity, implying intrinsically slow rotations, as shown in the left and right panels of Figure 2.8.The critical rotational

velocities of massive stars are constrained by the  $\Omega - \Gamma$  limit, which considers the influence of radiation pressure (Maeder & Meynet 2000). The first critical velocity ( $v_{\rm crit,1}$ ) is the velocity at which the centrifugal force balances gravity at the star's equator without considering radiation pressure:

$$v_{\text{crit},1} = \sqrt{\frac{2 GM}{3 R}} = v_{\text{Kep}} \tag{2.101}$$

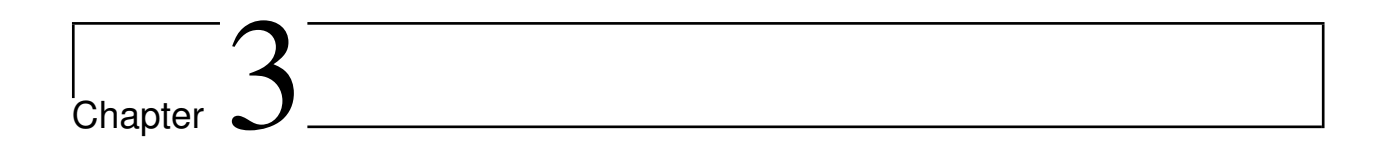
The second critical velocity ( $v_{\text{crit,2}}$ ) accounts for the radiation pressure through the Eddington factor ( $\Gamma$ ), representing the ratio of radiation to gravitational forces:

$$v_{\text{crit,2}} = v_{\text{crit,1}} \sqrt{1 - \frac{L}{4\pi cGM}} = v_{\text{Kep}} \sqrt{1 - \Gamma}$$
 (2.102)

In case of SMSs that are dominated by the radiation pressure, one must use  $v_{\rm crit,2}$  expression over the other. Stars approaching the Eddington limit are thus compelled to rotate more slowly, balancing the increased radiation pressure against gravitational cohesion.

The stellar structure remains resilient to rotational effects. As a result, rotational mixing processes, encompassing shear diffusion and meridional circulation, diminish in significance due to the star's rapid evolution. A central conundrum for the evolution of SMSs pertains to the constraints on the angular momentum of material being accreted. To address this, two plausible mechanisms emerge: gravitational torques and magnetic fields. These mechanisms have the potential to facilitate the shedding of surplus angular momentum during the accretion phase. Gravitational torques, as shown by Begelman et al. (2006), and Hosokawa et al. (2016), emanate from significant deviations from axial symmetry in gravitationally unstable supermassive accretion discs. On the other hand, magnetic fields, although generally considered secondary in the accretion dynamics of SMSs, could play a more pronounced role under specific conditions. To further understand the role of magnetic fields, it becomes imperative to consider studies like those by Woods et al. (2017) and Tanaka et al. (2017). They postulate that the magneto-rotational instability (MRI) could be pivotal in enhancing the angular momentum transport in supermassive accretion discs. In the event of a rapid accretion-induced collapse, the resulting stellar remnants, black holes, or neutron stars, depending on their progenitors, may be suffused with significant angular momentum.

In conclusion, understanding how rotation affects supermassive stars is crucial due to angular momentum's central role, shaping their formation and fate in a variety of complex ways.



# Improvements to the Geneva stellar evolution code

# 3.1 Evolution of massive stars using the Geneva code

The Geneva stellar evolution code (GENEC) has undergone significant evolution over the past fifty years. This chapter serves as a detailed review of these developments, setting the context for my research on accreting supermassive stars without rotation and rotating massive stars. GENEC is grounded in the foundational equations of stellar structure and evolution, as established by Kippenhahn & Weigert (1990). These include the hydrostatic equilibrium, mass continuity, energy conservation, and energy transport equations. Adapted for both rotational and non-rotational scenarios Maeder (2009), GENEC's approach models stars as concentric shells, utilizing the Newton method and a block tridiagonal Jacobian matrix for resolving the stellar evolution equations Kippenhahn & Weigert (1990). Pre-main sequence (preMS) evolution forms an integral part of GENEC. Early models by Henyey et al. (1955) and Salpeter (1954) envisioned preMS stars as primarily radiative. Hayashi (1961)'s convective models introduced the concept of the Hayashi Line, now a crucial component in GENEC's preMS models. Rotation's integration into GENEC significantly enhanced its capabilities. Shellular rotation, as proposed by Zahn (1992), allowed for a more accurate representation of rotational effects in stellar dynamics, leading to modified structure equations Meynet & Maeder (1997a). GENEC has seen improvements in areas such as nuclear reaction networks, atomic diffusion processes, and elemental abundances Ekström et al. (2012a). Convection treatment, based on the Schwarzschild and Ledoux criteria and MLT, has also been refined.

Before my research began, GENEC had established comprehensive models for rotating massive

and non rotating supermassive stars. The sections that follow will detail the code, delving into the specific physics and computational methods used. My own contributions to GENEC will be highlighted in a subsequent section, followed by in-depth discussions on various aspects of stellar physics, including the effects of rotational prescriptions and variable accretion rates.

# 3.1.1 Rotating main sequence models

We being this discussion by recalling the equations of stellar structure. These equations are a set of differential equations that govern the internal structure and evolution of a star. These equations are central to the field of astrophysics and provide a comprehensive framework for understanding how stars function.

• The hydrostatic equilibrium equation ensures that the inward gravitational force is balanced by the outward pressure gradient force in a star.

$$\frac{dP}{dr} = -\frac{GM(r)\rho(r)}{r^2} \tag{3.1}$$

where P is the pressure, G is the gravitational constant, M(r) is the mass within radius r, and  $\rho(r)$  is the density at radius r. This equilibrium is crucial for maintaining the stability of a star throughout its lifetime.

• The mass continuity equation describes how mass is distributed within the star.

$$\frac{dM(r)}{dr} = 4\pi r^2 \rho(r) \tag{3.2}$$

Here, M(r) represents the mass enclosed within radius r, and  $\rho(r)$  is the density at radius r. This equation is fundamental for calculating the mass of the star at different layers.

 The energy transport equation explains how energy is transferred from the star's core to its surface.

$$\frac{dT}{dr} = -\frac{3}{4ac} \frac{\kappa \rho L(r)}{4\pi r^2 T^3} \tag{3.3}$$

T is the temperature, L(r) is the luminosity at radius r,  $\kappa$  is the opacity, and a and c are the radiation constant and the speed of light, respectively. This equation is key for understanding how stars emit light and heat.

• The energy generation equation accounts for the production of energy in the star's core through nuclear reactions.

$$\frac{dL(r)}{dr} = 4\pi r^2 \rho(r)\epsilon(r) \tag{3.4}$$

where L(r) is the luminosity at radius r,  $\rho(r)$  is the density, and  $\epsilon(r)$  is the energy generation rate per unit mass. This equation is essential for understanding the life cycle of stars and their luminosity.

The inclusion of rotation adds complexity and depth to the models, necessitating a shift from traditional assumptions. It introduces new dynamics due to the combined effects of gravity and centrifugal force in a star's rotating frame. This section will delve into how these rotational aspects are represented and handled in the Geneva stellar evolution code.

Rotation in GENEC has been implemented under the framework of shellular rotation theory. Here, it is theorized that if there is pronounced horizontal turbulence along the isobars, the angular velocity can be perceived as constant on these surfaces (Zahn 1992). With these modifications, the quartet of equations representing the stellar structure evolution is presented as (Meynet & Maeder 1997a):

$$\begin{cases}
\frac{\partial P}{\partial M_{P}} = -\frac{GM_{P}}{4\pi r_{P}^{4}} f_{p}, \\
\frac{\partial r_{P}}{\partial M_{P}} = \frac{1}{4\pi r_{P}^{2} \bar{\rho}}, \\
\frac{\partial L_{P}}{\partial M_{P}} = \epsilon_{nucl} - \epsilon_{\nu} + \epsilon_{grav} = \epsilon_{nucl} - \epsilon_{\nu} - c_{P} \frac{\partial T}{\partial t} + \frac{\delta}{\rho} \frac{\partial P}{\partial t}, \\
\frac{\partial lnT}{\partial M_{P}} = -\frac{GM_{P}}{4\pi r_{P}^{4}} f_{P} \min \left[ \nabla_{ad}, \nabla_{rad} \frac{f_{T}}{f_{P}} \right],
\end{cases} (3.5)$$

The gradients, represented as  $\nabla$ , are characterized as:

$$\nabla_{ad} = \frac{P\delta}{\bar{T}\bar{\rho}c_P},\tag{3.6}$$

$$\nabla_{rad} = \frac{3}{16\pi acG} \frac{\kappa l P}{m\bar{T}^4},\tag{3.7}$$

In Meynet & Maeder (1997a) it is shown that despite a potential cannot be defined, defining what is the mean density over an isobar allows to keep these equations in such forms. In the respective convective and radiative zones. The functions  $f_P$  and  $f_T$  are defined as:

$$f_P = \frac{4\pi r_P^4}{GM_P S_P} \frac{1}{\langle q^{-1} \rangle},\tag{3.8}$$

$$f_T = \left(\frac{4\pi r_P^2}{S_P}\right)^2 \frac{1}{\langle g \rangle \langle g^{-1} \rangle}.$$
 (3.9)

Here,  $M_P$ ,  $r_P$ ,  $L_P$  symbolize the mass, radius, and luminosity within the isobar characterized by pressure P and temperature T. Further descriptions of these variables can be found in Meynet & Maeder (1997a).

To properly resolve the system denoted by (3.5), one must duly factor in several pivotal physical quantities. These include:

- The Equations Of State (EOS), which guide the determination of thermodynamic variables through different evolutionary phases and structural layers of the star;
- The rates of nuclear reactions, which are indispensable for computing both the energy produced or absorbed over time and mass due to nuclear reactions ( $\epsilon_{nucl}$ ) and the emission of neutrinos ( $\epsilon_{\nu}$ );
- Opacities, which are instrumental in deriving the temperature gradient in radiative zones, represented by  $(\nabla_{rad})$ ;
- An established method for treating convection to compute the convective flux and another approach for handling diffusion.

#### Shellular rotation theory

In the study of massive stars, the impact of axial rotation on their structure and evolution has been studied in various contexts. Recent endeavors have shown a multitude of effects resulting from this axial rotation, with most important ones being associated with the transport of both angular momentum and chemical species in stellar interiors (Maeder & Meynet 2005). These effects can greatly influence various facets of stellar models, including age-correlated variations in surface compositions and velocities, evolutionary trajectories, the type of supernova events, remnants, and the genesis of new species. Such changes are quite clear when comparing the non-rotating models with rotating ones, especially when performing population synthesis or models evaluating the chemical evolution of galaxies.

At the heart of our discussion is the concept of shellular rotation, first introduced by Zahn (1992) and later expanded by Maeder & Zahn (1998). This theory suggests that the angular velocity  $(\Omega)$  is almost constant on isobaric surfaces. This happens because there are no strong temperature or density gradients in these directions to oppose shear turbulence. As a result, a large "horizontal" diffusion coefficient,  $D_h$ , is present.

In the context of shellular rotation, the equation that describes how chemical elements move becomes much simpler. It turns into a diffusive equation, as described by Zahn (1992):

$$\rho \frac{\partial X_i}{\partial t} \bigg|_{M_r} = \frac{1}{r^2} \frac{\partial}{\partial r} \left( \rho r^2 D_{\text{chem}} \frac{\partial X_i}{\partial r} \right)$$
 (3.10)

Here,  $X_i$  signifies the abundance of isotope i in terms of mass fraction, while  $D_{\text{chem}}$  represents the pertinent diffusion coefficient for chemical elements' transport.

In differentially rotating stars, the time evolution of angular velocity,  $\Omega$ , is carefully mapped at each radial level r, ensuring a comprehensive depiction of  $\Omega(r,t)$ . As shown by Zahn (1992), the equation directing the transport of angular momentum in this context is:

$$\rho \frac{\partial}{\partial t} (r^2 \Omega)_{M_r} = \frac{1}{5r^2} \frac{\partial}{\partial r} (\rho r^4 \Omega U_2(r)) + \frac{1}{r^2} \frac{\partial}{\partial r} \left( \rho D_{\text{ang}} r^4 \frac{\partial \Omega}{\partial r} \right)$$
(3.11)

In this equation,  $D_{ang}$  is the relevant diffusion coefficient for angular momentum's transport.  $U_2$  is expressed in the equation as  $U(r,\theta) = U_2 P_2 Cos(\theta)$ , where  $U(r,\theta)$  is the radial component of the meridional circulation velocity and  $P_2$  is the legendre polynomial of the second order.

While the equations described here for rotating models embrace the nuances of the shellular rotation theory, they stay away from the dynamo theory implications suggested by Spruit (2002).

#### **Diffusive/Viscosity Coefficients**

In this section, we look at the equations that use different diffusion coefficients. We explain how these coefficients work in Equations 3.11 and 3.10.

For stars without magnetic fields, the coefficient for transporting chemicals,  $D_{\rm chem}$ , has two parts:  $D_{\rm shear}$  and  $D_{\rm eff}$ .  $D_{\rm shear}$  is for moving chemicals and angular momentum because of shear instability.  $D_{\rm eff}$  is for moving chemicals due to meridional currents and horizontal turbulence in the diffusive part of the equation(Chaboyer & Zahn 1992). In these stars, the coefficient for transporting angular momentum,  $D_{\rm ang}$ , is the same as  $D_{\rm shear}$ .

In stars with magnetic fields,  $D_{\rm chem}$  has three parts:  $D_{\rm shear}$ ,  $D_{\rm eff}$ , and the Tayler-Spruit dynamo's chemical transport,  $\eta_{\rm TS}$ . For moving angular momentum,  $D_{\rm ang}$  combines  $D_{\rm shear}$  and the Tayler-Spruit dynamo's viscosity,  $\nu_{\rm TS}$ . We only consider magnetic coupling for moving angular momentum because it's stronger than meridional currents. But for moving chemicals,  $D_{\rm eff}$  is the main factor.

#### Vertical Shear Diffusion: $D_{\rm shear}$

The coefficient  $D_{\rm shear}$  addresses the vertical transport of both chemical species and angular momentum, arising from turbulence caused by differential vertical rotation. Distinct expressions for this coefficient emerge from the works of Maeder (1997) and Talon & Zahn (1997).

Adopting a scenario where the radiative diffusive coefficient *K* overwhelms other factors and

shear instability barely influences energy transport, Maeder (1997) postulates:

$$D_{\text{shear}} = f_{\text{en}} \frac{H_P}{g\delta} \frac{K}{\left[\frac{\varphi}{\delta} \nabla_{\mu} + (\nabla_{\text{ad}} - \nabla_{\text{rad}})\right]} \left(\frac{9\pi}{32} \Omega \frac{\text{d} \ln \Omega}{\text{d} \ln r}\right)^2$$
(3.12)

In this formulation,  $f_{\rm en}$  signifies the proportion of accessible energy contributing to mixing, assumed as  $f_{\rm en}=1$ . Other parameters like  $H_P$ , g,  $\varphi$ , and K are rooted in various astrophysical phenomena, from pressure scale height to gravitational acceleration.

On the other hand, Talon & Zahn (1997) offers a nuanced variation, incorporating  $D_h$ , the horizontal turbulence diffusion coefficient:

$$D_{\text{shear}} = f_{\text{en}} \frac{H_P}{g\delta} \frac{(K + D_h)}{\left[\frac{\varphi}{\delta} \nabla_{\mu} \left(1 + \frac{K}{D_h}\right) + (\nabla_{\text{ad}} - \nabla_{\text{rad}})\right]} \left(\frac{9\pi}{32} \Omega \frac{\text{d} \ln \Omega}{\text{d} \ln r}\right)^2$$
(3.13)

In this context, it's pivotal to understand the role and significance of each parameter, from  $H_P$  and g to the various gradients such as  $\nabla_{\mu}$  and  $\nabla_{\rm rad}$ , to paint a comprehensive picture of the stellar interiors.

#### The Horizontal Turbulence, $D_{ m h}$

Horizontal turbulence in stellar environments can be significantly influenced by shear occurring along an isobar. This shear, caused by differential rotation on an isobar, can be the result of meridional currents. Over time, various formulations of this phenomenon have been proposed by multiple researchers, aiming to capture the essence of the physical processes in play. These expressions come with inherent parameters that have been adopted as suggested in their original studies. To delve deeper into the justifications of these parameter choices, readers are encouraged to refer directly to the primary publications.

Three distinct formulations for  $D_h$  exist in scholarly texts:

#### 1. Zahn's Formulation (1992): Zahn proposed:

$$D_{h} = r |2V(r) - \alpha U(r)| \tag{3.14}$$

Here,  $\alpha = \frac{1}{2} \frac{d \ln(r^2 \Omega)}{d \ln r}$ , and V(r) denotes the horizontal component of the meridional circulation velocity.

#### 2. Maeder's Formulation (2003): Maeder, in his study, presented:

$$D_{h} = A r (r\Omega(r) V |2V - \alpha U|)^{1/3}$$
(3.15)

In this expression,  $\alpha$  remains consistent with Zahn's definition, and the constant A holds the value 0.002.

#### 3. Mathis' Formulation (2004): Mathis postulated:

$$D_{h} = \left(\frac{\beta}{10}\right)^{1/2} \left(r^{2}\Omega\right)^{1/2} \left(r\left|2V - \alpha U\right|\right)^{1/2} \tag{3.16}$$

Once again,  $\alpha$  is taken from Zahn's expression, and the parameter  $\beta$  is assigned a value of  $1.5 \times 10^{-6}$ .

In these formulations,  $\Omega$  stands for the angular velocity averaged over latitudinal variations on an isobar. Due to the robustness of horizontal turbulence, fluctuations of angular velocity relative to latitude on an isobar are anticipated to be minimal.

### Effective Diffusion: $D_{\rm eff}$

For the chemical species' effective mixing, most contemporary approaches employ the coefficient  $D_{\text{eff}}$ , as defined by Chaboyer and Zahn:

$$D_{\text{eff}} = \frac{1}{30} \frac{|r \ U_2(r)|^2}{D_{\text{b}}}.$$
 (3.17)

The 1/30 factor emerges from an integration procedure and is not an arbitrary parameter. Although U displays some dependence on  $D_h$ , such dependence is generally minimal, especially when  $D_h$  is much smaller than K, as witnessed in numerous models. As expressed in the aforementioned equation,  $D_{\rm eff}$  is inversely related to  $D_h$ . This relationship can be metaphorically understood by picturing horizontal turbulence restricting vertical motion, similar to how a potent horizontal gust might divert smoke ascending from a chimney.

#### Magnetic Diffusivity: $\eta_{TS}$

The magnetic models computed in this thesis are anchored in the Tayler-Spruit calibrated dynamo as outlined in Eggenberger et al. (2022b). Rooted in the foundational theory of the Tayler-Spruit dynamo (Spruit 2002), this model has been refined to align with the observed internal distributions of angular velocity in subgiant and red giant stars, as inferred from asteroseismic examinations.

A pivotal aspect of this magnetic modeling is the transport of chemical elements by magnetic instability, which is represented by the magnetic diffusion coefficient,  $\eta_{TS}$ . In scenarios devoid of

any instability, this coefficient reverts to the ohmic diffusion coefficient, as presented in Spitzer (1956). When conditions conducive to magnetic instability are met, the precise values of  $\eta_{TS}$  and the Alfven frequency can be discerned, contingent on the threshold conditions triggering the instability, as elaborated in Eggenberger et al. (2022b).

It's noteworthy to mention that in the grand scheme of stellar processes, this magnetic diffusion doesn't bear much weight, especially when juxtaposed against the chemical transport facilitated by  $D_{\rm eff}$ . Despite being side-stepped in our models, it's imperative to compute this quantity given its instrumental role in the subsequent expression for magnetic viscosity, discussed in the following sections.

#### Characterizing Magnetic Viscosity: $\nu_{TS}$

Astrophysical models often incorporate the parameter  $\nu_{\rm TS}$  to describe the transport of angular momentum influenced by magnetic fields. In a research conducted by Eggenberger et al. (2022b), the expression for magnetic viscosity was articulated as:

$$\nu_{\rm TS} = \frac{\Omega r^2}{q} \left( C_{\rm T} q \frac{\Omega}{N_{\rm eff}} \right)^{3/n} \left( \frac{\Omega}{N_{\rm eff}} \right), \tag{3.18}$$

where we employ n=1. Herein, several pertinent parameters come into play. The effective Brunt-Vaisala frequency squared,  $N_{\rm eff}^2$ , is represented as a sum of contributions from temperature,  $N_T^2 = g\delta/H_p(\nabla_{\rm ad} - \nabla_{\rm rad})$ , and the mean molecular weight,  $N_\mu^2 = g/H_p\nabla_\mu$ . The coefficient  $C_{\rm T}$ , set at 216, plays a pivotal role in aligning theoretical models with observational data. To elaborate, this specific choice for  $C_{\rm T}$  facilitates the reproduction of core rotation rates of sub giants, as determined through asteroseismological studies by Gehan et al. (2018). In contrast, the Tayler-Spruit dynamo in its seminal form proposed by Spruit (2002) adopted  $C_{\rm T}=1$ . Eggenberger et al. (2022b) later introduced a calibrated version of the Tayler-Spruit dynamo, assigning it the aforementioned value of  $C_{\rm T}$ . Intriguingly, this calibrated Tayler-Spruit dynamo offers an evolutionary trajectory for core rotation that mirrors the methodology outlined by Fuller et al. (2019). To maintain scientific rigour, it's paramount to underscore the conditions under which this magnetic angular momentum transport becomes relevant. Specifically, it becomes significant when the shear parameter q, defined as  $q = \left|\frac{\partial \ln \Omega}{\partial \ln r}\right|$ , surpasses a threshold, denoted as  $q_{\rm min}$ . Eggenberger et al. (2022b) offers insight into this threshold:

$$q_{\min} = C_{\mathrm{T}}^{-1} \left(\frac{N_{\mathrm{eff}}}{\Omega}\right)^{(n+2)/2} \left(\frac{\eta}{r^2 \Omega}\right)^{n/4}.$$
 (3.19)

In conclusion, understanding magnetic viscosity through the parameter  $\nu_{TS}$  and the nuances

of its computation is crucial for accurate stellar modeling, particularly for phenomena such as core rotation in red giants.

#### Different approach towards rotation

In understanding the internal processes of stars, horizontal turbulence's role in mixing chemical elements stands out as a cornerstone. This turbulence operates in multiple facets, enabling a deeper comprehension of stellar interiors. Foremost, it curtails the inhibiting effect of the  $\mu$ -gradients in  $D_{\rm shear}$ , as discussed by both Maeder (1997) and Talon & Zahn (1997). Next,  $D_h$  is inversely proportional to  $D_{eff}$ , therefore the larger it is, the smaller the value of  $D_{eff}$  and lower the efficiency of transport; a perspective aligned with Chaboyer & Zahn (1992)'s findings.

A pivotal distinction arises when assessing the transport of angular momentum by meridional currents. Specifically, during the Main-Sequence phase, an advective equation represents this transport. This representation's advective nature remains uncontested. However, numerous models opt for approximating this advective process with a diffusive equation, which introduces errors. The diffusive model enforces a unidirectional transport of angular momentum from faster to slower rotating star regions. Conversely, the accurate advective model might allow bi-directional transport. Thus, employing a diffusive approach could misrepresent not just the magnitude but, more critically, the direction of effects.

This diffusive representation also introduces the  $f_C$  parameter. Meridional currents differ in efficiency when transporting angular momentum versus chemical species. Chaboyer & Zahn (1992) provides a detailed exposition on this matter. Essentially, a volume of stellar material's specific angular momentum hinges on its proximity to the rotational axis. In contrast, the transport of the chemical elements does not depend on the distance between the fluid element that is moving and the axis of rotation. Accounting for the advective process circumvents the need for an  $f_C$  parameter, which otherwise describes the differential efficiency in transporting angular momentum and chemical species by meridional currents. Furthermore, models utilizing the  $f_C$  parameter tend to modify the transport efficiency for both angular momentum and chemical species across all processes. For instance, Prat et al. (2016) demonstrated that the transport efficiency, when induced by vertical shear turbulence, remains consistent for both angular momentum and chemicals. This implies an  $f_C$  value approximately equal to 1, whereas typical model values hover around 0.02 to 0.03.

Another stark contrast between the diffusive methodology and our approach concerns accounting for the "shellular" rotation profile, typified by a near-constant angular velocity across an isobar. Our model ascribes this shellular state to powerful horizontal turbulence, unaffected by

the stable stratification present in radiative zones. We account for this turbulence with a diffusion coefficient, denoted  $D_h$ . The precise value of this diffusion remains debated, yet explicitly incorporating it in our models negates the need for the  $f_{\mu}$  parameter. Fully diffusive models, however, omit this horizontal diffusion. The resulting consequence is the introduction of the  $f_{\mu}$  parameter. Strong horizontal turbulence, when explicitly incorporated, can counteract the inhibitory effects of chemical composition gradients (expressed as  $\mu$  gradients). Absent this turbulence, the  $\mu$ -gradients effectively obstruct chemical mixing in zones where such mixing is vital. Studies by both Meynet & Maeder (1997a) and Maeder (1997) offer approaches that integrate the effects of robust horizontal turbulence, thereby diminishing the  $\mu$ -gradient's inhibitory influence.

To summarize, our approach, grounded in physical principles, obviates the need for the  $f_C$  and  $f_\mu$  parameters. Through this, we aim for a more accurate representation of stellar processes. Now we will move on to other aspects of GENEC that are used for computing rotating GENEC models.

#### **Nuclear Reaction Network and Rates**

GENEC offers a meticulous calculation of hydrogen burning via the pp chains or the CNO tri-cycle. It explicitly traces the evolution of primary nuclear species. For helium burning, these reactions are considered:

- $3\alpha$  reactions
- ${}^{12}\mathrm{C}(\alpha,\gamma){}^{16}\mathrm{O}(\alpha,\gamma){}^{20}\mathrm{Ne}(\alpha,\gamma){}^{24}\mathrm{Mg}$
- ${}^{13}C(\alpha, n){}^{16}O$ ,
- $^{14}N(\alpha, \gamma)^{18}F(\beta, \nu)^{18}O(\alpha, \gamma)^{22}Ne(\alpha, n)^{25}Mg$
- ${}^{17}O(\alpha, n)^{20}Ne$
- $^{22}$ Ne( $\alpha, \gamma$ ) $^{26}$ Mg.

A total of 15 isotopes have their nuclear reactions and abundance fluctuations determined: H,  $^{3}$  He,  $^{4}$  He,  $^{12}$  C,  $^{13}$  C,  $^{14}$  N,  $^{15}$  N,  $^{16}$  O,  $^{17}$  O,  $^{18}$  O,  $^{20}$  Ne,  $^{22}$  Ne,  $^{24}$  Mg,  $^{25}$  Mg,  $^{26}$  Mg. In H-burning regions, Ne - Na and Mg - Al nuclear reactions might be taken into consideration. It's worth noting that for Pop III stellar models, a distinct H-burning reaction treatment was developed (Ekström et al. 2006). Meanwhile, during He-burning, neutron capture reactions can be regarded.

The nuclear reaction rates in the Geneva code predominantly come from the NACRE database (Angulo et al. 1999). Nevertheless, for certain reactions, more recent rates have been integrated, as detailed in Ekström et al. (2012a).

#### **Elemental Abundances and Opacities**

GENEC utilizes opacity tables from the OPAL group (Iglesias & Rogers 1993), complemented by the molecular opacities from Ferguson & et al. (1994) at reduced temperatures. We calibrate the initial abundances on the sun, which gives other parameters at a given time. The opacity tables cater to both the customary solar abundances by Noels & Grevesse (1993) and the updated tables from Asplund et al. (2004, 2009).

For models charted at solar metallicity, initial abundances are derived via a solar calibration with GENEC. Using this, the solar luminosity, radius, and surface composition of Noels & Grevesse (1993) at the sun's age (4.57 Gyr) are attained. These results hinge on an initial helium mass fraction  $Y_i=0.2735$ , an initial heavy elements to hydrogen mass fraction ratio  $(Z/X)_i=0.0274$ , and a mixing-length parameter of  $\alpha=1.600$ .

#### **Treatment of Convection**

Nuclear reactions within stellar cores produce energy. This energy travels to the surface via radiation and convection. While structural and nuclear aspects are well-defined, energy transport mechanisms, particularly convection, are less certain due to their complex nature and the challenges in observation-based modeling.

Convection, a 3-D process, occurs when radiation alone cannot move energy outward. In 1-D stellar evolution models like GENEC, convection is defined using the Schwarzschild and Ledoux criteria (Kippenhahn & Weigert 1990). These criteria determine where convection will occur, balancing gravitational and buoyancy forces. A region is stable against convection if:

$$\nabla_{rad} < \nabla_{ad} + \frac{\varphi}{\delta} \nabla_{\mu} \tag{3.20}$$

where  $\nabla_{rad}$  and  $\nabla_{ad}$  are the radiative and adiabatic temperature gradients, respectively.  $\varphi$  and  $\delta$  relate to thermodynamic derivatives. Absent a mean molecular weight gradient,  $\nabla_{\mu} = 0$ , and we revert to the Schwarzschild criterion:

$$\nabla_{rad} < \nabla_{ad} \tag{3.21}$$

If these criteria indicate stability, radiation transports energy; otherwise, convection prevails. GENEC assumes near-instantaneous mixing in convective zones due to the rapid turnover. The mixing-length theory (MLT) is the standard approach, treating fluid elements as cells with an average displacement l, the mixing length. It must benoted that MLT is just used for computing the energy transfer in the outer convective zone where convection is non-adiatic. In interior convective

zones, convection is adiabatic and thus there is no need of the MLT (which is used in non adiabatic zones) to compute the temperature gradients which is equal to the adiabtic one in these zones:

$$l = \alpha_{MLT} H_P \tag{3.22}$$

Here,  $\alpha_{MLT}$  is a calibration parameter. Its value depends on mass and metallicity and influences convective efficiency (Chun et al., 2018). MLT's implementation in GENEC follows traditional methods (Böhm 1958), but may include modifications, such as additional parameters to adjust for temperature gradients and mixing velocities.

#### Advantages and Challenges of 1D treatment of convection

The Mixing-Length Theory (MLT) models convection by relating it to local quantities, thus easing the computation of stellar models. While it provides a simplified view of convection, its representation significantly deviates from actual stellar behavior.

Implementing convection in 1-D stellar evolution models like GENEC presents challenges, especially at convective boundaries. With the Ledoux or Schwarzschild criteria, convective material at boundaries has non-zero velocity, indicating potential overshoot. The actual extent of turbulent convective overshoot in 3-D is uncertain, and assessing its efficiency is difficult.

Efforts to model this behavior with 3-D hydrodynamic models are ongoing. However, the high Reynolds numbers in these regions lead to computational intensity. Without a robust 3-D treatment, 1-D models adopt a simplified convection approach, incorporating prescriptions for overshoot and additional free parameters.

Overshoot regions are typically represented in two ways. The step-overshoot model extends the convective boundary by a distance  $d_{ov}$ , tied to the pressure scale height  $H_P$  and a free parameter  $\alpha_{ov}$ :

$$d_{ov} = \alpha_{ov} H_P \tag{3.23}$$

Alternatively, an exponential diffusive overshoot can be applied, where the diffusion coefficient  $D_{ov}$  in the overshoot region is:

$$D_{ov} = D_0 \exp\left(-\frac{2z}{f_{ov}H_P}\right) \tag{3.24}$$

Here,  $f_{ov}$  is a free parameter, typically around 0.016. Constraining these parameters through observations is complex and ongoing. Factors such as mass and metallicity influence  $\alpha_{ov}$  and  $f_{ov}$ , adding to the process's intricacy.

Because of the use of free parameters, GENEC's convection modeling with MLT aligns with a range of stellar observations. Yet, the precision is limited, and 3-D simulations suggest MLT's inability to capture certain dynamics. For instance, Arnett & Moravveji (2017) and Cristini (2017) showed the inadequacies of MLT's energy flux predictions. They suggested that mass entrainment and stiffness of the convective boundary are a result of 3D treatment of convection, which should be considered in future GENEC models.

#### **Equation of state**

The Geneva code predominantly employs the equation of state tailored for a mixture of perfect gas and radiation. This also encompasses the partial ionization in the topmost layers (Schaller et al. 1992). Although this equation of state is apt for massive stars, solar-type stars necessitate a more specialized one. GENEC offers two distinct equations of state for computing solar-type stars: the MHD (Mihalas 1998; Däppen 1998) and the OPAL equation of state (Rogers et al. 1996; Nayfonov et al. 1999).

#### **Mass Loss**

Massive stars experience a different set of challenges (Georgy et al. 2013a). For them, radiative mass loss is not a phenomenon restricted to later evolutionary stages. Instead, it profoundly impacts their entire lifecycle, from the main sequence phase onwards. Throughout their existence, massive stars boast powerful stellar winds driven by their intense luminosities. These winds lead to the ejection of significant masses over time. For a more intricate understanding of the mass loss prescriptions for massive stars in various stages of their evolution, the research by Ekström et al. (2012a) serves as an essential reference. Beyond the radiative form of mass loss, both low and high mass stars may experience what's termed as 'mechanical mass loss'. This phenomenon gets triggered when a star's surface velocity reaches critical values, making the equatorial regions of the star prone to expelling material. When a star rotates at or near its break-up velocity (the speed at which the centrifugal force counteracts gravity), it can start shedding material from its equatorial regions. GENEC determines the mass loss rate during these episodes by assessing the angular momentum that needs shedding. This mechanism ensures the star's surface velocity reverts to subcritical values and is described in Georgy (2010).

Stellar mass loss, both radiative and mechanical, stands as a pivotal factor in the lifecycle of stars, impacting their structure, evolution, and eventual fate. From the serene, prolonged main sequence phase of low mass stars to the tumultuous, wind-driven lives of massive stars, mass loss processes sculpt their journeys.

#### **Numerical Techniques in GENEC**

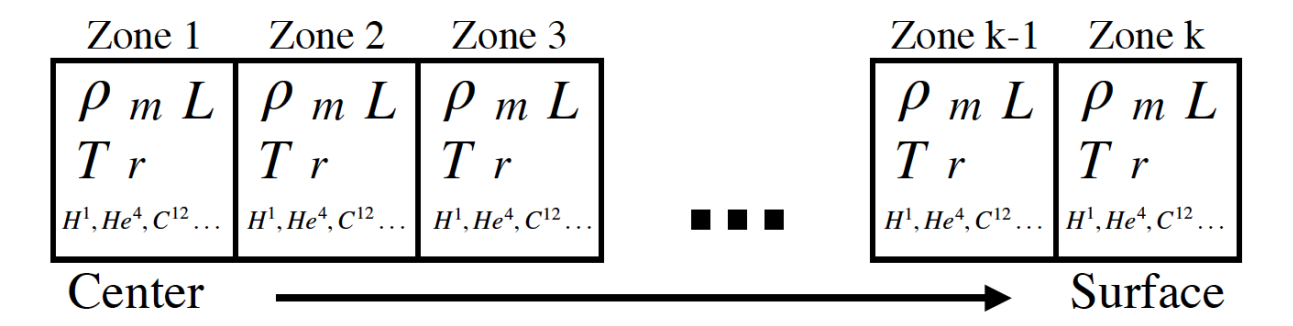


Figure 3.1: Schematic division of a star into k zones with tracked quantities in each zone. In GENEC, the layers are numbered 1 to k from surface to center. Image adapted from Farrell et al. (2022a).

The final section of this chapter will describe the diverse numerical methods and techniques used by GENEC to produce massive and supermassive star models. The star is modeled as around 1000 concentric mass shells for standard massive, rotating stars and around 400 shells for accreting, non rotating supermassive star models. Essential variables for each shell, like mass, radius, temperature, density, and luminosity, are calculated alongside the mass fraction of isotopes. The evolution strategy progresses one time-step at a time, using the Newton method to refine solutions until residuals meet a defined threshold. Each step involves creating a block tridiagonal Jacobian matrix of derivatives, then solving the corresponding linear system for solution corrections.

At the start of a model computation, GENEC initializes by reading input files. GENEC initializes by allocating memory for the model, setting up isotopic data, nuclear reactions, the equation of state, opacity, and physical constants. Once initialized, the model progresses in time. At each step, GENEC checks if the spatial mesh requires adjustment to optimize zone distribution, inserting or removing zones as necessary. It computes various quantities such as thermodynamic gradients and overshooting region properties, and adjusts the mass accordingly. After these steps, the updated star mass and composition are resolved using repeated Newton iterations. If the solution aligns with the set spatial and temporal resolutions, it is approved. Model calculations are then saved, and the subsequent time step's duration is computed. Managing the spatial mesh and time step is crucial in stellar evolution models due to the significant changes that can occur within small interior regions of a star. High resolution is essential for accurately capturing these changes. The lifespan of stars can span orders of magnitude, necessitating precise time steps from 10 Gyr for a  $1M_{\odot}$  star to a single day for the silicon burning phase of a massive star. Time steps in GENEC are carefully calibrated to ensure both convergence within a manageable number of iterations and

practical computation of the star's full evolution. At each step's conclusion, GENEC evaluates the next time step's duration, considering factors like the previous step's length and the changes observed in the star's model.

# 3.2 Numerical convergence of massive star models in GENEC

#### 3.2.1 Introduction and Purpose

The sun\_data\_parser\_3.py script is a Python utility specifically crafted for assisting with the computation of massive star models in GENEC. It focuses on the detailed analysis of rotating massive stars, particularly those with characteristics akin to our Sun in terms of metallicity. The script shines in scenarios where stars exceed  $60~M_{\odot}$  and are transitioning through the core helium burning stage, advancing towards the Wolf-Rayet (WR) phase, characterized by intense mass loss and complex evolutionary dynamics. In our numerical models, the stellar structure is categorized into three regions: 1) The atmosphere is assumed to be a mass-negligible layer with constant luminosity. 2) The envelope, also with constant luminosity, accounts for the effects of partial ionization and non-adiabatic convection. 3) The interior is where the comprehensive set of structural equations are fully resolved, assuming adiabatic convection and complete ionization.

The boundary between the interior and the envelope, defined as the Fractional Interior Transition Mass (FITM), varies throughout the star's life cycle. FITM is defined as the mass coordinate within the stellar model that demarcates the interior from the envelope, expressed as a fraction of the star's total mass. For instance, a FITM value of 0.999 indicates that the transition from the envelope to the interior takes place at 99.9% of the star's total mass.

The distinction between the envelope and the interior lies in their physical characteristics and the equations governing them. As the star evolves, especially into the red supergiant phase, the cooler outer layers extend the region of partial ionization, necessitating adjustments to the FITM. A well-calibrated FITM ensures continuity at the junction, with matching radius, pressure, and temperature values at the envelope's base and the interior's top. To handle changes in FITM smoothly, particularly during rapid surface composition changes due to mass loss, an automated procedure has been implemented. This ensures consistent model convergence by dynamically adjusting the FITM.

#### 3.2.2 Core Functionalities

1. **File Handling and Data Extraction:** The script initiates its process by creating a list of .1 files (each representing a star model's time-series data) using the make\_file\_list function.

These files are crucial as they contain the entire simulation data set for each star model. It then employs the sun\_data class to systematically parse these files. This class is adept at segregating and interpreting the sections and data within the files, typically demarcated by specific markers like '# modnb age' and '#j xmr p t'.

- 2. Data Organization and Accessibility: Upon identifying the relevant data sections, the script extracts key information such as column names and corresponding values. This data is meticulously organized into dictionaries, making it readily accessible for further analysis. The structure is such that data related to specific parameters can be quickly retrieved using dictionary keys.
- 3. Analysis of Stellar Evolution Parameters: In the realm of stellar simulations, certain parameters like radius, pressure, temperature, and luminosity are of paramount importance. The script is adept at analyzing these parameters to provide a comprehensive view of the star's condition at various simulation stages. It specifically looks for anomalies like radius inversion and pressure inversion. These are crucial indicators of potential issues in the simulation's numerical convergence.
- 4. Convergence Issue Identification and Resolution: A standout feature of the script is its ability to identify and suggest resolutions to numerical convergence problems. This is critical in simulations, especially for stars undergoing dramatic changes like those approaching the WR stage. The script offers actionable insights, such as adjusting the Fraction Inside Transition Mass (FITM), a key parameter in these simulations. It guides the user on when to alter and revert FITM to optimize the simulation's accuracy and stability.
- 5. Enhanced Support for Wolf-Rayet Stage Simulation: As stars near the WR stage, monitoring temperature and luminosity becomes increasingly important. The script includes functionality to track these indicators, signaling the onset of this critical phase. During this phase, the script's recommendations for adjusting FITM are particularly vital, ensuring the simulation accurately captures the complexities of the WR stage.

#### 3.2.3 Conclusion

Overall, sun\_data\_parser\_3.py stands as a specialized, user-friendly tool for monitoring advanced evolutionary phases of massive stars in GENEC. It monitors crashes regarding radius and density inversions and provides suggestions with regards to changing FITM.

# 3.3 Hydogen burning plateau in accreting stars

#### 3.3.1 Problem Summary

In the pre-main sequence (preMS) phase of the GENEC code, there is a challenge with the evolution of supermassive stars during hydrogen burning. The models appropriately initiate the main sequence when the temperature is adequate for hydrogen burning, indicated by the declining hydrogen mass fraction at the center of the star. However despite the nuclear reactions occurring the center of the star, the central mass fraction of hydrogen does not decrease but instead fluctuates and stays constant. We called this behaviour as the hydrogen burning plateau problem and it was present for all accreting stellar models with constant accretion rates upwards of  $10^{-3}~{\rm M}_{\odot}/{\rm yr}$ . Notably, models with a higher accretion rate of 0.1 solar masses per year exhibit this plateau early in their evolution when the central mass fraction of hydrogen reached 0.6. Models with a lower accretion rate of 0.01 solar masses per year also reach a plateau, albeit with less fluctuation. This was clearly an un-physical phenomenon that was due to numerical issues in the code rather than actual physical process.

#### 3.3.2 Key Observations

The issue is specific to the preMS version of GENEC where models undergo accretion. The plateau manifests not at the onset of hydrogen burning but later in the evolutionary process. Eliminating initial deuterium and helium-3 (by setting their abundances to zero in the initial files) does not resolve the issue. Instead, it alters the timing and occurrence of the plateau. The helium mass fraction at the center shows a similar trend to that of hydrogen. As central mass fraction of hydrogen begins to show fluctuations and plateau, so does the helium mass fraction.

#### Methodology

The investigation focuses on the energy production in GENEC and involves comparing generated energies to pinpoint discrepancies. The energy from hydrogen burning is calculated by the equation provided below, which should balance with the energy output as luminosity since neutrino energy is negligible during core hydrogen burning.

$$(M_H(t) - M_H(t+dt)) \cdot 0.007 \cdot c^2 = \frac{1}{2} (L_{\text{nuc}}(t) + L_{\text{nuc}}(t+dt)) \cdot dt$$
 (3.25)

Here,  $M_H$  represents the mass of hydrogen, t is time, dt is the time step between two models, and  $L_{\text{nuc}}$  is the luminosity due to nuclear burning of hydrogen. The constant c is the speed of light.

This equation is applied to the outer layers of the star at various stages of evolution. A Python script calculates the discrepancy. The chosen model for this analysis has an accretion rate of 0.1 solar masses per year.

#### **Test 1: Analysis of Evolutionary Energy Discrepancies**

An accreting stellar model produces energy via various means;  $E_{lum}$  is the integrated energy emitted under the form of radiation by the star between two times.  $E_{nuc}$  is an estimate of total energy relesead in the star by the transformation of hydrogen into helium between two time steps. The remaining energy comes from gravitational contraction and other sources (such as neutrinos etc). The first test looks at this energy generation in detail, specifically focusing on the total reservoir of energy ( $E_{lum}$ ) and the energy generated by nuclear reactions ( $E_{nuc}$ ). To explore the source of this issue, we looked at two consecutive sequences of models. For instance, we compared models 140131 and then 140141 ,followed by 140141 and 140151 and so on. Upon calculating these values, we found that in nearly all the models before the plateau began to appear,  $E_{nuc} \approx E_{lum}$ . Once the plateau arises, we found that the actual discrepancy between  $E_{lum}$  and  $E_{nuc}$  would exceed a factor of 1.5. We compiled a list of models where such a behaviour was present and a few of such models are shown in Table 3.3.2.

Model Numbers	Reservoir Energy $(E_{\text{nuc}})$	<b>Actual Energy</b> ( $E_{\text{lum}}$ )			
140131, 140141, Mr 111618	$3.94 \times 10^{52}$	$8.36\times10^{52}$			
150131, 150141, Mr 124000	$1.09 \times 10^{53}$	$7.80 \times 10^{52}$			
160031, 160041, Mr 134000	$1.19 \times 10^{53}$	$9.64 \times 10^{52}$			
170031, 170041, Mr 146000	$1.59 \times 10^{53}$	$1.19 \times 10^{53}$			
180231, 180331, Mr 156000	$3.72 \times 10^{52}$	$1.01 \times 10^{53}$			
191531, 191541, Mr 164000	$7.58 \times 10^{52}$	$8.08 \times 10^{52}$			
200131, 200141, Mr 174000	$9.83 \times 10^{52}$	$1.04 \times 10^{53}$			

Models 140131 and 180231 show a discrepancy greater than a factor of 2. These significant differences mark them as prime candidates for deeper investigation. The subsequent objective is to locate the internal region of the star where this discrepancy occurs. Moreover, the analysis will determine if the discrepancy is consistent across several models or isolated to specific instances.

Adjusting the test mass location used in calculating the energies may reveal changes in the energy balance. Understanding whether the discrepancy progressively increases or is model-specific will provide insights into the nature of the energy generation and loss in these stars.

#### Test 2: Analyzing Hydrogen Abundance

A dedicated script was developed to examine the hydrogen abundance discrepancies in greater detail. The analysis focused on a graph, referred to as 3.2, where the hydrogen abundance is plotted against the stellar mass. This graph is crucial for verifying hydrogen abundance consistency before integration. In the plot, two lines represent models 140131 and 140141. The lines appear consistent, indicating no pre-integration discrepancies in hydrogen abundance. So far, no real issues could be detected as evidenced in fig. 3.2. Further investigation is required.

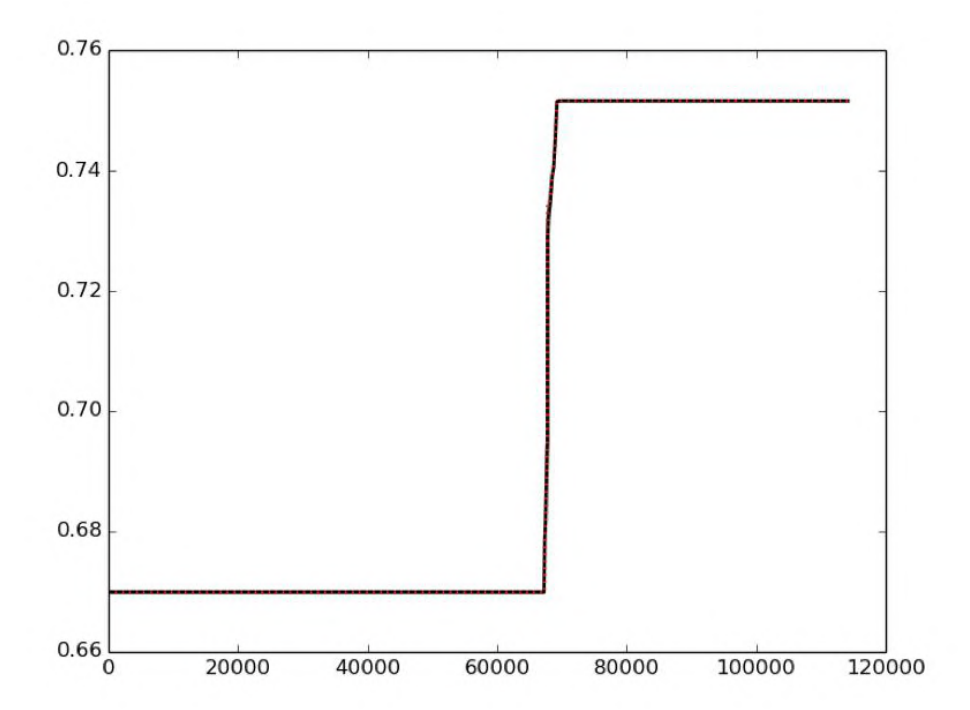


Figure 3.2: Hydrogen abundance as a function of stellar mass for models 140131 and 140141, showing consistent pre-integration levels.

#### **Test 3: Discrepancy in Energy Generation**

Test 3, shown in Fig. 3.3, scrutinizes models 140121 and 140131, where the energy discrepancy reaches approximately a factor of 10. This test is pivotal for future analyses. The plot features two distinct curves:

- The black curve corresponds to the plot of  $M_r$  versus  $\varepsilon_1$  (nuclear energy generation rate from the '.v' file,  $\varepsilon_{\text{nuc}}$ ).
- The red curve represents the change in nuclear energy, computed as  $\Delta 0.007 M_{\rm H} c^2$ , based on the hydrogen abundance.

The x-axis of the plot denotes the stellar mass in solar units (0.1  $M_{\odot}/yr$ ). A significant spike is observed between masses 67800 and 68000, pinpointing the primary source of energy discrepancy. This level of detail is unprecedented in previous observations.

Furthermore, yellow vertical lines on the plot correspond to the addition of new layers in the model (Schrit). It is observed that the discrepancy tends to arise with the addition of a considerable number of new layers. Notably, the density of these yellow lines is greatest in the mass range 67800 to 68000, which coincides with the peak of the discrepancy. While other masses show the addition of new layers, they do not exhibit a significant energy discrepancy.

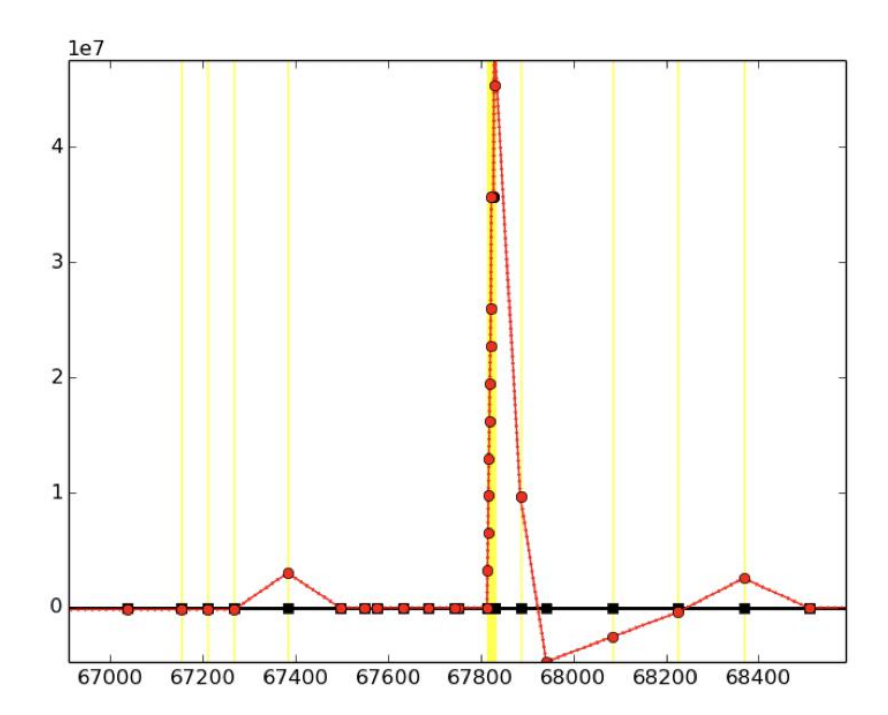


Figure 3.3: Plot of a  $0.1~M_{\odot}/yr$  model at the point of encountering the plateau. The model number being analysed is 140121. The plot shows the nuclear energy generation rate and the corresponding change in nuclear energy based on H abundance, highlighting the significant energy discrepancy between masses 67800 and 68000. The Y-axis is the nuclear energy generate rate and X-axis represents the mass of the star in solar masses. The description of the coloured lines in provided in the adjoining text.

This suggests that the routine responsible for layer addition, Schrit, may be a contributing factor to the observed energy discrepancy. The correlation between the density of new layer additions and the spike in discrepancy is a compelling lead for further investigation. A possible explanation could be as follows: Adding new layers to a model can artificially alter the composition of chemical elements. This is because the properties of the newly added layers need to be estimated or interpolated from adjacent layers. Consequently, it's not certain that the integrated quantity of an isotope will remain consistent when these new layers are accounted for.

#### **Test 4: Analyzing Hydrogen Abundance Variations**

This test investigates the variation in hydrogen (H) abundance between models 140121 and 140131. Fig. 3.4 shows two lines indicating the difference in H abundance. The dotted lines represent the H fraction from model 140121, and the solid black line corresponds to model 140131. The plot reveals that changes in H fraction coincide with the addition of new layers (marked by yellow lines). The forthcoming test will determine whether these discrepancies occur within the convective or radiative regions of the star.

#### **Test 5: Locating Discrepancies in Star Layers**

The discrepancy is observed in a newly created layer, marked by Schrit (yellow line). Ideally, the black line and the dotted lines, which represent the H abundance between two models, should align; however, they do not. This suggests that hydrogen is being artificially generated in the model. Notably, this artificial generation of hydrogen occurs concurrently with the addition of new layers (Schrit, yellow lines) in the code. This discovery pinpoints the exact region and cause of the discrepancy. Additionally, light grey lines denote radiative layers, while dark grey lines represent convective layers, indicating that the problem exists within the radiative layer.

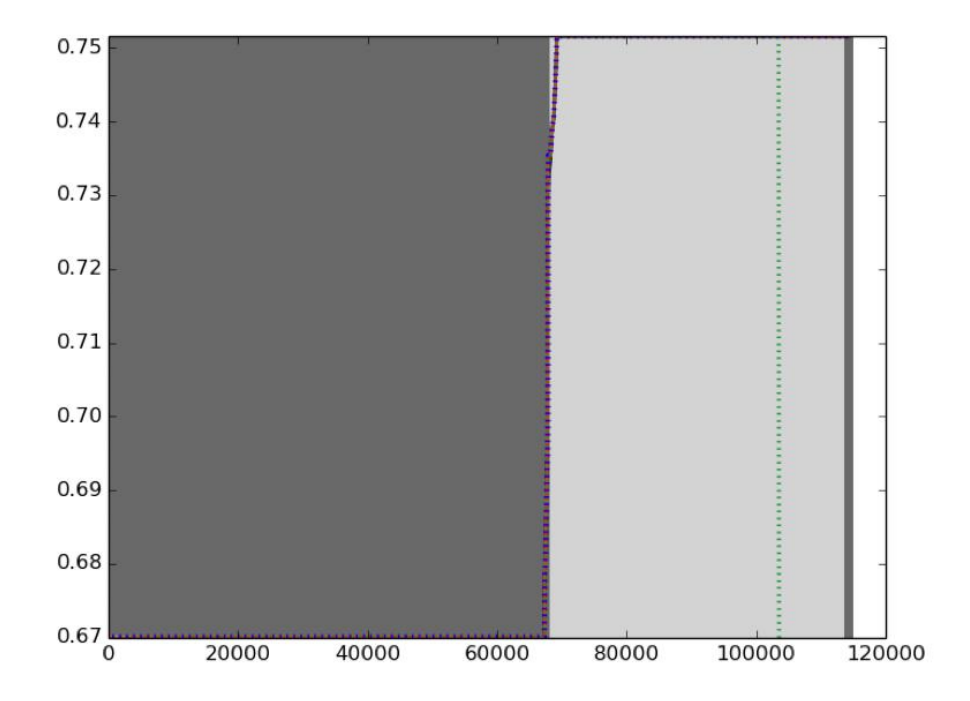


Figure 3.4: Discrepancy in hydrogen abundance linked to the addition of new layers, with radiative and convective layers marked by light and dark grey shading, respectively. The y axis is the central mass fraction of hydrogen and the x axis is the mass of the model in solar masses.

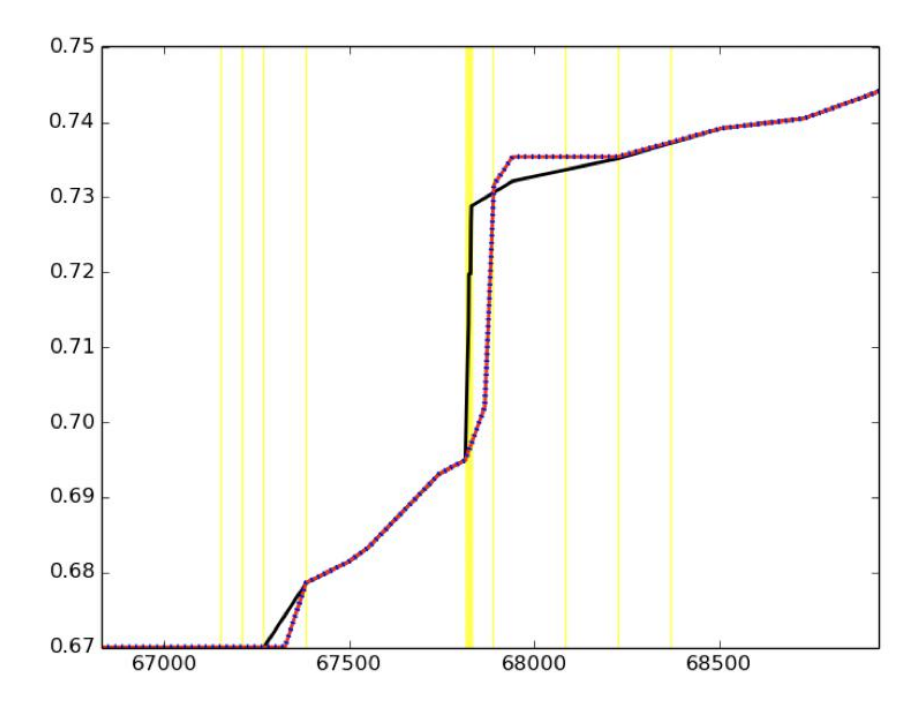


Figure 3.5: A zoom in shown in the region where the discrepancy arises. The mass fraction missmatch here shows the exact location of the issue.

## Solution to the Discrepancy Problem

The discrepancies in hydrogen abundance and layer addition within the GENEC models were resolved through targeted code modifications. Key changes were made in order to avoid any artificial appearance of hydrogen in the star when layers are added.

Correcting layer tracking The variables used for correctly tracking layer numbers during accretion, were not being shifted appropriately. This caused the addition of a new layer that will bring excess of hydrogen in the star. Previously this layer would be simply added without adjusting the numbering of previous layers. Addition of a number of such layers in the subsequent evolution would pile up and cause the mass fraction to artifically plateau. This issue was rectified, and the layers were renumbered to account for the addition of a new surface layer. These changes were implemented to mirror the physical process of accretion accurately. As a result, all the accreting supermassive models could be computed beyond the early core hydrogen burning phase

# 3.4 Enhancements to Accretion Handling in GENEC Models

#### 3.4.1 Problem Identification

In the study of supermassive stars, numerical convergence issues arose when accreting large amounts of mass onto a  $2\,M_\odot$  seed at rates exceeding  $0.1\,M_\odot$ /yr. Moreover, as the stars approached the main sequence and commenced hydrogen burning, the timesteps within GENEC would automatically increase. This led to unrealistically large masses being accreted between timesteps, further exacerbating convergence problems.

#### 3.4.2 Solution Implementation

To address these issues, the '.prems.f90' file, particularly the 'accrini' subroutine, was enhanced. We adjust the timesteps in such a way that a maximum of 1% of the current mass is accreted. A key addition to the subroutine is the condition that the timestep 'dzeitj' must not exceed 1% of the characteristic accretion time, calculated as ' $0.01 \times gms/xmdot_{accr}$ '. This change guards against the timestep becoming excessively large and thus limits the amount of mass accreted in each step. Furthermore, the initial mass 'xmini' is adjusted only if the accreted mass during one timestep exceeds the current mass, ensuring consistency with the physical process of accretion.

An additional modification was to delay the onset of accretion until after the first 10 models had been computed. This allowed the hydrostatic seed to reach a better state of convergence before accretion began, facilitating the eventual accretion of mass at a rate of 1000  $M_{\odot}/yr$  onto the 2  $M_{\odot}$  seed.

#### 3.4.3 Results

The implemented solutions resulted in a significant improvement in numerical convergence during the critical phases of stellar evolution. By delaying the start of accretion, the initial models could stabilize, thereby enabling the simulation of extremely high accretion rates without the previously encountered numerical difficulties.

# 3.5 Implementation of Variable Accretion Rate in GENEC

#### 3.5.1 Motivation

In the early stages of stellar formation, accretion plays a pivotal role in determining the mass and evolutionary trajectory of stars. Research in cosmological structure formation suggests that accretion rates are not constant but vary significantly over time. According to simulations of gas accretion flows in the primordial lambda-CDM universe by Yoshida et al. (2006), the accretion rate decreases as the mass of the star increases. This inverse relationship is expected since, in the dense environments of early star formation, the initial conditions are highly turbulent and can supply large amounts of gas rapidly. As the star grows, the surrounding gas depletes, and the gravitational potential deepens, reducing the infall rate. Implementing a variable accretion rate in stellar evolution codes like GENEC allows for a more realistic simulation of the growth of supermassive stars, reflecting the dynamic processes that govern the early universe.

#### 3.5.2 Mass dependent Accretion law

The variable accretion law by Yoshida et al. (2006) has been incorporated into GENEC's premain sequence evolution file, 'preMS.f90', allowing the code to adjust the accretion rate based on the current stellar mass. For a star with a mass less than 300 solar masses, the accretion rate is set to follow a power law with a decline proportional to  $M^{-\frac{2}{3}}$ . For masses greater than this threshold, the accretion rate declines more steeply, proportional to  $M^{-1.7}$ . This variable rate is crucial to accurately simulate the mass growth of supermassive stars, ensuring that the accretion process naturally slows down as the star's mass increases.

The mathematical representation of this accretion law is as follows:

$$\dot{M}_{\rm accr} = \begin{cases} 0.045 \times M^{-(2/3)}, & \text{if } M < 300 M_{\odot} \\ 16.3 \times M^{-1.7}, & \text{otherwise} \end{cases}$$
(3.26)

#### 3.5.3 Integration of Variable Accretion Rates from Cosmological Simulations

Background and Motivation Following the introduction of the Yoshida et al. (2006) accretion law in GENEC, the next advancement involved implementing a variable accretion rate derived from large-scale hydrodynamical and cosmological simulations. These simulations examine primordial and mini haloes, each featuring unique accretion rates influenced by the complex physics of early universe star formation. Factors such as the density of the interstellar medium, turbulence within the halo, and the halo's mass contribute to varying accretion rates. Incorporating

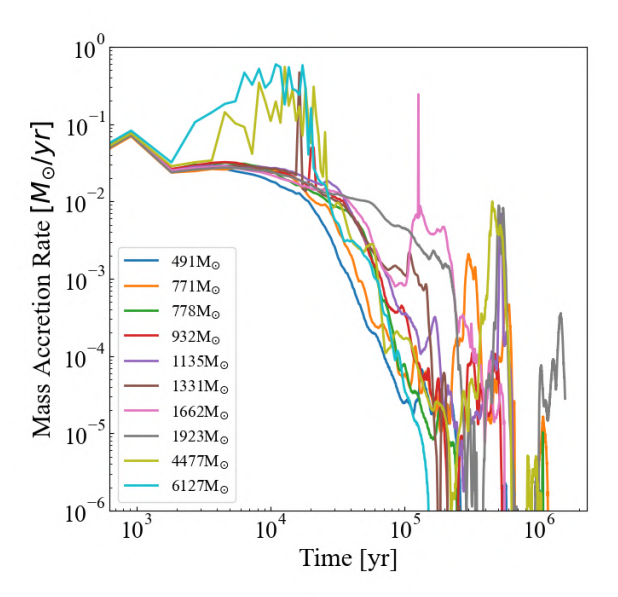


Figure 3.6: Accretion rate history of the ten massive PopIII models computed using GENEC by reading external accretion rate tables. The data for each star are taken from Regan et al. (2020a).

these rates into GENEC was a critical step towards simulating the formation of supermassive stars more realistically. An example of models computed using the variable accretion rates is shown in Figure 7.10. These accretion rates were read by GENEC using data presented in external files.

Challenges and Achievements Implementing these variable accretion rates required additional modifications to GENEC. These changes enabled the software to handle the turning on and off of accretion, a crucial feature for simulating the complete lifecycle of supermassive stars. The successful integration of these rates allowed for the simulation of stars from their formation to the end of their lifetimes.

# 3.6 Incorporation of metals and isotopes Accretion in Metal-enriched Environments

Traditionally, supermassive star models in GENEC have been computed assuming zero metallicity, aligning with the characteristics of Population III stars. However, emerging insights from cosmological simulations, such as the influence of primordial magnetic fields and the merging of slightly evolved stars, necessitate the consideration of non-zero metallicity environments. These environments are rich in various elements and isotopes, deviating from the simplistic PopIII composition. To achieve this in GENEC, we changed the code to take the initial value used at the start of computation as the ISM value. This composition was then accreted.

#### 3.6.1 Streamlined Computational Tools for Supermassive Star Analysis

#### **Key Enhancements in SMS Modeling**

The analysis of supermassive stars (SMS) has been significantly advanced by improvements in two key computational tools: the Ultimate Kippenhahn script and the Geneva Stellar Evolution Code.

#### Ultimate Kippenhahn Script Upgrades:

- File Loading Efficiency: Processing time reduced from over 10 minutes to under 10 seconds.
- Enhanced Plotting Capabilities: Introduction of new plotting parameters for improved SMS dynamics representation.
- New Variable Integration: Inclusion of crucial variables such as isobars and isotherms for in-depth SMS internal process analysis.

#### • GENEC Enhancements:

- makeini Program: Refined to generate more accurate initial structures, supporting a broader range of masses and metallicities, and improved chemical composition setup.
- rbin2010 Program: Enhanced for effective preparation of initial models, ensuring detailed parameter adjustments and GENEC compatibility.

**Overall Impact:** These enhancements have significantly increased the efficiency and accuracy of SMS research, enabling more rapid data processing and precise modeling.

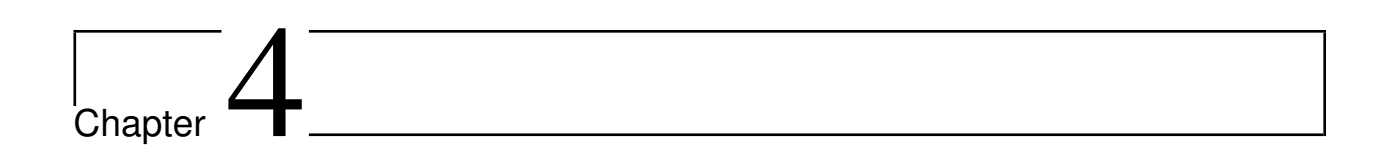
#### 3.7 Conclusion

The Geneva Stellar Evolution Code (GENEC) has undergone significant enhancements to effectively model Supermassive Stars (SMS). These improvements address the unique challenges presented by these massive entities, ranging from accretion dynamics to metallicity aspects.

A notable enhancement in GENEC addresses the hydrogen burning plateau problem, which
was a significant challenge in earlier SMS models. The SMS models can now correctly compute core hydrogen burning and reach the end of core-silicon burning.

- GENEC's initial use of the Yoshida accretion law evolved to include variable accretion rates
  from hydrodynamical and cosmological simulations. This adaptation reflects more realistic
  scenarios in primordial halos and mini halos, where accretion rates are influenced by complex astrophysical processes.
- The revised GENEC now accounts for the accretion of metals and trace isotopes, moving beyond the zero-metallicity focus of previous models. This development is crucial for simulating metal-enriched SMS models, aligning with insights on primordial magnetic fields and star mergers.
- Enhancements in the Ultimate Kippenhahn script and GENEC have improved supermassive stars (SMS) analysis. Upgrades include rapid file loading, advanced plotting, and integration of critical variables in the Kippenhahn script, alongside refined initial structure generation and model preparation in GENEC. These improvements significantly boost efficiency and precision in SMS research, enhancing understanding of their evolution and behavior.

The advancements in GENEC, including variable accretion rates, visualization tools, and initial structure generation, have profoundly contributed to SMS research. These enhancements enable GENEC to compute SMS models that can be evolved until the end of their evolution over accretion rates that span over 10 orders of magnitude.



# Massive stars: Impact of rotational prescriptions

This chapter is adapted from the paper Nandal et al. (2023b). Stellar rotation greatly influences the evolution of stars, manifesting in varied phenomena from internal chemical mixing to changes in surface velocities. It plays a pivotal role in determining a star's position in the Hertzsprung Russell (HR) diagram and has implications for the mass limits and evolutionary endpoints of stars. However, integrating the effects of rotation into stellar models presents challenges due to the myriad processes involved and the differing methodologies employed in the literature. Recognizing these complexities, our study aims to address discrepancies in the current understanding by examining both non-magnetic and magnetic star models, specifically of 15 and  $60~{\rm M}_{\odot}$  at solar metallicity. In this chapter there are three primary goals:

- 1. Compare and contrast the evolutionary tracks, lifetimes, and surface compositions for stars with different initial conditions and rotational implementation.
- 2. Analyze the internal angular velocities and delve into the stellar cores' properties at the culmination of the core helium-burning phase.
- 3. Investigate the intriguing boron depletion observed at the onset of core hydrogen burning in massive rotating stars, which promises insights into the internal mixing process.

This chapter is structured to provide a systematic overview of the research. We initiate with a detailed examination of the transport equations used in rotating models in chapter 2. This is followed by a discussion on their implementation in the star models in Sect. 4.2. Results for the 15  $M_{\odot}$  and 60  $M_{\odot}$  models, considering the effects of hydrodynamic instabilities due to rotation, are

presented in Sections 4.3 and 4.3.7. We then detail the magnetic models in Sect. 4.3.10 and conclude our findings in Sect. 4.3.13. Through this comprehensive analysis, we endeavor to enrich the understanding of rotational effects on stellar evolution.

# 4.1 Background literature

The study of the impact of rotation in stellar evolution has been at the forefront of research over the years (e.g. Maeder & Meynet 2012, and references therein). When a star rotates, it doesn't merely spin; its very fabric alters, causing shifts in its structural equilibrium and form (Kippenhahn & Thomas 1970; Meynet & Maeder 1997b). This domino effect in a star instigates several instabilities, leading to the transport of essential elements and angular momentum (with transport equations well-articulated by Endal & Sofia 1981; Zahn 1992; Maeder & Zahn 1998; Spruit 2002, in 1D stellar models).

This phenomenon isn't just internal. Rotation affects a star's external behavior, notably impacting mass loss through line-driven stellar winds (Maeder 1999; Heger et al. 2000; Maeder 2002; Müller & Vink 2014; Bogovalov et al. 2021). In extreme scenarios, a star can even shed its mass mechanically when rotation speeds counteract gravity's pull (Krtička et al. 2011; Georgy et al. 2013a). This external dynamic interplay often finds representation in the Hertzsprung Russell (HR) diagram, where a star's life journey is mapped. Chemically homogenous evolution showcases this journey, where rotation-induced mixing dramatically alters a star's HR path (Maeder 1987; Mandel & de Mink 2016; de Mink & Mandel 2016; Song et al. 2016).

Moreover, the thresholds or "mass limits" governing stellar events, such as entering the Wolf-Rayet phase (Meynet & Maeder 2005) or confronting a pair-instability supernova, fluctuate with rotational factors (Chatzopoulos & Wheeler 2012; Marchant & Moriya 2020). Such rotation dynamics also meddle with nucleosynthesis in massive stars. This interference, although subtle, leaves a noticeable footprint on specific isotopes, highlighting isotopes like <sup>26</sup>Al, <sup>14</sup>N, and the intriguing s-process (Palacios et al. 2005; Brinkman et al. 2021; Martinet et al. 2022; Brinkman et al. 2023; Meynet & Maeder 2002; Pignatari et al. 2008; Frischknecht et al. 2016; Choplin et al. 2018; Limongi & Chieffi 2018; Banerjee et al. 2019). The influence of rotation becomes even more pronounced when we approach its pre-supernova stage. Here, the looming core collapse and the characteristics of what remains post-collapse are significantly molded by the star's rotation history (Hirschi et al. 2004, 2005b; Limongi & Chieffi 2018; Fields 2022).

Zooming out to larger astrophysical puzzles, rotation emerges as a cornerstone. From deciphering the mysteries behind long Gamma Ray bursts' progenitors to uncovering the origins of the universe's primary nitrogen, rotation offers invaluable insights. It even sheds light on the mass and spin boundaries of celestial giants like black holes and neutron stars (Hirschi et al. 2005a; Yoon et al. 2006; Chiappini et al. 2006a; Heger et al. 2005; Fuller & Ma 2019; Griffiths et al. 2022; Fuller & Lu 2022).

The effects of rotation has been explored by various stellar evolution groups with their own codes (Brott et al. 2011; Ekström et al. 2012c; Choi et al. 2016; Limongi & Chieffi 2018; Renzo & Götberg 2021; Nguyen et al. 2022; Pauli et al. 2022; Renzo et al. 2023). However, a lack of uniformity in these models' approaches, especially in handling angular momentum and chemical dynamics, often leads to divergent results even with identical initial parameters. Such inconsistencies are deeply rooted in the nuances of individual model codes and the intricacies of the embedded physical processes.

This brings us to an essential categorization in the realm of rotating star models: the non-magnetic and magnetic divide. It's crucial to note that "magnetic" in this context isn't about an external magnetic field (Meynet et al. 2011; Keszthelyi et al. 2020). Instead, it delves deeper, focusing on internal dynamos driven by magnetic instabilities, such as the Tayler-Spruit dynamo theory (Spruit 2002). While Ekström et al. (2012c); Choi et al. (2016); Limongi & Chieffi (2018); Nguyen et al. (2022) offer glimpses into non-magnetic models, magnetic models find champions in Heger et al. (2005); Brott et al. (2011).

To lend clarity to this discussion, the GENEC stellar code's evaluation in Meynet et al. (2013) sets a precedent. Our current exploration, however, delves deeper and wider. We critically examine both non-magnetic and magnetic star models, particularly of 15 and  $60 \, M_\odot$  at solar metallicity, shedding light on evolutionary trajectories, surface transformations, core developments, and more in Sect. 4.3. Of particular interest is the boron depletion early in massive rotating stars. This phenomenon, rather than indicating external factors, provides a unique window into internal star mixing (Fliegner et al. 1996; Proffitt et al. 1999; Proffitt & Quigley 2001; Venn et al. 2002; Mendel et al. 2006; Frischknecht et al. 2010; Proffitt et al. 2016). Our findings also compare the influences of different model prescriptions, especially in stars heavily affected by wind-induced mass loss.

# 4.2 Additional physics

The details regarding the rotational prescriptions are presented in Chapter 3. Here, a few additional sections describing the physics related to this work is presented.

#### 4.2.1 Hydrostatic effects due to rotation

Rotation significantly impacts the hydrostatic structure of stars. Initiated by the centrifugal force, this effect contrasts the structure of rotating stars with their non-rotating counterparts (Chandrasekhar 1933; Kong et al. 2015). Rotation disrupts the spherical symmetry inherent in non-rotating stars. Centrifugal forces lead to an oblate star shape, a deformation that varies the temperature gradients along the rotation axis and in the equatorial plane. Consequently, this morphological change affects the brightness and chromatic properties of the star based on its latitude (von Zeipel 1924; Espinosa Lara & Rieutord 2011). To depict stars on the Hertzsprung-Russell (HR) diagram, the chosen parameters are the bolometric luminosity and a surface-averaged effective temperature, represented by L and  $T_{\rm eff}$ , respectively. The latter's definition is particularly interesting:

$$L = 4\pi R^2 \sigma T_{\text{eff}}^4 = S\sigma T_{\text{eff}}^4 \tag{4.1}$$

Here, R symbolizes the radius of a sphere that has a surface, S, equivalent to the deformed star. It's crucial to note that a star's observed luminosity can vary with its inclination. Especially for rapidly rotating stars, the luminosity differs when viewed pole-on versus equator-on. Yet, in our models, these rotational effects are negligibly small. Additionally, the rotational deformation alters the star's mechanical equilibrium, distinguishing it from that of non-rotating stars. To address these hydrostatic effects, we adopt the methodology proposed by Kippenhahn & Thomas (1970). Although this method is primarily devised for cylindrical angular velocity distribution, its application extends to shellular rotation, as discussed in Meynet & Maeder (1997b).

#### 4.2.2 Angular Momentum Advection Equations

A core aspect of our study revolves around the equations governing the transport of angular momentum. Before delving into their intricacies, it's paramount to ensure their accuracy and alignment with the code. At a fundamental level, the equation for chemical species transport is diffusive. Contrarily, the angular momentum equation exhibits advecto-diffusive characteristics. Prior to certain simplifications, applicable mainly to chemical species, both equations are inherently advecto-diffusive. As demonstrated by Chaboyer & Zahn (1992), the advecto-diffusive equation for chemical species simplifies to a purely diffusive equation under strong horizontal turbulence. Meridional currents play a pivotal role in the transport of angular momentum. Their influence is especially pronounced when meridional current-driven transport dominates, such as in rotating massive stars during their core Hydrogen burning phase devoid of dynamo effects.

Several equations elucidate this phenomenon. Let's enumerate them:

$$\Theta - \frac{2}{3} \frac{r\Omega^2}{g} \frac{\partial \ln \Omega}{\partial \ln r} = 0 \tag{4.2}$$

$$A + H_T \frac{\partial}{\partial r} \left( \frac{\Theta}{\delta} \right) - H_T \frac{\partial}{\partial r} \left( \frac{\Lambda}{\delta} \right) - \frac{\Theta}{\delta} + \chi_\mu \Lambda + \frac{\chi_T}{\delta} \Lambda + \frac{\Lambda}{\delta} - (\chi_T - 1)\Theta = 0$$
 (4.3)

$$U_2 + \frac{P}{\rho g C_P T (\nabla_{ad} - \nabla_{rad} + \frac{\phi}{\delta} \nabla_{\mu})} \frac{L}{M_*} (E_{\Omega} + E_{\mu}) = 0$$
(4.4)

$$\frac{\partial(r^2\Omega)}{\partial t} - \frac{1}{5\rho r^2} \frac{\partial}{\partial r} \left(\rho r^4 \Omega U_2\right) \tag{4.5}$$

In these equations:

$$E_{\Omega} + E_{\mu} = 2 \left[ 1 - \frac{\Omega^{2}}{2\pi G \rho} - \frac{\epsilon}{\epsilon_{m}} \right] \frac{\tilde{g}}{g}$$

$$+ \frac{\rho_{m}}{\rho} \left( \frac{r}{3} \frac{\partial A}{\partial r} + \frac{2H_{T}}{r} \frac{\Theta}{\delta} - \frac{2}{3} \Theta - \frac{2H_{T}}{r} \frac{\phi}{\delta} \Lambda \right)$$

$$+ \frac{\epsilon}{\epsilon_{m}} \left( A - \chi_{T} \Theta - (\epsilon_{T} - \chi_{T}) \frac{\Theta}{\delta} + (\epsilon_{\mu} + \frac{\varphi}{\delta} \epsilon_{T}) \Lambda \right)$$

$$+ 2H_{T} \frac{\rho_{m}}{\rho} \frac{U_{2}}{K} \frac{\Theta}{\delta}$$
 (4.6)

The above set of equations characterize the transport of angular momentum and its interrelation with various stellar properties. However, it's important to calibrate these equations with observational data to ensure their validity across different stellar regimes.

#### 4.2.3 Hydrodynamical Instabilities in Radiative Zones Due to Rotation

Stellar hydrodynamics, particularly in radiative zones, is influenced by rotation-induced instabilities. In non-magnetic stellar models with initial solid body rotation, the onset of radial and horizontal angular velocity gradients is imminent. These gradients materialize due to factors such as changes in chemical composition and internal structure attributed to nuclear burning, as well as energy and angular momentum loss at the star's surface. These internal angular velocity gradients subsequently instigate turbulence, facilitating the transport of both chemical species and angular momentum. However, this transport mechanism is believed to be highly anisotropic. In the radial direction within radiative zones, these instabilities confront the stabilizing influence of temperature and chemical composition gradients, often termed as medium stratification or entropy gradient. Consequently, vertical transports are subdued when juxtaposed against horizontal transports. The latter transpire along equipotentials or isobars where no opposing forces are

present, resulting in enhanced turbulence. Notably, when the centrifugal force remains conservative, equipotentials equate to isobars. However, under a shellular distribution of angular velocity, one must exclusively refer to isobaric surfaces.

With these physical insights, Zahn (1992) devised a coherent portrayal of the interplay between meridional currents and shear instabilities. A foundational premise of this description is that intense horizontal turbulence ushers the star towards a state of shellular rotation. In this state, isobaric layers exhibit nearly constant angular velocities, denoted as  $\Omega$ . Nearly constant implies that  $\Omega$  variations across isobaric surfaces are negligible, and one can resort to the first term in a series expansion of  $\Omega$  using Legendre polynomials. Such constancy also holds for temperatures, densities, and chemical compositions across these surfaces. These insights birthed the conceptualization of shellular models.

Intriguingly, these shellular models align well with one-dimensional (1D) representations. The governing stellar structure equations can be revamped using methodologies inspired by Kippenhahn & Thomas (1970) and adapted by Meynet & Maeder (1997b) to yield solutions for average stellar structure attributes within each layer. To capture the subtle variations with latitude, one can employ expansions in Legendre polynomials. Consequently, these models occasionally earn the descriptor '1.5D' due to their nuanced approach that goes beyond traditional 1D modeling. In sum, rotation-induced hydrodynamical instabilities in radiative zones of stars play a pivotal role in shaping their internal dynamics. Comprehensive models like those of shellular rotation offer invaluable insights, bridging observational phenomena with theoretical underpinnings. Future explorations in this domain hold promise for deepening our understanding of stellar evolution and behavior.

# 4.2.4 Understanding Shear Diffusion Coefficients: A Deep Dive into Stabilizing Effects and Transport Processes

Shear diffusion coefficients, critical in stellar hydrodynamics, represent the fundamental tools for understanding transport processes in stellar interiors. For any transport mechanism to be effective, specific conditions must be met to overcome inherent stabilizing forces within the star. One of the pivotal metrics that codify these requirements is the Richardson criterion for non-magnetic models (refer to Chandrasekhar 1961). This criterion encapsulates the need for the excess energy arising from differential rotation to surpass the stabilization offered by the temperature and chemical gradients, also referred to as the entropy gradient. As per Maeder (see Eq. 2.2 in 1997), the Richardson criterion is mathematically expressed as:

$$R_{i} = \frac{g\delta(\nabla' - \nabla + \frac{\phi}{\delta}\nabla_{\mu})}{H_{p}\frac{dV_{\phi}}{dz}} > Ri_{crit}$$
(4.7)

Here,  $R_i$  symbolizes the Richardson number. The notations  $\nabla'$  and  $\nabla$  delineate the thermal gradients inside a fluid element and its surrounding medium,  $\nabla_{\mu}$  represents the gradient of mean molecular weight, g stands for gravity, and  $H_p$  signifies the pressure scale height.  $dV_{\phi}/dz$  conveys the differential azimuthal velocity in relation to a direction orthogonal to the isobaric surface. The terms  $\delta$  and  $\phi$  are derived from partial logarithmic derivatives concerning temperature and chemical composition. While a critical Richardson number of 1/4 is conventional, it can occasionally reach values as high as 1. This criterion plays an indispensable role in shaping the expression for the vertical shear diffusion coefficient.

Notably, strict adherence to the Richardson criterion might thwart chemical element transport in radiative zones with  $\mu$ -gradients. Meynet & Maeder (1997b) delineated that differential rotation amplitudes seldom attain sufficient magnitude in regions with mean molecular weight gradient, preventing instability manifestation. In an illuminating insight, Maeder (1997) postulated that the restrictive nature of the Richardson criterion, originally intended for non-turbulent mediums, becomes malleable in the presence of inherent turbulence, especially along the horizontal plane. This turbulence ensures that excess energy from differential rotation constantly fuels a mixing, the intensity of which is contingent upon available energy. Consequently, instead of a binary (on/off) instability mechanism, a continuous mixing ensues, regulated by accessible driving energy. This novel perspective culminated in a reimagined formulation of the diffusion coefficient responsible for chemical element and angular momentum transport due to shear.

Parallel thoughts emerged from Talon & Zahn (1997), albeit leading to distinct formulations. They attributed the strong horizontal turbulence, an omnipresent entity in rotating models, to diluting  $\mu$ -gradients. Such turbulence diminishes disparities between the mean molecular weights characterizing fluid element interiors and the surrounding medium, thereby fostering instability by mitigating hindrance from  $\mu$ -stratification for upward-moving fluid elements. Sect. 3 elaborates on the  $D_{\rm shear}$  deduced from this approach.

Another pivotal coefficient,  $D_h$ , represents horizontal shear diffusion, detailing transport due to the robust horizontal turbulence along isobaric surfaces. Deciphering a definitive expression for  $D_h$  remains challenging, given its rootedness in meridional currents and the intricate interplay with horizontal differential rotation. However, some guiding principles from physical units, experimental insights, and prior academic discourse aid in shaping its formulation. One non-negotiable criterion for  $D_h$  is its strength in enforcing shellular rotation. Essentially, it should facilitate nearly

constant  $\Omega$  values along isobaric surfaces swiftly, overpowering any efforts from processes like meridional currents that seek to induce  $\Omega$  disparities across latitudes. Lastly, a noteworthy observation is that  $D_{\rm h}$  typically overshadows  $D_{\rm shear}$ . The rationale lies in the inherent challenges faced by any shear instability orthogonal to an isobar. It contends with the stabilizing effects of density and temperature gradients, causing shear turbulence in this direction to wane in comparison to its counterpart along an isobar. Consequently, the diffusion coefficient encapsulating it,  $D_{\rm shear}$ , remains significantly inferior to  $D_{\rm h}$ .

In summation, shear diffusion coefficients underpin our comprehension of stellar transport processes, ensuring that we navigate the intricate tapestry of stellar hydrodynamics with robust mathematical tools and intuitive physical principles. Future endeavors in this domain beckon us to fathom the deeper intricacies of these coefficients, bridging observational nuances with theoretical frameworks.

#### 4.2.5 Magnetic models

#### **Background description**

The foundation of the magnetic model is built upon the Tayler-Spruit (TS) dynamo mechanism (Spruit 2002), albeit with modifications proposed by (Eggenberger et al. 2022b). Before delving into these modifications, it's important to understand that the TS dynamo originates from the premise that the radial component of an initial, diminutive magnetic field will undergo twisting by differential rotation. As this progresses, the azimuthal component, which experiences a linear growth in amplitude over time, will start to dominate the radial one. Eventually, this azimuthal component becomes unstable. Given that the energy extractable from the magnetic field is limited, the initial instabilities to surface should be those that minimize energy consumption. Radial instabilities, aiming to counter the stabilizing effects of the entropy gradient in a radiative zone, deduce that the most conducive instabilities expand predominantly in the horizontal direction. This concept is somewhat reminiscent of the  $D_h$  theory proposed by Zahn in 1992. However, in this context, the instability emerges from magnetic field instability not associated with horizontal differential rotation. Studies by Tayler (1973) and Pitts & Tayler (1985) have illuminated that a feeble azimuthal field is susceptible to destabilization through a kink and pinch type instability once certain conditions are met. This, in turn, generates a new, modest radial field that undergoes winding up, subsequently producing an azimuthal field that becomes unstable. This completes the dynamo loop. In this thesis, we aim to explore the consequences of different choices for these diffusion coefficients on massive star models. We hope that observations will either indicate support

for one of the prescriptions over the others or bring to light the potential changes (or lack thereof) in the stellar model outputs due to these choices. Conducting such numerical experiments with the same stellar evolution code is crucial to focus specifically on the implications of these different diffusion coefficient choices.

The subsequent category of models under consideration is magnetic models. The magnetic models we discuss here are based on the theory put forth by Spruit (2002). According to this theory, sufficiently strong differential rotation in radiative zones can amplify a magnetic field. This amplified field, via Lorentz forces, induces viscosity, leading to angular momentum transport. In our study, as will be detailed subsequently, this coupling robustly establishes nearly solid-body rotation across a major portion of the radiative envelope, especially during the Main-Sequence phase. The dynamo theory initiates with a minuscule radial magnetic field component. This radial component experiences winding in regions with differential rotation, leading to the formation of a toroidal field. However, a toroidal field is inherently unstable. The initial instability to manifest is the Tayler instability. This instability triggers a slight displacement of the toroidal field in planes orthogonal to the rotation axis. Following this, differential rotation distorts the radial component of the magnetic field lines, thereby completing the dynamo cycle. Furthermore, the Tayler magnetic instability also facilitates the transport of chemical elements.

The aforementioned magnetic processes are delineated using diffusive equations, applicable to both the transport of chemical elements and angular momentum transport, as described by Spruit (2002). This characterization stems from the geometric nuances of the magnetic instability, encompassing the entire toroidal field. This stands in stark contrast to meridional currents which represent localized movements. In the context of these models, the principal agent for angular momentum transport is the Tayler magnetic instability. As our discussions will highlight, meridional currents are largely inconsequential. If incorporated, an advective equation would also necessitate resolution. Given the nearly flat angular velocity profile imposed by magnetic coupling, meridional currents would essentially work towards restoring minuscule gradients. This implies an inward transport of angular momentum within the star, diametrically opposing the outward trajectory predicted by a diffusive equation. Under these conditions, we argue that neglecting the angular momentum induced by meridional currents is more judicious than representing this process through a diffusive equation. Here, the concern isn't just the magnitude of the effects but notably, the direction, which could be erroneously interpreted.

#### **Underlying physics**

In the magnetic models under discussion, the primary mechanism driving the transport of angular momentum is magnetic viscosity. Conversely, for the transport of chemical elements, meridional currents take precedence. The diffusion coefficient (responsible for mixing chemical species) derived from the Tayler instability is considerably small, rendering it ineffective in inducing significant changes. As previously mentioned, when addressing the transport of chemical elements, a diffusive approach aptly characterizes the meridional currents, a methodology we've employed in our present models. As previously discussed, expressions for the magnetic viscosity,  $\nu$ , and magnetic diffusivity,  $\eta$ , are indispensable. The viscosity, being linked to the Lorentz force, necessitates a determination of the magnetic field. This is equivalently expressed as the Alfven frequency,  $\omega_A = \frac{B}{\sqrt{4\pi} n r}$ .

One essential condition is that the magnetic amplification timescale matches the damping timescale. The former, denoting the time required to intensify the radial magnetic field to an azimuthal counterpart of equivalent amplitude, is represented as

$$\tau_{\rm amp} = \frac{1}{\Omega a} \frac{B_{\Phi}}{B_r} = \frac{N_{\rm eff}}{\omega_{\Delta} \Omega a},\tag{4.8}$$

where  $N_{\rm eff}=\frac{\eta}{K}N_T^2+N_\mu^2$ . Here, the relationship  $B_\Phi=\sqrt{4\pi\rho}r\omega_{\rm A}$  and  $B_r=\frac{B_\Phi\omega_{\rm A}}{N_{\rm eff}}$  has been utilized. The damping timescale is given by

$$\tau_{\rm damp} = \frac{1}{C_T} \frac{1}{\omega_{\rm A}} \frac{\Omega}{\omega_{\rm A}},\tag{4.9}$$

with the factor  $C_T$ , introduced by Eggenberger et al. (2022b), accounting for inherent uncertainties in this timescale. Balancing these two timescales, we derive

$$\frac{\omega_{\mathcal{A}}}{\Omega} = C_T q \frac{\Omega}{\frac{\eta}{K} N_T^2 + N_\mu^2}.$$
(4.10)

This equation, however, presents a pair of unknowns:  $\omega_A$  and  $\eta$ . To decipher it, a secondary equation is warranted, derived from constraints on the instability domain's lengthscale. These constraints dictate that this lengthscale should be both extensive enough to avoid rapid damping and limited enough to permit the shear's surplus energy to negate the stabilizing effects of the entropy gradient. Assuming these lengths equal, we are on the brink of triggering instability. Drawing from established research, we obtain

$$\left(\frac{\omega_{\mathcal{A}}}{\Omega}\right)^4 = \frac{\frac{\eta}{K}N_T^2 + N_\mu^2}{\Omega^2} \frac{\eta}{r^2\Omega}.$$
 (4.11)

Solving these paired equations provides values for  $\omega_A$  and  $\eta$ . Further, for instability onset, the shear, q, should exceed a threshold,  $q_{\min}$ :

$$q_{\min} = \frac{1}{C_T} \left(\frac{N_{\text{eff}}}{\Omega}\right)^{\frac{3}{2}} \left(\frac{\eta}{\Omega r^2}\right)^{\frac{1}{4}}.$$
 (4.12)

It is pivotal to recognize that  $\eta$  and  $\nu$  permeate the entire radiative region. If the condition  $q_{\min}$  is unmet,  $\eta$  is dictated by the expression in Eq.4.9. When the condition is satisfied, the resolution of Eq. 4.10 alongside the expression in Eq. 4.11 determines  $\eta$ . In our magnetic models, two further hydrodynamical instabilities are factored in: the first corresponds to shear (both vertical and horizontal) and the second to meridional currents. In these models, we've chosen  $D_{\text{shear}}$  based on Maeder (1997) and  $D_{\text{h}}$  from Maeder (2003). The impact of different choices for these quantities in the magnetic models remains unexplored in this paper. For angular momentum transport, we focused solely on the diffusive component. The influence of advection is omitted, largely because angular momentum transport is predominantly governed by magnetic coupling. This oversight should not significantly alter results. It's also worth noting that if meridional current transport were described using a diffusive equation, it would inaccurately dictate transport in a counterintuitive direction.

#### 4.2.6 The present numerical experiments compared to other works

Our group's previously published non-magnetic stellar model grids (Meynet et al. 2013) utilized the expression for  $D_{\rm shear}$  from Maeder (1997) and the value of  $D_{\rm h}$  from Zahn (1992). Aligning with labels in Table 1, these grids employ the prescriptions of model A.

The magnetic models presented herein diverge considerably from those discussed in Paper III. Firstly, in Paper III, we used the values for  $D_{\rm shear}$  and  $D_{\rm h}$  from (Meynet et al. 2013). Secondly, we consistently employed the  $\eta$  value derived from the resolution of the fourth order equation, which differs from Eq.4.11 since Paper III always utilized the  $\eta$  expression valid for unstable scenarios. Contrasting our methodology with rotating models published using other codes like MESA, notable differences arise:

- When meridional currents are dominant in angular momentum transport, we approach them
  by resolving an advective equation, as opposed to MESA's diffusive one.
- Parameters like  $f_C$  and  $f_\mu$  are not utilized in our approach.

#### 4.2.7 A Deep Dive into Stellar Model Parameters

We adopted same physical ingredients (except for rotation) as in Ekström et al. (2012b). Among the various nuances, a central choice in these models is the inclusion of a moderate step overshoot, captured quantitatively by  $\alpha_{\rm ov}=0.1$ . Pertinent astrophysical phenomena such as mass loss rates are assiduously accounted for, while surface magnetic fields are conspicuously absent from these considerations. A striking feature of these stellar models is the rotation of convective zones; they simulate the behavior of solid bodies, ensuring chemical homogeneity within. Our research has strategically honed in on two initial masses:

- 1. We first inspect a model with an initial mass of  $15\,\mathrm{M}_\odot$ . This archetype is particularly relevant to single stars evolving into the red supergiant phase post the Main Sequence (MS). The grand finale of this evolutionary stage witnesses these stars undergoing a type IIP supernova explosion.
- 2. The subsequent focus shifts to the  $60~M_{\odot}$  stellar model. The model transitions from the Main Sequence phase into a Luminous Blue Variable and subsequently into a Wolf-Rayet phase. Such an evolutionary pathway is notably representative of massive stars at solar metallicity. The dominant influence here is the mass loss, especially when considering the upper echelons of stellar masses.

Diving deeper into the computational nuances, throughout the MS phase, our models rely on the comprehensive advective-diffusive approach. As the models transition to the core helium burning phase, a shift is made to a purely diffusive methodology. Our current research focuses on avoiding the adjustment of uncertain parameters to fit observational data. In essence, we have refrained from force-fitting our models to mirror specific observational patterns, a practice that often characterizes the computation of rotating models . Instead, our guiding principle has been to maintain consistent physical assumptions across all models. This approach pertains especially to the parameter  $f_{\rm en}$  in  $D_{\rm shear}$ . The assumption here is the complete harnessing of the excess energy in differential rotation, commonly referred to as the shear energy. This energy is conceptualized as the primary driving force behind transport mechanisms. Moreover, we have adopted a critical Richardson number equal to 1/4. Given that these assumptions are underpinned by a common scientific rationale, their application remains invariant across various prescriptions. Consequently, our overarching goal is to overlap the consequences of distinct physical methodologies without resorting to specific tunings for observations. Despite these varying methodologies, the outputs of our models are intrinsically coherent, given their shared foundational physical assumptions.

Table 4.1 serves as a comprehensive repository of all the models scrutinized in this study. An array of information is systematically catalogued:

- The first column provides the model label.
- Column 2 describes the prescription used: 'Ma97' and 'TZ97' represent that the shear diffusion expression is defined by Maeder (1997) and Talon & Zahn (1997), respectively.
- Indicators 'Za92', 'Ma03', and 'MZ04' in column 2 also signify that the horizontal diffusion coefficient's expression comes from Zahn (1992), Maeder (2003), and Mathis et al. (2004), respectively.
- Time-averaged equatorial velocity during the MS phase is showcased in column 3.
- Column 4 specifies the MS lifetime.
- Surface helium abundance (mass fraction) at the MS phase's culmination appears in column
   5.
- Column 6 delineates the N/H ratio at the surface by the end of the MS phase, normalized to the N/H value's inception.
- The genuine star mass at the core H-burning phase's termination is presented in column 7.
- Core He-burning lifetime and the durations spent in red ( $\log T_{\rm eff} < 3.68$ ), blue ( $\log T_{\rm eff} > 3.87$ ), and yellow (3.68  $< \log T_{\rm eff} < 3.87$ ) segments of the HR diagram are specified in columns 8, 9, 10, and 11 respectively.
- Column 12 exhibits the time ratio between the blue and red sections.
- Surface helium's mass fraction is captured in column 13.
- The genuine star mass at the core He-burning phase's end is documented in column 14.
- Columns 15, 16, and 17 respectively detail the masses of helium cores, carbon-oxygen cores, and remnants, acquired using the formula from Maeder (1992). Notably, helium and CO core masses are determined by identifying the first shell (from the surface inward) where the helium mass fraction, or the aggregate mass fraction of carbon and oxygen, exceeds 0.75.

On a final note, it's important to recognize that differences among models with identical initial masses, resulting from different rotational mixing prescriptions, can sometimes be nuanced. These subtle variations might be obfuscated by numerical choices or be too minute to be discerned

Table 4.1: Some properties of the models computed in the present work.

		$\overline{v}_{\rm eq}$ km s <sup>-1</sup>	$t_{ m H}$ My	$Y_{s-EndH}$	$\log \frac{(N/H)}{(N/H)_{\text{ini}}}$	$M_{\rm EndMS}$ $M_{\odot}$	$t_{ m He}$ Mv	$t_{ m blue}$ My	$t_{ m red}$ Mv	$t_{ m yel}$ Mv	$\frac{t_{\mathrm{red}}}{t_{\mathrm{blue}}}$	$C_{c-EndHe}^{12}$	$Y_{s-EndHe}$ $M_{\odot}$	$ m M_{EndHe}$ $ m M_{\odot}$	$ m M_{He}$ $ m M_{\odot}$	$M_{\rm CO}$ $M_{\odot}$	$M_{\rm rem}$
					15	$M_{\odot}$ , $v_{\rm ini}/v_{\odot}$		.4,υ <sub>ini,sτ</sub> :0.014	$_{\rm rrf} = 26$	0 km s	-1						
							Z=	0.014									
A	Ma97, Za92	188	13.72	0.290	0.62	14.70	1.37	0.04	1.23	0.10	27.89	0.25	0.38	11.20	5.08	3.01	1.66
В	TZ97, Za92	196	13.70	0.268	0.24	14.74	1.13	0.00	1.13	0.00	-	0.30	0.33	13.37	5.83	3.46	1.77
C	Ma97, Ma03	203	12.97	0.280	0.57	14.68	1.58	1.09	0.38	0.12	0.35	0.30	0.37	10.31	4.56	2.57	1.54
D	TZ97, Ma03	201	11.94	0.266	0.31	14.78	1.71	0.05	1.59	0.06	30.61	0.18	0.33	11.78	4.64	2.85	1.62
E	Ma97, MZ04	172	12.69	0.276	0.53	14.75	1.55	1.05	0.38	0.11	0.36	0.30	0.36	13.46	4.51	2.48	1.52
F	TZ97, MZ04	179	11.40	0.267	0.44	14.80	1.72	1.27	0.33	0.11	0.26	0.25	0.33	13.90	4.31	2.87	1.62
C*	Ma97, Ma03	199	12.44	0.271	0.43	14.75	1.22	0.00	1.21	0.01	6040	0.34	0.31	13.69	4.85	2.72	1.58
G	Non-Rotating	0.00	11.26	0.231	0.42	14.80	1.37	0.37	1.11	0.00	2.98	0.30	0.30	13.43	5.19	3.10	1.68
					60	$M_{\odot}$ , $v_{\rm ini}/v$	crit = 0	$4v_{\rm ini}$ ,	$_{\rm ref} = 34$	10 km s	-1						
						O,,		=0.014									
A	Ma97, Za92	175	4.55	0.808	1.682	38.58	0.36	0.36	0.00	0.00	0.00	0.20	0.27	17.54	17.54	16.93	5.23
В	TZ97, Za92	174	4.43	0.250	1.681	39.15	0.37	0.37	0.00	0.00	0.00	0.20	0.28	15.88	15.87	15.23	4.71
C	Ma97, Ma03	173	4.68	0.904	2.020	38.08	0.35	0.35	0.00	0.00	0.00	0.19	0.28	19.60	19.59	18.82	5.80
D	TZ97, Ma03	170	4.60	0.252	2.121	38.30	0.35	0.35	0.00	0.00	0.00	0.19	0.28	19.53	19.50	18.70	5.76
C*	Ma97, Ma03	173	3.88	0.535	1.287	37.51	0.37	0.37	0.00	0.00	0.00	0.23	0.28	14.75	19.88	18.98	5.97
G	Non-Rotating	0.00	3.53	0.493	1.287	36.36	0.40	0.37	0.00	0.00	0.00	0.22	0.28	13.11	19.84	18.37	5.74

observationally, especially during the MS phase in the HR diagram. However, we wish to emphasize that our computational methodologies have remained steadfastly consistent. This consistency ensures an accurate portrayal of the relative impact of distinct prescriptions on stellar evolution.

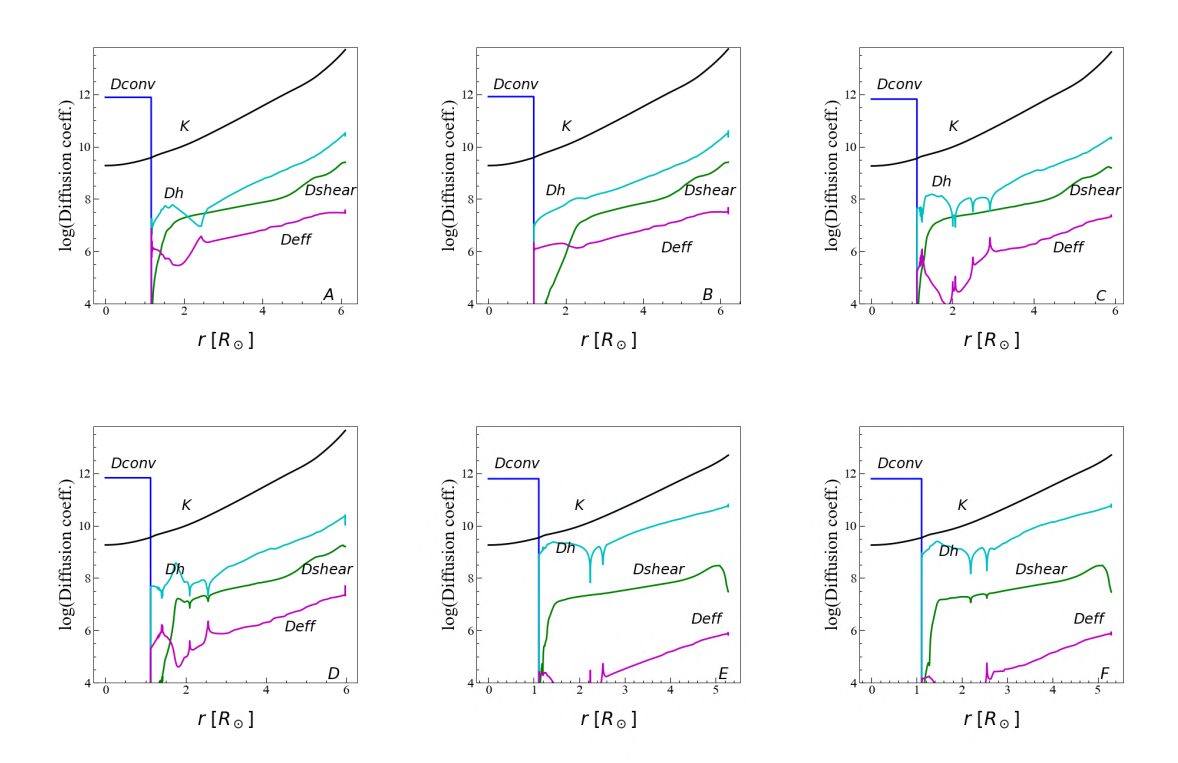


Figure 4.1: Internal profiles of K the thermal diffusivity,  $D_{\rm conv}$  the convective diffusion coefficient,  $D_{\rm shear}$  the shear diffusion coefficient,  $D_{\rm h}$  the horizontal turbulence coefficient and  $D_{\rm eff}$  the effective diffusivity in 15  $M_{\odot}$  models at solar metallicity. Each panel is labeled with a letter corresponding to the first column of Table 1. The profile is taken when the central mass fraction of hydrogen  $X_c = 0.35$ .

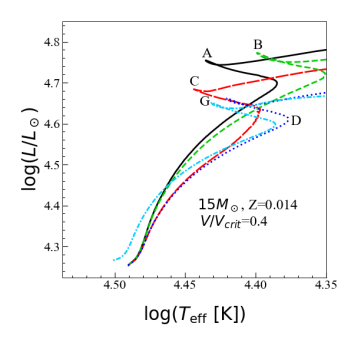
### 4.3 The Non-Magnetic 15 $M_{\odot}$ Stellar Models and Their Diffusion Coefficients

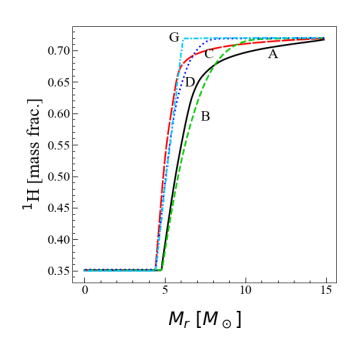
Herein, we present findings centered on the non-magnetic models of stars with an initial mass of  $15 \, \mathrm{M}_{\odot}$ , depicted in Fig. 4.1. This section particularly hones in on the diffusion coefficients that play a pivotal role in their evolution. When one observes Figure 4.2, it portrays how these diffusion coefficients vary with the star's radius at a specific stage of its lifecycle - when its central hydrogen mass fraction is 0.35. While there's a plethora of data and nuances in this figure, certain characteristics stand out across all six models under consideration:

- 1. **The Convective Core**: This is the central region of the star, where convective motions dominate. In all models, this core exhibits high diffusion coefficients, roughly around 10<sup>12</sup> cm<sup>2</sup> s<sup>-1</sup>. Notably, this high value is primarily due to the convective processes at play, not the star's rotation.
- 2. **Thermal Diffusion Coefficient**: Designated as *K*, this coefficient sees an outward increase. It is notably higher than the coefficients that describe rotational instabilities. The implication here is that while rotational instabilities exist, they don't play a dominant role in energy transport, given the swift timescale of thermal diffusion.
- 3. **Horizontal Diffusion** ( $D_h$ ): Predominantly influencing the radiative region, this coefficient ensures that the star's rotation is more 'shellular' than solid-body.

Now, rotation isn't just a passive feature of a star. It can actively induce mixing, allowing elements from the core to make their way to the surface. In the context of a star's Main Sequence (MS) phase, an element's journey from core to surface traverses four distinct zones:

- Zone 1 The Convective Core: This is where chemical species experience efficient transport.
   The size of this zone isn't fixed; it's a product of various processes, including the degree of overshooting from the core, semi-convection efficiency at the convective boundary, and the star's chemical makeup. External factors, like mass loss, also play a role.
- 2. **Zone 2 Above the Core**: Right above the convective core lies a region with a gradient in mean molecular weight. This gradient arises from the mismatched timescales of nuclear reactions and mixing in the star's radiative envelope. The steeper gradients closer to the core smooth out as one moves away as seen in the middle panel of Fig. 4.2. In this zone, the key diffusion coefficient is  $D_{\rm eff}$ , whose value depends largely on the chosen  $D_{\rm h}$ .





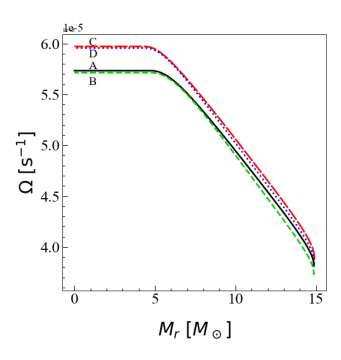


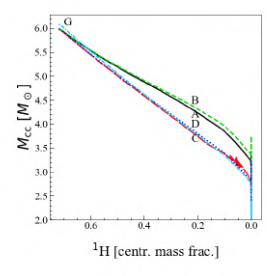
Figure 4.2: *Left panel*: Evolutionary tracks during the MS phase in the Hertzsprung-Russell diagram of the 15  $M_{\odot}$  at Z=0.014 and with  $V_{\rm ini}/V_{\rm crit}=0.4$ . The letters 'A','B','C', 'D' and 'G' correspond to the models described in Table 9.2. *Centre panel*: variation of the mass fraction of hydrogen as a function of the Lagrangian mass coordinate when central mass fraction of hydrogen is 0.35 (Xc=0.35). *Right panel*: Evolution of angular velocity versus the internal mass coordinate at Xc=0.35 through hydrogen burning.

- 3. **Zone 3**: Here, the formula  $\frac{\varphi}{\delta}\nabla_{\mu}$  is notably larger than the difference between the adiabatic and radiative temperature gradients. In this region, the kind of vertical shear diffusion coefficient used makes a difference. Notably, when compared,  $D_{\text{shear}}(\text{M97}) > D_{\text{shear}}(\text{TZ97})$ .
- 4. **Zone 4 Outer Layers**: In these layers above Zone 3,  $D_{\rm shear}$  dominates the mixing process. Interestingly, the value of this coefficient remains consistent whether one employs the models from Maeder (1987) or Talon & Zahn (1997). This is particularly evident in areas devoid of  $\mu$ -gradients, where the coefficient ratios approach unity due to the smaller nature of  $D_{\rm h}$  in comparison to K.

Stellar modeling, especially when it dives into the nuances of diffusion coefficients and rotational mixing, is a complex endeavor. This exploration of non-magnetic  $15~M_{\odot}$  models shows the processes at play within these massive celestial bodies. Whether it's the nature of convection, the impact of rotation on element transport, or the intricacies of diffusion coefficients, understanding these mechanisms is crucial to demystifying the lives of stars.

#### 4.3.1 Summary on the Vertical Shear Diffusion Coefficient $D_{\text{shear}}$

The vertical shear diffusion coefficient,  $D_{\rm shear}$ , significantly impacts stellar model dynamics. Observing the top two panels of Figure 4.1, distinct differences emerge between Maeder (1997) and Talon & Zahn (1997)'s interpretations. Switching from Maeder (1997)'s to Talon & Zahn (1997)'s  $D_{\rm shear}$  expression, while maintaining Zahn (1992)'s  $D_{\rm h}$ , highlights discrepancies in the  $D_{\rm h}$  profiles. These differences stem from the chemical structure's changes due to  $D_{\rm shear}$  alterations, affecting the models' evolutionary paths. Notably, using Maeder (1997)'s  $D_{\rm shear}$  reduces the dominance zone



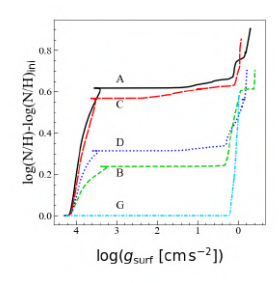


Figure 4.3: *Left panel*: Mass of the convective core in solar mass as a function of central mass fraction of hydrogen  $X_c$  in different 15  $M_{\odot}$  models. *Right panel*: Evolution of the surface abundance ratio N/H (normalised to its initial value and in logarithmic scale) as a function of log  $g_{surf}$  for the same models as those presented in the left panel. In both panels, the letters have the same meaning as in Fig. 4.2.

of  $D_{\rm eff}$ , a result of Maeder's stronger value. In contrast, Talon & Zahn (1997)'s approach leads to less pronounced  $\mu$ -gradients at the start of evolution. In the outer radiative zone, both approaches yield similar values. Overall, models based on Maeder (1997)'s  $D_{\rm shear}$  exhibit more mixing after the Main Sequence phase than those using Talon & Zahn (1997), impacting their trajectories on the Hertzsprung-Russel (HR) diagram as seen in the left panel of Fig. 4.2.

#### 4.3.2 Analysis on the Horizontal Shear Diffusion Coefficient $D_{\rm h}$

The middle section of Figure 4.1 shows the diffusion coefficients in models at the midpoint of the Main Sequence (MS) phase using the  $D_{\rm h}$  expression from Maeder (2003). In this scenario, there is a notable reduction in  $D_{\rm eff}$ , linked to the increased value of  $D_{\rm h}$ . Remarkably, models incorporating  $D_{\rm shear}$  as defined by Maeder (1997) display more extensive mixing compared to those utilizing Talon & Zahn (1997)âconsistent with observations under the  $D_{\rm h}$  framework of Zahn (1992). Further analysis, seen in the bottom panels of Figure ??, examines the impact on diffusion coefficients when employing the  $D_{\rm h}$  formula from Mathis et al. (2004). This approach leads to higher values compared to previous models, consequently reducing  $D_{\rm eff}$  as  $D_{\rm h}$  approaches K. This dynamic lessens the difference in results stemming from the two  $D_{\rm shear}$  expressions.

The overall diffusion coefficient for chemical species combines  $D_{\rm eff}$  and  $D_{\rm shear}$ . Here,  $D_{\rm eff}$  plays a crucial role, especially near the edge of the convective core. Changes in mixing efficiency in this area can influence the size of the convective core. Future discussions will delve into this connection and its effects on surface abundances. Notably, the absence of  $D_{\rm eff}$  doesn't hinder surface enrichment. As the MS phase progresses, the convective core's mass decreases, leading to a region with a  $\mu$ -gradient. In this region,  $D_{\rm shear}$  becomes the dominant factor in guiding the mixing process, confirming earlier observations.

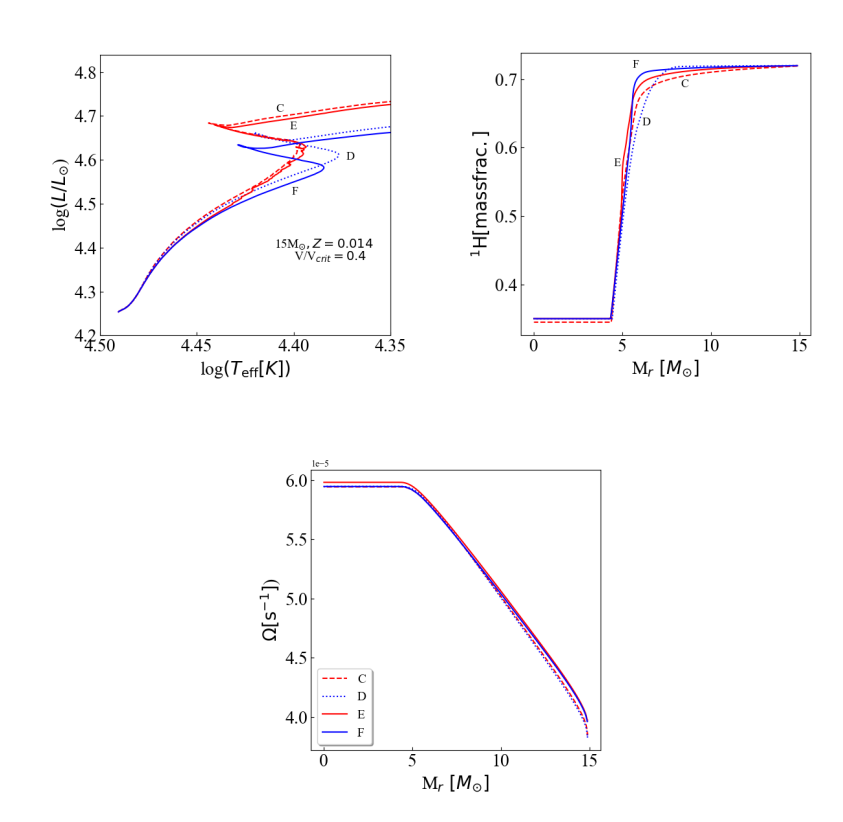


Figure 4.4: Left panel: Evolutionary tracks during the MS phase in the Hertzsprung-Russell diagram are shown for models C, D, E and F (see Table 1) as a function of the Lagrangian mass for the  $15~\rm M_{\odot}$  at Z=0.014 and with  $V_{\rm ini}/V_{\rm crit}=0.4$ . Middle panel: Abundance of Hydrogen in mass fraction ranging from the center to the outer envelope of the models when the central mass fraction of hydrogen  $X_{\rm c}$ =0.35. Right panel: Variations of the angular velocity versus the mass coordinate for the same models as those shown in the middle panel.

#### 4.3.3 Tracks and lifetimes

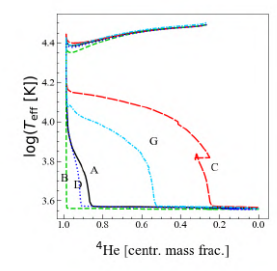
In Fig. 4.2, the left panel presents the evolutionary trajectories of rotating  $15~M_{\odot}$  models using varied rotation prescriptions. The non-rotating track is denoted by the cyan dashed-dotted line (G). Previous research (Faulkner et al. 1968; Kippenhahn et al. 1970; Endal & Sofia 1976; Meynet & Maeder 1997b) has shown that rotation leads to a shift in the Zero Age Main Sequence (ZAMS) towards lower effective temperature and luminosity, attributed to the hydrostatic effects of rotation. It's crucial to note that at ZAMS, the star remains chemically homogenous, rendering mixing effects absent. The hydrostatic effects on the ZAMS don't vary with the diffusion coefficient prescriptions.

#### Impact of changing $D_{\rm shear}$

Examining models A and B from Fig. 4.1, differences emerge when transitioning the  $D_{\rm shear}$  expression from Maeder (1997) to Talon & Zahn (1997). Model A exhibits a bluer and more luminous profile than model B, primarily because of enhanced mixing in A, resulting from a larger  $D_{\rm shear}$  value in zone 3.

Fig. 4.2's middle panel reveals deeper mixing in Model A compared to Model B, evident from the diminished hydrogen mass fraction beneath the surface. Moreover, nitrogen surface enrichment is more substantial in Model A, as seen in Fig. 4.3. This heightened enrichment in Model A is attributed to the augmented chemical element transport, causing increased inward diffusion of hydrogen in its radiative zone. Consequently, for similar  $D_{\rm eff}$  values, Model A tends to have a more pronounced accumulation of hydrogen near the convective core than Model B, resulting in a steeper gradient in Model A. This highlights that increased mixing in one area can lead to steeper gradients elsewhere.

The HR diagram's Main-Sequence band is contingent not just on the overshooting parameter but also on the rotation model utilized. Different rotational models can alter this boundary, emphasizing the importance of rotational mixing physics in Main-Sequence band analyses. While the convective core masses in Models A and B exhibit similar evolutions, as depicted in Fig. 4.3, their Terminal Age Main Sequence (TAMS) positions differ, as shown in Fig. 4.2. Thus, when adjusting models using the TAMS position in the HR diagram, it's crucial to account for the potential effects of rotation physics on this position (Martinet et al. 2022).



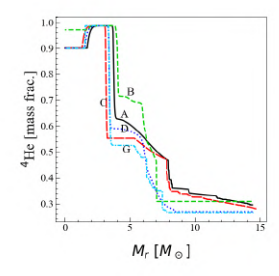


Figure 4.5: *Left panel*: Evolution of the effective temperature as a function of the central helium abundance for different  $15M_{\odot}$  models. *Right panel*: Helium profile versus the mass in different  $15M_{\odot}$  models when the central Helium mass fraction is 0.90. In both panels, the letters have the same meaning as in Fig. 4.2.

#### Impact of changing D<sub>h</sub>

Comparing Models C and D, which share the same  $D_{\rm shear}$ , we observe distinct characteristics. Notably, these models possess higher  $D_{\rm h}$  values than Models A and B but exhibit reduced  $D_{\rm eff}$  values. As a result, the convective cores in these models are smaller, as depicted in Fig. 4.3. Consequently, their chemical mixing is less profound, leading to evolutionary tracks that are less luminous compared to Models A and B. The distinctions between tracks C and D are qualitatively similar to those between Models A and B. Noteworthy is that Model C, even with its considerably reduced  $D_{\rm eff}$  value just above the core, still displays notable surface enrichment, as seen in Fig. 4.3. This behavior can be attributed to the decreasing mass of the convective core over time. An extended comparison involving Models E and F with Models A to D is available in Fig. 4.4. Model E parallels Model C in its evolutionary path, while Model F aligns more with Model D, albeit with a marginally reduced luminosity and a bluer turn off point.

#### Impact on main sequence lifetime

The Main Sequence (MS) lifetimes of the 15  $M_{\odot}$  stellar models are tabulated in the fourth column of Table 4.1. In comparison to the non-rotating counterpart, rotation extends the core hydrogen burning phase across all models by a margin of 1 - 22%. Specifically, the models utilizing  $D_{\rm h}$  from Maeder (2003) and  $D_{\rm shear}$  from Talon & Zahn (1997) (models D and F) witness the most minimal MS lifetime extension, ranging between 1 and 6%.

#### 4.3.4 Internal and Surface Rotations, Surface Abundances

Stellar models, particularly the non-magnetic ones, heavily rely on meridional circulation as the primary means of transporting angular momentum. Each of our models consistently utilizes an identical equation to compute these meridional currents. However, the equation is uniquely influenced by the expression for  $D_{\rm h}$ , which modifies the  $U_2$  equation via its multiplicative factor (1+ $D_{\rm h}/K$ ). In a significant number of our models, the value of  $D_{\rm h}$  is considerably smaller compared to K. Thus, while the variation of  $D_{\rm h}$  can influence the equation, the overall effect on angular momentum transport remains marginal. The internal rotation profiles of our models, particularly during the midpoint of the MS phase, are exhibited in Fig. 4.2. Observations reveal that models with heightened  $D_{\rm h}$  values generally manifest more rapid core rotations.

The mean surface rotational velocity, spanning the entirety of the MS phase, is meticulously cataloged in the third column of Table 4.1. The data indicates an average velocity hovering around 188 km s $^{-1}$ . Subtle deviations, usually within the range of  $\pm 8\%$ , emerge based on the specific coefficients and expressions applied. Consequently, it becomes evident that changes in these coefficients impart only a moderate effect on surface rotation velocities. Further intricacies arise when considering the diffusion coefficients. Adjustments in these coefficients naturally reshape the stellar chemical composition, which then has cascading effects, notably impacting both the stellar radius and the rate of mass loss due to stellar winds. Such changes, in turn, exert an influence on the surface rotation dynamics. Nevertheless, it's worth noting that the ending masses of the MS phase across different 15  $M_{\odot}$  models demonstrate minimal deviations. As presented in column 4 of Table 4.1 $^1$ , the variations in surface velocities maintain their modest nature.

Drawing our attention to surface enrichment, we find this parameter is particularly sensitive to the chosen diffusion coefficients, a phenomenon explicitly depicted in Fig. ??. Notably, the choice of  $D_{\rm shear}$  exerts a more profound influence on surface enrichment compared to  $D_{\rm eff}$ . Observational data indicates that models employing the expression for  $D_{\rm shear}$  proposed by Maeder (1997) consistently display enhanced enrichment towards the conclusion of the MS phase. This outcome is consistent, irrespective of the specific  $D_{\rm h}$  value selected. Digging deeper into core He-burning lifetimes, which are tabulated in column 8 of Table 9.2, we find these durations range between 8 to 15% of the entire MS lifetimes. A discernible trend emerges: models with greater  $D_{\rm h}$  values often correlate with extended core He-burning phases and present larger fractions of  $\tau_{\rm He}/\tau_{\rm H}$ .

To further enhance our understanding, we analyze the evolution of the effective temperature in relation to the star's central helium mass fraction for the 15  $M_{\odot}$  models, as visually represented in Fig. 4.5. Primarily, Model C and, to a more nuanced extent, the non-rotating Model G diverge in behavior from their counterparts. Throughout the core He-burning phase, these models prominently maintain effective temperatures exceeding 6000K ( $\log T_{\rm eff} > 3.8$ ). Models that transition

<sup>&</sup>lt;sup>1</sup>It's pertinent to highlight that mass loss rate uncertainties often induce more significant variations, as detailed in (Renzo et al. 2017)

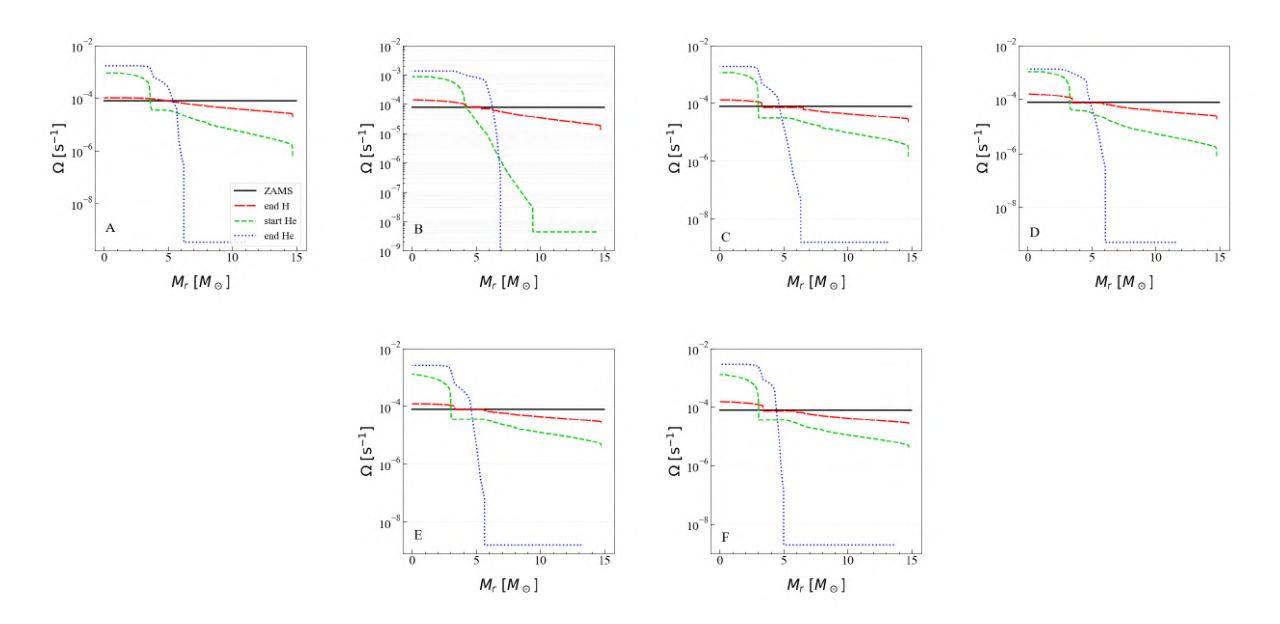


Figure 4.6: Angular velocity profiles as a function of mass for different 15  $M_{\odot}$  models at various evolutionary stages. The letters have the same meaning as in Fig. ??.

directly to the red supergiant stage follow a Kelvin-Helmholtz timescale, contrasting with those that linger in the blue phase, which align more closely with a nuclear-burning timescale. These diverging evolutionary paths undeniably influence both the blue-red supergiant ratio and case B mass transfer in closely bound binary systems.

#### 4.3.5 He-burning lifetimes and blue-red supergiant ratios

Expanding further on the helium core fraction, upon reaching a fraction of 0.9, both Model C and Model G present markedly lower helium concentrations directly above the H-burning shell. Elevated helium concentrations in this region, especially above the He-core, generally lean towards favoring a more red-aligned position during the core He-burning phase. This observation is harmonious with prior findings documented by Maeder & Meynet (2001a) and Farrell et al. (2022b). Intriguingly, the internal mixing levels in Models C and G exhibit considerable disparity. Despite this, a commonality emerges: both models gravitate towards an extended blue supergiant phase during their inaugural HR gap traversal. Such behavior underscores the importance of understanding that durations spent within specific effective temperature domains during HR gap transitions are inherently tied to the nuanced shifts in internal chemical element distributions, especially within regions close to the H-burning shell.

#### 4.3.6 Difference of the Structure at the End of the Core He-Burning Phase

The end of the core He-burning phase represents a critical juncture in stellar evolution. Two significant components to consider here are the helium (He) and carbon-oxygen (CO) cores. Their masses, which can be elucidated from columns 14 and 15 of Table 9.2, serve as essential indicators of the star's evolutionary progression.

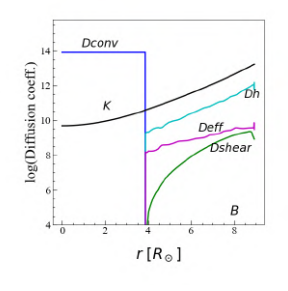
In comparing rotating models, a stark disparity is apparent. The relative difference in the helium core size, determined by the equation  $(M_{\rm He}^{\rm max}-M_{\rm He}^{\rm min})/M_{\rm He}^{\rm min}$ , is a notable 28%. This variation is considerably largeâover twice the magnitude compared to the difference between a non-rotating model, one with a step overshoot of  $0.25 {\rm H}_p$  and another devoid of any overshooting, as has been previously reported by Maeder & Meynet (1987).

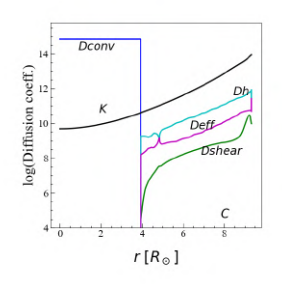
Delving deeper, we discern a correlation between the values of  $D_{\rm h}$  and the size of the helium cores. Specifically, models embracing larger values of  $D_{\rm h}$  consistently manifest smaller helium cores during this phase of their evolution. When we pivot our focus to the CO core and remnant masses in rotating models, the relative differences widen further: about 40% for the CO core and approximately 17% for the remnant masses. To arrive at this relative change for the CO core and remnant masses, we adopted an analogous computation method as the one used for helium cores. Furthermore, to estimate the remnant mass, we leaned on the relation between the CO core mass and the remnant mass, a relation established by Maeder (1992).

The above observations bring a pivotal realization to the fore: the choice of rotation prescription profoundly influences the core sizes. Surprisingly, this impact even eclipses that of a moderate core overshoot seen in non-rotating models. The implications of this finding are twofold. First, it underscores the intricacies and nuances inherent in stellar modeling. Second, and perhaps more crucially, it amplifies the call for a more profound comprehension of the underlying physics driving these variations.

To visualize the evolutionary dynamics of these stars, one can turn to Figure 4.6. This figure paints a vivid picture of the angular velocity fluctuations across different models during several evolutionary junctures. Initially, during the end of the core H-burning phase, the differences seem almost negligible. This uniformity stems from the consistent equations used to compute the transport of angular momentum by the meridional currents. Moreover, the influence of the parameter  $D_{\rm h}$  on these equations remains relatively weak. However, as the stellar evolution progresses, subtle and not-so-subtle changes to the star's chemical structure start to manifest. These alterations inherently modify the star's trajectory in the HR diagram. Consequently, the internal rotation evolution also experiences a shift.

# Dconv Leading to Dconv Defit A Defit





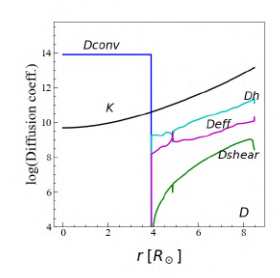


Figure 4.7: Variation as a function of the radius of K the thermal diffusivity,  $D_{\rm conv}$  the convective diffusion coefficient,  $D_{\rm shear}$  the shear diffusion coefficient,  $D_{\rm h}$  the horizontal turbulence coefficient and  $D_{\rm eff}$  the effective diffusivity in different 60  $M_{\odot}$  models at solar metallicity. The letters correspond to models computed with the prescription given in the second column of Table 9.2. The profiles are taken when the central mass fraction of hydrogen  $X_c = 0.35$ .

Emphasizing this point, the left panel of Fig. 4.5 depicts a striking phenomenon. As different models embark on their core He-burning phase, they position themselves either on the blue or the red spectrum of the HR diagram. The physical ramifications of this positioning are significant. Stars that find themselves in the blue region are more compact compared to their counterparts in the red zone. This difference in compactness translates into considerable variations in angular velocity among the models at the dawn of the core He-burning phase. Consequently, by the end of this phase, the actual masses across the models differ by an impressive marginâupwards of 30%.

However, some features remain consistent across all models. A standout observation is the significant discrepancy between the angular velocity of the core and the surface. Specifically, at the end of the core He-burning phase, this ratio skyrockets to about 7-8 orders of magnitude. This colossal difference is not a mere anomaly but a consistent pattern across the board. One can infer that rapidly rotating cores are a staple in all models, given a specific condition. They only account for the hydrodynamic instabilities ushered in by rotation and deliberately exclude any instabilities triggered by magnetic forces.

#### 4.3.7 Analysis and Interpretation of the 60 $M_{\odot}$ Stellar Models

#### Diffusion Coefficients in 60 M<sub>☉</sub> Models: A Comparative Overview

In the midst of the core H-burning phase for the 60  $M_{\odot}$  models, a standout observation is the dominance of  $D_{\rm eff}$ , as exemplified in Fig. 4.7. This dominance is notably in contrast with the behavioral patterns noticed in the 15  $M_{\odot}$  models. In the latter,  $D_{\rm shear}$  consistently emerged as the prevailing diffusion coefficient, save for regions just proximate to the convective core.

Further inquiry into the  $60~M_{\odot}$  models revealed an interesting rotational behavior. An overtly flat rotation profile becomes evident across a vast expanse of the star's total mass. This behavior

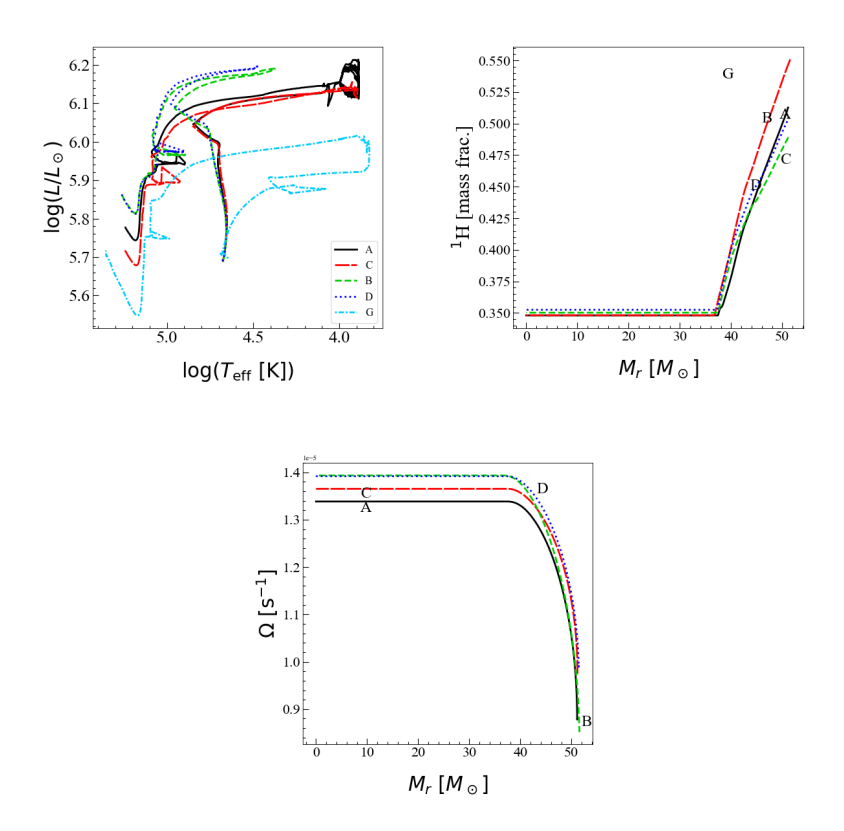


Figure 4.8: (*Left panel*) Evolutionary tracks in the Hertzsprung-Russell diagram,(*centre panel*) abundance of Hydrogen ranging from the center to the outer envelope of the models at Xc=0.35 versus the lagrangian mass coordinate and (*right panel*) the variation of angular velocity as a function of the Lagrangian mass coordinate in 60  $M_{\odot}$  at Z=0.014 and with  $V_{\rm ini}/V_{\rm crit}=0.4$ . The letters 'A','B','C' and 'D' and 'G' correspond to the models as described in Table 1.

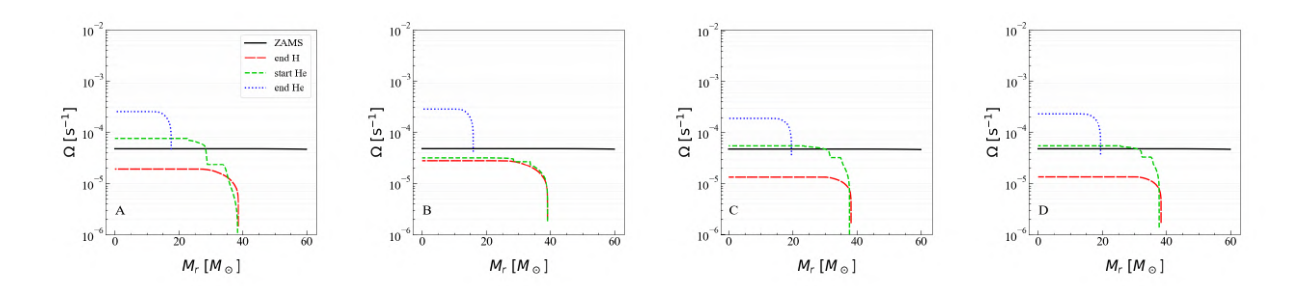


Figure 4.9: Variation of angular velocity profiles as a function of mass for  $60 \, M_{\odot}$  for model A, B, C, D and C\* from left to right (see Table 4.1).

can be attributed to two primary factors: the expansive nature of the convective cores and the stripping away of radiatively differentially rotating layers due to mass loss. This phenomenon can be visualized in the right panel of Fig. 4.8.

The occurrence of solid body rotation within these stellar models leads to significant thermal imbalances. This is primarily due to pronounced deformations in the external stellar layers which exhibit rotational characteristics akin to the core. Such behavior induces elevated velocities in the meridional currents. A noteworthy parallel can be drawn between these models and the magnetic models, especially with respect to the transport mechanisms of chemical species. Within the purview of magnetic models, such a flat rotational profile is consequent to the dynamo processes in effect.

#### Characterization of Stellar Tracks and their Evolutionary Implications

Astrophysical research has been perennially intrigued by the evolutionary trajectories of stars, often represented by their tracks. The  $60 \, M_{\odot}$  model offers an intricate tapestry of such evolutionary pathways, which, when deciphered, offers profound insights into stellar life cycles.

A visual representation of these tracks, coupled with the distribution of hydrogen within the model when the central hydrogen mass fraction is pegged at 0.35, is presented in the left and central panels of Fig. 4.8. Delving into the hydrogen profiles portrayed in the central panel, they correlate to specific positions on the HR diagram, particularly at  $\log L/L_{\odot}=5.87$ . Among the array of models analyzed, Model B, distinguished by its elevated surface hydrogen abundance, manifests the lowest effective temperature at this specific luminosity value. Conversely, Model C, characterized by a diminished surface hydrogen presence, exhibits the highest effective temperature. This observed behavior adheres to established astrophysical tenets. As stars progressively veer towards achieving a chemically homogeneous structure, their corresponding positions on the HR diagram naturally shift towards bluer hues. However, it's imperative to underscore the relatively minute variations manifesting here; these differences are restricted to margins under 2% and 5.5% in  $\log L/L_{\odot}$  and  $\log T_{\rm eff}$ , respectively.

As these models traverse towards the terminal stages of the MS phase, these variances become more accentuated. Notably, in models C and D, as the central hydrogen mass fraction plummets below 0.3, the magnitudes of the convective cores surpass those evident in models A and B. This trend is discernible in Fig. 4.8. This engorgement of the convective cores in models C and D is consequent to their heightened  $D_{\rm eff}$  values. Adding a layer of complexity is the observed decrement in values of  $D_{\rm h}$  in these models when referenced against the formulations presented by Maeder (2003) as opposed to those by Zahn (1992). This dynamics can be rationalized by the pronounced

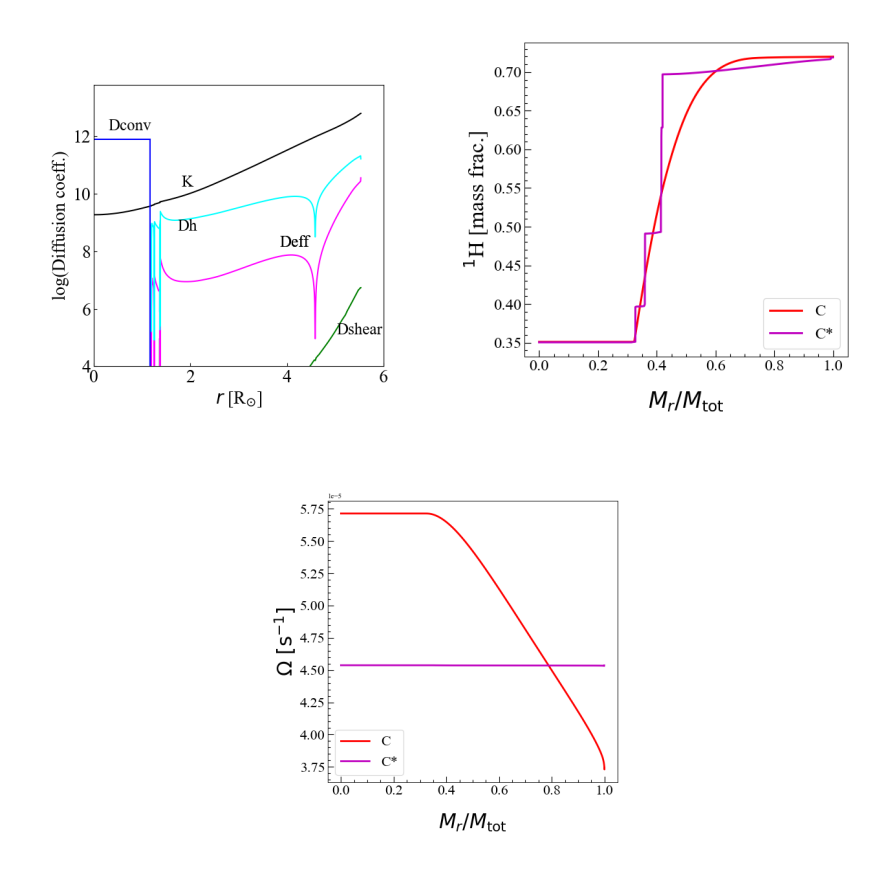


Figure 4.10: Left panel Internal profiles of K the thermal diffusivity,  $D_{\rm conv}$  the convective diffusion coefficient,  $D_{\rm shear}$  the shear diffusion coefficient,  $D_{\rm h}$  the horizontal turbulence coefficient, and  $D_{\rm eff}$  the effective diffusivity in the 15  $M_{\odot}$  C\* model with internal magnetic fields at solar metallicity. The quantities are plotted when the central mass fraction of hydrogen  $X_c = 0.35$ . Middle panel Variation of the H-mass fraction versus the lagrangian mass coordinate. Right panel Variation of the angular velocity versus mass in 15  $M_{\odot}$  for the C\* and C models at the end of H-burning.

mass loss phenomena which result in substantial depletions in angular momentum, culminating in a reduced  $\Omega$ . It's evident that, approaching the twilight of the MS phase, these models register mass losses surpassing  $20\,\mathrm{M}_\odot$ . Given the intrinsic presence of  $\Omega$  in the  $D_\mathrm{h}$  formulations by Maeder (2003) and Mathis et al. (2004), its diminishing value as the  $60\,\mathrm{M}_\odot$  models progress is aligned with the escalation of  $D_\mathrm{eff}$ . This offers a comprehensive understanding as to why, in models C and D, the magnitudes of the convective cores at the closure of the MS phase are more pronounced than in their counterparts, models A and B.

#### **4.3.8** Surface Velocities and Abundances in 60 M<sub>☉</sub> Stellar Models

The evolution of surface velocities during the Main Sequence (MS) phase in the  $60 \text{ M}_{\odot}$  models remains consistent across different prescriptions, as shown in Models A to D in Table 9.2. However, a disparity emerges when considering surface abundances. Models C and D exhibit helium mass

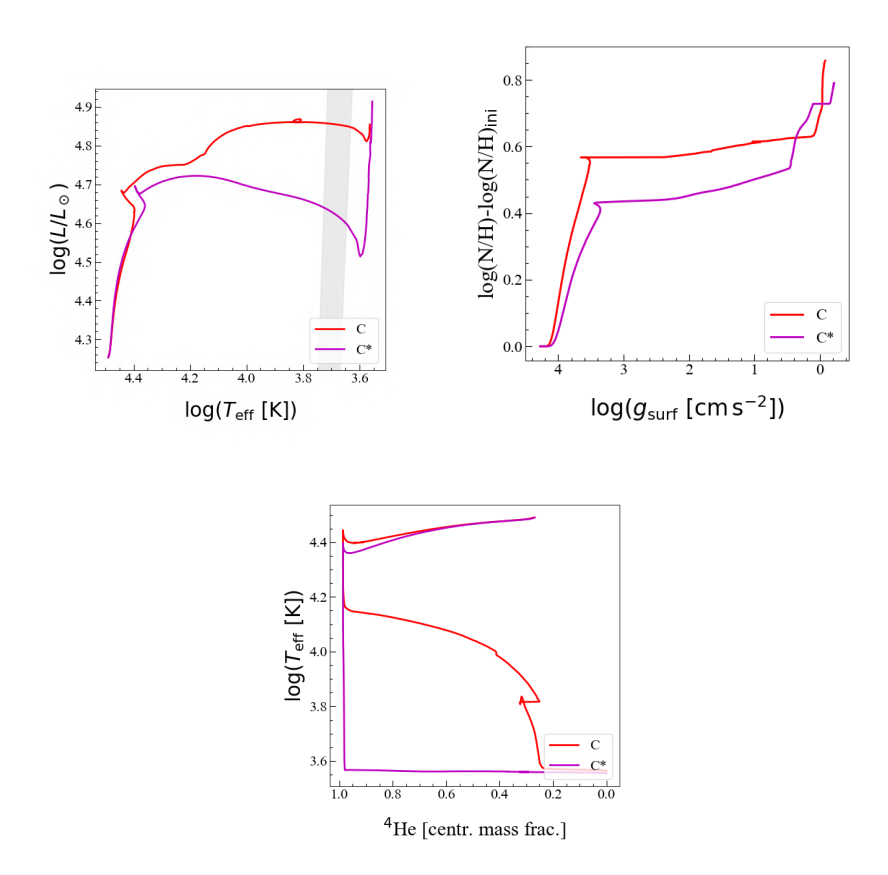


Figure 4.11: For models C and C\* of 15  $M_{\odot}$  with  $V_{\rm ini}/V_{\rm crit}=0.4$  are shown *Left panel*: The evolutionary tracks in the Hertzsprung-Russell diagram during the MS phase; *Middle panel*: The change in the nitrogen over hydrogen ratio normalised to the initial value versus the surface gravity *Right panel*: The variation of the effective temperature as a function of the central helium mass fraction.

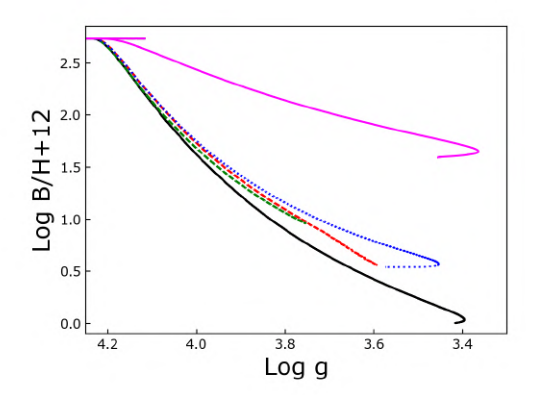


Figure 4.12: Evolution of the B/H ratio (in number) at the surface of models A (continuous black curve), B (dashed green curve), C (dashed red curve), D (dotted blue curve) and C\* (magenta continuous curve) models as a function of the surface gravity.

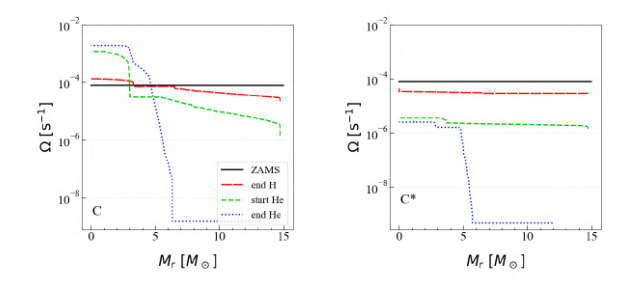


Figure 4.13: Variation of the angular velocity as a function of the lagrangian mass coordinate in  $15M_{\odot}$  at different evolutionary stages. The *left panel* is for the non-magnetic model C. The *right panel* shows the magnetic model C\*.

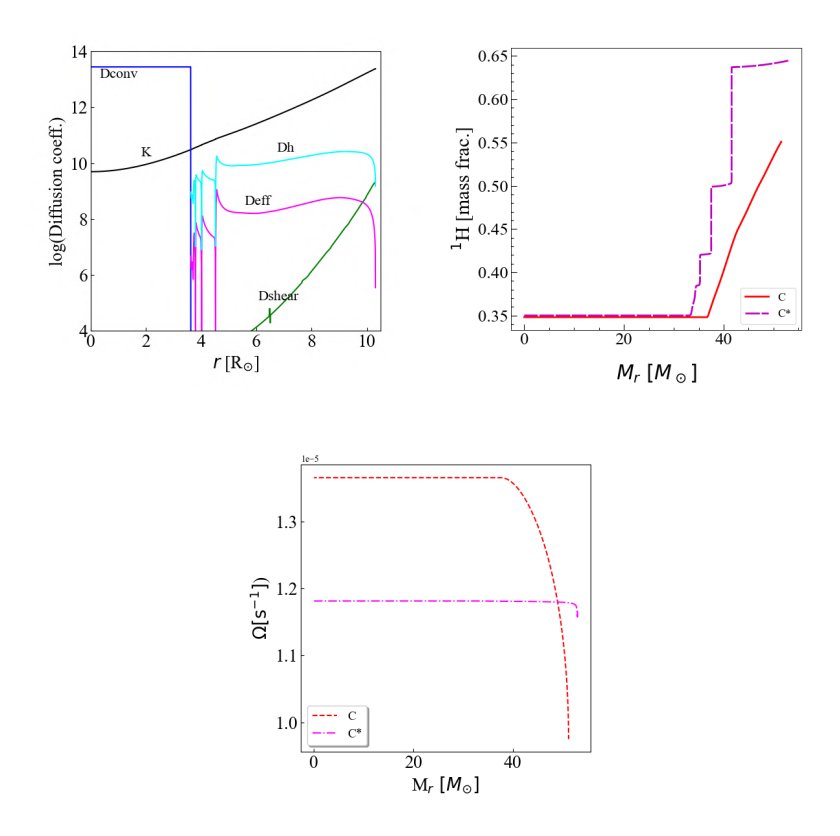


Figure 4.14: Same as Fig. 4.1 for 60  $M_{\odot}$  models.

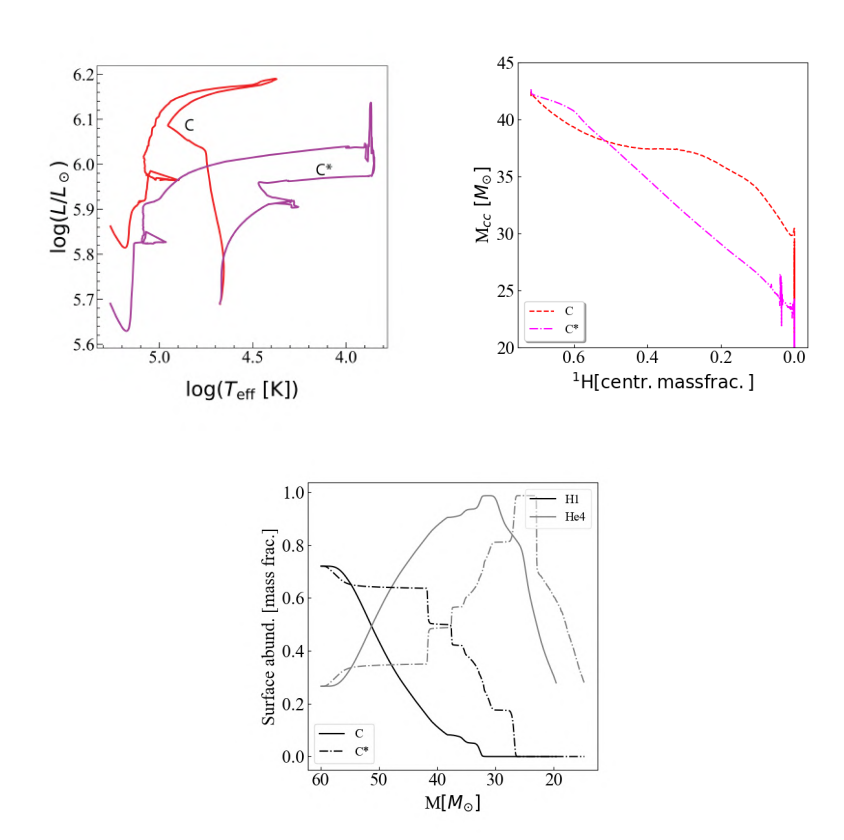


Figure 4.15: Evolutionary tracks in the Hertzsprung-Russell diagram (left panel), variation of convective core mass versus the central mass fraction of hydrogen (center panel) and the surface abundances of hydrogen, helium, carbon, nitrogen and oxygen against the mass for models 'C' and 'C\*' as described in Table 1.

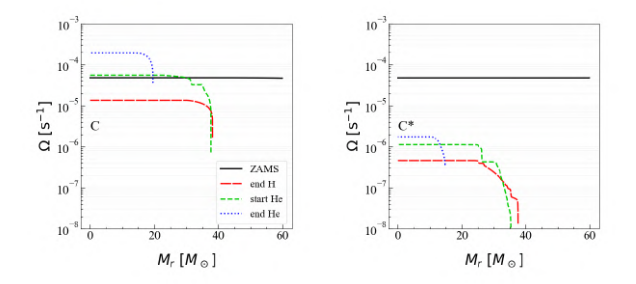


Figure 4.16: Same as Fig. 4.13 for 60  $M_{\odot}$  models

fractions on the surface that are approximately 20% higher than those of Models A and B. Given that all models have comparable total masses at the MS phase's conclusion, this distinction can be attributed to the more efficient internal mixing in Models C and D, driven by an increased  $D_{\rm eff}$ .

#### **4.3.9** Post-MS Evolution of 60 M<sub>☉</sub> Stellar Models

All  $60~\rm M_{\odot}$  models progress to the Wolf-Rayet (WR) phase post-MS. The upper left panel of Fig. 4.15 indicates that during the WR phase, the luminosity for non-magnetic models ranges between 5.65 and 5.8. This variation remains below 50% and is dependent on the prescription employed. Models initialized with a rotation of  $0.4~V/V_{\rm crit}$  show a reduction in core He-burning lifetimes by approximately 8 to 13% in comparison to non-rotating models. The disparity in lifetimes between prescription models stands at 5%, which aligns closely with the minimal variance observed between rotating and non-rotating models.

Tab. 4.1 lists the core masses at the termination of the core He-burning phase. Models C and D, characterized by enhanced mixing, have He-cores that are roughly 4  $M_{\odot}$  larger than those in Models A and B, marking a difference of about 20%. These models also possess increased CO core and remnant masses, suggesting a likely evolution into black holes. The differences amount to 2-3  $M_{\odot}$  for the CO cores and slightly over 1  $M_{\odot}$  for the remnant mass, both approximating a 20% variance. Despite these differences, the eventual fate of these stars, becoming black holes, remains unchanged across rotational prescriptions.

Fig. 4.9 presents the internal angular velocities for models A through D at various evolutionary stages. All models exhibit comparable angular velocity patterns, indicating that diffusion coefficient alterations indirectly influence internal angular velocity. In the  $60~\rm M_{\odot}$  models, the dominating factor in their evolution is stellar winds. During the Wolf-Rayet phase, the surface velocities are reduced, averaging between 20-30 km s<sup>-1</sup>, attributable to significant mass loss. Consequently, these models are predicted to give rise to low-spin black holes with a spin parameter,  $a_* \sim 0.003~\rm ^2$ .

#### 4.3.10 Magnetic Models

#### The 15 M<sub>☉</sub> Model

Stellar magnetic fields play a pivotal role in the evolution of massive stars, and their effects on stellar structures are profound. One stellar model that accentuates these effects is the  $15\,\mathrm{M}_\odot$  model with a calibrated TS dynamo, termed Model C\*.

<sup>&</sup>lt;sup>2</sup>The spin parameter is defined as  $cJ/(GM^2)$ , with c being the light speed, J the total angular momentum, G the gravitational constant, and M the star's end-of-evolution mass. Values from the core He-burning phase's end are primarily considered here.

#### **Diffusion Coefficients and Model Comparisons**

Taking a closer look at the left panel of Fig. 4.14, we observe the diffusion coefficients for the  $15 \text{ M}_{\odot}$  Model C\*. One might assume that introducing magnetic effects would drastically alter the values of the diffusion coefficients  $D_{\text{shear}}$  and  $D_{\text{h}}$ , but intriguingly, these expressions remain identical to those in the non-magnetic Model C. The essence of our investigation here revolves around the differences and nuances introduced by magnetism, comparing Model C\* to Model C.

A standout feature in Model  $C^*$  is the dominance of magnetic viscosity in the transport of angular momentum. In contrast, the coefficient  $D_{\text{eff}}$  mainly governs the transportation of chemical elements. Because of the minimal magnitude of the shear diffusion coefficient, any alteration to its expression barely affects the chemical element transport.

#### Hydrogen Profile and Chemical Mixing

Delving into the intricacies of hydrogen distribution, the middle panel of Fig. 4.11 showcases the hydrogen profile midway through the core H-burning phase. A cursory comparison with the non-magnetic model (model C illustrated in red) reveals more pronounced gradients in the magnetic model just above the core. These gradients are interspersed with almost plateaued zones.

Such a complex structure emanates from the retreating convective core. As it recedes, it leaves behind a region with chemical gradients. These gradients experience a limited degree of mixing due to the action of  $D_{\rm eff}$ . There's an interesting dynamic at play in regions just above the core. Here, the mixing isn't as robust as in the area above where meridional currents are more potent. This establishes an intermediary zone with a mixing timescale that outlasts both the convective core and the radiative envelope. This, in turn, contributes to the staircase-like configurations in the hydrogen profile.

The magnitude of influence of the expression for  $D_h$  cannot be understated. For our current discussion, we've incorporated the expression posited by Maeder (2003). Alternatively, using the formulation by Zahn (1992) would result in a far more vigorous chemical mixing. A comprehensive analysis of these dynamics, however, will be detailed in subsequent papers.

#### Effects of $D_{\text{eff}}$ and Hydrogen Movement

Switching our gaze back to the left panel of Fig. 4.1, it becomes evident that the magnitude of  $D_{\rm eff}$  in Model C\* is considerably larger than  $D_{\rm shear}$  in Model C. This disparity leads to a fascinating phenomenon in the magnetic model. Hydrogen, rather than dispersing, tends to drift inward, amassing just above the convective core. This inward drift, coupled with the reduction

of  $D_{\rm eff}$  above the core, results in pronounced hydrogen gradients. This differential diffusion has an observable impact on the stellar rotation profile. The enhanced viscosity levels in the magnetic model facilitate a flattened rotation profile during the core H-burning phase's midpoint, a trait clearly visible in the right panel of Fig. 4.10.

#### **Main Sequence Evolution**

Moving along the evolutionary timeline, during the Main Sequence (MS) phase, the magnetic model for the  $15~M_{\odot}$  star displays a broader spectrum of effective temperatures compared to its non-magnetic counterpart. This variance can be attributed to the diminished mixing in the magnetic model. These mixing dynamics come to the fore in the left panel of Fig. 4.11.

Furthermore, the surface abundance evolution, depicted in the middle panel of Fig. 4.11, reinforces the reduced mixing assertion. Additionally, the relationship between the effective temperature and the helium mass fraction at the core is intriguing. As illustrated in the right panel of Fig. 4.11, post-MS phase, the magnetic model swiftly transitions into a red supergiant. In contrast, the non-magnetic model undergoes a significant portion of its helium burning at higher effective temperatures. These differences in evolutionary trajectory are largely due to minor alterations in the abundance profiles near the H-burning shell, as articulated by Farrell et al. (2022b).

#### Boron Abundance as an Indicator

In Fig. 4.12, we show the variation of the boron abundance at the surface of the A, B, C, D and  $C^*$  models. As briefly mentioned in the introduction, boron does not need to be dredged down very deeply inside the star to be affected by nuclear reactions. It is is destroyed via proton capture at temperatures of around  $6 \times 10^6$  K (see e.g. Proffitt et al. 1999), making it a good indicator of mixing in the outer layers of stars, where  $D_{\rm shear}$  dominates in non-magnetic models and  $D_{\rm eff}$  in magnetic ones. Despite some differences, models A, B, C, and D exhibit similar qualitative evolution, largely due to the fact that the depletion of boron occurs primarily in zone 4, where the two  $D_{\rm shear}$  expressions yield comparable values. Nonetheless, the depletion of boron in magnetic models is weaker than in non-magnetic models (at a fixed initial mass, rotation and metallicity), which could be used to differentiate between the two types of models. Further research is necessary to investigate this possibility, but it is clear that magnetic models exhibit distinct behaviors in the boron versus log g, boron versus nitrogen surface abundances, and boron versus surface rotation planes. In Figure ??, we compare the angular velocity distribution of a non-magnetic model (left panel) and a magnetic model (right panel). At the end of the core He-burning phase, the magnetic model displays a core angular velocity three orders of magnitude lower than the non-magnetic

model. This difference suggests that the angular momentum of the remnant would decrease by three orders of magnitude, resulting in a proportional increase in its spin period; assuming the angular momentum of the part of the star that becomes the neutron star remains constant post-He-burning.

#### 4.3.11 The 60 $M_{\odot}$ Model

The complex interplay between magnetic forces, angular momentum, and chemical diffusion in stars can be well appreciated by examining the  $60~M_{\odot}$  model. This model offers a captivating platform to understand how magnetism molds the evolutionary journey of such massive celestial entities.

#### **Diffusion Coefficients and Trends**

A key facet of this model is its diffusion coefficients, as graphically portrayed in the left panel of Fig.4.14. A quick analysis reveals intriguing parallels with the previously discussed 15  ${\rm M}_{\odot}$  model. Specifically, within the radiative zone, angular momentum transport predominantly hinges on magnetic viscosity. Meanwhile, the transportation of chemical species owes its behavior to  $D_{\rm eff}$ . However, there exists a rather narrow zone near the star's surface where  $D_{\rm shear}$  outpaces  $D_{\rm eff}$ . This unique region emerges due to the differential rotation playing out in the star's outermost layers. This dynamic can be discerned more clearly by examining the right panel of Fig.4.14, which throws light on this outer differential rotation.

#### Hydrogen Profile and Core H-Burning Phase

Shifting focus to the star's core, the middle panel of Fig. 4.14 visualizes the hydrogen abundance profile right at the core H-burning phase's midpoint. This magnetic model paints a picture of an H-rich exterior envelope. Moreover, a pronounced gradient seamlessly links this envelope to the convective core. A comparative perspective reveals that the  $60~M_{\odot}$  model's behavior mirrors its  $15~M_{\odot}$  counterpart, as demonstrated in the middle panel of Fig. 4.10. Furthermore, the right panel of Fig. 4.14 showcases the variation in angular velocity concerning the Lagrangian mass coordinate. During the core H-burning phase, the magnetic model delineates a core that rotates at a marginally slower pace, about 15% slower than its non-magnetic equivalent. This is complemented by a subdued differential rotation in the star's outer layers.

#### **Evolutionary Tracks and Impacts of Magnetism**

Magnetic instabilities leave an indelible imprint on the  $60~M_{\odot}$  star's evolutionary trajectory. A case in point is the illustration in the left panel of Fig. 4.15. Model C, characterized by vigorous internal mixing, evolves in an almost vertical trajectory, staunchly remaining blue. In stark contrast, the magnetic model veers towards the red. In a deep dive into the convective core dynamics, the middle panel of Fig. 4.15 underscores a fascinating observation. The convective core in the non-magnetic model notably eclipses its magnetic counterpart in terms of size for a significant duration of the core H-burning phase. Moreover, the surface abundance evolution presents another layer of differentiation. As depicted in the right panel of Fig. 4.15, the surface's hydrogen mass fraction plunges below 0.4 when the star's actual mass hovers around 35  $M_{\odot}$  in the magnetic model. Meanwhile, this threshold is reached when the mass is around 50  $M_{\odot}$  in the non-magnetic variant.

#### **Angular Velocity Variations and Core Rotation**

To encapsulate the nuanced variations in the core's rotation between magnetic and non-magnetic models, one must delve into Fig. 4.16. This figure offers a side-by-side comparison, drawing parallels between the angular velocities at different evolutionary phases. The magnetic model, under the rigorous influence of the magnetic field, showcases a substantially slower core rotation. By the conclusion of the core He-burning phase, this deceleration is so profound that the rotation diminishes by two entire orders of magnitude in comparison to the non-magnetic model.

#### 4.3.12 Additional prescriptions E and F

We discuss here the models computed with the  $D_h$  of Mathis et al. (2004) and compare them with the models computed with the  $D_h$  of Maeder (2003).

Figure 4.17 is the analog of Fig. 4.2 for models C, D, E and F. We see that models C and E (using the  $D_{\rm shear}$  of Maeder (1997), but different  $D_{\rm h}$  expression (C the expression by Maeder (2003) and E, the expression of Mathis et al. (2004)) have very similar evolutionary tracks (see left panel). The model C shows a slightly smoother gradient of hydrogen than model E. Models F and D use the  $D_{\rm shear}$  of Talon & Zahn (1997) with the two different  $D_{\rm h}$ . They present steeper chemical gradients above the convective core than models C and E that uses the  $D_{\rm shear}$  by Maeder (1997). This illustrates the fact that the choice  $D_{\rm shear}$  impacts the degree of the chemical mixing. The angular velocity profiles between all these four models are nearly indistinguishable, illustrating the fact that the choice of  $D_{\rm shear}$  and  $D_{\rm h}$  has little impact on the angular momentum transport in the

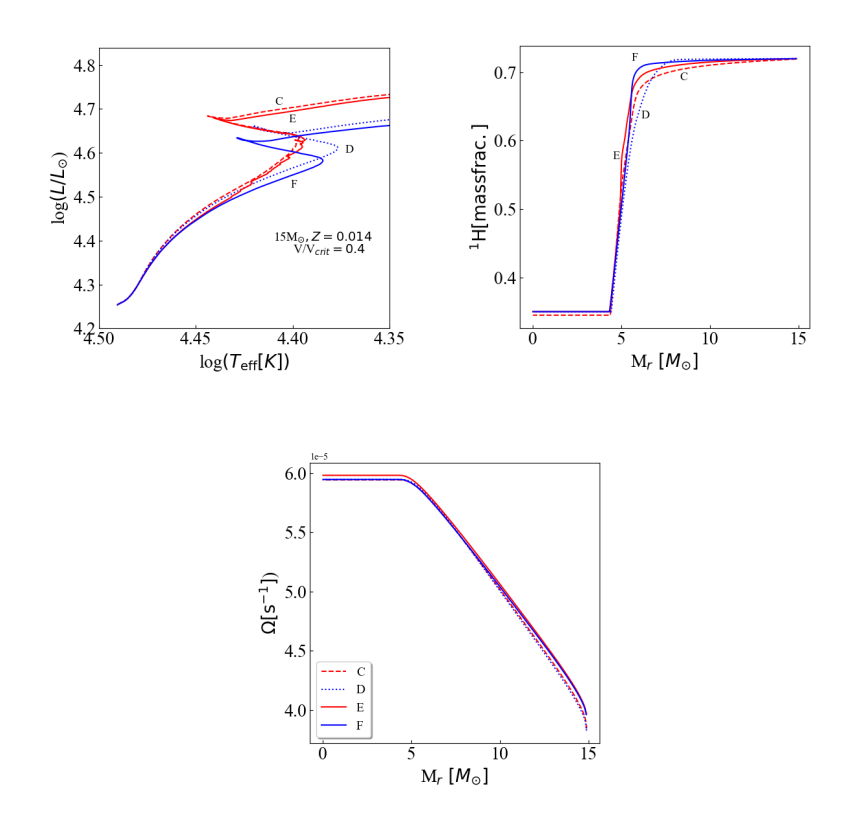


Figure 4.17: *Left panel*: Evolutionary tracks during the MS phase in the Hertzsprung-Russell diagram are shown for models C, D, E and F (see Table 1) as a function of the Lagrangian mass for the  $15~\rm M_{\odot}$  at Z=0.014 and with  $V_{\rm ini}/V_{\rm crit}=0.4$ . *Middle panel*: Abundance of Hydrogen in mass fraction ranging from the center to the outer envelope of the models when the central mass fraction of hydrogen  $X_{\rm c}$ =0.35. *Right panel*: Variations of the angular velocity versus the mass coordinate for the same models as those shown in the middle panel.

star. For the initial rotation considered here, the changes in the chemical mixing does not change so much the evolution as to indirectly impact the profile of  $\Omega$ . The evolution of the convective core masses are compared in the right panel of Fig. 4.18. They are not showing any striking differences. On the other hand, we see that the surface enrichments are significantly different between these models (see the middle panel of Fig. 4.18). Globally, the models using the  $D_{\rm shear}$  of Maeder (1997) (C and E) are more mixed than those using the  $D_{\rm shear}$  of Talon & Zahn (1997) (D and F). The abundances of helium as a function of the lagrangian mass coordinate when the mass fraction of helium at the centre is 0.9 is shown in the right panel of Fig. 4.18. We can see that the profiles of models E and F are very similar to the one in model C. Thus we expect that those models will spend a fraction of their core He-burning phase in a blue region of the HR diagram, which is indeed the case (see Fig. 4.19). This supports the view that any helium enrichment in the H-burning shell tends to produce an evolution towards the red supergiant stage along a Kelvin-Helmholtz timescale.

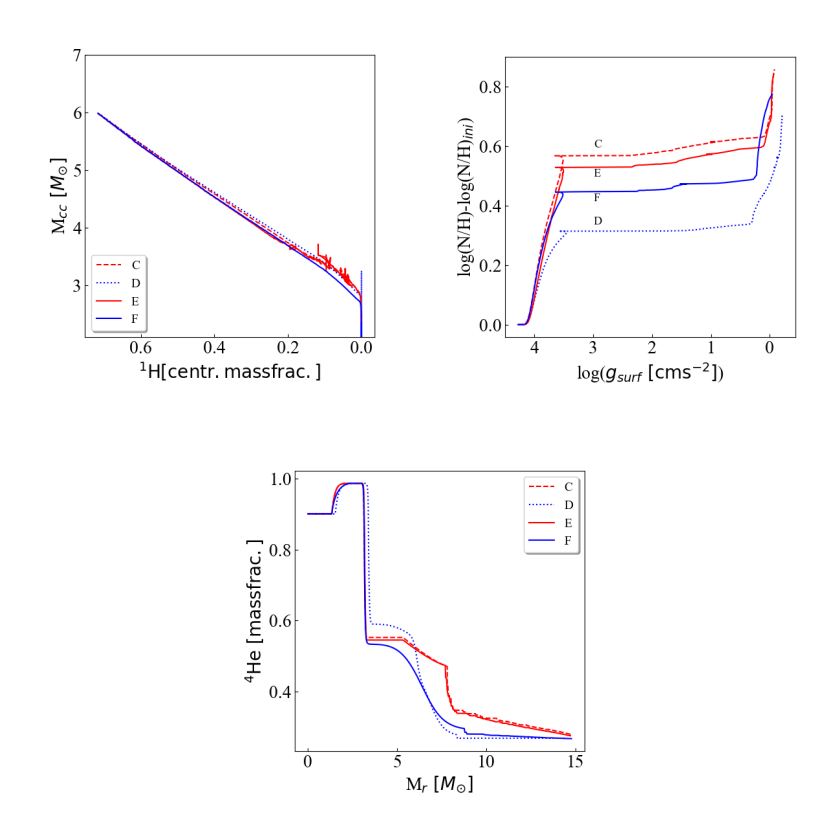


Figure 4.18: Left panel: Evolution of the convective core mass during the MS phase as a function of central mass of hydrogen. Center panel: The abundance ratio of nitrogen and hydrogen at the surface normalised to their initial values versus the surface gravity. Right panel: Profile of the helium mass fraction against the mass coordinate when the central helium fraction ( $Y_c$  is 0.90). The letters 'C','D','E' and 'F' correspond to the models with different prescriptions as described in Table 1.

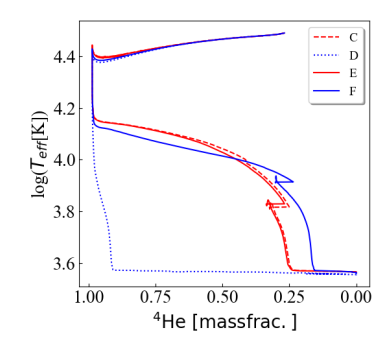


Figure 4.19: Evolution of the effective temeprature as a function of the mass fraction of helium at the centre during the core He-burning phase for the models C, D, E and F.

#### 4.3.13 Discussion and Conclusions

We conducted an investigation to discern the effects of modifying the rotational prescription on our stellar models, with other physical parameters held constant. The results highlight the criticality of selecting appropriate expressions for  $D_{\rm shear}$  and  $D_{\rm h}$  in non-magnetic models, with each choice leading to distinctive results based on the initial mass and rotational velocity. Furthermore, a pronounced divergence is observed between magnetic and non-magnetic models. We outline our main conclusions as follows:

- 1. Modifying the diffusion coefficients in non-magnetic models primarily influences the star's chemical makeup. Notably, it doesn't significantly alter angular momentum transport.
- 2. Regardless of diffusion coefficients or initial mass, **non-magnetic** models consistently exhibit rapid core rotations post the core He-burning phase, corroborated by findings from Georgy et al. (2009).
- 3. In magnetic contexts, angular momentum transport is predominantly governed by magnetic instabilities. These models, particularly for 15 and  $60~M_{\odot}$  stars, demonstrate consistent rotation profiles during the main sequence. Such observations align with prior work by Heger et al. (2005) and Fuller & Ma (2019).
- 4. The choice of diffusion coefficients plays a pivotal role in dictating chemical element mixing and subsequent trajectories in the HR diagram. For instance, in non-magnetic settings, the selection of  $D_{\rm shear}$  can significantly influence the evolutionary path of the 15  ${\rm M}_{\odot}$  model, in contrast to the 60  ${\rm M}_{\odot}$  model.
- 5. Enhancing  $D_{\rm h}$  in the non-magnetic 15  ${\rm M}_{\odot}$  model modifies transport adjacent to the convective core, predominantly where  $D_{\rm eff}$  prevails. Selection of  $D_{\rm h}$  from Maeder (2003), as opposed to Zahn (1992), results in diminished convective cores and subsequently less luminous trajectories.
- 6. Reductions in  $D_{\rm eff}$  tend to decrease mixing. However, this reduction might not be impactful if the radiative envelope contains elevated levels of  $D_{\rm shear}$ , especially in regions proximate to the core with robust chemical gradients during core H-burning.
- 7. Our calculations align with those presented by Maeder & Meynet (2001b) and Farrell et al. (2022b), emphasizing the commencement of the core He-burning phase as a red supergiant, contingent on helium enrichment near the H-burning shell. The duration required for a star

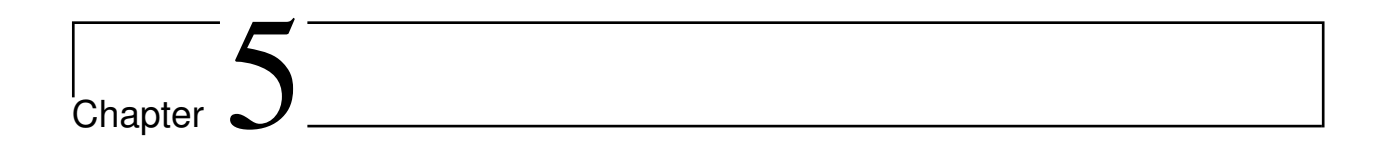
to traverse the HR gap post the MS phase is pivotal in gauging the blue to red supergiant ratio, which has profound implications for close binary evolution.

- Variations in MS lifetimes between rotating models with different diffusion coefficients are comparable to those observed between rotating and stationary models with or without moderate core overshoot.
- Post He-burning, core masses exhibit discrepancies based on the employed prescriptions, with variations being even more pronounced than when contrasting non-rotating models with or without moderate overshoot.
- 10. The  $60 \text{ M}_{\odot}$  model exhibits pronounced sensitivity to mass losses due to stellar winds, with diffusion coefficient alterations exerting minimal influence.
- 11. In non-magnetic  $60 \text{ M}_{\odot}$  models, the chief agent for chemical mixing is  $D_{\text{eff}}$ . Both convection and mass loss contribute to the swift conversion into an almost uniform rotating core, escalating the transport of chemical elements.
- 12. Models adopting  $D_h$  expressions that are overtly dependent on  $\Omega$ , and which undergo substantial mass losses, show that  $D_{\text{eff}}$  values rise over time. This can be attributed to the decline of  $\Omega$  due to mass loss, leading to  $D_h$  reductions and subsequent increases in  $D_{\text{eff}}$ .
- 13. For magnetic models,  $D_{\rm eff}$  predominantly governs chemical mixing. It's influenced by the choice of  $D_{\rm h}$  but remains impervious to  $D_{\rm shear}$  when rotation profiles are flat. Our investigation only presents magnetic models that use the  $D_{\rm h}$  from Maeder (2003). The extent of mixing observed in both the 15 and 60  $M_{\odot}$  magnetic models is notably less than in corresponding non-magnetic models with the same  $D_{\rm h}$ .

Our observations suggest that step overshoot modifications can influence the reproduction of the observed width of the MS band. For instance, a diminished step overshoot value is necessitated when incorporating  $D_{\rm shear}$  values from Maeder (1997). Such findings render Model A consistent with contemporary stellar model grids developed by the Geneva group, most notably as documented by Ekström et al. (2012c). Analysis of Fig. 4.1 reveals that both Models C and E require negligible alterations when integrated with  $D_{\rm shear}$ , as presented in Maeder (1997), whereas more recalibrations are necessary for Models B, D, and F.

While it remains a complex endeavor to infer the most accurate physical processes from surface observations, asteroseismology provides a promising avenue to unravel angular momentum

transport mysteries in both massive and lower mass stars. It's noteworthy that our current magnetic models are congruent with internal rotations documented for the Sun and with asteroseismic constraints coming from the study of subgiants, as referenced in Eggenberger et al. (2019) and Eggenberger et al. (2022a). Massive stars, albeit with fewer constraints, pose the challenge of accurately pinpointing the causative factors behind observed variations in rotational behaviors.



## Chemical signatures of PopIII massive stars in the early Universe

This study explores the chemical signatures of massive stars, specifically Population III (PopIII) stars, and their impact on the early universe's chemistry and is adapted from the paper Nandal et al (2023 submitted). Recent observations of high-redshift galaxies, notably GN-z11 (Oesch et al. 2016) and CEERS-1019 (Finkelstein et al. 2017), show elevated nitrogen-to-oxygen (N/O) abundance ratios. These observations suggest complex chemical processes during the universe's nascent stages (Bunker et al. 2023; Cameron et al. 2023; Charbonnel et al. 2023; Marques-Chaves et al. 2023). Our investigation builds upon prior research into the effects of rotational prescriptions on massive stars. The choice of diffusion coefficients in non-magnetic models, explored in our previous work, highlighted the critical role of these parameters in shaping the stars' chemical and rotational properties (Georgy et al. 2009; Heger et al. 2005; Fuller & Ma 2019). We now extend this understanding to model massive stars across various metallicities and masses, aiming to link their evolution to the observed chemical abundances in early galaxies. The primary focus of this study is to use the stellar models for massive stars computed by the GENEC group (Tsiatsiou et al submitted, Sibony et al in prep, Nandal et al in prep), ranging from 9 to 120  $M_{\odot}$ , across different metallicities (0,  $1 \times 10^{-5}$ , and solar). By adopting standard rotational prescriptions identified in our earlier work, we aim to predict the observable chemical signatures of these stars. The comparison of our model predictions with the observed N/O, C/O, and O/H values in galaxies like GN-z11 and CEERS 1019 will offer insights into the stellar processes prevalent in the early universe.

We also consider the chemical peculiarities observed in other high-redshift galaxies, such as the Lynx Arc and Sunburst Arc, which exhibit similar high N/O ratios (Fosbury et al. 2003). The inclusion of these galaxies provides a broader scope for assessing the impact of massive stars on

galactic chemistry. Our approach integrates population synthesis models to predict the overall yield of N/O, C/O, N/C, O/H, and Ne/O ratios from massive stars. We overlaped these theoretical predictions with observational data to better understand the elemental abundance patterns in high-redshift galaxies.

#### 5.1 Introduction

Observations of galaxies with high redshifts, such as GN-z11 (Oesch et al. 2016) and CEERS-1019 (Finkelstein et al. 2017), have revealed noteworthy enhancements in nitrogen. GN-z11, at a redshift of z=10.6 (Bunker et al. 2023), displays a nitrogen-to-oxygen (N/O) abundance ratio exceeding four times the solar value, a finding that challenges established theories (Cameron et al. 2023). This elevated ratio, compared to both lower redshift galaxies and those with higher metallicities, points to complex chemical activities in the early universe (Vincenzo et al. 2016; Berg et al. 2019).

CEERS-1019, situated at a redshift of z=8.678, exhibits advanced chemical development, as indicated by its pronounced N IV]  $\lambda 1486$  emission line (Tang et al. 2023). Studies by Marques-Chaves et al. (2023) report exceptionally low C/N and high N/O ratios in CEERS 1019. These unusual chemical abundances call for further exploration into the processes of elemental formation and star formation in the early universe.

In addition to these, other galaxies with high N/O ratios have been identified both in the distant and more recent past. Notable examples include the Lynx arc (Fosbury et al. 2003) and the sunburst arc at high redshifts, and Mrk996 at lower redshifts. The role of massive, very massive, and supermassive stars (MSs, VMSs, and SMSs) is becoming increasingly evident in influencing the chemical composition of these galaxies (Woods et al. 2020). Their contribution to nucleosynthesis and potential involvement in forming central massive black holes are key aspects of understanding stellar evolution in relation to the development of galaxies (Denissenkov & Hartwick 2014; Gieles et al. 2018; Hosokawa et al. 2010a; Natarajan et al. 2023).

In response to these unique observations, numerous studies have investigated the early universe galaxies' characteristics. Kobayashi & Ferrara (2023) highlighted a dual-burst model for rapid chemical enrichment, focusing on the pivotal role of Wolf-Rayet stars during the secondary burst phase. Research by Gratton et al. (2019) has offered insights into the chemical attributes of early Universe globular clusters, paralleling the patterns seen in galaxies such as GN-z11. Furthermore, Charbonnel et al. (2023) and Nagele & Umeda (2023) examined the significant influence of metal-rich stars, particularly in the  $10^3 - 10^5 M_{\odot}$  mass range, on the chemical composition of

early galaxies. Diverse approaches to studying stellar evolution have been pursued. The effect of rapid stellar rotation has been thoroughly investigated by Meynet & Maeder (2006) and Choplin et al. (2018). Their work suggests that swift rotation in massive stars markedly affects their nucleosynthetic yield, corroborated by models from Chiappini et al. (2006a). Additionally, the role of pair-instability supernovae, explored by Heger et al. (2002), provides deeper insights into stellar dynamics in the universe's formative periods.

This chapter takes a comprehensive approach to stellar evolution. We calculate the stellar yields of massive stars, ranging from 9 to 120  $M_{\odot}$ , across various metallicities (0,  $10^{-5}$ ,  $4\times10^{-4}$ , 0.002, 0.006, and 0.014). By hypothesizing that all mass above the remnant or CO core is ejected, and employing an initial mass function (IMF) for population synthesis, we aim to predict the aggregate yield in terms of N/O, C/O, N/C, O/H, and Ne/O. We then compare our results with the observed data from GN-z11 and CEERS 1019, aiming to provide new insights into the elemental abundance patterns in high-redshift galaxies. This chapter is structured as follows: Section 5.2 outlines the stellar evolution models and methodologies used to determine the remnant mass of the models, the mean mass of ejecta, and the population synthesis models. Section 5.3 examines the transport mechanisms for chemical species and calculates the mean abundances for individual stars ( $\mathbf{X_{io}}$ ) and for the entire halo ( $\mathbf{X_{ip}}$ ). Section 5.4 delves into the effects of binary stars, contrasts standard and fast-rotating models, and predicts abundances based on our models, comparing them with previous studies. Finally, Section 5.5 summarizes our findings and outlines future research directions.

#### 5.2 Stellar models and enrichment

This work utilizes a library of stellar models in the mass range of  $9M_{\odot} \leqslant M_{\rm ini} \leqslant 120M_{\odot}$  across a variety of metallicities: Population III (Z=0), Extremely Metal-Poor  $(Z=10^{-5})$ , and other specific metallicity values up to Solar metallicity (Z=0.014), computed using GENEC. The initial surface velocities are set at 40% and 70% of the critical rotation. Critical rotation is defined by  $v_{\rm crit} = \sqrt{\frac{2}{3} \frac{GM}{R_{\rm p,crit}}}$ , where  $R_{\rm p,crit}$  is the polar radius at critical velocity.

The models follow shellular rotation theory as proposed by Zahn (1992), assuming near uniform rotation along an isobar. Chemical species transport is managed by a purely diffusive equation. More information about these models can be found in Murphy et al. (2021a); Tsiatsiou et al. (in prep.); Sibony et al. (in prep.); Groh et al. (2019); Georgy et al. (2013b); Eggenberger et al. (2021); Ekström et al. (2012a). Notably, these models do not include the effects of magnetic fields.

The Pop III models in this study do not incorporate wind mass loss, although minimal mechan-

ical mass loss is considered (Murphy et al. (2021a); Tsiatsiou et al. (in prep.)). For other models, radiative, supra-Eddington, and mechanical mass losses are included, as detailed in Ekström et al. (2012a). Supra-Eddington mass loss occurs when the star's outer layers exceed the Eddington luminosity, defined by  $\Gamma_{\rm Edd} = \frac{\kappa L}{4\pi cGM}$ . This phenomenon can be facilitated by mechanisms such as anisotropic radiation, where radiation pressure varies in different directions, allowing mass loss to occur through less radiated paths. Additionally, instabilities within the radiation field can lead to localized regions where radiation pressure significantly exceeds gravitational pull, promoting mass loss. Magnetic fields can also channel material away from the star, reducing the overall radiation pressure experienced by the accreting matter. Lastly, the presence of dense, clumpy material can shield parts of the star from radiation, enabling supra-Eddington accretion rates. Mechanical mass loss happens when the surface velocity reaches the critical limit, causing the outer layers to detach.

#### 5.2.1 Integrated Abundance Ratios

Our study investigates a scenario where stars modify the chemical composition of their surrounding interstellar medium (ISM) via mass loss. This process could occur through various mass-loss episodes, such as stellar winds, prior to the star's demise, or at the end of its evolutionary path through a supernova. The total mass ejected by a star,  $M_{\rm ej}(M_{\rm ini},Z)$ , is calculated as the sum of mass lost due to stellar winds and supernova events, expressed as  $M_{\rm ej}(M_{\rm ini},Z) = M_{\rm winds}(M_{\rm ini},Z) + M_{\rm SN}(M_{\rm ini},Z)$ . We assume immediate mixing of this ejected mass with the ISM, combining all mass loss during the star's life with the mass ejected at death and diluting it within the ISM. This section provides an overview of our method for calculating the diluted abundances of individual elements ejected by a population of stars.

We begin by determining from our stellar models the mass ejected at each timestep due to mass loss, summing the abundance of each element between the remnant mass in Sect. 5.2.1 and the star's surface at the final timestep. Once we have the mass of each element ejected by stars of each initial mass and metallicity, we simulate populations of stars following an initial mass function (IMF; details in Sect. 5.2.1). Each population corresponds to a specific metallicity, allowing us to ascertain the mass of each element ejected into the ISM. Finally, we calculate the [N/O] and [C/O] abundance ratios in the ISM post-enrichment by diluting the ejecta (with interstellar medium material having an abundance equal to the initial abundances of the considered stellar models). Further information about the computation of remnant masses is provided in Sect. 5.2.1, Sect. 5.2.1 outlines the population synthesis model, and details our enrichment model.

#### **Remnant Masses**

Determining the chemical abundances at the end of a star's life requires setting a lower bound for integration, referred to as the mass-cut  $M_{\rm cut}$ . Mass below this limit will be trapped in the remnant, while the rest is ejected. We compute this mass-cut using models from Farmer et al. (2019); Patton & Sukhbold (2020). Farmer et al. (2019) studied massive helium stars under different conditions to predict the pair-instability mass gap. Patton & Sukhbold (2020) investigated naked CO cores of varying masses and carbon fractions, applying the 'Ertl criterion' (Ertl et al. 2016, 2020) to determine whether the star would explode or implode.

Five scenarios are considered, based on the CO core mass at the end of helium-burning:

- 1. If  $M_{\rm CO} < 1.4 \, M_{\odot}$ , the remnant is a white dwarf (WD) with mass  $M_{\rm rem} = M_{\rm CO}$ .
- 2. For  $1.4 M_{\odot} < M_{\rm CO} < 2.5 M_{\odot}$ , the remnant is a neutron star (NS) with mass  $M_{\rm rem} = 1.4 M_{\odot}$ .
- 3. If  $2.5\,M_{\odot} < M_{\rm CO} < 10\,M_{\odot}$ , we use central carbon mass fraction data and Patton & Sukhbold (2020)'s Fig. 3 to assess whether the star explodes into a NS or implodes into a black hole (BH). Explosion results in an NS of mass  $M_{\rm rem} = M_4$  (as per Patton & Sukhbold (2020)'s Table 1), while implosion yields a BH of mass  $M_{\rm rem} = \min{(M_{\rm CO} + 4, M_{\rm tot})}$ , following Farmer et al. (2019)'s analytic fit.
- 4. For  $10 M_{\odot} < M_{\rm CO} < 38 M_{\odot}$ , the star implodes into a BH with mass  $M_{\rm rem} = \min{(M_{\rm CO} + 4, M_{\rm tot})}$ .
- 5. Stars with  $M_{\rm CO} > 38\,M_{\odot}$  are evaluated using Farmer et al. (2019)'s Table 1 for their fate and remnant mass. Pair-instability supernovae (PISN) in this range eject all matter, leaving no remnant.

We explore two scenarios: the detailed approach as described, using  $M_{\text{cut}} = M_{\text{rem}}$ , and a simpler method where all matter above the CO core is ejected, setting  $M_{\text{cut}} = M_{\text{CO}}$ .

#### **Enrichment model**

The total mass of element i ejected by a star with an initial mass  $M_{\text{ini}}$  at metallicity Z, denoted as  $M_{\text{ej},i}(M_{\text{ini}}, Z)$ , is calculated by:

$$M_{\text{ej},i}(M_{\text{ini}}, Z) = \int_0^{t_f} \dot{M}_{\text{wind}} x_{i,s}(t) + \int_{M_{\text{out}}}^{M_{\text{tot}}} x_{i,t_f}(M_r) dM_r, \tag{5.1}$$

where  $t_f$  represents the star's final age,  $\dot{M}_{\rm wind}x_{i,s}(t)$  is the mass ejected by winds per unit time,  $x_{i,s}(t)$  is the surface mass fraction of element i at time t, and  $x_{i,t_f}(M_r)$  is the mass fraction of

Z	$X_{^{1}H}$	$X_{ m ^4He}$	$X_{12C}$	$X_{^{13}\mathrm{C}}$	$X_{14}$ N	X <sub>16</sub> O	$\chi_{^{20}\mathrm{Ne}}$
	Initial mass fraction						
0 (Pop III)	0.7516	0.2484	0	0	0	0	0
$10^{-5} \text{ (EMP)}$	0.7516	0.2484	1.3e-06	4.3e-09	1.0e-07	6.8e-06	9.2e-07
$4 \times 10^{-4} $ (I Zw 18)	0.7507	0.2489	6.5e-05	7.9e-07	1.9e-05	1.6e-04	5.4e-05
0.002 (SMC)	0.7471	0.2509	3.3e-04	4.0e-06	9.4e-05	8.2e-04	2.7e-04
0.006 (LMC)	0.7381	0.2559	9.8e-04	1.2e-05	2.8e-04	2.5e-03	8.0e-04
0.014 (Solar)	0.7200	0.2660	2.3e-03	2.8e-05	6.6e-04	5.7e-03	1.9e-03

Table 5.1: Initial abundances (in mass fraction) of the isotopes of interest, in the stellar models and in the ISM for the different metallicities we explore.

element i at the mass coordinate  $M_r$  in the star's last computed timestep. The mass fraction of element i in a star's ejecta,  $X_{ej,i}(M_{ini}, Z)$ , is calculated as the ratio:

$$(M_{ei,i}(M_{ini}, Z)/M_{ei}(M_{ini}, Z))$$
 (5.2)

For a population of stars, the mass fraction of element i in the collective ejecta,  $X_{ej,i}(Z)$ , is given by:

$$X_{\mathrm{ej},i}(Z) = \frac{\sum\limits_{M_{\mathrm{ini}}} n(M_{\mathrm{ini}}) \times M_{\mathrm{ej},i}(M_{\mathrm{ini}}, Z)}{\sum\limits_{M_{\mathrm{ini}}} n(M_{\mathrm{ini}}) \times M_{\mathrm{ej}}(M_{\mathrm{ini}}, Z)},$$
(5.3)

where  $n(M_{\rm ini})$  is the number of stars in the population with mass  $M_{\rm ini}$ , determined by our selected Initial Mass Function (IMF) (see Sect. 5.2.1).

The ejected mass then interacts with the interstellar medium (ISM), resulting in a blend of the stars' ejecta and the ISM. The ISM's mass involved in this interaction is  $M_{\rm ISM}$ . We introduce a dilution factor f(Z), the ratio  $M_{\rm ISM}/M_{\rm ej}(Z)$ , where  $M_{\rm ej}(Z)$  is the total mass ejected by the star population at metallicity Z. We vary f(Z) from 1 to 1000.

We use this parameter to estimate the final composition of the mixture of the star's ejecta and the ISM. We define  $X_{i,m}(Z)$  as the mass fraction of element i in this mixture, calculated using the principle of mass conservation:

$$X_{i,m}(Z) * (M_{ej}(Z) + M_{ISM}) = M_{ej,i}(Z) + X_{i,0}(Z) * M_{ISM},$$
 (5.4)

where  $X_{i,0}(Z)$  is the mass fraction in the ISM prior to any enrichment. We provide in Table 5.1 the initial chemical compositions of the ISM for the different metallicities at which we generate populations. These are also the initial compositions of the stars. Indeed, stars form from the ISM gas, and the composition of the ISM does not change until the first elements are ejected from stars.

By substituting the dilution factor f(Z) into the equation, we can simplify it to:

$$X_{i,m}(Z) * (1 + f(Z)) = X_{e_i,i}(Z) + f(Z) * X_{i,0}(Z),$$
(5.5)

or, isolating  $X_{i,m}(Z)$ :

$$X_{i,m}(Z) = \frac{X_{ej,i}(Z) + f(Z) * X_{i,0}(Z)}{1 + f(Z)}.$$
(5.6)

#### **Impact of the Initial Mass Function**

Our approach utilizes a parametric method to assess the chemical feedback of massive stars. We apply either a Salpeter Initial Mass Function (IMF) with  $\alpha=-2.35$  or a top-heavy IMF with  $\alpha=-1$ , considering stellar masses ranging from  $m_{\rm min}=9\,M_{\odot}$  to  $m_{\rm max}=120\,M_{\odot}$ . Given that our stellar models at various metallicities include initial masses of 9, 20, 60, 85, and  $120\,M_{\odot}$ , we segment the continuous mass distribution into discrete bins centered around these specific masses. Our analysis is confined to massive stars, those with an initial mass  $M_{\rm ini}>9\,M_{\odot}$ , which contribute to the enrichment of the interstellar medium (ISM).

In total, we examine four distinct scenarios for each metallicity level. These scenarios include two methodologies for defining the mass threshold above which material is ejected from stars, and two different IMF parameters ( $\alpha$ ). We refer to these scenarios as 'Salpeter above remnant', 'Salpeter above CO core', 'Top-heavy above remnant', and 'Top-heavy above CO core'.

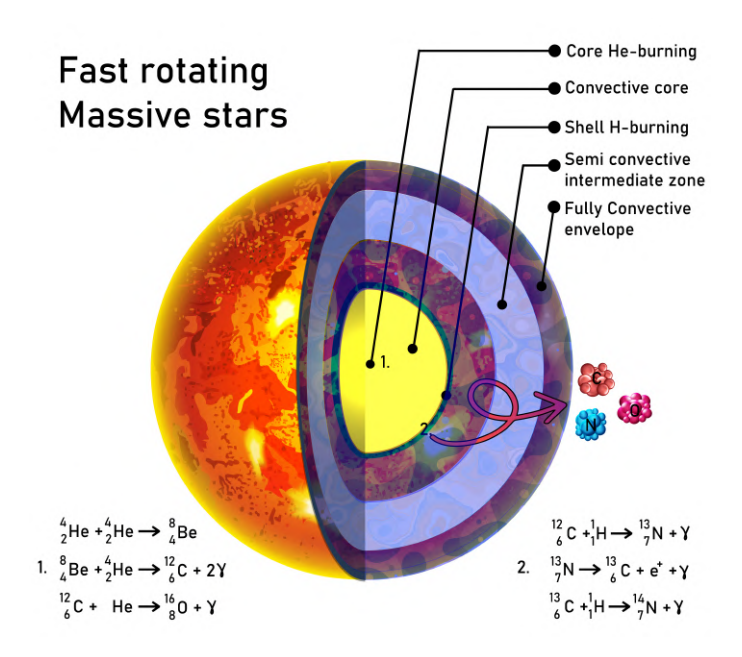


Figure 5.1: Illustration which depicting the interior and the transport of chemical species in fast rotating massive stars during core He-burning phase.

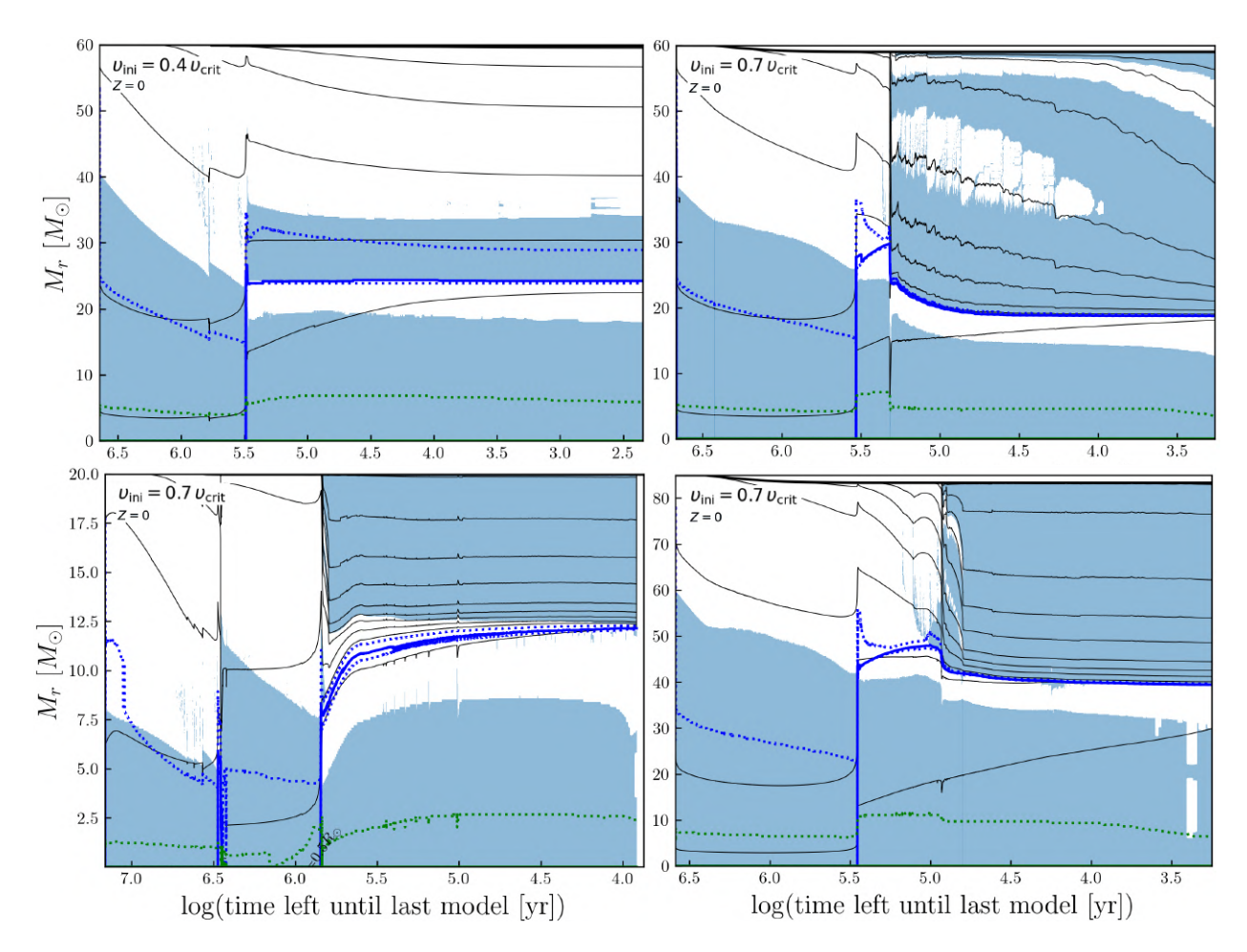


Figure 5.2: Kippenhahn diagrams displaying the structural evolution in lagrangian coordinates. Pop III models are presented with  $20~M_{\odot}$ ,  $60~M_{\odot}$  and  $85~M_{\odot}$ , and with an initial rotation of 40% and 70% of the critical one. The last evolutionary stage for all the models is the end of core Heburning phase. The blue regions are convective areas, while the white ones are the radiative areas. The black lines are the iso-radius lines. The blue and green lines corresponds to the core H- and He-burning phase, respectively. The solid lines indicate the peak of the energy generation rate and the dashed ones signify the 10% of the energy generation rate for each burning phase.

#### 5.3 Results

#### 5.3.1 Mechanism of Transport of Chemical Species

In massive stars, nuclear reactions generate energy through complex chemical networks, which vary based on the star's metallicity. For Population III (PopIII) stars in their main sequence, the predominant energy generation in the core is through the proton-proton (pp) chain, complemented by a portion of energy from the CNO cycle. Although the CNO cycle produces some nitrogen, this production is not sufficient to account for the total nitrogen yield observed in these stars. In stars with higher metallicity, the presence of elements like carbon, nitrogen, and oxygen during the main sequence enhances nitrogen production in the core. However for the PopIII stars, this amount is still significantly lower than the total nitrogen output observed at the end of the star's evolutionary path. At other metallicities (for instance at solar), nitrogen is also produced by the transformation of the initial C and O into N by the CNO cycle.

A critical factor impacting the nitrogen transport to the stellar surface is the structural composition of massive stars during their main sequence phase. Regardless of their initial metallicity, these stars typically exhibit a convective core surrounded by a radiative envelope. While efficient mixing within the core may transport a limited amount of nitrogen to the edge of the convective core, further transport to the stellar surface is constrained. The vertical mixing coefficient in the radiative envelope is not sufficient to enable this transportation, thereby limiting the outward movement of nitrogen.

#### 5.3.2 Post-Main Sequence Evolution and Chemical Transport

Rotating massive star models undergo a drastic change in their structure after the end of the core hydrogen burning phase. Figure 5.2 shows Kippenhahn diagrams of the  $60\,M_\odot$  Pop III models with moderate ( $v_{\rm ini}/v_{\rm crit}=0.4$ ) and fast ( $v_{\rm ini}/v_{\rm crit}=0.7$ ) rotation. Both models transition from a fully convective core and a radiative envelope to a more complex structure. As core helium burning commences, the fast-rotating model at  $60\,M_\odot$  at zero metallicity.(bottom panel of Fig. 5.2) has a convective core that extends towards the H-burning shell. The  $^{12}$ C produced via the triple- $\alpha$  reaction (denoted by 2 in Fig. 5.1) is fed into the H-burning shell. This  $^{12}$ C in the H-burning shell subsequently produces  $^{14}$ N through the CNO cycle. Its injection into the H-burning shell also boosts the energy production of the region, and leads to the formation of an extended intermediate convective zone. The size of this convective zone depends on the rotation of the star as shown in Fig. 5.2: the moderately-rotating model has a smaller intermediate zone when compared to the fast-rotating model of the same mass. The consequence of the extended convective zone is the abil-

ity to transport the freshly produced  $^{14}$ N (denoted by 2 in Fig. 5.1) to the surface and this is most efficient in the case of the fast-rotating  $60\,M_\odot$  model. In this study, the  $v_{\rm ini}/v_{\rm crit}=0.7$  model produces the strongest enrichment of  $^{14}$ N. Additionally, the same extended intermediate convective zones are also responsible for transporting  $^{16}$ O to the surface during the core He-burning phase. Finally, as the energy production in the H-burning shell is boosted, the helium-rich core recedes and an intermediate radiative zone is formed between the He-burning core and H-burning shell. A detailed discussion on this transport mechanism is beyond the scope of this thesis and will be described in more detail in Tsiatsiou et al (in prep.). It must be noted that although the mechanism to transport Nitrogen and other elements from the H-burning shell to the surface via convective zones is present in such models, it is not the reason for their ability to enrich the ISM. Since such stars are expected to lose mass either above the CO core or above the remnant, the only process that is required to produce strong N enrichment of ISM is the transport of carbon from the core to the H-burning shell. If a model is able to accomplish this, it will be able to enrich the ISM with N and other elements.

#### 5.3.3 Ejected Material Composition from Individual Stars

This section examines the ejected material composition as a function of stellar mass and metallicity. Table 5.2 presents this information, where we initially consider the material ejected by each star before its interaction with the interstellar medium (ISM). The table's first column lists five metallicities, and the second column indicates the initial mass of the stellar models. The third column shows the initial surface velocities in  $\text{km s}^{-1}$ . The fourth column details the final evolutionary stage reached by each model, while the fifth column indicates the model's final mass at this stage. Column six defines the mass of the carbon-oxygen (CO) core, identified where the helium mass fraction ( $Y_c$ ) drops below  $10^{-3}$ . Columns seven and eight, following the approach described in Sect. 5.2.1, display the type and mass of the stellar remnant, respectively. Column nine quantifies the total mass of elements ejected via stellar winds. Columns ten to sixteen detail the mass lost of individual elements due to these winds. Column seventeen calculates the total mass lost at the end of the star's life by subtracting the remnant mass (column eight) from the final total mass (column five). Finally, columns eighteen to twenty-four show the mass lost of each element due to a supernova at the end of the star's evolution.

Observing the final masses of the models (column five), a clear relationship between mass and metallicity emerges. For instance, at solar metallicity, a 9  $M_{\odot}$  model loses only about 0.65  $M_{\odot}$  up to the core carbon burning stage, while a 120  $M_{\odot}$  model sheds approximately 101  $M_{\odot}$ . This discrepancy is attributed to the model's greater luminosity enhancing radiation pressure, which

contributes to stronger stellar winds. Metallicity also significantly influences the final mass. Comparing  $60~M_{\odot}$  models at solar and  $10^{-5}$  metallicity, the solar metallicity model's final mass (17.98  $M_{\odot}$ ) is much lower than its  $10^{-5}$  metallicity counterpart (56.39  $M_{\odot}$ ), underscoring the impact of metals on stellar opacity and mass loss.

The total mass loss due to stellar winds (column nine) varies with both mass and metallicity. A  $60~M_{\odot}$  PopIII star loses less than 1% of its mass, while its solar metallicity counterpart loses about 70% due to winds. Comparing wind-driven mass losses of 9 and 120  $M_{\odot}$  models at  $10^{-5}$  metallicity, the 9  $M_{\odot}$  model sheds only 0.04% of its total mass, while the 120  $M_{\odot}$  model loses around 3%, indicating a weaker correlation of mass loss with stellar mass compared to metallicity. Notably, for higher mass models (85 and 120  $M_{\odot}$ ), no remnant forms (as indicated by pair-instability supernovae in column seven), leading to the assumption that the entire mass is ejected into the ISM.

	$M_{ m ini}$	Vini	Last stage	$M_{ m fin}$	$M_{\rm CO}$	Remnant	nt				Wind ejecta	ecta							Final eve	ent ejecta			
Z	7	1-m o-1		17		-	1,7	Total	H	$^4\mathrm{He}$	12C	T3C	$^{14}N$	091	$^{20}\mathrm{Ne}$	Total	Ħ	$^{4}\mathrm{He}$	$^{12}C$ $^{13}C$	T <sub>3</sub> C	$^{14}N$	160	$^{20}\mathrm{Ne}$
	⊙ <i>I</i> M	KIII.S				1,	_				Ψ.								W				
	6	649	end He-b	9.00	1.39	MD	∞	4	.,	[ ´			.04e-12	1.59e-14	2.36e-20	7.61						.,	.65e-05
	20	835	end He-b	19.97	89.8		∞		٠,		~	•	.95e-12	8.22e-14	3.98e-19	7.29		4				•	.71e-06
0 (PopIII)	09	1080	end He-b	29.00	14.44	BH	4			-	. 4		.80e-10	2.81e-12	1.21e-17	40.56							.43e-05
$v_{\rm ini}/v_{\rm crit} = 70\%$	82	1150	end He-b	83.33	33.07	BH	37.07			• •		_	.35e-10	9.56e-12	3.70e-17	46.26						~	.04e-04
	120	1230	$x(^{4}\text{He})_c = 0.20$	117.60	61.65	PISN	_			-			.17e-09	1.71e-11	6.03e-17	117.60						•	.60e-03
	6	372	$x(^{12}C)_c = 0.32$	8.99	0.00	MD	2	_	_		_		.36e-36	2.68e-38	1.07e-46	8.10						.,	.86e-05
	20	471	$x(^{12}C)_c = 0.16$	20.00	3.98		1		(,)				.13e-34	1.96e-36	1.07e-41	18.21							.06e-03
0 (PopIII)	09	613	$x(^4\text{He})_c = 2.35 \times 10^{-3}$	59.70	19.37	BH	_						.08e-11	8.04e-13	3.77e-18	36.33		(1					.86e-13
$v_{\rm ini}/v_{\rm crit} = 40\%$	82	629	$x(^4\text{He})_c = 0.03$	83.98	30.46	BH	_			•			.75e-11	1.37e-12	6.17e-18	49.52		_					.15e-09
	120	208	$x(^{4}\text{He})_c = 0.09$	116.44		PPISN	30.55			-/			.39e-10	1.25e-11	5.04e-17	85.89	22.93						0.03
	6	300	$x(^{12}C)_c = 0.02$	8.76	1.12						1	-/	.88e-07	7.49e-06	7.43e-08	7.64							80.0
	20	351	end C-b	19.98	2.98		~				w		.63e-08	1.49e-08	2.53e-09	13.00							.23e-05
$10^{-5}$ (EMP)	09	447	end C-b	56.39	13.42	BH	7				(,)		0.02	6.80e-03	1.92e-06	38.97							.61e-04
$v_{\rm ini}/v_{\rm crit} = 40\%$	82	483	end C-b	55.42	37.36		9					• •	.82e-04	6.24e-05	8.75e-06	14.06						•	.13e-04
	120	522	end C-b	84.56	59.44	_	_			-	~		.74e-04	7.03e-05	9.89e-06	84.56							4.73
	6	270	$x(^{12}C)_c = 4.12 \times 10^{-3}$		1.15					ļ.,	.,	-′	.45e-06	4.70e-06	2.24e-06	7.63							0.03
	20	326	end C-b		4.84		_			. ,	~		.68e-05	5.44e-05	2.62e-05	10.14		ш,			~	4	.96e-04
$4 \times 10^{-4} \text{ (I Zw 18)}$	09	398	end C-b		22.93		3				. 4		.27e-03	9.13e-04	4.19e-04	22.88						•	.51e-04
$v_{\rm ini}/v_{\rm crit} = 40\%$	82	430	$x(^{12}C)_c = 0.08$	57.83	40.05		0			-/	4	•	42e-03	1.46e-03	7.57e-04	14.23						•	.17e-04
	120	498	$x(^{12}C)_c = 0.03$		61.26	PISN	0.00			-/	.,	•	:.68e-03	1.39e-03	7.03e-04	92.29							6.55
	6	255	$x(^{12}C)_c = 4.77 \times 10^{-3}$	8.74	1.14		L				,	"	:.36e-05	4.69e-05	2.05e-05	7.60							0.05
	20	306	end C-b	18.28	4.23		~						.02e-04	8.31e-04	3.54e-04	10.05		4			.,		.47e-03
0.002 (SMC)	09	407	end C-b	39.12	26.58	BH	∞						0.02	6.52e-03	4.89e-03	8.54		_					.67e-03
$v_{\rm ini}/v_{\rm crit} = 40\%$	82	408	end C-b	51.11	_	-	0				~		.71e-03	4.75e-03	2.51e-03	9.11							0.07
	120	438	end C-b	85.58	76.56	PISN	_			•			0.03	6.28e-03	7.04e-03	82.58							6.72
	6	243	$x(^{12}C)_c = 0.36$	8.57	1.00		_				•		17e-04	4.79e-04	2.05e-04	7.57						_	.25e-03
	20	300	end C-b	13.02	4.33	BH	~				. 4		0.01	0.01	5.32e-03	4.69		(1)			•		.58e-03
0.006 (LMC)	09	385	end C-b	32.78	28.19	BH	6				. 4		0.14	80.0	0.02	09.0						4	.19e-04
$v_{\rm ini}/v_{\rm crit} = 40\%$	82	392	end C-b	35.81	29.91	BH	_				4		0.10	0.73	0.03	1.90							.33e-03
	120	447	end C-b	52.44	45.07 I	bPISN 4	4				4,		0.11	1.37	0.02	9.70							0.11
	6	248	end C-b	8.35	1.18		_			Ĭ.,	.,		.73e-03	2.14e-03	9.03e-04	7.17	3.42						90.0
	20	274	end C-b	7.18	4.36						-		90:0	0.04	0.02	0	0						0
0.014 (Solar)	09	346	end C-b	17.98	13.96		17.96	42.02	10.90	27.40	2.61 8	3.96e-04	0.23	0.56	80.0	0.02	0		0.01		4	1.45e-03	.65e-05
$v_{\rm ini}/v_{\rm crit} = 40\%$	82	368	end C-b	26.39	21.44	BH	4						0.31	0.88	0.10	0.95	0						.63e-03
	120	390	end C-b	19.04	14.86		9				. 4		69.0	0.49	0.18	0.19	0	0.05			1.08e-20	.,	3.17e-04

Table 5.2: Properties of the stellar models, masses of various isotopes ejected by winds and by the final events at the end of stellar evolution.

#### **Hydrogen Production**

The total mass of hydrogen (<sup>1</sup>H) produced by the models across six different metallicities is listed in column 18 of Table 5.2 and represented as a mass fraction (in black) in Fig. 5.3. Across all models, <sup>1</sup>H consistently emerges as the second most abundant element in the ejecta, except for the 9 and 20  $M_{\odot}$  models where it predominates. This pattern is attributed to the significant mass loss in larger stars, enabling the ejection of matter from deeper layers enriched in heavier elements. In contrast, the 9  $M_{\odot}$  model, which undergoes minimal mass loss, retains a high hydrogen content upon mass ejection. Examining Fig. 5.3, we note that the mass fraction of hydrogen (depicted in black) is 0.35 for both the cases of ejecting mass above the remnant and above the CO core. A notable trend arises in the hydrogen content ejected by models through stellar winds, as shown in column 8 of Table 5.2. Hydrogen remains the dominant element in the ejecta across all models and metallicities, with the sole exception of the 9  $M_{\odot}$  model at  $0.6 \times 10^{-3}$  metallicity, where it ranks second. This prevalence of hydrogen in the ejecta is explained by the fact that wind-driven mass loss primarily occurs during the core helium and core hydrogen burning stages, which collectively constitute nearly the entire lifespan of these stars. Throughout these stages, the stellar envelope predominantly contains hydrogen, with helium concentrated in the core (during core helium burning) or not yet produced (during core hydrogen burning).

#### **Helium Production**

Helium ( $^4$ He) stands as the predominant element in the ejecta of all models across various metallicities for masses above 20  $M_{\odot}$ , as detailed in column 19 of Table 5.2 and illustrated in Fig. 5.3. The ejected helium content appears to vary with metallicity, particularly when comparing models with the same initial mass, such as the 60  $M_{\odot}$  models. The solar metallicity model, for instance, retains only  $5 \times 10^{-3} M_{\odot}$  of  $^4$ He at the end of its evolution, whereas the zero-metallicity counterpart expels about 23  $M_{\odot}$ . This trend mirrors that of hydrogen (discussed in Section 5.3.3), where higher metallicity models tend to eject more helium during their evolution due to enhanced stellar winds, resulting in reduced helium mass at the end of their lifecycle.

#### **Carbon Production**

As previously discussed in Section 8.4.1,  $^{12}$ C is predominantly synthesized during the core helium-burning stage of a star's life. The total mass of  $^{12}$ C ejected by various models is tabulated in column 20 of Table 5.2, and its mass fraction across different models is depicted in red in Fig. 5.3. At  $10^{-5}$  metallicity, all models expel a similar percentage of  $^{12}$ C relative to their total mass in the

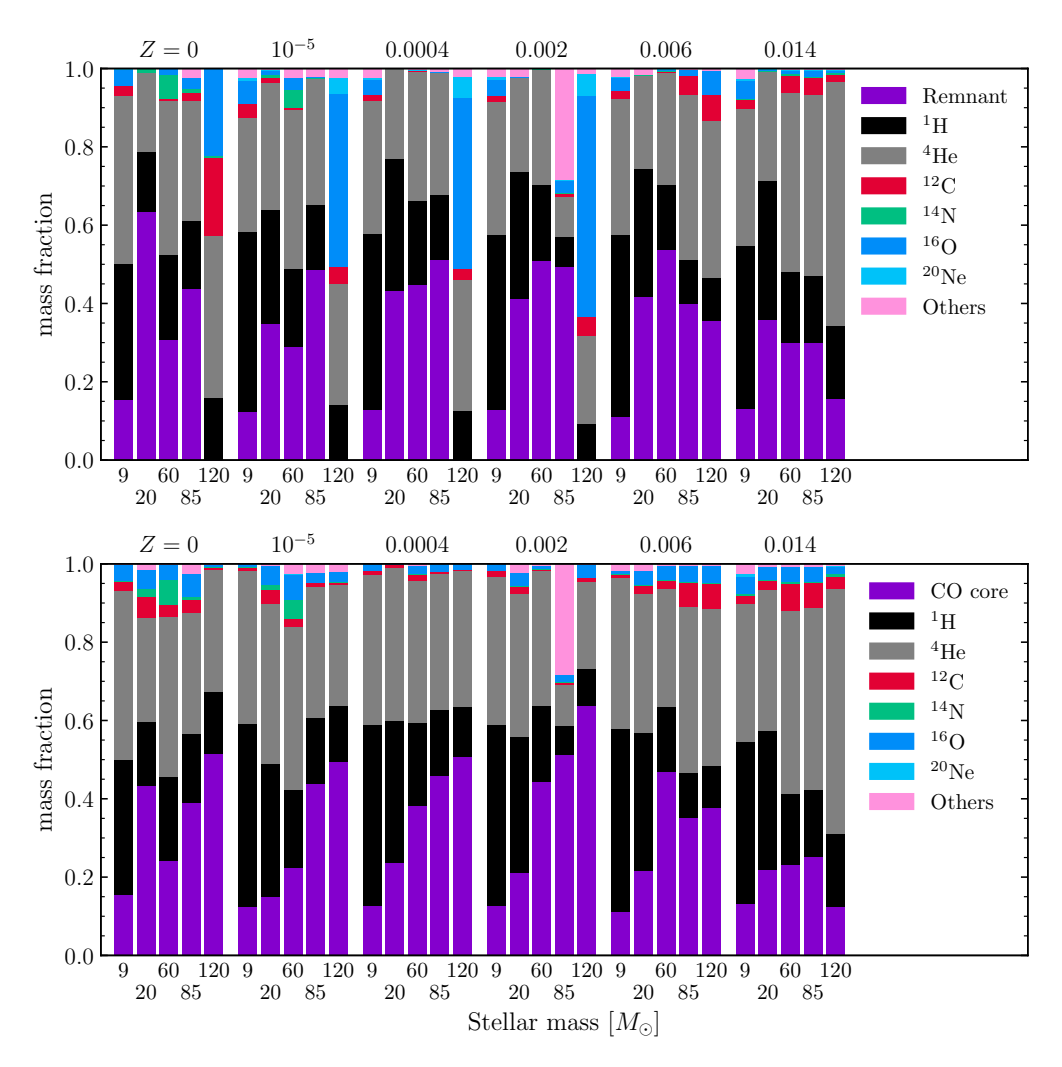


Figure 5.3: Integrated abundances at the last computed model for all models of all metallicities. *Top panel:* The integrated abundances above the remnant mass. *Bottom panel:* the integrated abundances above the CO core mass. Keep only popIII, EMP and solar

final ejecta. This consistent  $^{12}$ C ejection can be attributed to its production in the latter stages of evolution, limiting the time available for significant  $^{12}$ C mass loss via winds. With increasing metallicity, the higher mass models, specifically those at 60 and 85  $M_{\odot}$ , tend to eject a larger percentage (around 3.7%) of  $^{12}$ C compared to the 9 and 20  $M_{\odot}$  models (approximately 0.08%). The 120  $M_{\odot}$  models, especially at zero metallicity, stand out by expelling a substantially higher percentage of  $^{12}$ C (up to 40%) relative to other masses at their respective metallicities. This increased  $^{12}$ C ejection in the 120  $M_{\odot}$  models is primarily due to the occurrence of pair instability supernovae (PISN), which leave no remnant and result in the expulsion of the star's entire mass into the ISM.

#### **Nitrogen Production**

The aggregate mass of <sup>14</sup>N expelled through stellar winds and at the final evolutionary stages is detailed in columns 14 and 24 of Table 5.2, respectively. This data, represented in green in

Fig. 5.3, shows the mass fraction of  $^{14}$ N. For zero metallicity stars, the predominant source of  $^{14}$ N is the  $60 M_{\odot}$  model, attributed mainly to its nearly fully convective structure, a byproduct of rapid rotation as depicted in Fig. 5.2. This indicates that fast-rotating Population III stars are significant producers of  $^{14}$ N. In contrast, models with higher metallicities, such as those at solar metallicity, do not generate  $^{14}$ N through the same process as Pop III and very metal rotating stars. At solar metallicity for instance there is no mixing between the He- and H-burning regions thus there is no nitrogen production coming from the transformation of the carbon and oxygen produced by the star. There is only production of nitrogen (in massive stars) in those zones transformed by CNO burning, due to the transformation of the initially abundances of Carbon and Oxygen into Nitrogen

#### **Oxygen Ejection**

Oxygen, primarily  $^{16}$ O, emerges in later stages of a star's life cycle. The mass of  $^{16}$ O lost due to stellar winds and at the culmination of the evolutionary process is presented in columns 15 and 25 of Table 5.2. Figure 5.3 illustrates the mass fraction of ejected  $^{16}$ O in blue.  $^{16}$ O ranks as the third most abundant element in the ejecta across various masses and metallicities. Interestingly, the data reveals that lower mass stars are more efficient in producing  $^{16}$ O, implying their crucial role in its synthesis. Notably, for the 120  $M_{\odot}$  models at zero,  $10^{-5}$ ,  $4 \times 10^{-4}$ , 0.002, and 0.006 metallicities,  $^{16}$ O dominates the ejecta, while at solar metallicity, it is the second most prevalent element.

#### 5.3.4 Abundance Ratios in Stellar Population Ejecta After Dilution

#### [N/O] and [C/O] Ratios

Figure 5.4 presents the  $\log [{\rm N/O}]$  and  $\log [{\rm C/O}]$  abundance ratios plotted against  $\log [{\rm O/H}] + 12$  in the ISM. These ratios are shown for varying dilution factors f (indicated by different markers on the plots) across four scenarios outlined in Sect. 5.2.1. The scenarios include different IMFs (dashed or solid lines) and mass-cuts (separated by columns), and are evaluated for three metallicities: Z=0 (Population III, cyan),  $Z=10^{-5}$  (EMP, green), and Z=0.014 (solar, grey). Observational data from various galaxies, sourced from Marques-Chaves et al. (2023), are also included for comparison. For simplicity, results for the other three metallicities ( $Z=4\times 10^{-4}$ , Z=0.002, and Z=0.006) are not displayed as they do not align with any observed data. While enrichment by WR stars at solar metallicity (Z=0.014) has been hypothesized as an explanation for observed abundance ratios, our results at this metallicity do not support this theory. Irrespective of the scenario or dilution factor, the  $[{\rm N/O}]$  values are consistently too low ( $\log [{\rm N/O}] \sim -1$  to -0.6) and

the [O/H] values too high ( $\log [O/H] + 12 > 8.7$ ) to match the observations.

The most accurate matches to the observed [N/O] ratios in CEERS-1019 and GN-z11 are found within our populations of fast-rotating Population III stars. The 'Top-heavy above remnant' scenario, in particular, replicates the  $\log$  [N/O] of CEERS-1019 ( $\log$  [N/O]  $\sim$  -0.11), while the 'Salpeter above remnant' scenario aligns with that of GN-z11 ( $\log$  [N/O]  $\sim$  -0.36). The two 'above CO core' scenarios, although not as precise, still provide reasonably close matches ( $\log$  [N/O]  $\sim$  -0.19 and 0.42 for Top-heavy and Salpeter IMFs respectively). However, the [C/O] ratios for the Population III populations are higher than observed values ( $\log$  [C/O]  $\sim$  -0.1 to 0).

In contrast, the  $Z=10^{-5}$  populations predict slightly lower [N/O] ratios, particularly for the Salpeter IMF ( $\log [{\rm N/O}] \sim -0.7$  to -0.5), except in the 'Top-heavy above CO core' scenario ( $\log [{\rm N/O}] \sim -0.38$ ). These models at  $Z=10^{-5}$  align better with observed [N/O] values in galaxies like the Lynx arc (z=3.357, Fosbury et al. 2003) and SMACS2031 (z=3.5, Patrício et al. 2016). However, they predict larger [C/O] ratios ( $\log [{\rm C/O}] \sim -0.42$  to -0.03), though more in line with observations than the Population III models.

The choice of IMF significantly influences the predicted [N/O] ratios at both Z=0 and  $Z=10^{-5}$ . The top-heavy scenarios suggest higher [N/O] values, by  $0.23-0.25\,\mathrm{dex}$  (Population III) and  $0.15-0.2\,\mathrm{dex}$  (EMP), than the Salpeter ones. This aligns with the fact that more massive stars are primary nitrogen producers. Interestingly, the top-heavy scenarios yield smaller [C/O] ratios for the  $Z=10^{-5}$  populations ( $0.28-0.08\,\mathrm{dex}$ ) but larger ratios for the Z=0 ones ( $0.01-0.07\,\mathrm{dex}$ ) compared to the Salpeter scenarios. The lower [C/O] ratios at  $Z=10^{-5}$  can be attributed to carbon being more abundantly produced than oxygen in less massive stars. However, the higher [C/O] ratios at Z=0 are somewhat unexpected and may be due to incomplete model computations, especially for the  $120\,M_\odot$  model which has not completed its core helium burning phase.

The effect of selecting the mass-cut above which material is ejected at the end of a star's life is nuanced, though generally minor. When ejecting above the future remnant's mass, the mass-cut coordinate is larger than the CO core's for the 20, 60, and  $85\,M_{\odot}$  models by about  $4\,M_{\odot}$  (refer to Sect. 5.2.1), identical for the  $9\,M_{\odot}$  models (which become white dwarfs), and considerably smaller for the  $120\,M_{\odot}$  models (ending in a PISN with  $M_{\rm rem}=0$ ). Generally, ejecting above the CO core increases the [N/O] ratio (by  $0.09-0.12\,{\rm dex}$ ) in EMP populations and decreases it (by  $0.06-0.08\,{\rm dex}$ ) in Pop III populations. It also elevates the [C/O] ratios in both metallicities ( $0.07-0.13\,{\rm dex}$ ) for  $Z=0,0.07-0.26\,{\rm dex}$  for  $Z=10^{-5}$ ).

The dilution factor's influence is most straightforward in Pop III stellar populations. Since their initial and the unenriched ISM's compositions include only  ${}^{1}H$  and  ${}^{4}He$ , dilution does not modify the [N/O] and [C/O] ratios. This explains why the Pop III curves in Fig. 5.4 are horizontal

lines that shift from right to left with increasing f. For EMP populations, with their initial  $^{16}$ O abundance surpassing  $^{12}$ C and  $^{14}$ N, their curves trend downwards with larger dilution factors.

We treat the dilution factor f as a variable parameter, but aligning our results with observed  $\log {\rm [O/H]} + 12$  values can constrain its range. Applying the fiducial interval of  $7.62 < \log {\rm [O/H]} + 12 < 8$  from Cameron et al. (2023) as a constraint, we find f generally falls between 29 and 141. Specific ranges vary, from 29 < f < 70 ('Salpeter above CO core' at  $Z = 10^{-5}$ ) to 59 < f < 141 ('Top-heavy above remnant' at  $Z = 10^{-5}$ ). Using Cameron et al. (2023)'s fiducial value of  $\log {\rm [O/H]} + 12 = 7.82$ , for the eight populations (four scenarios across two metallicities), we ascertain a dilution factor range of 44 < f < 89.

#### Predictions of other ratios

In this segment, we propose predictions for abundance ratios that could be observable in high-redshift galaxies. Although our models of fast-rotating Pop III and EMP populations align with observed [N/O] and [C/O] number ratios, forthcoming observations could either corroborate or challenge our predictions regarding other isotopes, thereby affirming or refuting our proposed enrichment process. We have calculated  $\log$  [He/H],  $\log$  [ $^{12}$ C/ $^{13}$ C], and  $\log$  [O/Ne] for each of the eight populations, presenting their values at the optimal dilution factor.

We observe that the [He/H] ratios are consistently close across all eight model configurations, with values spanning from  $\log$  [He/H] = -1.069 (for the 'Salpeter above remnant' scenario at Z=0) to  $\log$  [He/H] = -1.076 (for both 'above remnant' scenarios at  $Z=10^{-5}$ ). These ratios translate to He:H ratios in the range of 1:11.7 to 1:11.9, similar to the primordial ratio of 1:12. This similarity in ratios suggests that distinguishing between these scenarios using this ratio might be challenging. Nevertheless, at solar metallicity, our models yield a  $\log$  [He/H]  $\sim -1.03$ , equating to a He:H ratio of about 1:10.7; this is not a significant difference and but nevertheless could be important if becomes possible to distinguish this difference by observations. Therefore, observations should may differentiate between the predicted ratios at zero to extremely low metallicity and those at solar metallicity.

**Ratios of**  $^{12}$ **C**/ $^{13}$ **C:** The ratios of  $[^{12}$ C/ $^{13}$ C] demonstrate more variability. We observe larger ratios for Pop III populations, for scenarios utilizing a Salpeter IMF, and for those ejecting matter above the remnant. For Pop III populations, the values range from  $\log [^{12}$ C/ $^{13}$ C]  $\sim 2.12 - 2.15$  ('Salpeter above CO' - 'Salpeter above remnant') to  $\log [^{12}$ C/ $^{13}$ C]  $\sim 1.69 - 1.81$  (Top-heavy, same sequence). For EMP populations, the ratios are  $\log [^{12}$ C/ $^{13}$ C]  $\sim 1.52 - 1.69$  (Salpeter) and  $\log [^{12}$ C/ $^{13}$ C]  $\sim 1.43 - 1.65$  (Top-heavy), providing enough distinction to differentiate between the Z = 0 and

 $Z = 10^{-5}$  models.

Ratios of Ne/O: The [Ne/O] ratios also show significant variation across scenarios and metallicity. These ratios are considerably higher for the  $Z=10^{-5}$  populations than for the Z=0 ones and are typically higher in top-heavy scenarios compared to Salpeter ones. We find no clear trend in correlation with the chosen mass-cut. For Pop III models, the obtained values are  $\log [{\rm Ne/O}] \sim -3.63$  to -4.02 ('Salpeter above CO' - 'Salpeter above remnant') and  $\log [{\rm Ne/O}] \sim -3.16$  to -3.71 (Top-heavy). In the case of EMP models, the values are  $\log [{\rm Ne/O}] \sim -1.90$  to -1.03 (Salpeter) and  $\log [{\rm Ne/O}] \sim -1.78$  to -1.18 (Top-heavy). These variations are distinct enough to separate Pop III and EMP populations. Combining observations of the  $[^{12}{\rm C}/^{13}{\rm C}]$  and  $[{\rm Ne/O}]$  ratios could further refine constraints on different scenarios.

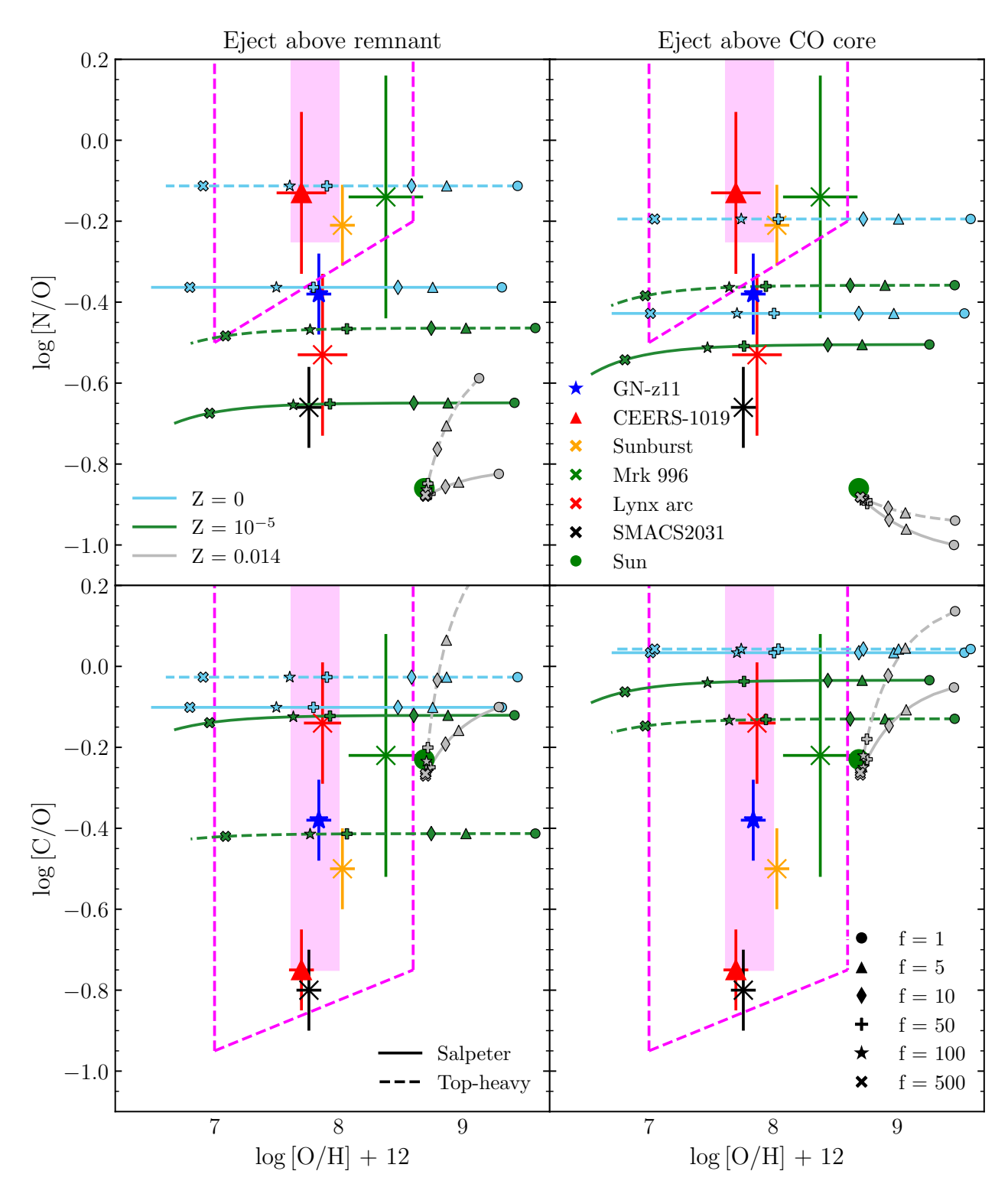


Figure 5.4: Abundance ratios in the diluted ISM with varying dilution factor f=1-1000. *Top row:* Plots for  $\log [{\rm N/O}]$  vs  $\log [{\rm O/H}]+12$ . *Bottom row:* Plots for  $\log [{\rm C/O}]$  vs  $\log [{\rm O/H}]+12$ . *Left column:* scenarios where the stars eject everything above the remnant mass, *right column:* scenarios where the stars eject everything above the CO core. In each panel, we show the results for three metallicities: Z=0 (Pop. III, cyan),  $Z=10^{-5}$  (EMP, green), and Z=0.014 (solar, grey). Solid lines represent populations sampled from a Salpeter IMF and dashed lines for a top-heavy IMF. The markers on these lines represent specific values for f=1-500. The other markers (as indicated on the *top right panel*), pink dashed lines and pink-shaded regions show results and lower bounds from observations, taken from Marques-Chaves et al. (2023).

#### 5.4 Discussion

#### 5.4.1 Standard versus Fast Rotating Main Sequence Stars

The Pop III models with fast  $(0.7 \, v/v_{\rm crit})$  and standard  $(0.4 \, v/v_{\rm crit})$  rotation rates are presented in the second and third rows of Table 5.2. When accounting for dilution effects and using a Salpeter IMF, the fast rotating models yield  $\log_{10}({\rm N/O})$ ,  $\log_{10}({\rm C/O})$ , and  $\log_{10}({\rm O/H}) + 12$  values of -0.37, -0.1, and 7.75 (at f = 100), respectively. In contrast, the standard rotating Pop III models produce significantly lower values of -2.93, -0.295, and 7.74, falling short of matching the observed data from GN-z11 and CEERS 1019 (see Fig. 5.4). This discrepancy is attributed to the lack of extensive convective zones in the envelopes of standard rotating models (illustrated in the left panel of Fig. 5.2), which restricts efficient chemical transport to the surface. Consequently, only the fast rotating Pop III models can replicate the observed chemical signatures in high-redshift galaxies such as GN-z11 and CEERS 1019.

#### 5.4.2 Ejection above Remnant versus CO Core

This study employs two methodologies to define the mass-cut for element ejection at the end of stellar life. The first approach is based on the findings from Patton & Sukhbold (2020) and Farmer et al. (2019), while the second assumes ejection of all matter above the CO core's mass coordinate. The latter, being overly simplistic, may not accurately reflect stellar processes. Similarly, the former approach is not without its uncertainties, particularly in predicting the type of stellar remnant (neutron star or black hole). This uncertainty significantly influences the mass-cut value, as illustrated by the example of a  $20\,M_\odot$  EMP star. Its fate, whether to implode into a black hole or explode leaving behind a neutron star, can lead to substantial differences in the mass and metallicity of ejected material. Similar considerations apply to higher mass models, where the distinction between a pair-instability supernova (PISN) and a pulsational pair-instability supernova (PPISN) can result in either ejecting or retaining about  $30\,M_\odot$  of material. Despite these uncertainties, our results, showcased in Fig. 5.4, demonstrate modest variations between different scenarios, underscoring the robustness of our findings. However, this caveat remains an important consideration in interpreting our results.

#### 5.5 Conclusion

This study represents a detailed exploration into the chemical compositions of high-redshift galaxies, with a primary focus on nitrogen-enhanced galaxies such as GN-z11 and CEERS-1019.

Employing the library of computed stellar models using Geneva stellar evolution code (GENEC), we meticulously modeled the stellar yields of massive stars, covering a range from 9 to  $120\,M_\odot$  across a spectrum of metallicities (models from works by Tsatsiou at al submitted, Sibony et al in prep and Nandal et al in prep). This extensive analysis has yielded significant insights into the processes of elemental synthesis in the early universe, providing a comprehensive understanding of the intricate dynamics at play.

• Fast Rotating Population III Stars Our investigation into the fast-rotating Population III stars has been one of the cornerstone achievements of this research. We discovered that these stars, particularly those rotating at  $0.7 \ v/v_{\rm crit}$ , are crucial in aligning with the observed abundance ratios in GN-z11 and CEERS-1019. The calculated values of  $\log_{10}(N/O) = -0.37$ ,  $\log_{10}(C/O) = -0.1$ , and  $\log_{10}(O/H) + 12 = 7.75$ , at a dilution factor of f = 100, are not only in close agreement with observational data but also highlight the crucial role of stellar rotation in the process of nitrogen enrichment in the early universe. This finding underscores the importance of rotational dynamics in influencing stellar nucleosynthesis and, consequently, the chemical evolution of galaxies in the early stages of the universe.

The fast-rotating models demonstrated a significantly enhanced capacity for the synthesis and transport of freshly synthesized <sup>14</sup>N to the stellar surface, a process intricately linked to the extended convective zones in these stars. An efficient mixing between the He-burning core and the H-shell is a keyfactor in the increased nitrogen abundance observed in these early galaxies. Our results suggest that the rotational speed of stars plays a pivotal role in determining their nucleosynthetic yield, particularly in the context of nitrogen, a critical element in understanding the chemical evolution of the universe.

• Contrasting metallicities Another significant aspect of our study is the contrasting chemical profiles exhibited by stars of different metallicities. While the Population III models showed strong alignment with the observed abundance ratios in high-redshift galaxies, models with metallicities  $Z=10^{-5}$ n could also reproduce the ratios whereas models at Z=0.014 failed to replicate these observations. This contrast is not only indicative of the unique nature of Population III stars but also highlights the complex relationship between stellar metallicity, mass, and nucleosynthetic output. The inability of higher metallicity models to match the observed ratios in GN-z11 and CEERS-1019 points to the distinct processes governing chemical enrichment in the earliest generations of stars.

This finding has far-reaching implications for our understanding of galactic evolution, particularly in the context of the formation and development of the first galaxies. It suggests

richment of the universe.

that the earliest stellar generations had a unique chemical signature, which could be crucial in tracing the evolution of galaxies and understanding the conditions prevalent in the early universe.

• Abundance predictions and setllar mass impact Our study extends beyond the conventional scope of elemental analysis by predicting abundance ratios such as [He/H], [Ne/O], and [ $^{12}$ C/ $^{13}$ C]. These predictions, covering a range of log [He/H] from -1.069 to -1.076, and log [ $^{12}$ C/ $^{13}$ C] between 1.43 and 2.15, are poised to serve as benchmarks for future observational studies. The significant variations in these ratios across different scenarios and metallicities provide crucial insights into the diverse nucleosynthetic processes in early galaxies. Furthermore, our models highlight the impact of stellar mass on the production of key elements. Lower mass stars, particularly those at 9  $M_{\odot}$  and 20  $M_{\odot}$ , predominantly produce  $^{16}$ O, a critical element in the formation of water and life-essential molecules. In contrast, higher mass stars, especially those undergoing pair-instability supernovae, play a vital role in synthesizing significant amounts of  $^{14}$ N and  $^{12}$ C. These elements are fundamental to the

development of organic compounds and life as we know it. The variation in elemental pro-

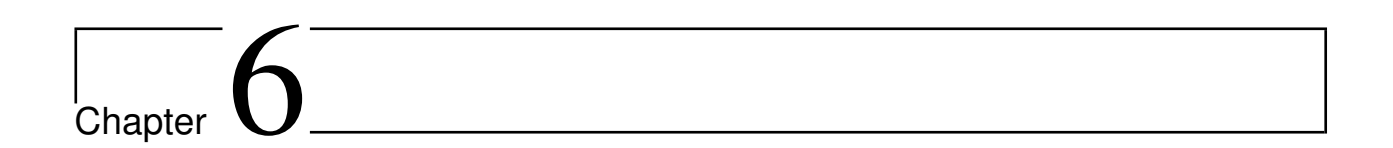
duction across different stellar masses underlines the complex interplay between mass and

nucleosynthetic processes, highlighting the diverse contributions of stars to the chemical en-

- Chemical transport mechanism The mechanisms of chemical species transport observed in our rotating massive star models have provided valuable insights into the structural changes these stars undergo post the core hydrogen burning phase. The transition from a fully convective core and a radiative envelope to a more complex structure has profound implications for the distribution and abundance of key elements. As core helium burning commences, the injection of <sup>12</sup>C into the hydrogen-burning shell, particularly in fast-rotating models, results in the production of <sup>14</sup>N and leads to the formation of extended convective zones. These zones play a crucial role in transporting freshly produced <sup>14</sup>N to the surface, thus contributing to the nitrogen enrichment observed in high-redshift galaxies.
- Role of Mass cut This research also sheds light on the role of different mass-cuts in determining the ejection of elements at the end of a star's life. The distinction between ejecting material above the remnant mass and above the CO core has significant implications for the resulting chemical composition of the ejecta. Our study reveals that ejecting above the CO core generally results in higher [N/O] ratios, particularly for the EMP populations, indicating the sensitivity of nucleosynthetic yields to the chosen mass-cut criteria.

Looking ahead, future research avenues could include exploring models incorporating the impact of internal magnetic fields on stellar evolution and nucleosynthesis. Additionally, integrating the yields from our stellar models into galactic chemical evolution models would offer a more comprehensive picture of galactic formation and evolution in the early universe. Such studies could significantly enhance our understanding of the intricate processes shaping the cosmos and provide new insights into the early stages of galaxy formation.

The role of massive stars, particularly those with fast rotation rates, is pivotal in shaping the chemical characteristics of early galaxies. The insights gained from this study not only corroborate existing theories but also pave the way for new explorations in the field, offering a deeper understanding of the processes governing early galactic environments.



# Extremely Massive stars: Formation and evolution

This work is adapted from the work by Nandal et al. (2023a). Stellar evolution studies have detailed our understanding of massive stars, particularly regarding the effects of rotation from the Zero Age Main Sequence (ZAMS). These investigations typically focus on stars up to approximately  $60\,\mathrm{M}_\odot$ . However, a crucial gap exists in our knowledge beyond this mass range, specifically for stars around  $3000\,\mathrm{M}_\odot$  and greater, classified as extremely massive Pop III stars (EMS). Their end-of-life events, either through supernovae or direct collapses to black holes, were responsible for introducing the first metals into the universe. This initial metal enrichment set the stage for subsequent stellar and galactic formations.

Our current stellar models lack a pre-Main Sequence (preMS) phase, which represents an important stage in the formation of stars. Integrating the preMS phase is essential for Pop III stars, given their unique formation conditions driven by high accretion rates. The zero metal content in Pop III stars requires adjustments in stellar opacity calculations, affecting radiative transport and internal stellar structures. Moreover, the limited metals alter nuclear reactions, impacting the overall lifetimes and evolutionary endpoints of these stars. While rotation is a key factor in the evolution of massive stars, its role in Pop III stars may vary due to their different internal dynamics and potential interactions with early cosmic magnetic fields. This chapter describes the formation and evolution of EMS section 6.3 and their impact is provided in section 6.4. Varying metallicity of such stars lead to varying final masses and chemical enrichment; this is stated in section 6.5. Finally, the conclusions are summed up in section 6.6.

#### 6.1 Literature review

The study of Pop III stars, particularly those with masses surpassing  $1000~M_{\odot}$ , is integral to understanding the early stages of our Universe. These stars, distinct due to their unique formation conditions, offer insights into elemental production and large-scale structural developments during the Universe's formative periods. Through supernova explosions, Pop III stars are posited to have been essential in the generation of heavy elements (Nomoto et al. 2006). Further, there is a hypothesis suggesting that accreting stars with zero or low metallicity might experience core collapse. Such processes could potentially lead to the formation of intermediate-mass black holes, acting as precursor structures for the genesis of supermassive black holes (Ohkubo et al. 2009). Additionally, recent astronomical observations, such as those associated with the high-redshift galaxy GN-z11, have reported strong nitrogen enrichment (Bunker et al. 2023; Cameron et al. 2023; Charbonnel et al. 2023). The presence and evolution of Pop III stars might offer an explanation for these phenomena. This work aims to construct and analyze evolutionary models of these accreting Pop III stars, specifically focusing on their influence on chemical, mechanical, and radiative feedback mechanisms operative in the Universe's early stages.

When modeling the formation and subsequent collapse of primordial molecular clouds, simulations have indicated the potential growth of Pop III stars to masses between 1000 and 10,000  $M_{\odot}$ (Larson 2000; Regan & Haehnelt 2009; Regan 2022). These figures change under different conditions. For instance, in the presence of atomically cooled hydrogen, the resultant star could have a mass exceeding 100,000 M<sub>☉</sub>. Such stars, due to their sheer size, are susceptible to collapse mechanisms driven by general relativistic instabilities (Hosokawa et al. 2013a; Haemmerlé et al. 2018). Given the variability in potential final masses, Pop III stars are theorized to have influenced the early Universe in a myriad of ways. A case in point: stars in the mass range of  $10^5$ - $10^6\ M_{\odot}$  could have been significant contributors to the early Universe's helium content (Hoyle & Tayler 1964). Additionally, these stars might have played a role in the <sup>26</sup>Al enrichment processes of the Milky Way (Hillebrandt et al. 1987c). Their evolutionary paths could also lead to the formation of supermassive black holes that we observe today, particularly at high redshifts like z>6 (Haemmerlé et al. 2020). In parallel research streams, Ohkubo et al. (2009) explored the possibility of accreting stars with low metallicity undergoing core collapse, subsequently leading to the birth of intermediatemass black holes. This complements the work by Ohkubo et al. (2009), who investigated Pop III star evolution up to 1000 M<sub>☉</sub> and concluded potential outcomes to include the formation of black holes ranging from 40 to 1000 M<sub>☉</sub>. Another relevant study by Ledoux et al. (1982) analyzed a  $3000 \text{ M}_{\odot}$  star's stability on the ZAMS. The results pointed towards a vibrational instability, likely triggered by the initiation of nuclear burning.

A widely accepted mechanism for the formation of such massive celestial entities is the cold disc accretion process, especially in primordial conditions. Here, accretion rates can average around  $10^{-3}M_{\odot}yr^{-1}$  but occasionally spike to values close to  $10^{-2}M_{\odot}yr^{-1}$  (Yoshida et al. 2006; Ohkubo et al. 2009; Hirano et al. 2014a; Hosokawa et al. 2016; Chiaki & Yoshida 2022). However, this process isn't without potential interruptions. As matter continues to accumulate, the accretion disc could become unstable, leading to fragmentation and potentially capping the final masses of Pop III stars (Susa 2019; Klessen & Glover 2023). Some researchers, like Chon & Omukai (2020a), argue that these fragmented protostars could eventually coalesce, resulting in a single, massive Pop III star with a mass close to  $10^5 M_{\odot}$ . Direct observations of these stellar giants remain challenging with current technology. Indirect methods, however, offer some promise. An example is the detection of specific UV emission lines, such as N III] and N IV], from GN-z11 by the JWST. This has sparked discussions and theories centered around the N/O abundance ratio in adjacent interstellar mediums (Bunker et al. 2023; Cameron et al. 2023). Among these theories, one proposes that the collision of massive stars with a SMS could give rise to a star with a mass nearing  $10^4 \text{ M}_{\odot}$  (Charbonnel et al. 2023). Another suggests that metal-enriched SMSs, with metallicity around  $0.1 \times Z_{\odot}$ , might achieve the necessary elemental abundances through their stellar winds and explosions (Nagele & Umeda 2023).

This work provides a deep dive into the evolution of Pop III stars, examining both variable and constant accretion rates until the cessation of core silicon burning. Initial results indicate that, during the core-He-burning phase, outer and intermediate convective zones emerge, enriching the stellar envelopes in helium and nitrogen. If these layers are expelled, it might result in substantial helium and nitrogen enrichment of the surrounding interstellar medium. The subsequent sections of this chapter will delineate our modeling approach, present a detailed analysis of Pop III stellar evolution under a constant accretion rate, and evaluate the impacts of these celestial behemoths on their surroundings. We'll also compare and contrast our findings with prior research and explore the potential links between our models and the chemical signature of GN-z11. The potential effects of altering metallicity in these stars will also be discussed before we conclude.

## 6.2 Detailed Examination of Our Accreting Star Models

#### 6.2.1 Core Physical Components

Our study is built upon the Geneva Stellar Evolution code (Eggenberger et al. 2008), a wellestablished computational framework for stellar modeling. This choice was motivated by its widespread use and acceptance within the astrophysical community and its robust set of features that facilitate intricate stellar modeling. We incorporated similar fundamental physical components as proposed by Ekström et al. (2012a). However, a critical distinction is our adoption of a primordial initial composition, a methodology inspired by Murphy et al. (2021b). Delving deeper into the mechanics of accretion, our model assumes that the inflow of matter arises through a geometrically thin cold disc. To define the state of the accreted material, we anchored our understanding to the principle that the specific entropy of the infalling matter mirrors that of the stellar surface (Haemmerlé 2014; Haemmerlé et al. 2016). In layman terms, this principle suggests that as matter is drawn towards the star, its inherent chaotic motion (or entropy) will resemble the outer layer of the star by the time it joins the star's body. This model operates under the implicit assumption that any excess entropy in the infalling matter dissipates and is emitted as radiation before its deposition on the stellar surface (Palla & Stahler 1992; Hosokawa et al. 2013a). This belief is rooted in the understanding of how matter behaves under gravitational influences and the associated energy exchanges. Current hydrodynamical models focusing on the formation of Pop III stars hint at accretion rates spanning a vast range, from as low as  $10^{-6} \,\mathrm{M_{\odot}/yr}$  to as high as  $10 \,\mathrm{M_{\odot}/yr}$  (O'Shea & Norman 2007; Yoshida et al. 2007; Hirano et al. 2014b; Hosokawa et al. 2016). For the purpose of this work, we elected to work with either a constant accretion rate of  $10^{-3}$  M<sub> $\odot$ </sub>/yr or variable accretion rates that are inspired by the hydrodynamical findings of Yoshida et al. (2007).

#### 6.2.2 Assumption of constant Accretion Rates

When one delves into studies that contemplate the modeling of accreting stars, especially those with immense masses surpassing  $10^3 M_{\odot}$ , a common assumption encountered is that of a constant accretion rate. This rate is perceived as a balanced interplay between matter continuously falling onto the star and various mechanisms causing mass loss (Hosokawa et al. 2013a; Woods et al. 2017; Haemmerlé et al. 2018). However, this assumption of constancy comes under scrutiny when one considers the results of hydrodynamic simulations associated with primordial star formation. Such simulations, rather than suggesting a constant inflow of material, depict a scenario where the accretion rate is in flux and varies with time (Chen et al. 2014; Sakurai et al. 2015; Wise et al. 2019; Regan 2022). The reasons for these variations are manifold, stemming from intricate dynamical interactions and feedback loops that preside over the star's growth trajectory.

In our endeavor to discern the implications of holding onto the constant accretion rate assumption on the final star structure, we embarked on a two-fold approach:

1. We constructed a model guided by the variable accretion rates as proposed by Yoshida et al. (2007), which are grounded in hydrodynamical simulations. 2. To furnish a point of comparison,

we simultaneously computed another model based on a fixed accretion rate, specifically  $2.62 \times 10^{-4} M_{\odot}/yr$ . This rate was meticulously chosen to ensure that the star reaches an identical final mass of 917  $M_{\odot}$ , mirroring the outcome of the model guided by the variable accretion rate.

A notable observation was that during the star's pre-main sequence, the variable accretion rate model exhibited a more aggressive accretion rate than its constant counterpart. This led to discernible differences in their respective journeys to the Zero Age Main Sequence (ZAMS). Specifically, the constant accretion rate model entered the ZAMS phase with a mass of  $34~{\rm M}_{\odot}$ , while the variable accretion rate model did so with a more substantial mass of  $120~{\rm M}_{\odot}$  (Fig. 6.1). Moreover, the lifespan of the constant accretion rate model during its main-sequence phase exceeded that of the variable rate model by 11%. Such variations could have significant implications for processes like ionising feedback.

However, as our study progressed deeper into the life cycles of these modeled stars, we observed a convergence in their behaviors. From the initiation of core hydrogen burning through to the culmination of core silicon burning, their evolutionary paths were strikingly alike. When we delved into parameters like radius and elemental abundance profiles, both models showcased extreme resemblances. This is crucial, as it indicates that despite differing accretion histories, the chemical and radiative outputs of these models are virtually indistinguishable. In light of these observations, one can surmise that while the initial journey might vary based on accretion histories, the final outcomes in terms of stellar structure don't display significant divergences. Thus, for the purposes of our subsequent discussions and analyses, we adopted the simpler assumption of a constant accretion rate.

#### 6.2.3 Implications and Forward-Look

The choice of accretion rate, be it constant or variable, is pivotal as it underpins the growth and development trajectory of massive stars. However, our research underscores that for stars of identical final masses, the accretion history doesn't notably alter the final stellar structure. This provides a simplification for subsequent studies and can serve as a guideline for those exploring similar domains. Yet, it's crucial to appreciate the nuance and the intricacies of these processes. While our models provide valuable insights, the universe is a complex entity, and a multitude of factors can influence stellar evolution. We thus encourage future researchers to continually challenge, validate, and build upon these findings to enhance our collective understanding of the cosmos.

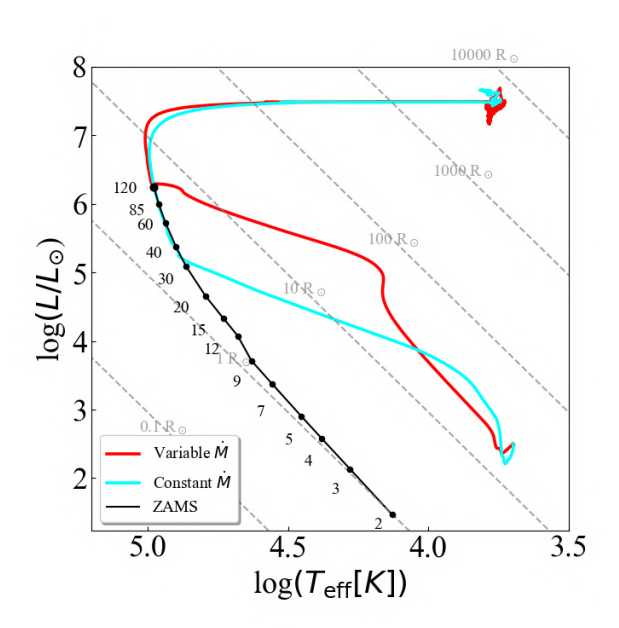
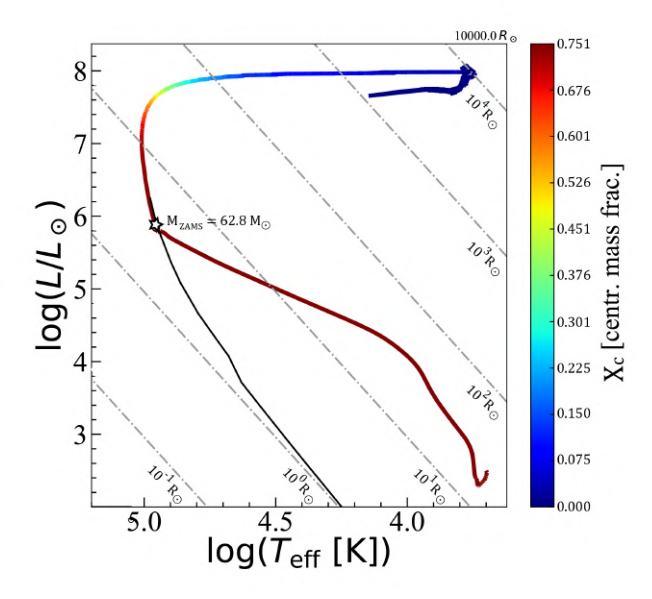


Figure 6.1: HR diagrams of two models with identical masses of 917  $\rm M_{\odot}$ , accreted until the end of core silicon burning. The red line depicts the model computed using the variable accretion rate from Yoshida et al. (2007), and the cyan line represents a model with a constant accretion rate of  $2.615x10^{-4}M_{\odot}/yr$ . The black line is the ZAMS line, and the dots indicate the masses in  $\rm M_{\odot}$ . The dotted grey lines are the iso-radius line, with values depicted in solar radii.



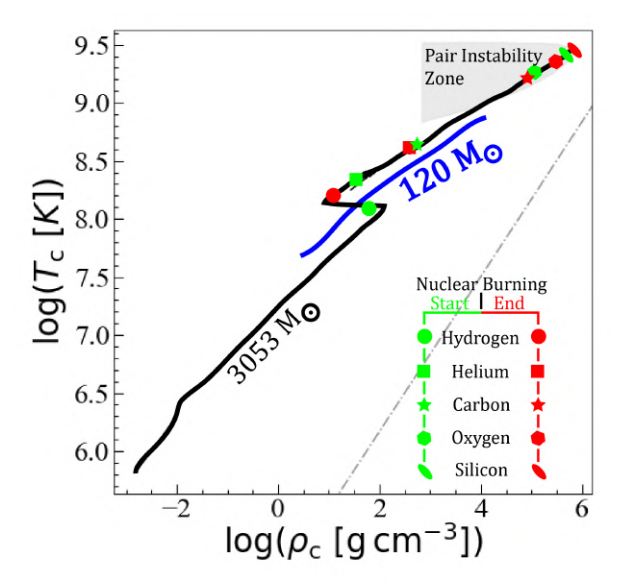


Figure 6.2: Evolution of a 3000  $M_{\odot}$  model at a constant accretion rate. Top panel: HR diagram depicting the evolution of a model until the end of core silicon burning with a constant accretion rate of  $10^{-3}M_{\odot}yr^{-1}$ . The black line represents the ZAMS line for Z=0 metallicity. The star symbol on the track represents the start of core hydrogen burning when the mass of the model is 62.8 . Bottom panel: Evolution of the central temperature versus the central density of the model. The blue line marks a 120 model at Z=0 metallicity, starting from ZAMS and ending at core helium burning.

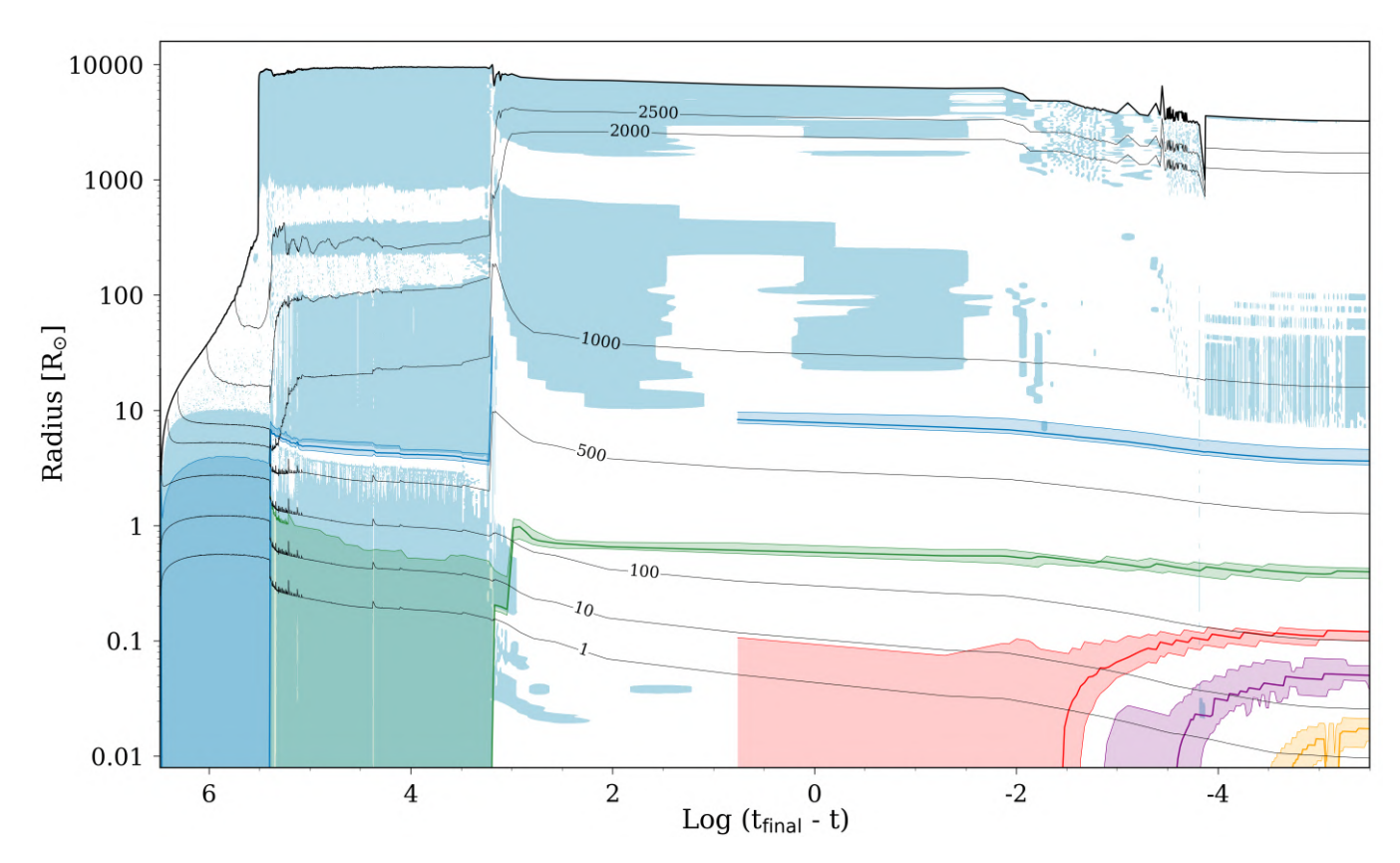


Figure 6.3: Internal evolution of the accreting model. The final mass is slightly above 3000 . The convective regions are shaded in light blue. Shaded darker blue, green, red, purple, and orange regions indicate regions of hydrogen, helium, carbon, oxygen, and silicon burning, respectively. Iso-contours of mass are indicated by black lines.

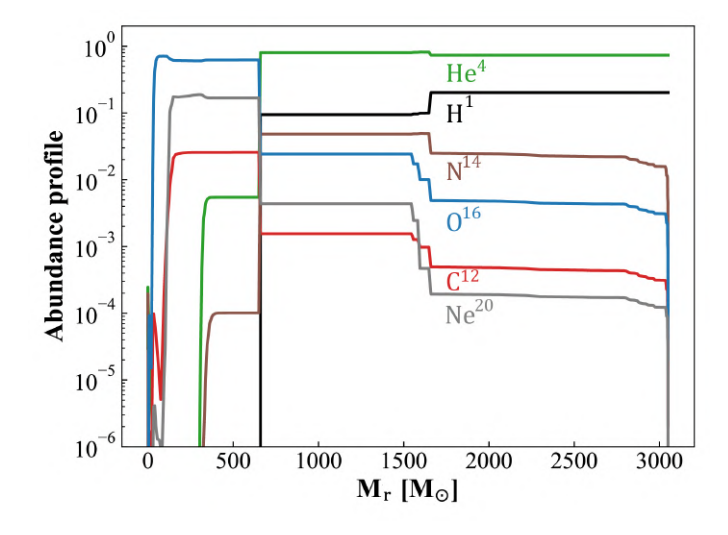


Figure 6.4: Abundance profile versus the mass coordinate of the zero-metallicity model with a constant accretion rate of  $1 \times 10^{-3} M_{\odot}/yr$  at the end of core silicon burning.

# 6.3 Evolution of Extremely Massive Accreting Pop III Stars

This section discusses the evolutionary trajectory of a zero-metallicity star undergoing a constant accretion at a rate of  $10^{-3}M_{\odot}$  per annum. Our study specifically emphasizes the star's trajectory within the Hertzsprung-Russell (HR) diagram, juxtaposed with the fluctuations in its central temperature and density, as illustrated in Fig. 6.2. At the conclusion of each nuclear burning stage, a range of physical parameters is tabulated for reference in Table 6.1.

#### 6.3.1 Pre-main-sequence phase

The model's starting point is anchored at a 2  $M_{\odot}$  mass, which is fully convective, possessing a central temperature  $T_c=6\times 10^5 K$ . This initial state is underscored by a chemical homogeneity, represented by mass fraction abundances:  $H^1=0.7516$ ,  $He^4=0.2484$ , and  $H^2=5.10^{-5}$ . As time progresses, the model experiences a gradual accretion-driven mass increase, pushing it to newer nuclear reactions. A significant milestone is reached when the central temperature surpasses  $1.6\times 10^6 K$ , leading to the ignition of deuterium within the core. Yet, this is just a precursor to a more pivotal phase transition, marked by the commencement of hydrogen-to-helium conversion within the core. At this juncture, the central temperature records  $1.26\times 10^8 K$ , with the accumulated mass rounding off to  $62.8 M_{\odot}$ .

#### 6.3.2 Core hydrogen burning

The core hydrogen burning phase is an intricate segment of the star's life, further divisible into two nuanced sub-phases. The first part witnesses an expansion of the convective core in terms of its radius and mass. Simultaneously, there's an observable escalation in the star's luminosity, yet its effective temperature retains relative stability. This dynamic between the stellar radius and the accruing mass can be succinctly expressed via the relationship  $R \propto M^{1/2}$ , a pattern aligning with the research presented by Hosokawa et al. (2012). As we transition to the latter phase, a notable deceleration in the growth trajectory of the convective core becomes evident. By the time core hydrogen reserves approach depletion, the star has burgeoned to an imposing  $2803M_{\odot}$  mass. Its effective temperature at this stage is logged at a value of 3.75. Intriguingly, this temperature indicates a 40% upswing from the temperature metrics recorded at the onset of core hydrogen burning. Comparing our model to traditional massive star models, clear disparities emerge, particularly in the temperature-density progression plots. A bulk of these deviations can be attributed to the continual mass increments experienced during this evolutionary phase.

#### 6.3.3 Core helium burning

In the aftermath of core hydrogen combustion, the star's core undergoes a contraction phase, inevitably resulting in a surge in its central temperature. This surge acts as a catalyst for helium ignition, achieved at  $2.80 \times 10^8 K$ . Throughout the core helium burning phase, the star exhibits characteristics synonymous with a red supergiant. Its radius, for instance, clocks in at a staggering  $10,000R_{\odot}$ . Such metrics present it as an outlier, especially when juxtaposed against typical luminous red supergiants, a phenomenon documented by Meynet et al. (2015). The helium burning taking place within the core induces the formation of a series of intermediate convective zones. These zones play a pivotal role, accelerating the transference of helium from the core to the surface. In parallel, carbon, another byproduct, gets channeled to the hydrogen burning shell. Here, carbon undergoes intricate processing via the CNO cycle, culminating in the creation of primary nitrogen. This nitrogen is subsequently relayed to the surface via the convective zones, highlighting the potential for significant primary nitrogen production, a phenomenon with potential ramifications for chemical feedback. Analyzing the star during this phase, it's evident that it adheres to a predictable evolutionary path in the temperature-density diagram. Concurrently, the relationship shared between stellar radius and mass undergoes a shift, evolving to adopt a near-flat trajectory.

Table 6.1: Selected quantities from the evolutionary model at the end of each burning stage.

Stage	Mass	Duration	Log T <sub>eff</sub>	log(g)	$Y_{ m surf}$	$M_{\mathrm{CO}}$
	$ m M_{\odot}$	yrs				$M_{\odot}$
$^{-2}$ H	5.7	$5.8 \times 10^4$	3.74	2.81	0.25	0.00
$^{1}\mathrm{H}$	2801	$2.7 \times 10^6$	3.76	-0.09	0.29	0.00
<sup>4</sup> He	3052	$2.4 \times 10^5$	3.77	-0.09	0.58	682
$^{12}$ C	3052	$1.2 \times 10^{1}$	3.77	-0.08	0.59	673
$^{20}$ Ne	3053	$9.9 \times 10^{-3}$	3.79	0.18	0.74	660
$^{16}O$	3053	$1.9 \times 10^{-3}$	3.94	0.88	0.74	660
<sup>28</sup> Si	3053	$5.8 \times 10^{-5}$	3.94	0.88	0.74	660

#### 6.3.4 Late Evolutionary stages

At the end of core helium combustion, the core's carbon abundance stands at 0.025. As the phase progresses, right before central carbon ignition, we observe central conditions transition to the pair-production domain, characterized by  $\Gamma_1 < 4/3$ . Approximately 10% of the CO core and

a further 2% of the aggregate mass lie within this domain. This phase, enduring around 12 years, mirrors the timescale seen in a 120  $M_{\odot}$  star.

The subsequent burning processes occur in a radiative core. The star undergoes a rapid neon photo-disintegration phase spanning mere days, followed by core oxygen burning, lasting less than a day. During this phase, a notable 56% of the CO core's mass (equivalent to 7% of the entire star's mass) lies in the pair-production region. As oxygen combustion draws to a close, the core transitions out of the pair-production domain. Exhaustion of core silicon is observed in roughly half a year, with 50% of the CO core (or 9% of the total mass) still within the domain. This may lead the star to collapse entirely, potentially giving birth to a black hole of approximately 3000  $M_{\odot}$ . Conversely, a fraction of the envelope might be expelled, resulting in a black hole ranging from 660 to 3000  $M_{\odot}$ . It is worth noting that predicting the specifics of such an explosion involves intricate physics, necessitating specialized hydrodynamical models to gauge both the detectability of the ensuing supernovae and their associated feedback (for detailed studies, see Ohkubo et al. 2009).

During these final stages, the star's luminosity is predominantly fueled by the energy transferred via neutrinos. Specifically, by the end of silicon combustion, neutrino luminosity surpasses photon luminosity by a factor exceeding a million. Using the parameters established by Haemmerlé (2021a), it's evident our model never enters the domain of general relativistic instability. Furthermore, under a consistent accretion rate of  $10^{-3} \, \mathrm{M}_{\odot}$  annually, the most massive star achievable slightly exceeds 3000  $\mathrm{M}_{\odot}$ . Barring external energy sources, such as the potential disintegration of Weakly Interactive Massive Particles (examined in works like Freese et al. 2008; Taoso et al. 2008), this stands as a definitive upper mass constraint. Understandably, the majority of this mass is accrued during the extended hydrogen nuclear combustion phase.

## 6.4 Influence of Massive Pop III Stars

To quantify the significance of these colossal stars, one must contrast their prevalence against typical massive stars. Taking the initial mass function (IMF) proposed by Kroupa (2001); Chabrier  $(2003)^1$ , for every  $10^5$  stars of  $20 \text{ M}_{\odot}$ , a solitary  $3000 \text{ M}_{\odot}$  star is anticipated. However, this ratio is sensitive to the chosen IMF. Adopting a top-heavy IMF, as explored by Baugh et al. (2005), adjusts the factor to 150, amplifying the significance of these hefty stars.

<sup>&</sup>lt;sup>1</sup>With the relation that the star count with initial mass M is linked to  $M^{-(1+x)}$ , where x = 1.3 for stars above 1  $M_{\odot}$ 

#### 6.4.1 Chemical Feedback

Refer to Figure 6.4 for the end-phase chemical composition post silicon combustion. Intermediate convective regions form during core helium burning, moving helium from the star's depths to its exterior. This results in a prominent helium augmentation at the surface: from an initial 0.25 to a concluding 0.74, which is unconventional for non-rotating, mass-conserving stars. Moreover, sections above the CO core display enrichment in nitrogen, oxygen, and to a smaller degree, carbon and neon. Consequently, their winds and eventual core collapse can significantly enrich their environment.

In an extreme scenario where the outer layer above the CO core detaches, the expelled matter would comprise 2400  $M_{\odot}$  of helium, 72  $M_{\odot}$  of  $^{14}N$ , 24  $M_{\odot}$  of  $^{16}O$ , 2.4  $M_{\odot}$  each of  $^{12}C$  and  $^{20}Ne$ . Contrasting this with a 20  $M_{\odot}$  Pop III model by Murphy et al. (2021b), it's evident a single 3000  $M_{\odot}$  star contributes  $^{14}N$  equal to over 50,000 20  $M_{\odot}$  stars.

Piau et al. (2006) alluded to an initial massive star generation depleting interstellar lithium, reconciling the lithium abundance discrepancy observed in the "Spite" plateau (Perivolaropoulos & Skara 2022). Our model also records lithium depletion in the 3000  $M_{\odot}$  star, yet its contribution might be minuscule compared to 20  $M_{\odot}$  stars. Intriguingly, if solely the exterior is expelled, it's devoid of iron, thus depleting lithium in interstellar space without iron enrichment. A comprehensive analysis is essential here.

Stars originating from the exterior of a  $3000\,\mathrm{M}_\odot$  supergiant would be helium-abundant, lithium-deficient, and showcase elevated N/C and N/O ratios, mirroring combined CNO and triple-alpha enhancements. The observed N/C and N/O in our model are 30 and 3, respectively. This bears resemblance to the CNO levels in iron-deficient stars, for instance, star HE1327-2326 Collet et al. (2006) with [Fe/H] -5.6. Probing whether these immense stars contribute to such chemical markers demands further exploration.

Recent observations of prominent NIII and NIV emissions in GN-z11 hint at considerable nitrogen enrichment in this galaxy (Bunker et al. 2023). With N/O ratios ( $\log(N/O) > -0.25$ ) in GN-z11 being fourfold of solar values (Cameron et al. 2023; Senchyna et al. 2023), several studies, such as those by Charbonnel et al. (2023) and Nagele & Umeda (2023), have posited supermassive stars (SMSs) as primary agents for such high nitrogen enrichment. For our zero-metallicity model, assuming the ejection of the entire envelope above the CO core, we have  $\log(N/O) = 0.45$  and  $\log(C/O) = -1.01$ . Depending on the ejected fraction of the envelope, these values can oscillate between  $0.45 < \log(N/O) < 0.75$  and  $-1.01 < \log(C/O) < -0.87$ . For a model with metallicity,  $Z = 10^{-6}$ , we note  $\log(N/O) \approx 0.55$  and  $\log(C/O) \approx -0.93$ . While our N/O ratio surpasses the lower

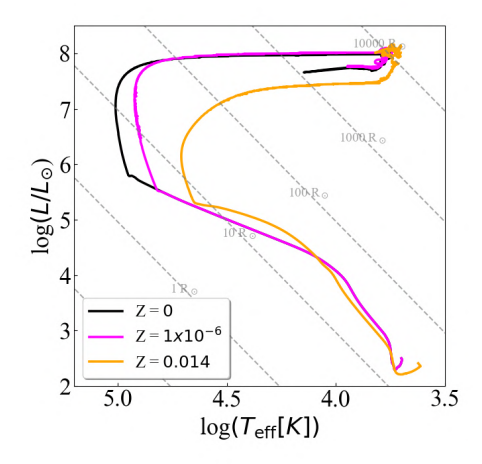


Figure 6.5: The evolution of three models comupted using a constant accretion rate of  $10^{-3}$  M $_{\odot}$ /yr until the end of core silicon burning. The black line represents the Z=0, magenta line is Z=1  $\times$   $10^{-6}$  and the orange line at Z = 0.014 metallicity. The isoradii lines are represented in grey.

threshold for GN-z11 from Cameron et al. (2023), the C/O ratio slightly undershoots. These findings imply that accreting Population III stars of around 3000 may indeed be behind the elevated N/O values in GN-z11. Nevertheless, in-depth comparisons with GN-z11 and upcoming JWST detections demand further studies.

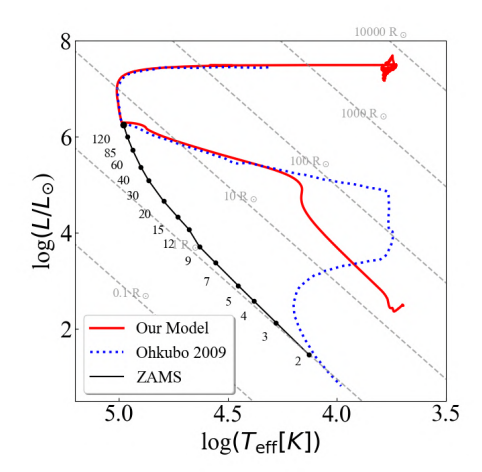
#### 6.4.2 Mechanical and Radiative Feedback

Mechanical energy from such objects can be expelled via stellar winds or supernova explosions. The red supergiant phase, post core helium combustion, exhibits an escape velocity of about 340 km/s -quadruple of a 20 M $_{\odot}$  red supergiant's 90 km/s. Hypothetically, if 1000 M $_{\odot}$  were shed during the red supergiant phase (implying a mass loss rate of several  $10^{-3}$  M $_{\odot}$ /yr), the resultant mechanical energy through winds would exceed that of a 20 M $_{\odot}$  red supergiant (that loses roughly  $10M_{\odot}$ ) by a factor of 1400. In this context, a singular 3000 M $_{\odot}$  star could contribute a mechanical energy equivalent to 1% of a total population of 20 M $_{\odot}$  stars. Luminosity-wise, one 3000 M $_{\odot}$  star can outshine a Pop III 20 M $_{\odot}$  star by 100 to 1000 times. Yet, its radiative feedback pales when compared with an assembly of  $10^5$  20 M $_{\odot}$  stars. Extreme stars might not be pivotal for ionizing photon generation, as the photon count per unit mass remains relatively unchanged in high mass stars (refer Sibony et al. 2022). Hence, whether mass resides in many less massive stars or fewer massive ones doesn't markedly affect the ionizing photon quota. Moreover, these extremely massive stars might evolve into intermediate mass black holes (BHs) between 100 and 1000 M $_{\odot}$ , which, when accreting matter, can emanate high-energy photons.

#### 6.4.3 Comparison with Previous Work

Ohkubo et al. (2009) delved into the evolutionary models of accreting massive stars, leveraging a mass-dependent accretion rate from the cosmological simulations proposed by Yoshida et al. (2007). In Fig. 6.6, we juxtapose our model inspired by Yoshida et al. (2007) against theirs. Our model embarks with an initial mass of 2  $\rm M_{\odot}$ , characterized by  $\rm log(\it L/\it L_{\odot}) = 2.46$  and  $\rm log(\it T_{\rm eff}) = 3.69$ . In contrast, Ohkubo et al. (2009)'s model initiates its trajectory at 1.5  $\rm M_{\odot}$  at  $\rm log(\it L/\it L_{\odot}) = 0.80$  and  $\rm log(\it T_{\rm eff}) = 3.98$ . The right panel of Fig. 6.6 further illustrates the stark variance in radii between the two models: our proto-stellar seed boasts a considerably enlarged radius of  $\rm 19~\it R_{\odot}$  when juxtaposed with the modest  $\rm \approx 1~\it R_{\odot}$  of Ohkubo et al. (2009). This discrepancy, however, exerts minimal influence over the subsequent evolutionary course.

Post an approximately  $10^5$  years of pre-main sequence (pre-MS) evolution-evidenced by the second shaded region in the right panel of Fig. 6.6âboth models culminate the pre-MS journey at  $120~{\rm M}_{\odot}$ , igniting core hydrogen combustion. Although their luminosity evolutions appear akin during this phase, a divergence emerges towards the termination of core hydrogen combustion. Our model reflects a reduced effective temperature with  $\log(T_{\rm eff})=4.47$ , whereas Ohkubo et al. (2009) exhibits a more elevated value of  $\log(T_{\rm eff})=4.90$ . This differentiation might arise from the different mechanisms of energy transport in their respective outer layers. Subsequent to the core hydrogen combustion phase, the models' evolutionary trajectories show pronounced contrast. Our model inclines towards the red, depicting an effective temperature of  $\log(T_{\rm eff})=3.73$ , while Ohkubo et al. (2009) concludes core silicon combustion at a notably warmer  $\log(T_{\rm eff})=4.32$ . These variances might lead to nuanced distinctions in their ionizing prowess, alongside radiative and chemical feedback mechanisms.



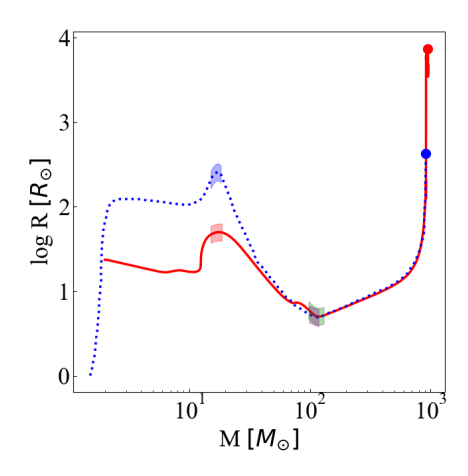


Figure 6.6: The evolution of accreting PopIII models following the accretion law of Yoshida et al. (2007) depicted in the HR diagram. The dotted blue line corresponds to the Y-1 model in Figure 5 of Ohkubo et al. (2009) and the solid red line represents the model computed in this work using . The black line represents the ZAMS line and the dots indicate the masses in  $M_{\odot}$ . The dotted grey lines are the isoradii with values depicted in the solar radii. *Right panel:* Evolution of radius versus mass of models shown in the left panel of this figure. Due to different initial conditions, both models possess a different radii during the pre-MS (first shaded region), and reach core hydrogen burning at near identical mass of 120  $M_{\odot}$  (second shaded region). A stark difference arises at the core Si burning as model by Ohkubo et al. (2009) finishes the evolution in blue at a radius of log(R)  $\approx 2.5$  (blue dot) whereas our model reaches the Hayashi limit with log(R)  $\approx 4$  (red dot).

# 6.5 Impact of Varying Metallicity

Traditionally, supermassive stars were believed to form in metal-free environments, denoted as Z=0. However, Chon & Omukai (2020a) has investigated the possibility of these stars forming in metal-enriched, atomically cooled halos through a process called super-competitive accretion. Further, Hirano et al. (2022) proposes that the interplay of magnetic fields during the accretion phase might enable the creation of supermassive stars even at a metallicity level of  $Z/Z_{\odot}=10^{-5}$ .

In order to understand the influence of metallicity on the evolution of approximately 3000  ${\rm M}_{\odot}$  stars, we examine models with a consistent accretion rate of  $10^{-3}~{\rm M}_{\odot}/{\rm yr}$ . These models are analyzed up to the end of the core silicon burning phase across three different metallicity levels: Z=0,  $10^{-6}$ , and 0.014, as visualized in Figure 6.5. All these models exhibit comparable pre-main sequence (pre-MS) evolutions, reaching the zero-age main sequence (ZAMS) at mass points of 63  ${\rm M}_{\odot}$ , 58  ${\rm M}_{\odot}$ , and 61  ${\rm M}_{\odot}$  for metallicity levels of 0,  $10^{-6}$ , and 0.014, respectively. Much like their massive counterparts, stars with higher metallicity display a larger radius and reduced  $T_{\rm eff}$  during their main sequence (MS) phase. This can be attributed to an increased presence of CNO elements in their cores and augmented opacities. Moreover, elevated metallicity expedites the growth of the

convective core mass during the MS phase, leading to an extended lifespan, diminished central temperature, and consequently, an increased final mass. Specifically, models with Z values of 0,  $1 \times 10^{-6}$ , and 0.014 culminate with final masses of 3053, 3285, and 3478  $M_{\odot}$ , respectively.

Analyzing the abundance profiles within these models post the core carbon burning phase reveals distinct variances in elemental distributions. Specifically, due to the existence of multiple intermediate convective zones in the outer 50% (in terms of  $M_r/M_{tot}$ ) of the 0 and  $10^{-6}$  metallicity models, hydrogen and helium are uniformly distributed within these regions, amounting to 294  $\rm M_{\odot}$  (10% of total mass) and 1138  $\rm M_{\odot}$  (37% of total mass), respectively. However, for the solar metallicity model, this consistent distribution is limited to the outermost 15%, where the mass fractions of hydrogen and helium are  $166 \rm \, M_{\odot}$  (4.7% of total mass) and 331  $\rm \, M_{\odot}$  (9.5% of total mass), respectively. In essence, our analysis emphasizes that alterations in metallicity can significantly influence the concluding mass of the star as well as the quantity and distribution of helium within its envelope.

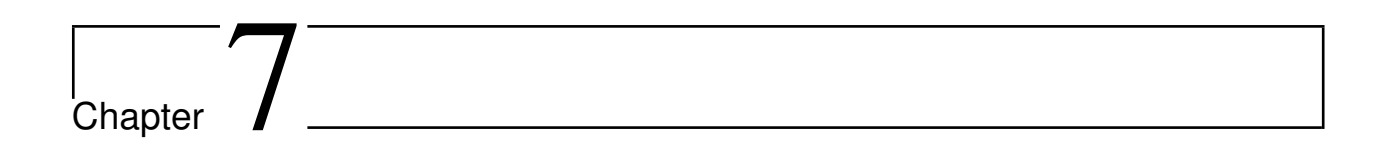
#### 6.6 Conclusion

This study delves into the evolutionary models of stars around  $3000 \text{ M}_{\odot}$ , exploring their progression and influence in terms of chemical, radiative, and mechanical interactions with their environment.

- Following core hydrogen combustion, our models display multiple intermediate convective zones beneath the convective envelope. This promotes intense chemical element mixing, resulting in helium-rich red supergiants with a final surface helium content of 0.74. This rich mix bolsters the star's potential as a nucleosynthesis source. Throughout subsequent burning stages, the star consistently resides within the red domain of the HRD.
- When assessing the influence of a singular  $3000~M_{\odot}$  star versus a collective of  $20~M_{\odot}$  stars, the former plays a notable role in primary nitrogen production. However, its mechanical and radiative feedback is comparable to the latter group.
- The models avoid general relativistic instability, but their central sections do engage in electronpositron pair production during oxygen combustion. Determining the outcome post core collapse necessitates hydrodynamical models.
- The highest achievable mass with a constant accretion rate of  $10^{-3}~M_{\odot}$  annually approximates 3000  $M_{\odot}$ . This boundary is dictated by the nuclear lifetime.

• The models with Z=0 and  $Z=10^{-6}$  could potentially enrich the interstellar medium, exhibiting log(N/O) ranges between 0.45 and 0.75, and log(C/O) values between -1.01 and -0.87. The exact enrichment depends on the envelope fraction that's dispersed. This hints that such  $3000~M_{\odot}$  stars might elucidate certain observations, such as the high redshift galaxy GN-z11, referenced in (Cameron et al. 2023).

For future studies, it would be valuable to account for detailed accretion rate histories originating from cosmological simulations. Potential disruptions in accretion might induce substantial mass losses, altering the star's ensuing evolution. Additionally, exploring the pulsational stability of such celestial bodies, coupled with the effects of varied convection, rotation, and magnetic fields, can further enhance our understanding.



# Variable accretion rate and preMS

This chapter is adapted from the paper by Nandal et al. (2023c) The birth and early life of a star are largely dictated by the process of accretion, wherein material from the surrounding environment is gravitationally drawn onto the forming star. At first glance, this process might appear as uniform. However, deeper investigation reveals that accretion rates can indeed be quite variable. Such variability is not a mere detail; it has profound implications for the star's development, particularly during its pre-main sequence (preMS) phase. Several factors give rise to this variability in accretion rates:

- 1. **Environmental Fluctuations:** Within molecular clouds, local changes in gas and dust density, influenced by turbulence or external forces like shock waves from neighboring stellar events, can modulate the material supply for accretion.
- 2. **Magnetic Fields:** The magnetic environment around a protostar can either enhance or impede accretion, based on its alignment and interaction with the infalling material.
- Feedback Mechanisms: Protostars emit powerful winds and radiation. These can push away the surrounding material, creating episodic accretion events when the outward pressure momentarily decreases.

The consequences of variable accretion are profound:

- **Bloating Phase:** A surge in accretion can cause the protostar to expand considerably, leading to the 'bloating phase'. This is a transitory state, but it affects the star's internal dynamics and its external appearance.
- Luminosity Waves: Fluctuating accretion rates lead to variations in the star's energy output.

  This can create 'waves' in its luminosity, offering insights into its accretion history.

• Evolutionary Path: Depending on the net accretion during the preMS phase, a protostar might evolve into either a blue or red supergiant. The star's eventual mass and chemical composition are intimately linked to its accretion history.

In conclusion, accretion is a nuanced process, with its variable rate being a pivotal determinant in shaping a star's infancy and eventual destiny. For astrophysicists, understanding this variability is vital, not only for comprehending individual stars but also for deciphering broader stellar population dynamics.

This chapter delves into the impact of variable accretion rates on the evolution of extremely massive stars. The objective is to determine a critical accretion rate that strikes a balance between the accretion timescale and the Kelvin-Helmholtz timescale, using a blend of numerical simulations and analytical developments (shown in section 7.4. Subsequently, the chapter explores the effects of this critical accretion rate on the evolution trajectories and compares the findings with existing research (section 7.5) and concludes in section 7.6.

#### 7.1 Literature review

Supermassive stars (SMSs) and massive Population III (PopIII) stars are considered crucial components in the process of forming black holes with masses between  $10^3$  and  $10^5$  M $_{\odot}$  in the early Universe. Observational data of distant quasars (Willott et al. 2010; Mortlock et al. 2011; Bañados et al. 2018; Wang et al. 2021) indicates the existence of supermassive black holes (SMBHs) with masses surpassing  $10^9$  M $_{\odot}$ . These observations impose stringent limits on the timeframes within which seed black holes can grow to such substantial masses. The problem's complexity is heightened by the discovery of an SMBH with a mass close to  $10^7$  at  $z \sim 8.7$  (Larson et al. 2023). Theoretically, these early SMBHs could originate from stellar mass black holes resulting from the end stages of PopIII stars. However, this pathway presents its own challenges. For a typical black hole with a mass of about 100 M $_{\odot}$  to expand 6 - 8 orders of magnitude within several hundred million years, it would need to continuously accrete at the Eddington rate. Moreover, these less massive black holes would need to navigate to their host galaxy's center and remain in the midst of a substantial gas inflow to achieve such masses.

Numerical studies, such as those by Milosavljević et al. (2009); Alvarez et al. (2009); Tanaka & Haiman (2009); Jeon et al. (2012); Smith et al. (2018), have probed this growth trajectory. The common consensus is that stellar mass black holes find it challenging to grow significantly due to the infrequent high-density gas environments necessary for rapid growth. Delving into the dynamics of these black holes in high-redshift galaxies, studies (Pfister et al. 2019; Beckmann et al. 2022)

have highlighted that those with masses under 10<sup>5</sup> M<sub>☉</sub> generate insufficient dynamical friction, preventing them from settling at the galaxy's center. Instead, they seem to meander through the galaxy (Bellovary et al. 2010; Tremmel et al. 2018). Given these complexities, recent research has pivoted towards examining if the early Universe could potentially have the right conditions conducive to the formation of SMSs and massive PopIII stars. Achieving true SMS formation would necessitate the star to approach the GR instability (Chandrasekhar 1964a), underpinned by sustained accretion until reaching masses of approximately  $10^5-10^6$  (Hosokawa et al. 2013a). The stars of interest in this work do not attain such large masses; they are instead termed as massive PopIII stars with masses often exceeding 1000  $M_{\odot}$ . A pivotal aspect is the almost metal-free nature of the first galaxies, which could potentially create conditions favoring the formation of massive, gravitationally unstable gas clumps without the interference of metal-induced fragmentation (Omukai et al. 2008). The formation mechanism of massive PopIII stars primarily hinges on achieving the necessary accretion rate that induces the star's photosphere to inflate and transition into a red supergiant, thereby mitigating radiative feedback and allowing the star's continued growth (Hosokawa et al. 2013a; Woods et al. 2017). This work zeroes in on understanding the nuances of this pivotal accretion rate.

Prior investigations into this aspect haven't pinpointed an exact rate. However, estimates indicate it being more than  $10^{-2}~\rm M_\odot~\rm yr^{-1}$  (Hosokawa et al. 2013a; Haemmerlé et al. 2018). Such high accretion rates might be realized in atomic cooling halos (Eisenstein & Loeb 1995; Haiman & Loeb 2001; Oh & Haiman 2002; Haiman 2006) or potentially during mini-halo mergers (Regan 2022). On larger scales, significant mass inflows could be a consequence of major galaxy mergers, catalyzing the creation of supermassive discs (Mayer et al. 2023; Zwick et al. 2023; Mayer et al. 2010b). In order to achieve optimal conditions for massive PopIII star formation, it may be imperative to significantly reduce, or at least suppress, the abundance of  $\rm H_2$  to prevent excessive fragmentation. Without this control, fragmentation could potentially influence the initial mass function in an undesirable manner. If stars with masses  $\lesssim 100~M_\odot$  form first, they might swiftly introduce metals to the environment, thereby curtailing the potential for the formation of more massive PopIII stars. Suppression of  $\rm H_2$  can be facilitated by nearby Lyman-Werner radiation sources (Shang et al. 2010; Latif et al. 2014a; Regan et al. 2017a). These radiation sources can dissociate  $\rm H_2$ , allowing the formation of larger Jeans masses, and consequently, the potential formation of more massive PopIII stars.

Furthermore, rapid assembly of dark matter haloes (Yoshida et al. 2003; Fernandez et al. 2014; Latif et al. 2022) and the presence of baryonic streaming velocities (Tseliakhovich & Hirata 2010b; Latif et al. 2014b; Schauer et al. 2015, 2017; Hirano et al. 2017; Schauer et al. 2021b) can endorse

the formation of massive PopIII stars. These factors establish conditions favorable for swift mass inflows, which in turn can trigger the formation of massive PopIII stars. It is plausible that a combination of these processes might be at play (Wise et al. 2019; Kulkarni et al. 2021). Promoting environments suitable for more massive PopIII star formation at the expense of  $\lesssim 100~M_{\odot}$  PopIII star habitats implies a need for uniquely rare conditions in the early Universe. Yet, it's noteworthy that the early Universe's exceptionally massive PopIII stars have been proposed as a way to align with the luminous readings observed in distant galaxies by JWST (Chon & Omukai 2020b; Trinca et al. 2023; Harikane et al. 2023b,a). Recent numerical analyses, emphasizing the creation of massive entities in moderate Lyman-Werner radiation fields, discovered that dynamical heating from both major and minor mergers can produce a smaller population of very massive stars (within the range of hundreds to thousands of  $M_{\odot}$ ) within a dominant dark matter halo (e.g. Wise et al. 2019; Regan et al. 2020b). These very massive stars sporadically undergo swift accretion (at rates  $\gtrsim 10^{-2} M_{\odot} / {
m yr}$ ) during interactions with gas overdensities in their host halo. However, these stars remain largely inactive, hinting at a potential to maintain an inflated photosphere only on rare occasions (Regan et al. 2020b; Woods et al. 2021). The intricate evolution patterns of these very massive and supermassive stars, especially when experiencing inconsistent rapid accretion over extended durations, remain an area of uncertainty.

A pivotal gap in current massive PopIII star formation models within cosmological contexts is the transition between the inflated 'red' phase and the more compact 'blue' phase of stellar evolution. Pinpointing the exact timeline and the precise accretion rate threshold for this transition has been a topic of discussion. The essence of this work revolves around comprehending the evolution of rapidly accreting massive PopIII stars, specifically with fluctuating accretion rates as described in the cosmological simulations of Regan et al. (2020b). Insights into this topic can elucidate several facets: stellar luminosity, stellar collision dynamics, radiative feedback, and the observable traits of these celestial bodies. Moreover, such massive stars are postulated to eventually undergo direct collapse into substantial black holes. This results in a generation of intermediate-mass black holes in the early galaxies, which could serve as the precursors to the recently identified CEERS SMBH (Larson et al. 2023).

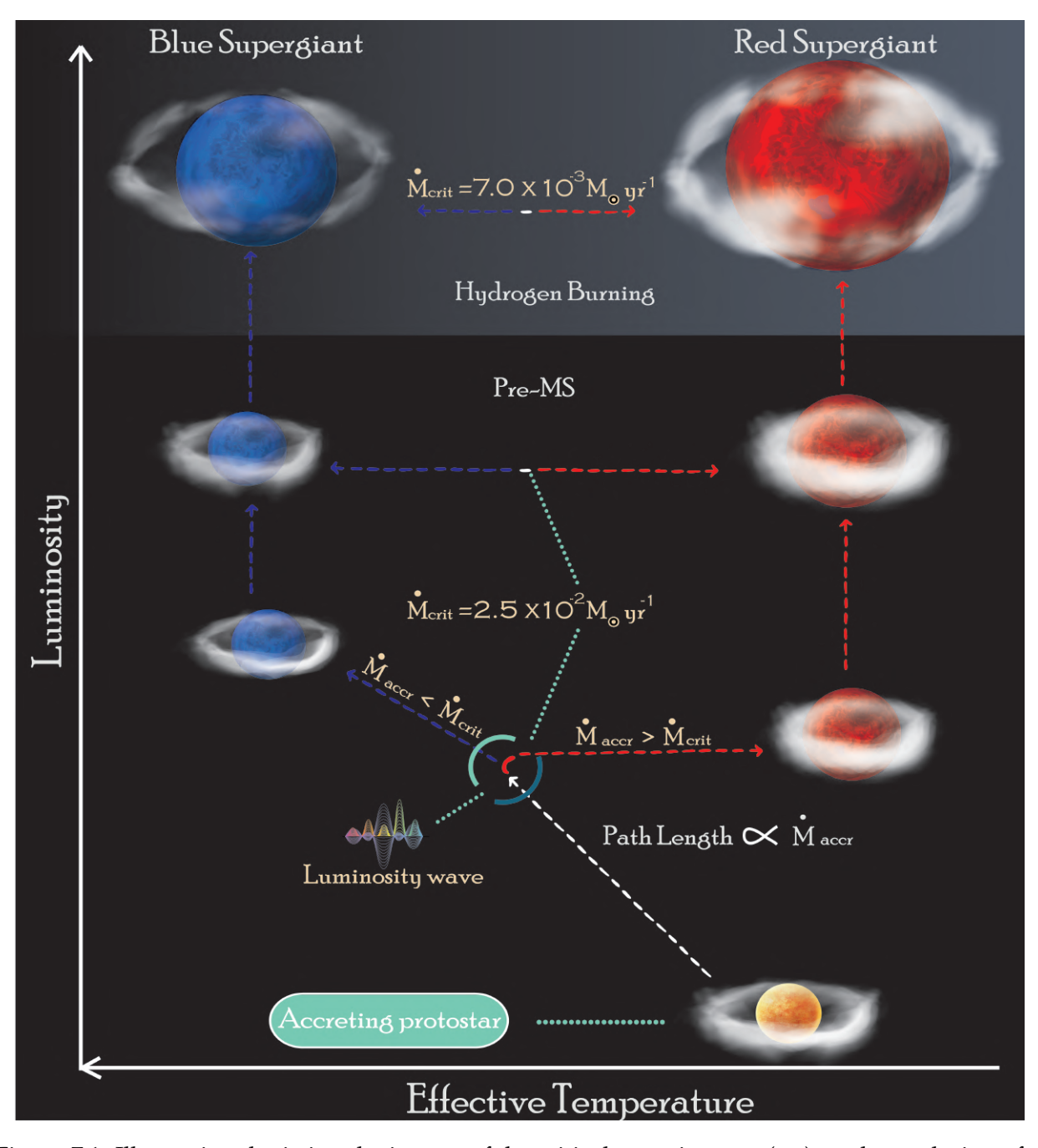


Figure 7.1: Illustration depicting the impact of the critical accretion rate ( $_{\rm crit}$ ) on the evolution of a star. The yellow object represents the protostellar seed and the wave pattern depicts the luminosity wave. The contraction towards blue is depicted with blue lines, whereas the expansion towards red is shown in red lines. The white and cloudy rings represent the accretion; this is denser in cases where the accretion rate is higher than  $_{\rm crit}$  and fainter when the accretion rate drops below  $_{\rm crit}$ . The black background depicts the pre-MS evolution and the grey background at the top marks the core hydrogen burning phase.

# 7.2 Accretion in Geneva Stellar evolution code

### 7.2.1 The stellar accretion rates

The stellar accretion rates employed in this study are derived from the radiation hydrodynamic simulations of Regan et al. (2020b). A comprehensive discussion of these simulations is beyond the purview of this paper. However, we provide a concise overview of the simulations and results, directing readers to the original publication for a more detailed exposition. The simulations executed by Regan et al. (2020b) were zoom-in simulations, utilizing the Enzo code (Bryan et al. 2014; Brummel-Smith et al. 2019). These focused on atomic cooling haloes previously identified in Wise et al. (2019) and Regan et al. (2020a)<sup>1</sup>. These haloes remained pristine (i.e., devoid of metals) and had no prior episodes of PopIII star formation. This state was maintained due to a blend of a moderate Lyman-Werner flux and the halo's swift assembly history (Yoshida et al. 2003; Fernandez et al. 2014; Lupi et al. 2021). The zoom-in approach facilitated a detailed, high-resolution examination of the gravitational instabilities within the atomic cooling halo, offering deeper insights into subsequent star formation events than what was attainable with the preliminary<sup>1</sup>, lower-resolution simulations.

From these enhanced resolution simulations, Regan et al. (2020b) observed that one of the haloes engendered 101 stars during its inaugural star formation phase. The aggregate stellar mass at the culmination of the simulations (around 2 Myr post the genesis of the first star) amounted to roughly 90,000  $M_{\odot}$ . Individual stellar masses spanned from about 50  $M_{\odot}$  to in excess of 6000  $M_{\odot}$ . The simulations' peak spatial resolution was  $\Delta x \approx 1000$  au, ensuring that individual star formation locales were discernible. Additionally, accretion onto each star's surface was meticulously tracked and cataloged throughout the simulation's duration. The accretion rates derived from these observations serve as the input for the stellar evolution modeling in this study.

### 7.2.2 Using the stellar accretion rates as input

From the cosmological simulations delineated earlier, we extracted 10 accretion histories from the available 101. The selection criteria were based on: (i) variability in accretion rates during the luminosity wave event and subsequent pre-MS stages, (ii) bursts in accretion rates during the hydrogen burning phases, and (iii) a final mass range spanning more than an order of magnitude. These ten models, characterized by variable accretion rates, are evolved from the pre-MS stage until the cessation of core helium burning utilizing the Geneva stellar evolution code (GENEVA)

<sup>&</sup>lt;sup>1</sup>The foundational simulations stem from the *Renaissance* simulation suite (Chen et al. 2014; O'Shea et al. 2015; Xu et al. 2016)

(Eggenberger et al. 2008). These models exhibit a uniform chemical composition, represented by X = 0.7516 and Y = 0.2484, and possess a metallicity of Z = 0. This is analogous to the parameters utilized by Ekström et al. (2012a) and Murphy et al. (2021b). Deuterium, with a mass fraction denoted by  $X_2 = 5 \times 10^{-5}$ , is incorporated as reflected in Bernasconi & Maeder (1996); Behrend & Maeder (2001) and Haemmerlé et al. (2018). All models are calculated with a FITM value of 0.999 (refer to section ?? in the Appendix). Accretion initiates onto low-mass hydrostatic cores, each with a mass represented by  $M_{\rm init}=2M_{\odot}$ . Such initial structures correspond to  $n\approx 3/2$  polytropes with consistent entropy profiles, meaning models commence their evolution as fully convective seeds. Accretion is modeled under the assumption that matter falls through a geometrically thin cold disc, with the specific entropy of the accreted material mirroring that of the stellar surface (Haemmerlé et al. 2013, 2016). This presumption infers that any surplus entropy in the matter accreted onto the star is radiated away prior to its reaching the stellar surface, consistent with Palla & Stahler (1992) and Hosokawa et al. (2010a). To accommodate accretion rates that fluctuate over time, in line with the hydrodynamic simulations, a new parameter was integrated into GENEVA. This parameter fetches the accretion rates from external files. Additionally, to ensure numerical convergence amidst accretion rate variations spanning six orders of magnitude, enhancements were applied to both spatial resolution and time discretization. This study excludes the effects of rotation and mass loss.

# 7.3 Evolution of accreting massive PopIII stars

The evolution of accreting massive PopIII stars was analyzed using the ten models with different physical parameters, as outlined in Table 7.3. These models are identified by their final mass; for instance, the 491  $M_{\odot}$  star is labeled as model 491. Significant accretion rates during the pre-MS and core hydrogen burning phases profoundly influence stellar progression. Figure 7.1 delineates the general trajectories and emphasizes the influence of accretion rate on dictating whether a star evolves into the red or blue supergiant phase. Figure 7.10 displays the accretion histories of the ten models examined in this research. Detailed exploration of the critical accretion rate values identified herein is reserved for the ensuing sections, with our analysis of the critical accretion rate in the pre-MS commencing first.

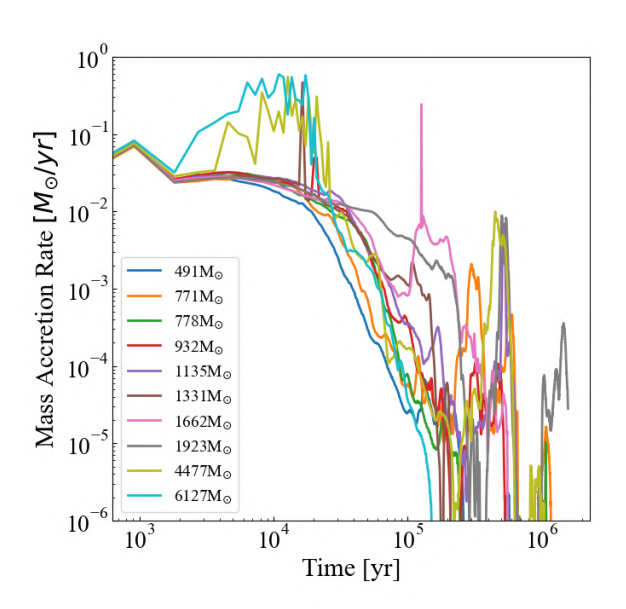


Figure 7.10: Accretion rate history of the ten massive PopIII models used in this work. The data for each star are taken from Regan et al. (2020a). The initial accretion rate is similar for each model; however, as the dynamical interaction between the stars and surrounding gas becomes dominant, the stars begin to migrate outwards and away from matter-rich zones and consequently the accretion rate decreases.

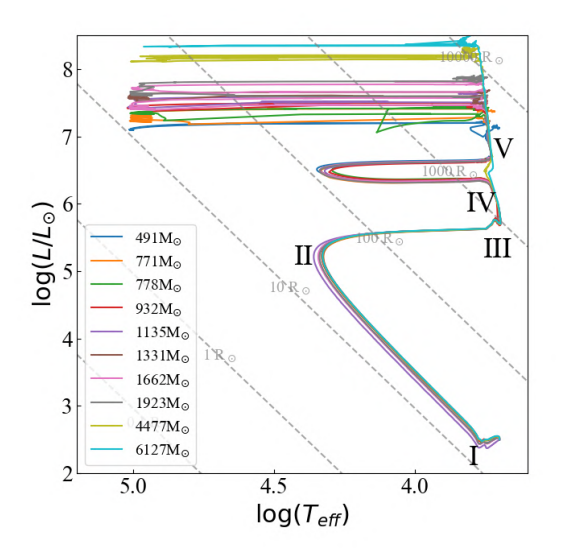
given in column 5. The surface helium abundance at the end of computation for all models is shown in column 6, and column 7 shows the final mass of the helium core.

given in column 5. The surface helium abundance at the end of computation for all models is shown in column 6, and column 7 shows the final mass of the helium core.

Table 7.1: Physical parameters of the ten models computed from the start of pre-MS until the end of core helium burning. Column 1 shows the final mass at the end of accretion. Column 2 highlights the total duration of pre-MS evolution in kiloyears whereas column 3 shows the total lifetime of models in megayears. The ratio of the time spent by models in red and blue is depicted in column 4. The mass fraction of hydrogen left in the centrer when models begin their final migration from blue to red in core hydrogen burning is

given in column 5. The surface helium abundance at the end of computation for all models is shown in column 6, and column 7 shows the final mass of the helium core.

Final Mass	$t_{ m preMS}$	$t_{ m total}$	$t_{ m red}/t_{ m total}$	$X_c$ at $\log$	$Y_{ m surf}$	$M_{ m He}$
$M_{\odot}$	kyrs	Myrs		$T_{\rm eff} = 4.00$	End He	$M_{\odot}$
491	9.16	2.07	0.08	0.00	0.40	114
771	8.84	2.16	0.11	0.00	0.45	175
778	8.60	2.03	0.11	0.00	0.49	173
932	9.00	1.84	0.13	0.00	0.50	242
1135	8.95	2.09	0.38	0.27	0.64	295
1331	8.70	1.86	0.18	0.05	0.50	327
1662	8.90	1.84	0.59	0.47	0.76	662
1923	9.00	1.93	0.36	0.20	0.58	756
4477	7.80	1.70	0.40	0.23	0.75	985
6127	6.86	1.51	0.47	0.26	0.76	1262



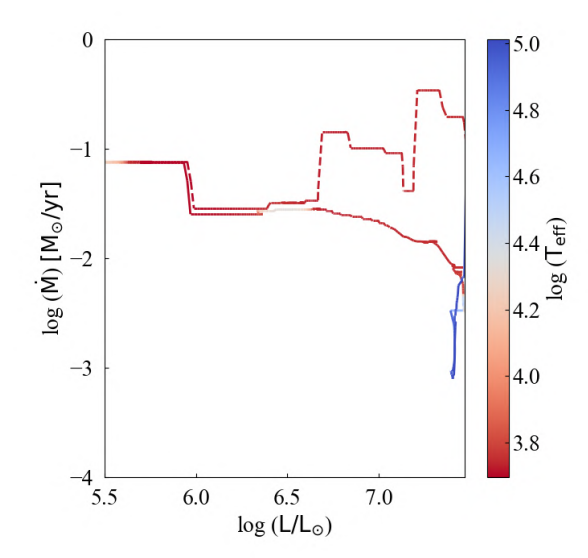
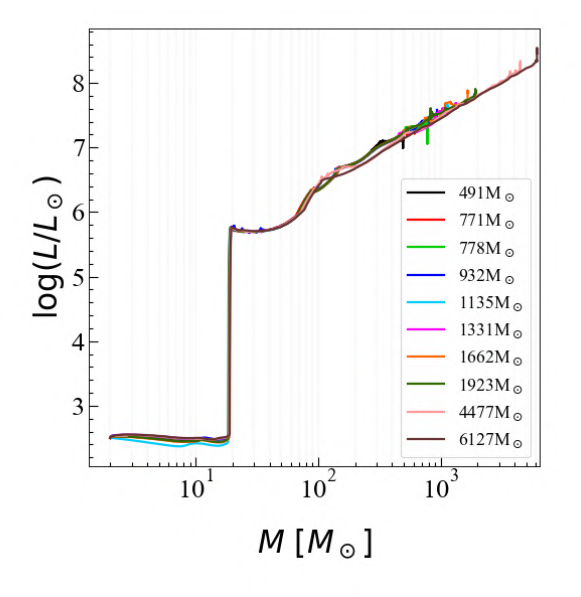


Figure 7.11: Evolution of accreting PopIII models. *Left panel:* HR diagram depicting the evolution for ten models with varying accretion rates. The models are labelled according to their final mass. Grey dashed lines represent isoradii. Models 491, 771, 778, 932, 1135, 1331, 1662, and 1923 have near-identical pre-MS accretion histories, unlike models 4477 and 6127. All models except 4477 complete accretion before hydrogen burning starts at  $\log{(T_{\rm eff})}=5.10$ . Computation stops after core helium burning, with all models in the red at  $\log{(T_{\rm eff})}\approx3.76$ . *Right panel:* Evolution of the accretion rate versus the luminosity for the 1662 (solid line) and 4477 (dashed line) models, colour-coded by the effective temperature. Quantities are displayed on a log scale, focusing on a zoomed-in region of the pre-MS. Both models share an identical accretion history until reaching a luminosity of  $\log{(L/L_{\odot})}=5.95$ . The 1662 model experiences a drop in the accretion rate below  $2.5\times10^{-2}M_{\odot}~\rm yr^{-1}$ , while the 4477 model remains above this value.



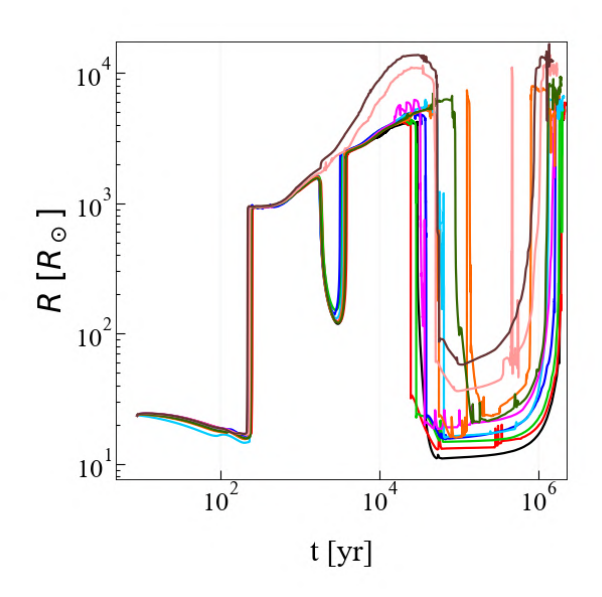


Figure 7.12: Variation of various physical parameters of accreting PopIII models. *Left panel:* Luminosity–mass relation depicted for all models. The increase in luminosity at 20 for all models corresponds to the luminosity wave breaking at the surface. Beyond this, luminosity evolves monotonically versus mass as L  $\propto$  M until the end of accretion history. *Right panel:* Evolution of radius versus age (in years) for all models. The colours used to represent models correspond to the label shown in the left panel. Despite models possessing unique accretion histories, the final state attained is a red supergiant star with radius ranging from 4000 R $_{\odot}$  to 10000 R $_{\odot}$ . Another feature depicted is the total lifetime of star is decreases slightly as the final mass increases, a result similar to the findings of massive star models. One indeed expects that for massive star, the core H-burning phase does not much depend on the mass since, due to the effects of radiation pressure,  $L \propto M$  and the stellar lifetime  $\propto M/L = {\rm constant}$ .

# 7.4 Detailed Analysis of Pre-Main Sequence Evolution

The pre-main sequence (pre-MS) phase provides crucial insights into the formation and early evolution of stars. Here, we present a comprehensive breakdown of the evolutionary stages for massive protostars and the factors that dictate their behavior.

# 7.4.1 Setting the Stage: Initial Conditions

Every star considered in this study embarks on its journey from a specific initial configuration, termed the hydrostatic seed. Here are the defining characteristics of these seeds:

- Mass:  $2 M_{\odot}$
- Radius:  $26 R_{\odot}$
- Luminosity:  $\log(L/L_{\odot}) = 2.50$
- Effective Temperature:  $\log(T_{\rm eff}) = 3.70$
- Accretion Rate:  $\approx 7.5 \times 10^{-2} \, M_{\odot} \mathrm{yr}^{-1}$

# 7.4.2 Evolutionary Trajectories on the Hertzsprung-Russell Diagram

Figure 7.11 sheds light on how each star evolves on the HR diagram, with significant events marked by roman numerals I to V. This journey, influenced by variable accretion rates, reveals intriguing patterns and outcomes.

### Luminosity Wave Onset and Stellar Core Dynamics (I-III)

At  $\log(L/L_{\odot})=2.47$  and  $\log(T_{\rm eff})=3.77$ , an interesting phenomenon, called the luminosity wave, kicks in. This wave is triggered by an increase in central temperature which subsequently reduces the central opacity. The net result is a transition of the stellar core from a convective nature to a radiative one. This lowered opacity amplifies luminosity production, facilitating the movement of central luminosity outwards. As a consequence, stars move to the blue section of the HR diagram. The extent of this movement is directly correlated with the accretion rate during the event, emphasizing the importance of accretion in shaping stellar paths.

# Cessation of Luminosity Wave and Red Transition (II)

After the luminosity wave travels for approximately 190 years, most models exhibit near-identical evolutionary paths. This synchronized behavior is attributed to their accretion rates ex-

ceeding  $3.1 \times 10^{-2}$ . However, certain accretion rates, specifically those above  $1.0 \times 10^{-3}$ , post the luminosity wave can push models to transition to the red region. This critical rate has been quantified to be greater than  $2.5 \times 10^{-2}$ . With a consistent accretion timescale, and a rising surface Kelvin-Helmholtz timescale, the models grow in size and form red supergiant protostars within a mere span of 4 years.

# **Evolutionary Divergence and Accretion Role (IV)**

As the evolution progresses, a clear divergence is observed in the paths at  $\log(L/L_{\odot}) = 5.70$  and  $\log(T_{\rm eff}) = 3.70$ . While most models, except 4477 and 6127, see a drop in accretion rate below the critical rate and hence contract towards the blue, models 4477 and 6127 don't share this fate. Their higher accretion rates ensure that they remain in the red region, consistently following the Hayashi line.

## Protostellar Convergence and Massive Sizes (V)

A significant event is observed when all models converge on the HR diagram at points  $\log(L/L_{\odot})=6.70$  and  $\log(T_{\rm eff})=3.73$ , continuing on the Hayashi line for around 20,000 years. At this stage, these entities boast impressive radii ranging between 4000 and 10,000  $R_{\odot}$ , rightfully earning the title of red supergiant protostars. The magnitude of the radii during this phase is intrinsically tied to the mass of the model, which in turn is governed by the average accretion rate till this point. Eventually, all models undergo contraction towards the blue region, with their radii shrinking to values less than  $60~R_{\odot}$ , setting the stage for core hydrogen burning. At this juncture, accretion activities reduce substantially or cease.

In summary, while the luminosity wave has a nuanced role in the pre-MS evolution of massive protostars, the critical accretion rate stands out as a dominant factor. Exceeding this rate can lead to the emergence of red supergiant protostars along the Hayashi line. On the other hand, falling below this rate triggers a contraction, moving the stars to the blue section of the HR diagram.

# 7.4.3 Core hydrogen burning evolution

Core hydrogen burning commences with all models at  $\log(T_{\rm eff}) \approx 5.00$  and a luminosity range between  $\log(L/L_{\odot})$  from 7.40 to 8.30 (see left panel of Figure 7.11). Numerical tests indicate that for the same values of luminosity and effective temperature at the Zero Age Main Sequence (ZAMS), the choice of accretion history does not impact the positions of the models (see section ?? of Appendix). We now examine three representative models: 491, 6127, and 4477.

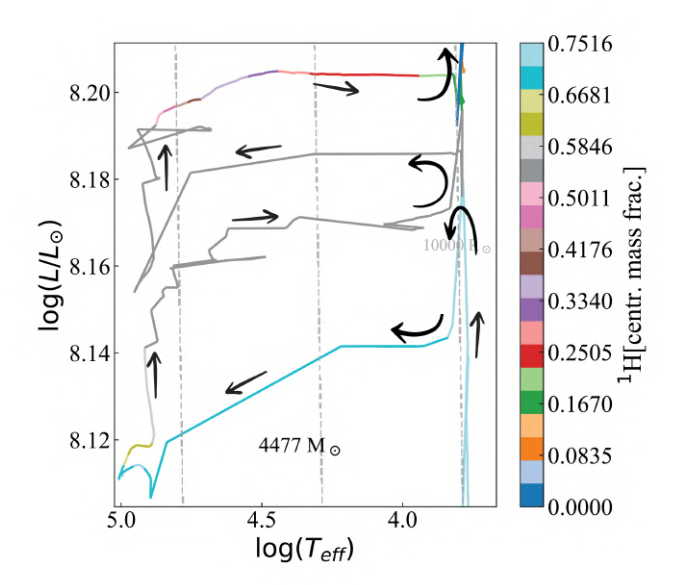


Figure 7.13: Magnified HR diagram of model 4477 (only the upper part is shown) depicting the migration between blue and red as a result of the variable accretion rate. The colour code follows the central mass fraction of hydrogen. The black arrows represent the evolutionary path taken by the model; the arrows emerge from the bottom right, which marks the pre-MS stage, and end at the top right, which denotes the end of the core hydrogen burning stage. The first migration from blue to red occurs at log (L/L $_{\odot}$ )  $\approx$  8.14 when accretion rate increases to 7.0×10<sup>-3</sup>, the new critical accretion rate during hydrogen burning. Upon reaching log (T $_{\rm eff}$ )  $\approx$  3.76, accretion rate is reduced below this critical value to 5.0×10<sup>-3</sup>. This transition from blue-red-blue occurs over a timescale 17.5 kyrs indicative of the thermal relaxation timescale during Hydrogen burning.

Model 491 is the least massive and experiences no accretion during core hydrogen burning. Hydrogen ignites in the core through the proton-proton (pp) chain and the  $3-\alpha$  reactions as the temperature exceeds  $1\times 10^8 \rm K$ . The Carbon-Nitrogen-Oxygen (CNO) cycle becomes the dominant energy source for the remainder of this phase (Woods et al. 2017; Haemmerlé et al. 2018). The top left panel of Figures 7.14 and 7.16 shows the structure of this least massive star (Model 491), with a convective core, a radiative intermediate zone, and an outer convective envelope. The convective core mass starts at 453  $M_{\odot}$  and completes the main sequence in 1.82 Myr with a final core mass of 243  $M_{\odot}$ .

Model 6127 has the highest final mass and also ceases accretion before hydrogen ignition in the core. It begins hydrogen burning in a convective core with an initial mass of 5741  $M_{\odot}$  and completes the main sequence in 1.25 Myr with a final core mass of 3593  $M_{\odot}$ . When the effective temperature reaches  $\log(T_{\rm eff})=4.00$ , the model is still undergoing hydrogen burning with 0.26  $X_c$  left in the core. Core hydrogen exhaustion occurs at the Hayashi limit, followed by structural expansion and the development of a convective envelope with intermediate convective zones (see

bottom left panel of Figure 7.15 and 7.17).

The 4477 model is distinguished from the other nine models by its unique accretion history which extends into the hydrogen burning phase, causing multiple blue-red transitions as depicted in Figure 7.13. It initiates hydrogen burning without accretion at  $\log(T_{\rm eff}) = 5.00$  and  $\log(L/L_{\odot}) = 8.11$ . After a mere 4.0 kyr, it encounters an accretion episode and ascends the Hertzsprung-Russell (HR) diagram to a nearly constant  $\log(T_{\rm eff}) = 4.91$  and  $\log(L/L_{\odot}) = 8.14$ . With an accretion rate exceeding  $7.0 \times 10^{-3} M_{\odot} \text{yr}^{-1}$ , the model uniquely migrates toward the red side of the HR diagram, revealing a critical accretion rate that significantly influences the model's radius during hydrogen burning. This migration occurs over a Kelvin-Helmholtz timescale of 17.5 kyr, considerably shorter than the nuclear timescales observed without accretion in all other models. Once the redward migration concludes, at  $\log(T_{\rm eff}) = 3.78$  and  $\log(L/L_{\odot}) = 8.19$ , the accretion rate diminishes to  $5.0 \times 10^{-3} M_{\odot} \text{yr}^{-1}$  after 8.5 kyr, initiating a final blueward transition lasting 1.0 kyr. Arriving on the blue side of the HR diagram at  $\log(L/L_{\odot}) = 8.15$  and  $\log(T_{\rm eff}) = 4.94$ , the model exhausts all accreting matter. It then embarks on its final redward journey on a nuclear timescale, persisting for 0.61 Myr, concluding this phase at  $\log(L/L_{\odot}) = 8.21$  and  $\log(T_{\rm eff}) = 3.79$ . The central right panel of Figure 7.15 and 7.17 displays particular trends during this phase, with a radius change at 0.45 Myr corresponding to a 25 kyr burst in accretion rate. Refer to the right-hand panel of Figure 7.12, which shows the sharp increase in radius of model 4477 at  $T\sim0.45$  Myr. A large outer convective zone forms before the end of core hydrogen burning. Similar to model 6127, the core hydrogen burning in this model concludes after it has reached the Hayashi track.

To summarize, a critical accretion rate of  $7.0 \times 10^{-3} M_{\odot} {\rm yr}^{-1}$  is identified during the core hydrogen burning phase, as indicated by model 4477. This accretion rate significantly affects the radius of the model during hydrogen burning and is the cause of the observed unique blue–red transitions. It is also noted that this critical accretion rate is lower than the accretion rate during the pre-main-sequence (pre-MS) evolution.

# 7.4.4 Helium Burning

During the core helium burning phase, all models exhibit similar evolutionary patterns, represented by the grey areas in Figures 7.14 and 7.15. Accretion has stopped for all models at this stage, and the evolution starts and finishes near the Hayashi line. We examine the least massive (model 491) and the most massive (model 6127) to understand this phase better. Model 491's core contracts until its central temperature hits  $2.80 \times 10^8 {\rm K}$ . Helium ignites in a convective core with a mass of 242  ${\rm M}_{\odot}$ . The outer layers become mostly convective, with 85% of the model being convective. This core helium burning stage lasts 0.23 Myr, ending with a helium core mass of 114  ${\rm M}_{\odot}$ .

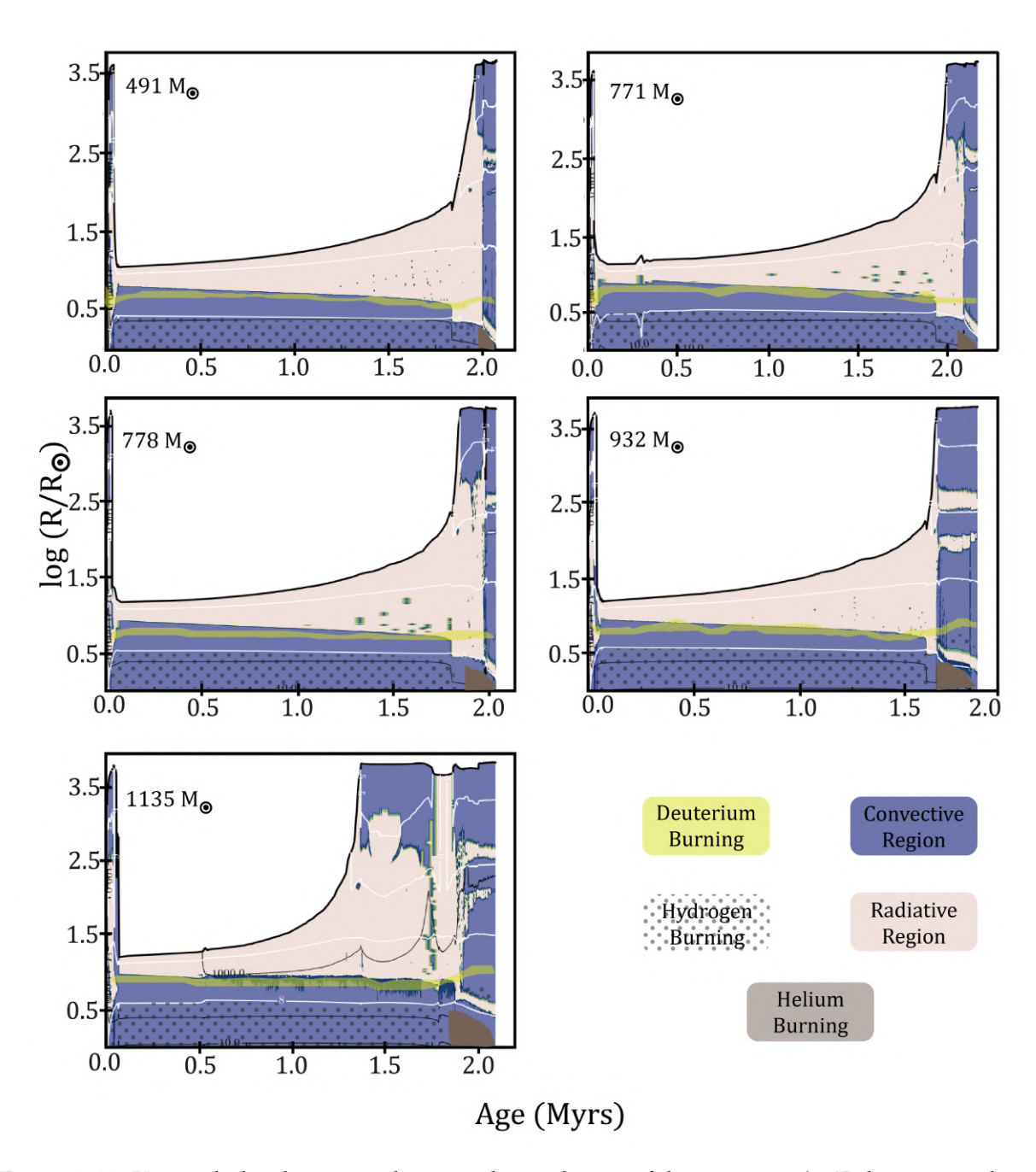


Figure 7.14: Kippenhahn diagrams showing the evolution of the structure (in Eulerian coordinates) as a function of time (Myrs) for the lowest-mass models. The blue and cream regions represent the convective and radiative zones respectively. The iso-masses are depicted by black lines whereas the isotherms of log(T[K]) = 5, 6, 7 and 8 are drawn in white lines. The translucent yellow regions show deuterium burning, dotted dark grey zones are hydrogen burning zones, dark grey zone highlights helium burning. The pre-MS evolution lifetime is much shorter than the nuclear burning lifetime, therefore the leftmost section of each plot represents this stage. Here the radius of all models fluctuates over 2 orders of magnitude. The hydrogen burning phase is marked by a shrinking convective core and an inflated radiative zone. Following a short contraction phase, all models expand and transition to a core helium burning phase with a near-full convective structure.

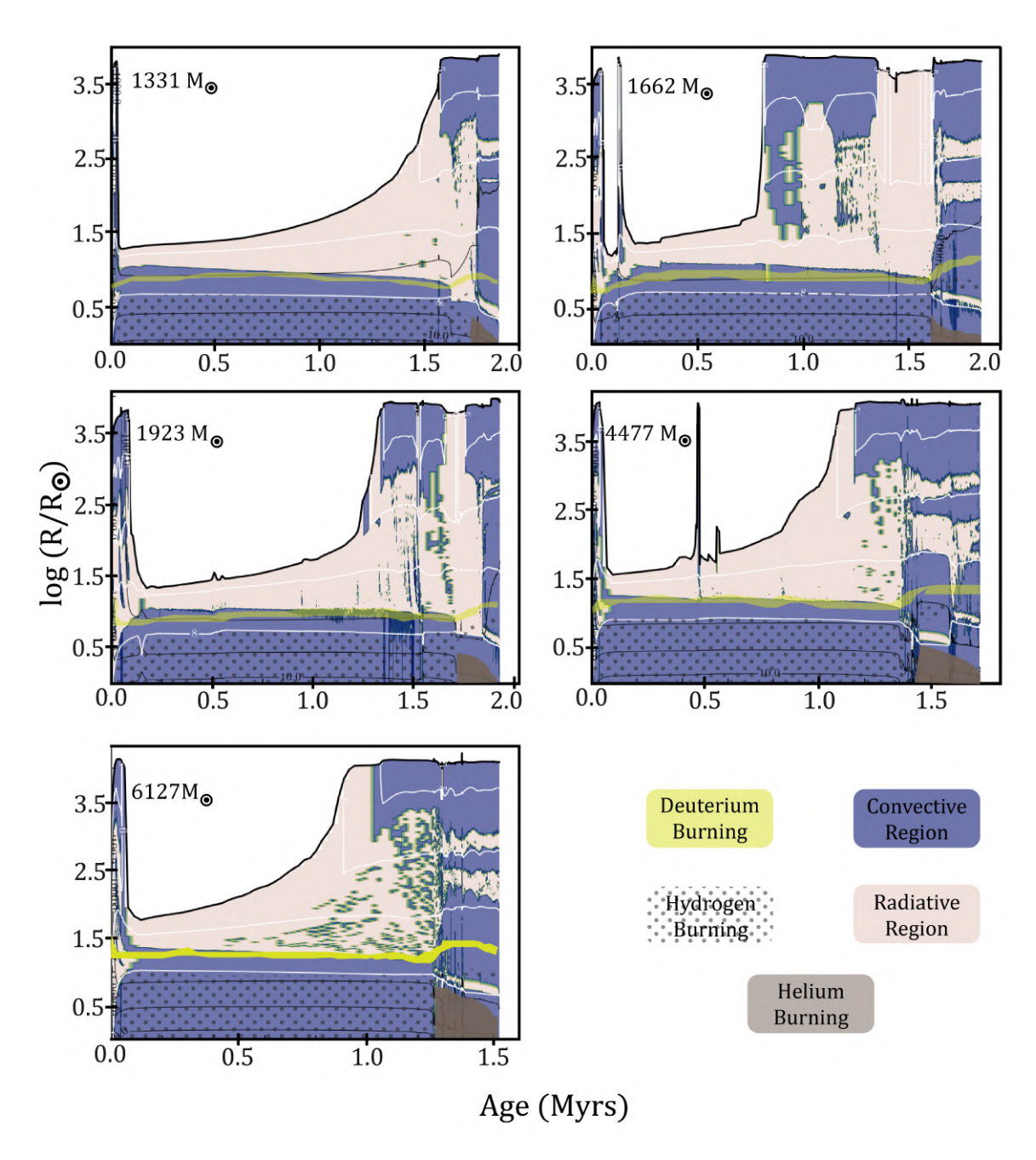


Figure 7.15: Kippenhahn diagrams similar to Figure 7.14 but for models with mass 1331, 1662, 1923, 4477 and 6127. The radii of these models is larger than the low mass models. The models depicted here transition to the red and expand their radius before the completion of core hydrogen burning phase. Model 4477 shows an exceptional behavior as it undergoes an expansion in radius during hydrogen burning. This is due to a burst of accretion experienced by this model.

Model 6127 has a nearly identical core helium burning phase to the other models but becomes almost fully convective right after core hydrogen burning ends. This convective nature allows all models to move helium from the core to the surface, even without rotational mixing. The duration of core helium burning is shorter, at 0.15 Myr, resulting in a final helium core mass of 1262  $M_{\odot}$ . The surface helium abundance of model 491 is  $Y_{\rm surf} = 0.40$ , while model 6127 shows a highly enriched surface with  $Y_{\rm surf} = 0.76$ , indicating a mass-dependent increase in surface helium.

The core mass at this stage's end is about one-quarter to one-sixth of the total mass, as shown in the last column of Table 7.3. If these objects form black holes, the mass range would be between two limits. The upper limit assumes the black hole acquires the star's entire final mass, while the lower limit considers the loss of the outer envelope above the helium core due to winds or instabilities before collapse, resulting in a black hole with mass equal to the helium core.

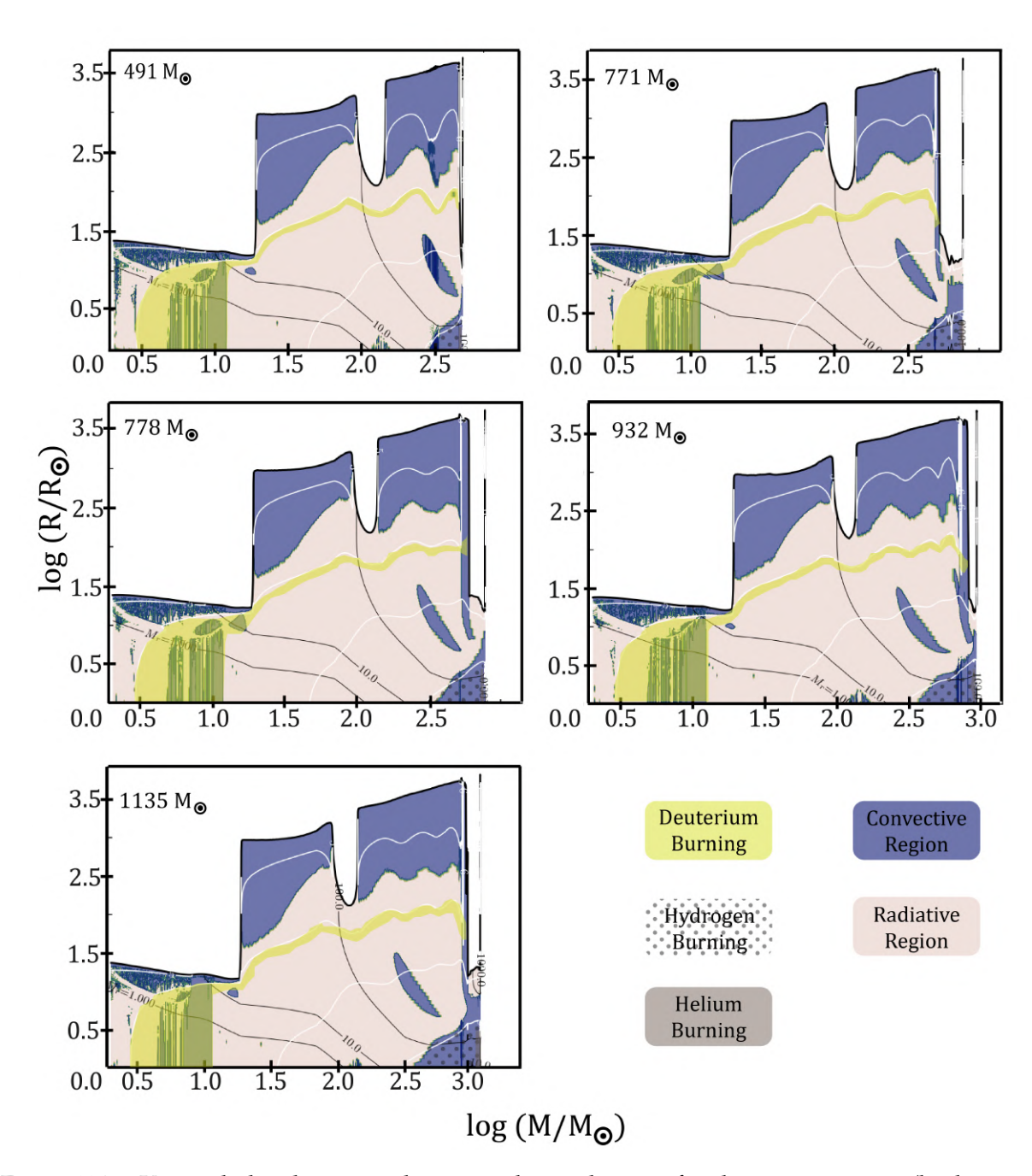


Figure 7.16: Kippenhahn diagrams depicting the evolution of radius versus mass (both axis represented in log scale) for low mass models. The details of diagrams are similar to Figure 7.14. In this version of diagrams, the change in radius during the pre-MS evolution of all models is clearly visible. All models undergo the luminosity wave at log  $(M/M_{\odot})$  = 1.3 and experience a strong increase in radius. The next noteworthy evolutionary trend is at log  $(M/M_{\odot})$  = 1.95 when model undergo a drop in accretion rate below  $_{\rm crit,preMS}$  which results in a decrease in radius. Eventually the accretion rate increases above the  $_{\rm crit,preMS}$ 

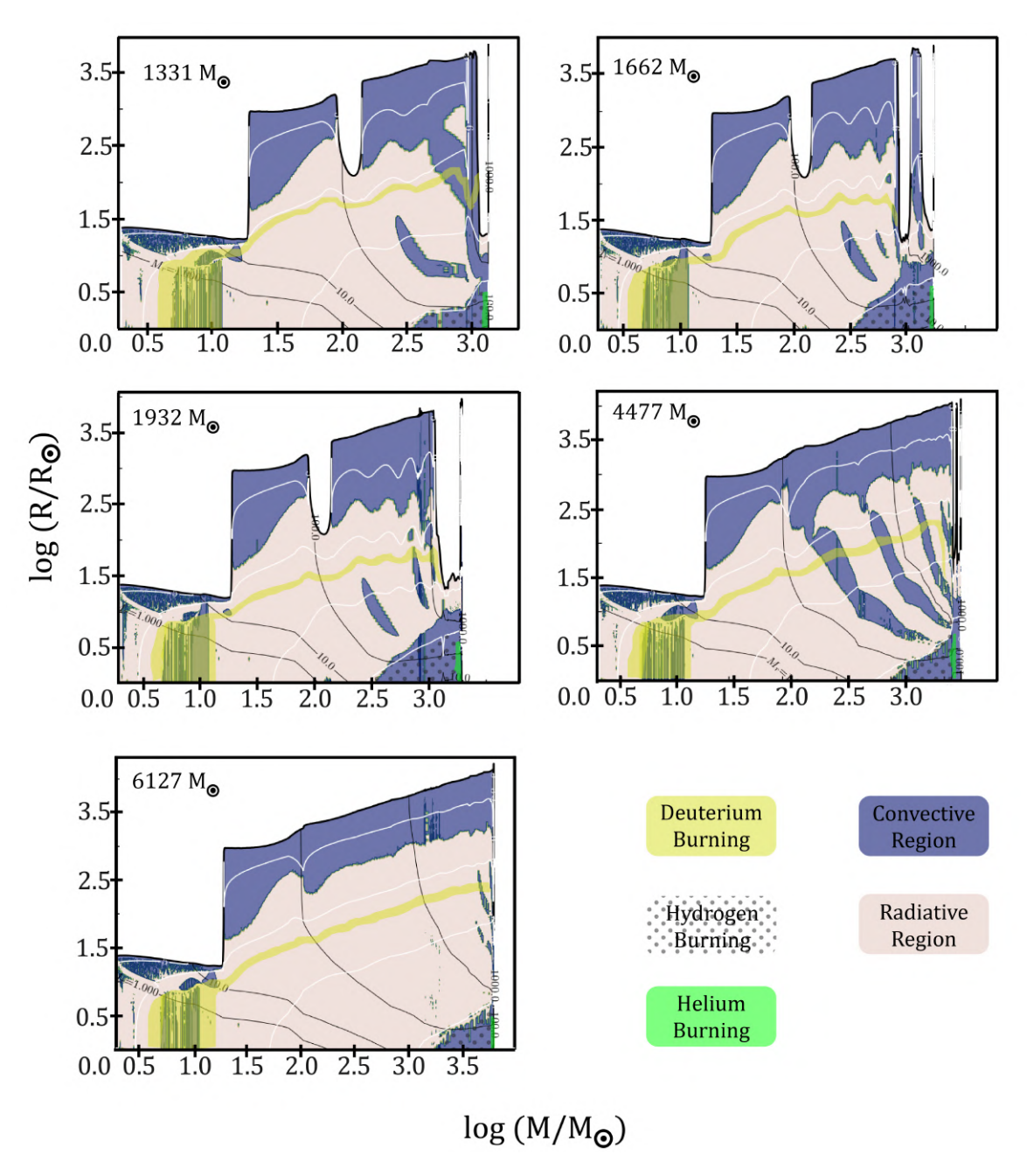


Figure 7.17: Kippenhahn diagrams depicting the evolution of radius versus mass (both axis represented in log scale) for high mass models with mass 1331, 1662, 1923, 4477 and 6127 .. The details of diagrams are similar to Figure 7.16.

# 7.5 Discussion

### 7.5.1 Determining the Critical Accretion Rate

The quest to pinpoint the critical accretion rate that dictates the development of a standard massive star has been central to research in the past twenty years. Initial investigations by Omukai & Palla (2001, 2003) looked into the critical accretion rate under spherical accretion conditions, arriving at a figure close to  $4 \times 10^{-3}$ . Building on these findings, Schleicher et al. (2013) examined how the Kelvin-Helmholtz contraction timescale compares with the accretion timescale and proposed a formula to calculate the critical accretion rate. They proposed that for a star to evolve along the Hayashi track under spherical accretion, the rate must be about  $1 \times 10^{-1}$ , which is higher than the previously mentioned study. Exploring a more practical scenario of accretion through a thin disc, Hosokawa et al. (2012) found that the critical accretion rate drops by an order of magnitude to around  $1 \times 10^{-2}$ . Later, Hosokawa et al. (2013a) employed the code to model and predicted the critical accretion rate for the scenario of cold disc accretion. Their findings suggested that to maintain a star in the red supergiant phase, the minimal accretion rate would be about  $1 \times 10^{-1}$ . This rate is particularly significant during the early pre-main-sequence stage when the internal gravitational energy has a pronounced effect on evolution, especially when the Kelvin-Helmholtz timescale outstrips the accretion timescale. The importance of the relative length of these timescales was underscored, affecting whether a star takes on a blue or red supergiant classification.

Vorobyov et al. (2013) improved upon the notion of a fixed accretion rate by using 2D hydrodynamic simulations that reflect a variable accretion rate, which includes bursts of high accretion and quieter periods, mimicking the irregular delivery of matter from fragmented clumps falling onto the star. Their work suggested that such fluctuations in accretion rate significantly influence the early stages of a star's growth. In the context of the evolution of early massive stars, Sakurai et al. (2015) also modelled variable accretion rates and estimated the threshold rate for forming either a red or a blue massive star to be near  $4 \times 10^{-2}$ . Furthermore, they recognized that since mass in such stars is densely packed towards the center, the global Kelvin-Helmholtz timescale may not accurately reflect the star's overall thermal timescale. Instead, they recommended examining the Kelvin-Helmholtz timescale of the star's outer layers to predict its transition into a red or blue supergiant.

Using the code, Haemmerlé et al. (2018) ran simulations on massive star models while maintaining steady rates of mass accumulation, ranging from  $10^{-3}$  to  $10^{1}$ . They observed that the model with a rate of  $10^{-2}$  showed fluctuating patterns in the Hertzsprung-Russell diagram but eventually stabilized near the Hayashi limit, reaching a mass over 600. This observation led them to suggest

a critical accretion rate of about  $1 \times 10^{-2}$ . In our study, we extend the scope of previous research by utilizing variable accretion rates that are in line with self-consistent cosmological simulations. Starting from the onset of the luminosity wave and continuing through to the end of the pre-main-sequence phase, our approach allows us to determine a more accurate critical accretion rate. We also conduct numerical experiments during the pre-main-sequence period, manually adjusting the accretion rates to more precisely measure this critical figure.

Our results indicate a critical accretion rate for the pre-main-sequence phase of  $= 2.5 \times 10^{-2}$ , which later decreases to  $= 7 \times 10^{-3}$  during the hydrogen-burning stage of stellar development. Our calculated pre-main-sequence critical accretion rate of  $2.5 \times 10^{-2}$  aligns closely with findings from Omukai & Palla (2001, 2003); Sakurai et al. (2015); Haemmerlé et al. (2018). Furthermore, our analysis, particularly with model 4477, reveals a previously unidentified critical accretion rate,  $\dot{M}_{\rm crit}$ , applicable during the core hydrogen-burning phase, not discussed in earlier studies. We ascertain this value to be  $\dot{M}_{\rm crit} = 7 \times 10^{-3}$  for the hydrogen burning stage.

To accurately find the critical accretion rate before the main sequence ( $\dot{M}_{crit,preMS}$ ), we tested model 932 during its early development. These tests involved setting steady rates of mass gain between  $1.0 \times 10^{-3}$  and  $3.1 \times 10^{-2}$ . We started these tests at point 'I' in Figure 7.11. We picked the lower rate based on earlier work by Woods et al. (2017); Haemmerlé et al. (2018) and the higher rate from our own simulations, which indicate a shift to a red state. At rates from  $1.0 \times 10^{-3}$  to  $5.0 \times 10^{-3}$ , the star shrank and moved to a blue state, suggesting a longer mass gain timescale than the surface cooling timescale.

At a higher rate of  $1.0 \times 10^{-2}$ , the star's path was unstable, swinging between blue and red on the Hertzsprung-Russell diagram. After gathering  $300 \text{ M}_{\odot}$  in 25,000 years, it settled into a red state. A further increase to  $2.0 \times 10^{-2}$  led to the same unstable path but reached a red state quicker, in 12,000 years, with a total mass of 152 M $_{\odot}$ . With rates between  $2.0 \times 10^{-2}$  and  $3.1 \times 10^{-2}$ , we observed that at  $2.5 \times 10^{-2}$ , the star moved directly to a red state with a mass of 19 M $_{\odot}$  in just 10 years. This indicates the critical rate before the main sequence as  $2.5 \times 10^{-2}$ .

In another test at point 'IV' (later in the early development phase), shown in Figure 7.11, the star briefly moved to a blue state when the mass gain rate decreased. If the rate dropped below  $2.5 \times 10^{-2}$ , the star moved to a blue state within the surface cooling timescale. From these tests, we confirm that the critical accretion rate before the main sequence is  $2.5 \times 10^{-2}$ .

We also conducted numerical tests on model 4477 during the core hydrogen burning phase to derive a more accurate  $\dot{M}_{crit,MS}$ . We selected constant accretion rates between  $1.0 \times 10^{-6}$  and  $2.5 \times 10^{-2}$ . It was observed that accretion rates under  $1.0 \times 10^{-3}$  did not alter the model's position on the HR diagram, as it continued to burn hydrogen in the blue region. When the rate reached

approximately  $4.0 \times 10^{-3}$ , the model exhibited an oscillation in effective temperature, ranging from  $T_{\rm eff} = 4.50$  to 4.75. An accretion rate of  $7.0 \times 10^{-3}$  caused the model to transition to the red region over a Kelvin-Helmholtz timescale, remaining on the Hayashi limit so long as this critical rate was sustained. We deduce that the critical accretion rate for the core hydrogen burning phaseâgiven a mass of 3984  $M_{\odot}$  and a central hydrogen abundance of 0.55âis  $\dot{M}_{crit,MS} = 7.0 \times 10^{-3}$ . Our understanding suggests that this accretion rate depends on both the mass and central hydrogen mass fraction. A thorough quantitative analysis, however, would necessitate further study, which is beyond the scope of this thesis.

# 7.5.2 Luminosity wave and crit

The relationship between the emergence of a luminosity wave and protostar expansion was initially investigated by Larson (1972). Using a model of a 2 star, Larson underscored the role of radiative entropy transfer once the core temperature hits  $9.0 \times 10^6$  K, a condition characteristic of the early pre-MS phase. This radiative entropy is conveyed from the center to the outer core boundary over a thermal relaxation timescale. As the wave advances outward, the star experiences a transitory radius expansion when the wave reaches the surface. The initial structure of the protostellar seedâwhether convective or radiativeâinfluences the luminosity wave's migration from the core to the surface, subsequently impacting the star's radius. This effect was examined by Stahler et al. (1986), who noted the extremely brief duration of this event (230 years) and posited the difficulty of observing such a quick process. Our research aligns with Stahler et al. (1986)'s conclusions, finding the wave's migration to last 190 years.

Further in-depth study of the luminosity wave's migration in accreting stars was conducted by Hosokawa et al. (2010b). With an accretion rate of  $3\times 10^{-3}~\rm M_\odot~\rm yr^{-1}$ , they determined that expulsion of the luminosity wave from the star's surface induces contraction towards the Zero Age Main Sequence (ZAMS). Subsequent studies by Hosokawa et al. (2013a), Woods et al. (2017), and Haemmerlé et al. (2018) extended the range of examined accretion rates and uncovered a critical rate coinciding with the luminosity wave's surface breach, dictating the star's shift towards either the blue or red regions. Our findings corroborate that the luminosity wave arises early in the pre-MS phase. All models, irrespective of accretion, display a radius increase when the wave breaks at the surface. The decision for a star's evolution towards the red or blue spectrum appears only marginally influenced by the luminosity wave, being primarily driven by the accretion rate. Crucially, as mentioned earlier, a critical accretion rate during the pre-MS of  $_{\rm crit,preMS} = 2.5 \times 10^{-2}~\rm M_{\odot}~\rm yr^{-1}$  is identified, beyond which models invariably move towards the red, independent of other ongoing physical phenomena.

# 7.5.3 Variable accretion rates and model comparisons

The transition away from a steady accretion rate is anticipated when the accretion disk surrounding a Population III (Pop III) star undergoes gravitational instability and fragments, a process described by Stacy et al. (2010). The inward migration of these fragments into the disk and eventually onto the star may lead to sporadic accretion bursts, suggesting a fluctuating accretion history as posited by Greif et al. (2012). The progression of Pop III stars through to the cessation of core silicon burning has been simulated by Ohkubo et al. (2009), who integrated variable accretion rates based on the studies by Yoshida et al. (2006) and Yoshida et al. (2007). Their models culminated in a blue supergiant phase with the helium burning stage concluding at  $\log(T_{\rm eff}) > 4.6$ . Contrarily, our findings indicate that our models transition to a red phase with  $\log(T_{\rm eff}) \approx 3.76$  at the onset of helium burning, maintaining this phase until the termination of their evolutionary cycle. This discrepancy may arise from differing approaches to the modeling of energy transport within the stars' outer layers.

Our models that incorporate variable accretion rates exhibit evolutionary trajectories akin to the red supergiant protostar models by Woods et al. (2017) and Haemmerlé et al. (2018) with accretion rates surpassing  $10^{-2} \, \mathrm{M_{\odot}} \, \mathrm{yr^{-1}}$ . Despite the variability in accretion rates, the work of Sakurai et al. (2016a) indicates that the expansion of the stellar radius during the initial pre-MS phase (time < 1000 years) parallels that of models assuming a constant accretion rate. This phenomenon is corroborated by our models, as illustrated in the right panel of Figure 7.12, and aligns with the observations reported by Sakurai et al. (2016a).

### 7.5.4 Impact of accretion on physical parameters

The accretion history, including episodic bursts, significantly influences the physical characteristics of our models. Despite the near-uniformity of the pre-MS lifetimes across all modelsâwhich inversely correlate with massâslight variations do emerge, attributable to fluctuations in the accretion rate during this phase, as exemplified by model 1923. Likewise, the overall lifespan of the models is impacted, as is observable in models 1135 and 1923. This phenomenon stems from these models accreting a substantial fraction of their final mass later in their accretion history, thus prolonging their duration compared to other models. The period spent in the red phase for each model escalates with mass due to the elevated mean accretion rate throughout their evolution. However, should the accretion history be erratic and surpass  $\dot{M}_{\rm crit,preMS}$ , the star is likely to experience a considerable portion of its life in the red, as is the case for model 1662, which resides in this phase for 59% of its total lifetime. Notably, due to the early formation of intermediate convec-

tive zones and an extended red phase, model 1662 exhibits significant surface helium enrichment, reaching a value of 0.76.

### 7.5.5 Kelvin-Helmholtz timescale versus accretion timescale

The decisive timescale that governs the evolutionary paths of accreting massive stars has been examined by Stahler et al. (1986); Omukai & Palla (2003); Hosokawa & Omukai (2009). These studies delineate the Kelvin-Helmholtz (KH) timescale, representing the thermal relaxation period during which a star can dissipate its gravitational energy ( $\tau_{KH} = GM^2/RL$ ), and juxtapose it with the accretion timescale, which is indicative of the time required for stellar mass increase ( $\tau_{accr} = M/\dot{M}$ ). The transition from blue to red in models is determined by the interplay between these timescales; models expand and turn red if  $\tau_{accr} < \tau_{KH}$ , but contract and shift blue when  $\tau_{accr} > \tau_{KH}$ . Nonetheless, during the pre-MS stage, some of our models (e.g., model 4477 in the right panel of Figure 7.11) persist in expanding and moving redward even when  $\tau_{accr} > \tau_{KH}$ , indicating a conundrum.

This discrepancy was initially probed by Sakurai et al. (2015), who suggested that the global KH timescale ( $GM^2/RL$ ) oversimplifies the situation. Instead, they propose considering the KH timescale at the star's surface layer, where rapid accretion prevents the outer layers from achieving thermal equilibrium, thereby driving the star redward. Thus, the appropriate metric is the KH timescale of these surface layers. Sakurai et al. (2015) define this as:

$$(t_{\rm KH,surf} = \frac{f \int s_{\rm rad} T \, dm}{\int dl}) \tag{7.1}$$

where  $s_{\rm rad}$  is the radiation entropy, T is temperature, m represents the mass of the enclosed region, l its luminosity, and f is the fraction of total entropy dissipated over the timescale. Sakurai et al. (2015) applied this formula to the outer 30% of the star, termed the envelope. We corroborate their findings in our models, confirming that where expansions towards the red occur, the surface layer KH timescale indeed exceeds the accretion timescale, i.e.,  $\tau_{accr} < \tau_{KH,surf}$ . The more rudimentary approach, which produces  $\tau_{accr} > \tau_{KH}$ , is thus misleading.

Moreover, by applying the surface Kelvin-Helmholtz timescale expression to models at the point of their transition from red to blue (for instance, model 1662 at  $\log(L/L_{\odot})=6.30$  in the right panel of Figure 7.11), we validate the critical accretion rate during the pre-MS phase ( $\dot{M}_{\rm crit,preMS}$ ), which we established through numerical experiments, to be  $2.5 \times 10^{-2} \ {\rm M}_{\odot} \ {\rm yr}^{-1}$ . At this critical intersection,  $\tau_{\rm accr} \equiv \tau_{\rm KH,surf}$ , and thus we can express the critical accretion rate as  $\dot{M}_{\rm crit,preMS} = \frac{M_{\rm envelope}}{\tau_{\rm KH,surf}}$ . During the pre-MS phase, the star's inner regions are subject to gravitational contraction

while the envelope undergoes expansion. Given that  $t_{\rm KH,surf}$  yields a more nuanced approximation of the timescale for a specific Lagrangian coordinate, it becomes crucial to utilize this timescale when ascertaining a transition from red to blue during the pre-MS evolution. Nonetheless, should accretion surpass  $\dot{M}_{\rm crit,MS}$  during the main-sequence phase of core hydrogen burning, as observed in model 4477, the star's interior regions would contract over a substantially elongated nuclear timescale. Consequently, in such scenarios, the global Kelvin-Helmholtz timescale is adequate for predicting the transition.

### 7.6 Conclusion

In this study, we have delved into the evolutionary trajectories of massive Pop III stars while considering the effects of variable accretion rates. The stellar evolution code GENEC was utilized to simulate the early stages of stellar development, and through this, we have conducted an indepth examination of the critical accretion rate, the influence of the luminosity wave, and the implications of accretion on the physical characteristics of these stars. Our key discoveries are outlined below:

- A critical accretion rate ( $\dot{M}_{\rm crit,preMS}$ ) of  $2.5 \times 10^{-2} {\rm M}_{\odot} \, {\rm yr}^{-1}$  has been identified, which signals the shift of massive Pop III stars into the red phase during disc accretion in the pre-main-sequence (pre-MS) phase. This benchmark aligns with previous findings and lays a solid groundwork for subsequent investigations.
- A pivotal accretion rate for the hydrogen-burning stage has been uncovered, valued at  $7.0 \times 10^{-3} \rm M_{\odot} \, yr^{-1}$ .
- The duration over which model 4477 undergoes a color transition from blue to red during its core hydrogen-burning phase spans 17.5 kyr. This interval is influenced by the critical main-sequence accretion rate ( $\dot{M}_{\rm crit,MS}$ ) and stands in comparison to the global Kelvin-Helmholtz timescale ( $\tau_{KH} \approx GM^2/RL$ ) of the star at the point of transition.
- The significance of the surface Kelvin-Helmholtz timescale has been reaffirmed in dictating
  the shift of a star towards the red or blue supergiant categories during the pre-MS phase, as
  opposed to the traditional global Kelvin-Helmholtz timescale.
- It has been evidenced that the luminosity wave exerts only a marginal effect on the initial pre-MS phase of stellar evolution; the trajectory towards either red or blue evolution is more substantially governed by the accretion rate.

 Our computational models have shown that fluctuating accretion rates wield a considerable influence on the physical parameters of Pop III stars, including aspects such as their overall lifespan, the duration spent in the red phase, and the extent of surface helium enrichment.

In conclusion, our research contributes significant insights into the initial phases of stellar evolution and the intricate mechanisms that dictate the lifecycles of primordial stars. The findings of our inquiry lay a firm groundwork for future explorations and the refinement of theories concerning the progression of massive Pop III stars. Considering the paramount importance of accurately determining the critical accretion rate for subgrid models in cosmological simulations, we advocate for the adoption of an accretion rate of  $\dot{M}=7\times 10^{-3} \rm M_{\odot} \, yr^{-1}$  as a standard in most scenarios. For instances where subgrid modeling is sensitive enough to encapsulate the pre-main-sequence (pre-MS) timescale, which is projected to be around 10 kyr, the critical accretion rate should be elevated to  $\dot{M}=2.5\times 10^{-2} \rm M_{\odot} \, yr^{-1}$ .

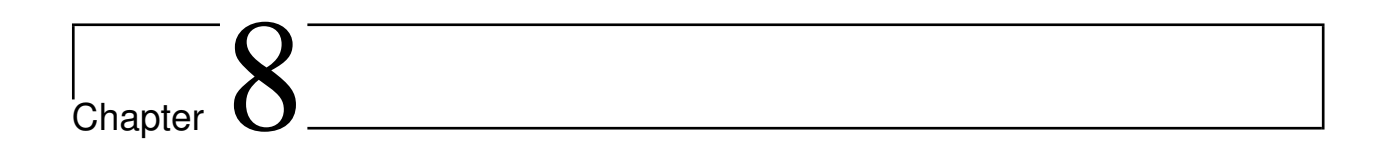
Prospective research in this domain may extend to a broader spectrum of accretion rates and delve into varied accretion profiles to deepen our comprehension of the factors influencing the patterns observed. Further enhancement of the models could be achieved by integrating more complex simulations of radiative transfer, stellar winds, and mixing processes. Such advancements are poised to enrich our collective knowledge of the Universe's nascent stages and the seminal influence of primordial stars in the cosmic tableau.

 $geometry\ xcolor\ colortbl\ tabularx\ graphicx\ multirow\ a4paper,\ total=170mm,257mm,\ left=20mm,\ top=20mm$ 

natbib

graphics graphicx epstopdf longtable url bm soul

[varg]txfonts pdflscape supertabular hyperref xcolor [normalem]ulem natbib amsmath



# Chemical signatures of PopIII supermassive stars

### 8.1 Introduction

This chapter is adapted from the work by Nandal et al 2024. Recent data from the James Webb Space Telescope (JWST), particularly of the high-redshift galaxies GN-z11 and CEERS-1019, have provided valuable insights into the early Universe. These observations have significant implications for our understanding of massive star formation and galaxy evolution during the Universe's early stages. Our study aims to connect the latest observational data with theoretical models of stellar evolution, focusing on massive Population III (Pop III) stars. These stars, formed shortly after the Big Bang and lacking in metals, play a crucial role in the chemical evolution of galaxies and the formation of supermassive black holes (SMBHs). Understanding Pop III stars is essential for explaining the early chemical enrichment of the Universe. The unique chemical signatures observed in GN-z11 and CEERS-1019, such as the high nitrogen-to-oxygen (N/O) ratios, challenge traditional models of stellar nucleosynthesis and galactic chemical evolution. These findings suggest a significant influence from very massive and supermassive stars in the early Universe. Building on our previous work, which modeled massive stars ranging from 491 to 6127 solar masses, this research investigates the chemical signatures of such massive objects. We aim to determine if our theoretical models can reproduce the observed N/O, C/O, and O/H ratios in high-redshift galaxies (see section 8.4, providing insights into the nature of Pop III supermassive stars (8.7).

# 8.2 Literature review

The observation of nitrogen-enhanced high-z galaxies, particularly in GN-z11 (Oesch et al. 2016) and CEERS-1019 (Finkelstein et al. 2017), has sparked a revolution in the study of the universe's earliest star and galaxy formation. GN-z11, located at a redshift of z=10.6 (Bunker et al. 2023), exhibits a N/O abundance ratio in its interstellar medium (ISM) that is more than four times the solar value ( $\log(N/O) > \sim -0.25$ ) (Cameron et al. 2023; Senchyna et al. 2023). This ratio is not only significantly higher than what is typically found in low-redshift galaxies and HII regions with comparable metallicity ( $12 + \log(O/H) < \sim 8.0$ ) but also slightly exceeds the values observed in galaxies with super-solar metallicities (Vincenzo et al. 2016; Berg et al. 2019). Although the C/O ratio of GN-z11 is consistent with normal values, it is poorly constrained (Cameron et al. 2023).

Similarly, CEERS-1019, at a redshift of z=8.678, displays strong nitrogen emission lines of N III and N IV, with the N IV]  $\lambda 1486$  being the most intense line in its rest-frame UV spectrum (Tang et al. 2023). This galaxy has an unusually high N/O abundance ratio of  $\log({\rm N/O})=-0.13\pm0.11$ , which is approximately 5.6 times the solar ratio. However, its C/O and Ne/O ratios, with values of  $\log({\rm C/O})=-0.75\pm0.11$  and  $\log({\rm Ne/O})=-0.63\pm0.07$  respectively, are relatively normal for its metallicity (Marques-Chaves et al. 2023).

These observations challenge the conventional theories of stellar yields and galactic chemical evolution, necessitating a reexamination of the dynamics of the early universe. In particular these unusual abundance patterns in high-z galaxies may be a signature of massive, very massive, and supermassive stars (MSs, VMSs, and SMSs) <sup>1</sup> in early galaxies. Moreover, these massive objects may well explain the appearance of central massive black holes in these galaxies as well (e.g. Natarajan et al. 2023) and their role in the formation of supermassive black holes (SMBHs) in the early universe is a subject of ongoing research (Hosokawa et al. 2010a; Ekström et al. 2012a; Woods et al. 2017; Haemmerlé et al. 2018; Woods et al. 2021).

A number of recent studies have attempted to explain the unusually high Nitrogen abundances (as well as the other metal abundances) observed in these high-z galaxies. Kobayashi & Ferrara (2023) explain these signatures using a rapid chemical enrichment mechanism via a dual-burst model where a quiescent period lasting approximately 100 Myr separates the bursts. In their model, Wolf-Rayet stars become the dominant enrichment source during the second burst - enriching the ISM with heavy elements. Their single burst model, like ours described here, requires the presence of massive stars with masses in excess of  $\sim 1000 \, \mathrm{M}_{\odot}$ . Along similar lines both Char-

 $<sup>^{1}</sup>$ We consider stars to be massive within 10-100  $M_{\odot}$ , very massive within 100-1000  $M_{\odot}$ , extremely massive within 1000-40,000  $M_{\odot}$  and supermassive with mass above 40,000  $M_{\odot}$  as described in the work by Woods et al. (2020)

bonnel et al. (2023) and Nagele & Umeda (2023) have studied the impact that metal enriched stars in mass range of  $10^3$  -  $10^5$  M $_\odot$  can have in high-z galaxies. In both of these studies the authors have been able to reproduce the high  $\log({\rm N/O})$  abundance ratios observed in GN-z11. Several other studies have sought to explore different stellar evolution channels on the early chemical evolution of the universe. For instance, Meynet & Maeder (2006); Choplin et al. (2018) investigated the impact of fast-rotation on the nucleosynthetic outputs of massive stars. These yields were then used in models for the early chemical evolution of the Milky Way by Chiappini et al. (2003, 2006b); Cescutti et al. (2013) showing that the chemical composition of the bulk of halo stars is compatible with yields coming from fast rotating models. The potential role of pair-instability supernovae in the early universe was analyzed by Heger et al. (2002). Although these studies have shed light on different aspects, the exact elemental yields and enrichment potential of VMSs and SMSs remain largely unexplored (Denissenkov & Hartwick 2014).

In this chapter, we adopt a novel approach by combining radiation hydrodynamic simulations and stellar evolution modeling to compute the expected metal yield from a population of massive Population III (PopIII) stars. Using the accretion rates from Regan et al. (2020b), we compute eleven PopIII models from the pre-main sequence (PreMS) until the end of core helium burning. We delve into the results of individual stellar models and the integrated halo population, revealing new insights into the N/O, C/O, and O/H number fractions, and taking into account the possible of an additional population of one hundred 20  ${\rm M}_{\odot}$  stars. Specifically, we find that chemical enrichment coming from the ejecta of very massive stars, computed with a variety of assumptions can reproduce the observed N/O number fractions, while we successfully match the observed C/O abundances when pulsations from the massive PopIII stars remove all mass above the CO core. Finally to match the O/H number fractions we require a dilution factor (given by the ratio of the mass of the ejecta to that of the interstellar medium with which the ejecta mixed) of 100, entirely consistent with expected ratios of chemical abundances in gas rich high-z galaxies. This study not only provides significant insights into the chemical enrichment of the early universe and the role of supermassive PopIII stars, but also underscores the necessity for further investigations into the complex but pivotal role of massive PopIII stars in the early Universe.

### 8.3 Methods

### 8.3.1 Cosmological Context

This study aims to estimate the metal enrichment resulting from massive stars undergoing pulsational mass loss in early Universe haloes. Utilizing the radiation hydrodynamical simulations

from Regan et al. (2020b), we extend our previous work (Nandal et al. 2023c) on critical accretion rates for massive PopIII stars. Specifically, we post-process the stars identified in Regan et al. (2020b) to compute their expected metal yields, employing the same stellar evolution code as in Nandal et al. (2023c).

For a comprehensive understanding of both Regan et al. (2020b) and Nandal et al. (2023c), we direct readers to the original papers. Briefly, Regan et al. (2020b) conducted cosmological zoom-in simulations using the Enzo code (Bryan et al. 2014; Brummel-Smith et al. 2019) to examine pristine, atomic cooling haloes. These simulations originated from the work of Wise et al. (2019) and Regan et al. (2020a), part of the *Renaissance* simulation suite (Chen et al. 2014; O'Shea et al. 2015; Xu et al. 2016). In this detailed study, Regan et al. (2020b) documented the emergence of 101 massive stars within a single halo, accumulating a total mass of about 90,000 within approximately 2 Myr since the first star formed. The stars varied in mass from 40 to over 6000 , and accretion rates ranged from below  $10^{-3}$  to nearly 1 at peak times.

The accretion rates from these cosmological simulations are critical inputs for our stellar evolution modeling, a unique aspect of this research. In Nandal et al. (2023c), we selected 11 datasets from the underlying cosmological simulations of Regan et al. (2020b), representing a diversity in accretion histories and stellar masses. We use these datasets to model stars with final masses between 491 and 6127 . Following the pre-main sequence (PreMS) stage to the conclusion of core helium burning, these stars were modeled using the Geneva stellar evolution code (GENEC) (Eggenberger et al. 2008). A consistent chemical composition was maintained (X = 0.7516, Y = 0.2484, Z = 0), and a deuterium mass fraction  $X_2 = 5 \times 10^{-5}$  was adopted, in line with prior studies. Each model began with a 2  $M_{\odot}$  fully convective seed, and accretion was simulated through a thin cold disc, following Palla & Stahler (1992) & Hosokawa et al. (2010a).

Nandal et al. (2023c) required various enhancements to GENEC, such as integrating functionality for variable accretion rates and improving spatial and temporal resolution to accommodate fluctuating accretion histories. However, the study did not explicitly include effects of rotation and mass loss. We assume these massive stars experience mass loss, potentially through pulsations or stellar winds induced by increased surface opacity changes due to convection. This work does not numerically model mass loss but tests various hypotheses under the assumption that some mass loss occurs during stellar evolution. Besides the 11 models already computed in Nandal et al. (2023c), we developed an additional model with a constant accretion rate of  $3.5\times10^{-3}$ , culminating in a final mass of 8904  $M_{\odot}$ . This model was created to explore the limits of metal enrichment in a halo, particularly focusing on matching the observed N/O, C/O, and O/H values in GN-z11 and CEERS 1019.

# 8.3.2 Massive PopIII Star (Nitrogen) Enrichment

Our approach to account for the abundance patterns observed in high-redshift galaxies like GN-z11 and CEERS1019 is based on enrichment by very and extremely massive PopIII stars. These stars start their evolution as accreting protostars during the pre-Main Sequence (pre-MS) phase, which typically lasts less than  $10^5$  years, as illustrated in Figure 8.1. Transitioning to the main sequence, they begin core hydrogen burning and initially have a convective core with a radiative envelope. This stage of evolution is detailed in Nandal et al. (2023c).

Should the star's accretion rate exceed approximately  $2.5 \times 10^{-3}$ , it can shift to the red phase either during pre-MS or MS. Our models include this transition. Post-main sequence, these stars turn red and develop a nearly fully convective structure before core helium burning commences. This convective activity promotes the transport of chemical elements from the core to the surface. We posit that the unstable nature of these massive PopIII stars, as suggested by Nagele et al. (2022), leads to substantial mass loss. The exact amount of mass lost through winds or pulsations is challenging to quantify; hence, we parameterize this by analyzing the impact of different mass loss amounts (see §8.4.3)<sup>2</sup>.

Upon completion of helium and silicon core burning, such stars might either explode as supernovae (Nagele & Umeda 2023) or collapse directly into black holes, as suggested by Montero et al. (2012). For stars with masses above approximately 260 , a direct collapse into a black hole is typically expected. However, certain mass ranges might lead to supernova explosions (e.g., Chen et al. 2014; Moriya et al. 2021), though observational evidence to define these ranges is lacking. In the case of massive PopIII stars with masses between  $10^3-10^4$ , we observe that the expulsion of surface material, enriched with nitrogen, can lead to a black hole accretion disk with high nitrogen content. This observation is a crucial signature of massive PopIII mass loss episodes and aligns with recent findings on nitrogen-rich quasars, as detailed in Bunker et al. (2023) and Cameron et al. (2023).

### **Model for the Wind Enrichment**

In our investigation, we explore a scenario where a star contributes to the chemical enrichment of its surrounding interstellar medium (ISM) by shedding mass during its evolution. Given the limited understanding of mass loss rates in contemporary massive stars (Sabhahit et al. 2023), and the lack of observational data for early universe massive stars, our approach involves parameterizing the mass-loss rates of these stars. We outline our parameterization method as follows. We

<sup>&</sup>lt;sup>2</sup>A method similar to Liu et al. (2021) was employed to investigate the impact of winds from Pop III massive stars.

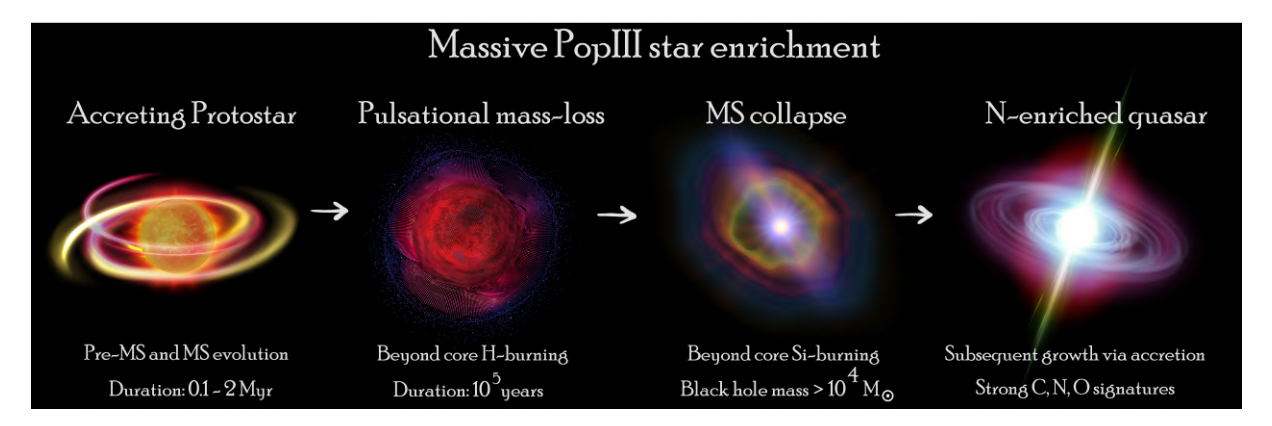


Figure 8.1: An illustration depicting the massive PopIII enrichment scenario. From left to right: (1) The formation of a massive PopIII star via accretion which generally occurs during the pre-MS but some stars may undergo short accretion phases during MS. If the accretion rate is below the critical limit described in Nandal et al. (2023c), the star migrates to blue. (2) The transition to red at the end of core helium burning leads to the formation of large convective zones and pulsational mass loss as shown by the red mesh. (3) The collapse of a MS may lead to additional mass ejected and the eventual formation of a black hole. (4) Further accretion of ejected material onto the black hole creats the conditions for allowing nitrogen absorption lines to appear, as in the case of GN-z11 and CEERS 1019.

assume the stars undergo mass loss during or after the core helium-burning phase. This is a stage when the star is in the red part of the HR diagram, potentially experiencing significant pulsational instabilities, and when the star's surface is rich in heavy elements, leading to increased opacity. The total mass of element i ejected by the star, denoted as  $M_{EJ}(i)$  in solar masses, is calculated as  $\bar{X}_i M_{EJ}$ , where  $\bar{X}_i$  represents the average mass fraction of element i in the star's ejecta, and  $M_{EJ}$  is the total mass ejected. The average mass fraction  $\bar{X}_i$  is defined by the equation:

$$\bar{X}_{i} = \int_{M_{\rm cut}}^{M_{\rm tot}} X_{i}(M_{\rm r}) \, \mathrm{d}M_{\rm r}/M_{\rm EJ} \tag{8.1}$$

where  $M_{\rm cut}$  is the mass coordinate above which mass loss is assumed,  $M_{\rm r}$  is the mass coordinate where Xi is evaluated. In this study, we consider three distinct values for  $M_{\rm cut}$ : 1) 10% of the star's total mass; 2) 40% of the star's total mass; and 3) all mass above the CO core. The CO core is identified as the region below which less than  $10^{-3}$  Helium mass fraction ( $Y_c$ ) is present. Thus, the mass below  $M_{\rm cut}$  is presumed to collapse into a black hole, with  $M_{\rm tot}$  being the star's total mass at the time of core collapse. The ejected mass from a star interacts with the interstellar medium (ISM), resulting in a combination of the star's ejecta and the ISM. This interaction involves a mass of the ISM denoted as  $M_{\rm ISM}$ . We introduce a dilution factor f, defined as the ratio  $M_{\rm ISM}/M_{\rm EJ}$ . Due to uncertainties in various factors, such as the dynamics of the explosion or collapse and the state of the ISM, we treat f as a variable parameter, which we vary from 1 to 1000 in our analysis. We denote  $X_{\rm io}$  as the mass fraction of element i in the ISM at the time of ejection.

In this model, mass ejection from a star occurs during the early stages of halo evolution. As stars progress through their life cycles and eject CNO-rich material into the ISM, the chemical composition of the ISM within the halo evolves over time. Initially, the chemical composition of a PopIII star is pristine, consisting only of hydrogen and helium, but it becomes enriched with CNO elements as the star evolves and releases material into the ISM.

Our study's critical goal is to estimate the final chemical composition of the mixture of the star's ejecta and the ISM. We calculate  $\mathbf{X_{im}}$ , the mass fraction of element  $\mathbf{i}$  in this mixture, based on the principle of mass conservation:

$$X_{im} \times (M_{EJ} + M_{ISM}) = \bar{X}_i \times M_{EJ} + X_{io} \times M_{ISM}$$
(8.2)

By incorporating the dilution factor  $\mathbf{f} = M_{\rm ISM}/M_{\rm EJ}$ , the above equation simplifies to:

$$X_{im} \times (1+f) = \bar{X}_i + f \times X_{io}$$
(8.3)

# 8.3.3 Extrapolation to Galactic Scale

To extend our model to a galaxy containing n stars, we define  $\mathbf{n}(\mathbf{M}_{\text{ini}})$  as the number of stars in the galaxy with initial masses in the range from  $\mathbf{M}_{\text{ini}}$  to  $\mathbf{M}_{\text{ini}}$  +  $\mathbf{d}\mathbf{M}_{\text{ini}}$ . The average mass fraction of element  $\mathbf{i}$  in the combined ejecta of all stars in the galaxy is calculated using the following formula:

$$X_{ip} = \sum_{M_{ini}} \frac{n(M_{ini}) \times \bar{X}_i(M_{ini}) \times M_{EJ}(M_{ini})}{n(M_{ini}) \times M_{EJ}(M_{ini})}$$
(8.4)

Here,  $X_{ip}$  represents the mass fraction of element i in the ejecta of all the stars. By assuming the same dilution factor f as before, we can calculate the mass fraction in the ISM after enrichment from the stars:

$$X_{imp} = \frac{X_{ip} + f \times X_{io}}{1 + f} \tag{8.5}$$

We assume that the formation of stars in the galaxy starts at zero metallicity, thus taking  $\mathbf{X_{io}}$  as zero for elements C, N, O, and 0.7516 for  $\mathbf{X_{H,ini}}$ . Consequently, for all elements except Hydrogen, the mass fraction in the ISM following enrichment can be approximated as:

$$X_{\rm imp} \approx \frac{X_{\rm ip}}{1+f} \tag{8.6}$$

Therefore, the mass fraction of element i in the ISM post-enrichment is essentially the ejected fraction,  $\mathbf{X_{ip}}$ , divided by the dilution factor,  $\mathbf{f}$ , especially if  $\mathbf{f}$  is significantly larger than 1. The initial mass function for the halo is determined from the simulation, as illustrated in Fig. 8.3. The

Table 8.1: Mean abundances in mass fraction of different chemical species in the mass ejected by 11 massive PopIII star models. The first column shows the final mass of each model and the second column depicts the mass of CO core at the end of core helium burning. The next 5 columns depict the mean abundances (see Eq.8.1 in mass fraction for  $^1H$ ,  $^4He$ ,  $^{12}C$ ,  $^{14}N$  and  $^{16}O$  when the outermost 10% of total mass is ejected. The following 5 columns are the mean abundance in the ejecta when 40% of outermost total mass is ejected and the final 5 columns when all the mass above CO core is ejected.

*17X								
$M_{ m tot}$ $M_{ m CO}$ $X_{ m H}$ $X_{ m He}$ $X_{ m C}$ $X_{ m N}$ $X_{ m O}$ $X_{ m H}$ $X_{ m He}$ $X_{ m C}$ $X_{ m N}$ $X_{ m O}$ $X_{ m H}$ $X_{ m He}$ $X_{ m C}$ $X_{ m N}$ $X_{ m O}$								
$(M_{\odot})$ $(M_{\odot})$	10%	40%	CO core					
491 104 0.360 0.43	30 0.002 0.056 0.150	0.256 0.450 0.002 0.079 0.2	10 0.235 0.451 0.002 0.084 0.224					
771 165 0.319 0.46	60 0.002 0.053 0.162	$0.235\ 0.466\ 0.002\ 0.074\ 0.2$	18 0.217 0.465 0.002 0.079 0.232					
778 163 0.299 0.47	73 0.003 0.038 0.180	0.240 0.454 0.002 0.058 0.2	35 0.220 0.447 0.002 0.065 0.253					
932 247 0.339 0.58	88 0.002 0.056 0.015	0.185 0.682 0.002 0.102 0.0	28 0.161 0.695 0.003 0.108 0.031					
1135 440 0.204 0.60	69 0.003 0.086 0.038	0.124 0.691 0.003 0.122 0.0	058 0.115 0.691 0.005 0.126 0.063					
1331 317 0.293 0.5	19 0.005 0.067 0.114	0.201 0.528 0.003 0.103 0.1	163 0.186 0.528 0.003 0.108 0.172					
1662 630 0.198 0.70	66 0.001 0.031 0.004	0.095 0.852 0.001 0.047 0.0	004 0.078 0.864 0.002 0.050 0.006					
1923 746 0.232 0.53	77 0.001 0.046 0.137	0.181 0.573 0.001 0.061 0.1	74 0.171 0.571 0.001 0.064 0.183					
3053 650 0.202 0.73	37 0.000 0.018 0.004	0.202 0.737 0.000 0.022 0.0	004 0.157 0.765 0.001 0.033 0.012					
4477 759 0.297 0.68	87 0.000 0.015 0.001	0.153 0.816 0.001 0.029 0.0	001 0.073 0.884 0.003 0.034 0.006					
6127 1252 0.173 0.7	779 0.001 0.039 0.006	0.079 0.855 0.001 0.056 0.	008 0.040 0.875 0.004 0.060 0.017					

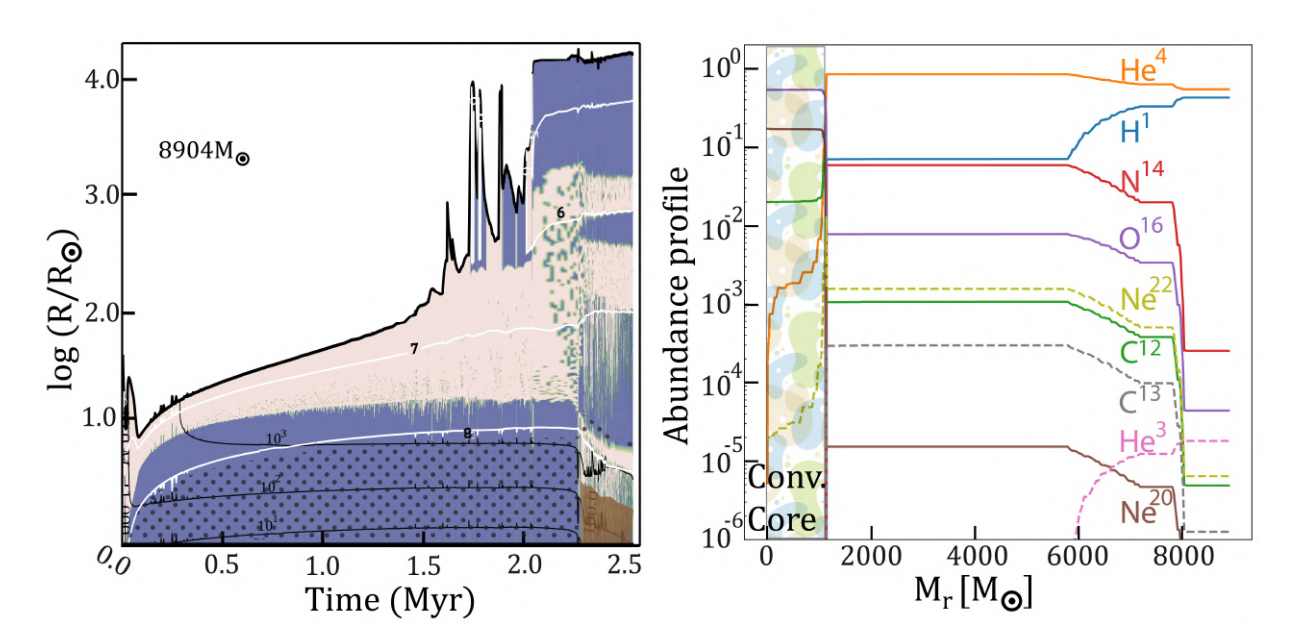


Figure 8.2: Test model with a final mass of 8904  $M_{\odot}$  computed using a constant accretion rate of 3.5until the end of core helium burning. *Left panel*: The Kippenhahn diagram showing the evolution of radius versus time. The blue and cream regions represents the convective and radiative zones respectively. Core hydrogen burning is shown in dotted zone and core helium burning in brown zone. The black lines represents the iso-masses and the white lines depict the iso-thermal lines. *Right panel*: The abundance profile inside the 8904  $M_{\odot}$  model at the end of core helium burning. The label for each element matches the corresponding line.

aim of this study is to systematically investigate the various integrated abundances (i.e.,  $\mathbf{X_{imp}}$ ) expected from very massive PopIII stars in the earliest galaxies.

# 8.4 Results

# 8.4.1 Transport of Chemical Species in Massive Pop III Stars

In our study, we explore the evolution of a typical massive Pop III star with a constant accretion rate. The left panel of Figure 8.2 illustrates the developmental stages of a star that ultimately reaches a mass of 8904  $M_{\odot}$ . This model, employing a constant accretion rate of  $3.5\times 10^{-3}$ , is inspired by the findings of Nandal et al. (2023a). They reported that the evolutionary paths beyond core hydrogen burning are remarkably similar, whether the accretion rate is constant or variable. Hence, this new model, alongside the 11 models from Nandal et al. (2023c), helps in understanding the advanced evolutionary stages and chemical structures of massive stars. It is important to note that this model's accretion history, unlike the other 11 models, was not derived from hydrodynamic simulations. Consequently, its stellar yields are not included in the overall calculations for the mini halo sub-population. This model primarily serves to elucidate the structure of such massive stars and to investigate their individual N/O, C/O, and O/H ratios later in this study.

The star undergoes a pre-main sequence (pre-MS) evolution lasting less than  $10^5$  years, initiating hydrogen burning in the blue region of the HR diagram with a log ( $T_{\rm eff}$ ) = 4.90 (Nandal et al. 2023c). Around 1.5 Myr into its evolution, the star begins to migrate towards the red side of the HR diagram. This migration phase, with an accretion rate lower than the critical  $\dot{M}_{\rm crit,MS} = 7.0 \times 10^{-3}$  $M_{\odot} \text{ yr}^{-1}$  identified by Nandal et al. (2023c), leads to oscillations between red and blue phases up to approximately 2 Myrs. As core hydrogen becomes depleted, the star settles in the red region with an effective temperature of log  $(T_{\rm eff}) = 3.70$ . During this phase, the star's structure transforms from a convective core with an extended radiative envelope into a configuration featuring a convective core, several intermediate convective zones, and an expansive convective envelope. This near-fully convective arrangement effectively transports chemical elements from the core to the surface, facilitating significant enrichment without rotational influences. Notably, this fully convective state only emerges at the end of core hydrogen burning, absent during earlier red-blue oscillations between 1.5 - 2 Myrs, as illustrated in the left panel of Figure 8.2. Our models, developed using the code, demonstrate that the structural characteristics of such stars are consistent across the mass spectrum of 200 -  $10^5$  M $_{\odot}$ , regardless of rotation. The right panel of Figure 8.2 presents the chemical abundance profile of a massive  $8904~M_{\odot}$  star at the conclusion of its core helium burning stage. The convective core extends up to a mass coordinate of 1142 M<sub>☉</sub>, above which the influence of extensive intermediate convective zones becomes apparent. The flat element profiles up to  $5800~M_{\odot}$  indicate robust mixing in these zones. Between  $5800~and~7800~M_{\odot}$ , smaller intermediate convective zones facilitate some degree of mixing, as evident from the negative gradient in the element abundance profiles (right panel, Figure 8.2). Additionally, a substantial convective zone extending from a radius of 1600 to 15848  $R_{\odot}$  and a mass range from 8000 to 8904  $M_{\odot}$  levels out the abundance profiles, significantly impacting the surface compositions. This nearfully convective structure alters the abundances of various elements such as  $^{1}H$ ,  $^{3}He$ ,  $^{4}He$ ,  $^{12}C$ ,  $^{13}C$ ,  $^{14}N$ ,  $^{16}O$ ,  $^{20}Ne$ , and  $^{22}Ne$  compared to their initial values.

During the core hydrogen burning phase, these massive stars are expected to generate energy via the CNO cycle, as discussed in Woods et al. (2017, 2021). However, the limited amount of CNO material restricts significant  $^{14}$ N production at this stage. Instead,  $^{14}$ N is predominantly produced during the core helium burning phase. The process begins with the synthesis of  $^{12}$ C in the helium-rich convective core via the triple- $\alpha$  reaction. This  $^{12}$ C is then conveyed to the adjacent hydrogen burning shell, where it facilitates the production of  $^{13}$ N, which eventually decays to  $^{13}$ C. The presence of  $^{13}$ C in the hydrogen burning shell leads to the production of  $^{14}$ N upon capturing a proton. The intermediate convective zones, extending from the hydrogen burning shell to the star's surface, enable the efficient transport of  $^{14}$ N within the stellar envelope. The red line in the right panel of Figure 8.2 highlights the variation of  $^{14}$ N abundance inside the star, with its highest concentration found at the hydrogen burning shell, starting from the mass coordinate of  $^{14}$ N emerges as the third most abundant element after  $^{1}$ H and  $^{4}$ He.

Similarly, the production of  $^{16}$ O is intimately linked to the generation of  $^{12}$ C, primarily occurring during the core helium burning phase in PopIII stars. Once formed,  $^{12}$ C undergoes  $\alpha$  capture to produce  $^{16}$ O, which is also conveyed to the surface, as indicated by the purple line in the right panel of Figure 8.2. The envelope displays the results of both hydrogen and helium burning processes, with the CNO cycle being instrumental in nitrogen formation and helium burning in generating carbon and oxygen. The final abundance patterns, as depicted in the right panel of Figure 8.2, emerge from a complex interplay of nuclear reactions and convective movements.

### 8.4.2 Integrated Abundances

In Table 8.1, we present the mean mass fraction of various isotopes in the ejecta of individual stars with different final masses,  $\bar{X}_i$ , for the 11 models discussed in §8.3.1. A noticeable trend emerges in the ejected abundances of hydrogen and helium, correlating with the increasing stellar mass. For instance, with a 10% mass loss parametrization, the integrated mass fraction of  $^1H$  at the end of core hydrogen burning decreases from 0.36 to 0.17. This reduction is attributed to the near fully convective nature of these massive stars, which facilitates extensive hydrogen mixing and fusion throughout their lifetimes. Consequently, the mean mass fraction of  $^4H$ e escalates with the star's mass.

The trends in the CNO elements' abundances exhibit significant variability across individual models. Focusing on model 6127, which makes a notable contribution among the 11 stars, we observe that <sup>14</sup>N is uniformly distributed inside the star. The mean mass fraction of <sup>14</sup>N ranges from 0.039 in the outermost 10% of the total mass to 0.060 when considering all mass above the CO core. A similar pattern is noticeable for <sup>12</sup>C, with mean abundances fluctuating from 0.001 in the 10% mass loss scenario to 0.004 for mass above the core. The comparatively lower quantities of <sup>12</sup>C across all mass-loss parametrizations stem from its conversion to <sup>14</sup>N and <sup>16</sup>O during the core helium burning stage. The integrated amount of <sup>16</sup>O varies from 0.006 at 10% to 0.017 for the mass above the CO core, indicating that most <sup>16</sup>O resides in the star's interior.

Examining the integrated mass fractions in Table 8.1, we discern general trends in the increase or decrease of abundances as a function of stellar mass, albeit with exceptions like model 1923. This anomaly is likely due to the accretion history of such models, where periodic bursts of accretion interspersed with quiescent phases extend into the core hydrogen burning phase, introducing fresh elements like hydrogen into the star. Consequently, the envelope of these stars exhibits a higher hydrogen abundance.

In summary, massive stars like model 6127 exhibit a predominance of their chemical content in the form of <sup>4</sup>He and also possess significant mass fractions of <sup>14</sup>N compared to other CNO elements. In contrast, <sup>1</sup>H is more prevalent in the overall mass fraction of lower mass models, such as model 491, which also exhibit a higher mass fraction of <sup>16</sup>O relative to <sup>12</sup>C and <sup>14</sup>N.

To estimate the mass of different elements ejected by other initial mass stars (beyond the 11 cases computed here) from the simulation of Regan et al. (2020b), we utilize linear interpolation. This method helps associate a CO core mass and an ejected mass of an isotope to the remaining 90 stars for which detailed evolutionary sequences were not computed. Fig. 8.3 illustrates the variation in the ejected masses of different elements based on the mass of the stellar models. The histogram superimposed on the figure represents the mass distribution of all stars from the cosmological simulation at corresponding masses.

A general trend across all elements is evident: the total amount of each element ejected increases with the consideration of a larger portion of the star for mass loss. This indicates that elements are well-mixed within the interiors and envelopes of all stars. As shown in all panels of Figure 8.3, the ejected mass of  ${}^4\text{He}$  (orange line) escalates with the rising mass of stars in the halo. This increase is attributed to the higher temperatures in the convective cores of more massive stars, facilitating the fusion of  ${}^1\text{H}$  into  ${}^4\text{He}$  and resulting in a depletion of  ${}^1\text{H}$  and an excess of  ${}^4\text{He}$ . In the right panel of Figure 8.3, focusing on the case where the entire mass above the CO core is ejected, it's evident that a single 6200  ${\rm M}_{\odot}$  star produces significantly more helium than a star in the 600-700

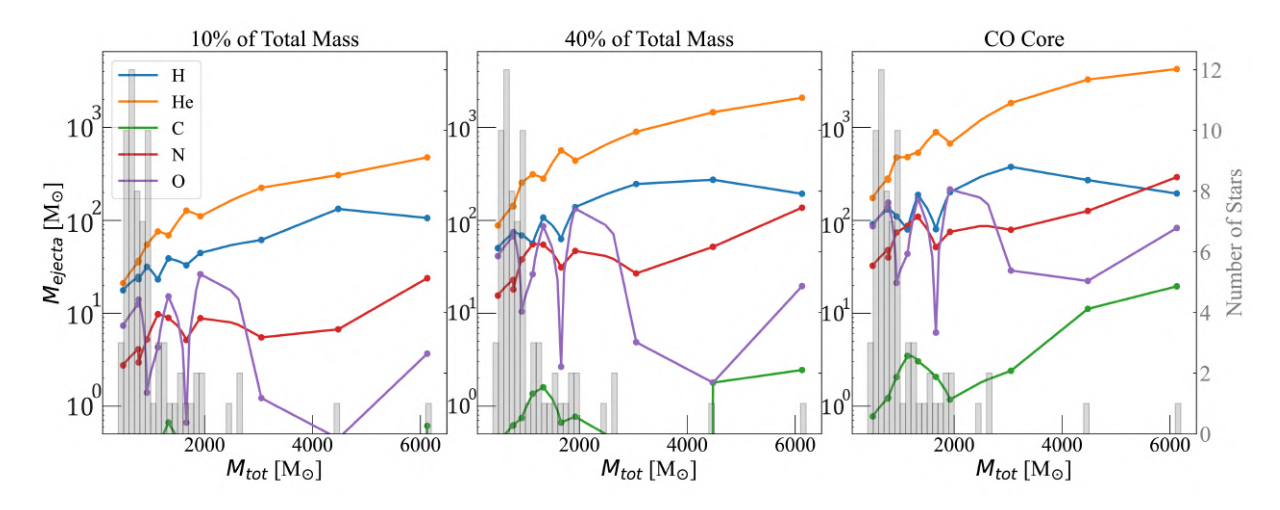


Figure 8.3: Mass ejected of various chemical species by each individual star in halo from Regan et al. (2020b). The first y-axis with lines and dots shows the ejected masses in  $M_{\odot}$  for a given element for all the individual stars in the simulation of Regan et al. (2020b). The dots connect the interpolated values between the 11 computed models and each dot on lines correspond to the 11 models computed until the end of core Helium burning. The second y-axis represents the number of stars in the histogram only. The bins in the histogram cover a width of  $100~M_{\odot}$  starting from  $40~M_{\odot}$  and ending at  $6200~M_{\odot}$ . The left panel shows the case when 10% of the total mass is ejected. The middle and right panel, the cases when 40%, and respectively the whole mass above the CO core is ejected.

## $M_{\odot}$ mass range.

The trend for ejected  $^{1}$ H (blue line) is qualitatively similar to  $^{4}$ He but exhibits a more complex profile for stars ranging from 1000-6000  $M_{\odot}$ . In the left panel of Figure 8.3, the total ejected mass of  $^{1}$ H increases, but in the middle and right panels, it peaks around 3000  $M_{\odot}$  and subsequently declines. This pattern is due to the more efficient hydrogen-burning shell in stars above 3000  $M_{\odot}$ , producing a higher quantity of  $^{4}$ He.

The integrated ejected mass of  $^{14}$ N (red lines) also increases with stellar mass, with the most massive stars contributing the majority of  $^{14}$ N. Conversely, the maximum  $^{16}$ O production (purple line) occurs in 2000  $M_{\odot}$  stars and diminishes with increasing mass. This trend is particularly pronounced in the 10% and 40% cases, suggesting that a substantial portion of  $^{16}$ O remains in the deeper regions of the star, with less mixing compared to other elements. A similar trend is observed for  $^{12}$ C (green line), especially when considering the CO core case (right panel of Figure 8.3), where the integrated ejecta mass of  $^{12}$ C is consistent with other species but resembles  $^{16}$ O in the 10% and 40% scenarios. These observations can be attributed to the fact that nitrogen originates from nuclear processes in the H-burning shell, while carbon and oxygen are produced in the deeper He-burning regions. Additionally, more massive stars typically exhibit larger mixed zones.

To evaluate if a progenitor galaxy could produce the high abundances observed in galaxies like GN-z11 and CEERS 1019, we aggregated the contributions from all individual stars within

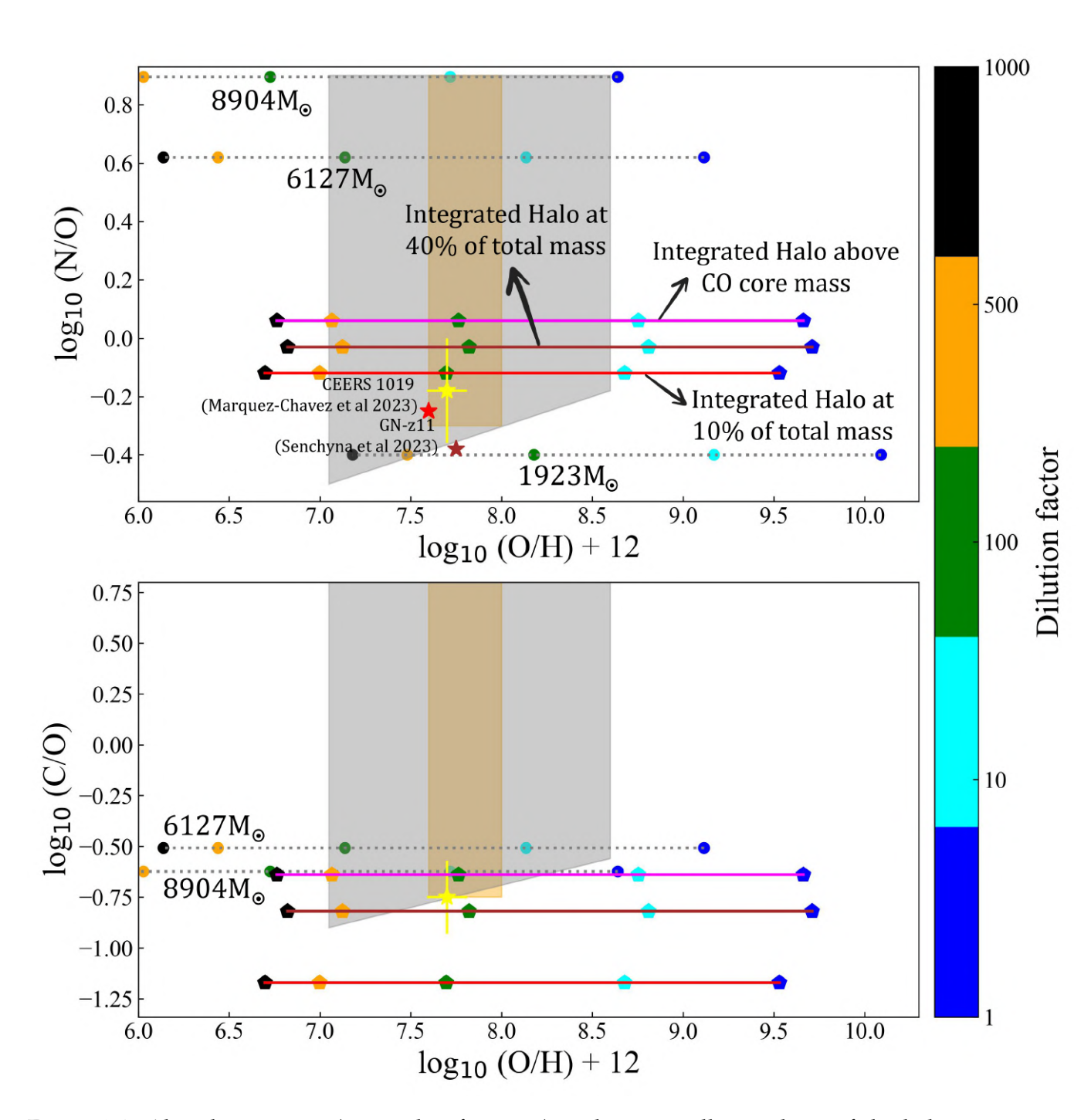


Figure 8.4: Abundance ratios (in number fractions) in the interstellar medium of the halo as a function of O/H (expressed as  $\log_{10}(\text{O/H})+12$ ). The dilution factor, f, is given by the colourbar. Dotted lines correspond to the abundance in the ejecta of an individual stellar model. The mass is indicated for each of them. The result for dilution factors equal to 1, 10, 100 and 1000 are shown by colored circles. The solid lines depict abundances after mixing the ejecta from all stars in the halo with varying amounts of pristine material: magenta for total mass above the CO core ejection, brown and red for 40% and 10% total mass ejection, respectively. Coloured pentagons on these lines indicate different dilution factors. The grey trapezoid and orange rectangle show conservative and fiducial abundances for GN-z11 from Cameron et al. (2023). *Top Panel*: The top panel shows the N/O abundances as a function of the O/H abundances both in log base 10 scale. The red and brown stars in the top panel are the photoionisation modelling results for GN-z11 by Senchyna et al. (2023). *Bottom Panel*: C/O versus O/H ratios represented in the log base 10 scale.

Table 8.2: The first column indicates the assumption for the mass lost. The columns 3 to 9 indicate the mean abundance (in mass fraction) of various isotopes in the ejected material by all the stars in the halo simulation of Regan et al. (2020b) with masses above 490  ${\rm M}_{\odot}$ . The quantities in these columns correspond to  $X_{ip}$  defined by Eq. 8.4. The next five columns show the valuos of  $\log_{10}(N/O)$ ,  $\log_{10}(C/O)$ ,  $\log_{10}(O/H) + 12$ ,  $\log_{10}(^{12}{\rm C}/^{13}{\rm C})$  and  $\log_{10}(^{22}{\rm Ne}/{\rm O})$  respectively, in the material composed from the sum of the ejecta of all the stars. The ratios are in number fractions.

Fraction	$M_{\rm ejecta}[M_{\odot}]$	$X_{\rm H1,p}$	$X_{\mathrm{He4,p}}$	$X_{\text{C12,p}}$	$X_{\rm N14,p}$	$X_{O16,p}$	$X_{\text{C13,p}}$	$X_{ m Ne22,p}$	log <sub>10</sub> (N/O)	log <sub>10</sub> (C/O)	log <sub>10</sub> (O/H)+12	$\log_{10}(^{12}\text{C}/^{13}\text{C})$	log <sub>10</sub> ( <sup>22</sup> Ne/O)
10% of $M_{\text{tot}}$	8900.7	0.35	0.55	0.003	0.04	0.06	0.0004	$5.7 \times 10^{-5}$	-0.17	-1.30	11.23	0.875	-3.02
$40\%$ of $M_{\text{tot}}$	32602.8	0.22	0.63	0.009	0.065	0.08	0.0005	$7.7 \times 10^{-5}$	-0.09	-0.95	11.56	1.25	-3.02
Above CO core	65866.5	0.20	0.65	0.012	0.07	0.07	0.0004	$8.8 \times 10^{-5}$	0.00	-0.76	11.54	1.47	-3.13

the population to determine their isotopic contributions, as presented in Table 8.2. A notable observation is the exceptionally high  $\log_{10}$  N/O mass fraction ratio (ranging from -0.17 for 10% of total mass to 0.00 for the mass above the CO core), coupled with elevated O/H ratios (11.23 for 10% of total mass and 11.54 for the mass above the CO core). Conversely, the C/O ratio is notably lower, predominantly due to the substantial depletion of  $^{12}$ C across all models (-1.30 for 10% of total mass and -0.76 for the mass above the CO core). This depletion pattern, where  $^{12}$ C is converted into  $^{14}$ N and  $^{16}$ O during the core helium burning stage, mirrors trends observed in massive stars, as detailed by Murphy et al. (2021a).

## 8.4.3 Impact of Dilution Factor

The abundance ratios derived from individual models and the entire galaxy reflect the ejection potential of these objects, without considering any pre-existing enrichment. To account for such pre-existing enrichment in the ISM, a dilution factor  $(f = M_{\rm ISM}/M_{\rm EJ})$  is introduced in subsequent calculations. Given the complexities in determining an exact dilution factor, we explore values ranging from 1 to 1000. These results are then juxtaposed with observational data from GN-z11 and CEERS 2019, as depicted in Figure 8.4. The figure displays data from select individual models alongside results encompassing all stars. The model with a final mass of 6127 M<sub>☉</sub> effectively replicates the N/O, C/O, and O/H values across a broad spectrum of dilution factors ( $f = 10 \rightarrow$ 100). The ejecta composition from all stars, using three distinct cutoff values, also aligns well with observed N/O number fractions of -0.13, -0.04, and 0.05 for 10%, 40%, and above the CO core, respectively. However, the closest match for the observed C/O number fraction in the two highredshift galaxies is -0.64, observed when ejecting the entire mass above the CO core. The O/H number fractions of 7.70, 7.80, and 8.75 for 10%, 40% of total mass, and all mass above the CO core for the entire galaxy closely approach the observational data with a dilution factor of 100. This factor aligns well with scenarios where 10% of the stellar mass is ejected, combined with a star formation rate of 0.1, representing a situation where the stellar mass constitutes only 10% of the total mass (stars and gas) of the clusters.

# 8.4.4 Massive PopIII Stars as Efficient Nitrogen Enrichers and Progenitors of High-z N-loud Quasars

The evolutionary paths of accreting massive Pop III stars, as shown in Figure 8.2, reveal significant nitrogen enrichment in their outer envelopes. This enrichment primarily occurs during the core helium burning phase, where <sup>12</sup>C plays a crucial role in producing <sup>14</sup>N. Nonetheless, these stars tend to deplete their <sup>12</sup>C reserves in this process. Examining integrated abundances across entire (sub-)galaxy populations, a clear pattern emerges: higher stellar masses correspond to lower fractions of <sup>1</sup>H and increased <sup>4</sup>He. In the first galaxy simulations by R20b, this mass range leads to notably high N/O and O/H ratios, coupled with a reduced C/O ratio due to significant carbon depletion in the models.

Incorporating the concept of dilution to evaluate the effect on the interstellar medium, the 6127  $M_{\odot}$  model closely matches observed N/O, C/O, and O/H ratios across a range of dilution factors from 10 to 100. Furthermore, using realistic mass cutoffs and a dilution factor of 100, the aggregate values from all massive stars closely align with observational data, as illustrated in Figure 8.4. This indicates that a subset of very massive PopIII stars can replicate the elemental abundances observed by JWST, particularly explaining the unusually high nitrogen abundances.

## 8.5 Discussion

## 8.5.1 Mass Ranges

The chemical profiles generated by massive PopIII stars are closely tied to their mass at various stages, including mass-loss events and at collapse. In Figure 8.4, we display the impact of individual stars from the Regan et al. (2020b) simulations and the collective influence of all stars. A single star with a mass under 1923  $M_{\odot}$  yields a  $\log_{10}(N/O)$  ratio of -0.37, which is on the lower spectrum of observed values. In contrast, the  $\log_{10}(C/O)$  ratio does not align with observed values. The next mass in the simulation, 2479  $M_{\odot}$ , produces a  $\log_{10}(N/O)$  ratio of 0.1 and  $\log_{10}(C/O)$  ratio of -0.7.

Stars in haloA exceeding 8904  $M_{\odot}$  exhibit  $log_{10}(N/O)$  ratios beyond 0.85 and  $log_{10}(C/O)$  ratios below -0.6, not matching the observed values for GN-z11 and CEERS 1019. This trend is dynamic, as ongoing ISM enrichment by subsequent star generations can modify these ratios. Notably, supermassive PopIII stars above 100,000  $M_{\odot}$ , which collapse prematurely during core hydrogen burning as per Haemmerlé et al. (2018), do not reach stages where substantial CNO elements are produced, typically occurring during core helium burning. Thus, both upper and lower mass

limits are discerned for massive PopIII stars to produce observed signatures. While this does not negate the existence of such massive stars, it suggests that stars in the approximate mass range of  $10^3-10^4~M_{\odot}$  are crucial to replicate the JWST-observed abundance signatures.

## 8.6 Impact of evolutionary stages on the integrated abundances

To explore the impact of late stages of evolution on the abundances, we calculated the integrated abundances of Hydrogen, Carbon, Nitrogen and Oxygen for the 3053  $M_{\odot}$  model as shown in table 8.3. We find that the integrated abundances do no vary significantly beyond the core Helium burning phase. This is due to the very short timescale of the subsequent phases which barely alters the total composition of the model. Therefore the 11 models computed until the end of core Helium burning provide sufficiently accurate results. The core is defined as the mass coordinate in star below which  $10^{-3}$  mass fraction of the previous chemical species is left. For instance, CO core has  $10^{-3}$  mass fraction of helium ( $Y_c$ ) is left in the core.

Table 8.3: The integrated abundance of various elements inside a  $3053 M_{\odot}$  model at zero metallicity computed until the end of core Si burning. Column 1 indicates various evolutionary stages. The integrated mass fraction of a given element is presented in columns 2, 3, 4 and 5.

<b>Evolutionary stage</b>	$ar{X_i} = \int_{M_{ m cut}}^{M_{ m tot}} X_i(M_r) dM_r/M_{ m EJ}$					
Z = 0.0	$^{1}H$	<sup>12</sup> C	$^{14}N$	<sup>16</sup> O		
End He burning	0.1570	0.00160	0.0380	0.0130		
End C burning	0.1570	0.0008	0.0330	0.0120		
End Si burning	0.1570	0.0008	0.0330	0.0120		

#### 8.6.1 Predicted Abundances

Our study aims to predict additional elemental abundances, making our model verifiable against future observations of objects like GN-z11 and CEERS 1019. Although focusing on a specific stellar mass range, our work underlines the potential of these supermassive stars (SMSs) in generating significant Nitrogen amounts and seeding massive black holes. Late Pop III star formation in pristine regions is also plausible.

We find the integrated ejected mass in our simulated galaxy predominantly enriched in helium: 0.55 mass fraction for 10% of the total mass and 0.65 for mass above the CO core. These fractions

lead us to predict undiluted  $\log_{10}(\text{He/H})$  ratios of -0.40 and -0.09, respectively, for all stars in the halo. Considering the interaction of helium and hydrogen-rich ejecta with the ISM, diluted  $\log_{10}(\text{He/H})$  ratios can be anticipated. For equal contributions from all stars' total ejecta and the ISM (f = 1), we obtain  $\log_{10}(\text{He/H})$  = -0.62. With stronger dilutions (f = 10, 100, 1000), this ratio drops to -0.99, -1.07, and -1.08, respectively. Since He/H ratios are key observables for massive stars (?), these predictions are pertinent for upcoming JWST observations.

## 8.6.2 Mass Ranges

Chemical signatures of massive PopIII stars are significantly influenced by their mass at different stages, including mass-loss events and collapse. Figure 8.4 illustrates both the impact of individual stars from Regan et al. (2020b) simulations and the collective effect of all stars. For instance, a star with mass less than 1923  $M_{\odot}$  results in a  $log_{10}(N/O)$  ratio of -0.37, aligning with the lower spectrum of observed values. However, the  $log_{10}(C/O)$  ratio does not match observed values. The next significant mass, 2479  $M_{\odot}$ , yields a  $log_{10}(N/O)$  ratio of 0.1 and  $log_{10}(C/O)$  ratio of -0.7.

Stars in haloA beyond 8904  $M_{\odot}$  exhibit  $log_{10}(N/O)$  ratios over 0.85 and  $log_{10}(C/O)$  ratios below -0.6, not matching the observed values for GN-z11 and CEERS 1019. This conclusion is timesensitive, as ongoing enrichment of the ISM by subsequent star generations can alter these ratios. Importantly, supermassive PopIII stars above 100,000  $M_{\odot}$ , prone to premature collapse during core hydrogen burning (Haemmerlé et al. 2018), do not reach the CNO production stage, typically occurring during core helium burning. This indicates the existence of both upper and lower mass limits where massive PopIII stars can produce observed chemical signatures. While this doesn't rule out the existence of such massive stars, it implies that stars in the  $10^3 - 10^4 M_{\odot}$  range are essential to replicate JWST-observed abundance signatures.

## 8.6.3 Predicted Abundances

Our goal is to predict additional elemental abundances, rendering our model testable against future observations like GN-z11 and CEERS 1019. Although our study focuses on a specific stellar mass range, it underscores the potential of these supermassive stars (SMSs) in Nitrogen production and seeding massive black holes. The possibility of Late Pop III star formation in pristine regions has been suggested in various studies.

We determine the integrated ejected mass in our simulated galaxy to be predominantly enriched in helium: 0.55 mass fraction for 10% of the total mass and 0.65 for mass above the CO

core. This leads to undiluted  $\log_{10}(\text{He/H})$  ratios of -0.40 and -0.09, respectively, for all stars in the halo. When helium and hydrogen-rich ejecta interact with the ISM, diluted  $\log_{10}(\text{He/H})$  ratios can be inferred. For equal contributions from all stars' total ejecta and the ISM (f = 1), we obtain  $\log_{10}(\text{He/H}) = -0.62$ . With stronger dilutions (f = 10, 100, 1000), the ratio decreases to -0.99, -1.07, and -1.08, respectively. As He/H ratios are significant observables for massive stars, these predictions are crucial for future JWST observations.

## 8.6.4 Comparison with Previous Studies

The discovery of NIII]  $\lambda$  1750 and CIII]  $\lambda\lambda$ 1909 lines in GN-z11 by Bunker et al. (2023) reveals unusually high N/O ratios at a redshift of z = 10.6. Utilizing emission line fluxes from Bunker et al. (2023), Cameron et al. (2023) quantitatively derived abundance ratios, finding log (N/O) > -0.25, log (C/O) > -0.78 and log (O/H)  $\approx$  7.82 for their fiducial model and log (N/O) > -0.49, log (C/O) > -0.95 and log (O/H)  $\leq$  8.60 for their conservative models, as shown in Figure 8.4.

Charbonnel et al. (2023), using the runaway collision scenario by Gieles et al. (2018), were the first to explore GN-z11's N/O, C/O, and Ne/O ratios. They utilized a supermassive star (SMS) model with masses around  $10^4~\rm M_\odot$  and metallicities ranging from -1.76 to -0.78. Their study suggested that fully convective SMS growing via collisions could transport chemical species effectively. Contrary to their approach, our study assumes a massive PopIII formation scenario where post H-burning evolutionary phases facilitate efficient chemical transport. Our single star models, like the 6127  $\rm M_\odot$  case, generate higher N/O and C/O ratios, while O/H ratios align for dilution factors between 10-100. When considering our entire massive star population, the integrated abundances closely match observed values, with O/H ratios fitting for a dilution factor of around 100.

Nagele & Umeda (2023) investigated metal enriched SMS models incorporating rotation, stellar winds, and explosions. Their models, spanning initial masses from  $10^3$  to  $10^5$  M $_{\odot}$ , were evolved until late carbon burning or the onset of GR instability. In contrast, our 932 M $_{\odot}$  model produces different ejected mass values, likely due to our models at zero metallicity, non-rotating nature, and lack of explicit mass-loss mechanisms. Nagele & Umeda (2023) favored higher mass models to explain GN-z11's abundances, while our  $10^5$  M $_{\odot}$  models yield significantly different  $\log_{10}(N/O)$ ,  $\log_{10}(C/O)$ , and  $\log_{10}(O/H)$ +12 ratios across various dilution factors.

Kobayashi & Ferrara (2023) proposed a dual starburst model for GN-z11's high Nitrogen levels, suggesting WR stars as key contributors in the second burst phase. Their single starburst model required stars over  $1000 \text{ M}_{\odot}$ , similar to our findings. Kobayashi & Ferrara (2023) also noted that the addition of typical  $20 \text{ M}_{\odot}$  massive stars, as we incorporated, does not significantly alter the

overall N/O ratio.

CEERS 1019, another high-z JWST galaxy, exhibits similar abundances to GN-z11. Marques-Chaves et al. (2023) analyzed CEERS 1019, identifying strong NIII and NIV emissions, and obtained similar abundance ratios. They hypothesized that (super-)massive stars over  $1000 \, M_{\odot}$  could explain these unusual abundances, aligning with our study and observations in present-day globular clusters (e.g., Denissenkov & Hartwick 2014; Gieles et al. 2018).

## 8.7 Conclusion

Our investigation has significantly advanced the understanding of massive PopIII stars, particularly in relation to their role in shaping the chemical landscape of early galaxies. This study leverages comprehensive simulations and data analysis to uncover the impact of massive PopIII stars on the chemical properties observed in the universe's nascent galaxies. Key findings from our research are summarized as follows:

- Significance of Mass Ranges: The chemical signatures of PopIII stars are heavily influenced by their mass. Stars with masses below approximately  $1900\,\mathrm{M}_\odot$  yield a  $\log_{10}$  (N/O) ratio of -0.37, which is lower than the observed values in specific high-redshift galaxies. Conversely, stars exceeding  $8900\,\mathrm{M}_\odot$  surpass the observed N/O ratios for galaxies such as GN-z11 and CEERS 1019. Therefore, the mass range of  $1900\,\mathrm{M}_\odot$  to  $8900\,\mathrm{M}_\odot$  is crucial for matching the observed chemical signatures.
- Role of a Very Massive PopIII Star Population: Our results indicate that a subset of very massive PopIII stars, specifically those with masses over 1000 M<sub>☉</sub>, can replicate the observed nitrogen abundance patterns in early galaxies observed by JWST, like GN-z11 and CEERS 1019. It's the contributions from the most massive stars within this sub-population that are pivotal in achieving the high nitrogen abundances observed. Lower mass stars within this group tend to dilute this pattern, indicating the necessity of a minority population of very massive PopIII stars in early galaxies to align with current observational data.
- **Predicted Halo Abundance**: The individual masses of massive PopIII stars have a significant impact on the overall chemical composition of their respective halos. Our model suggests that the aggregated ejections from all massive stars result in an environment rich in <sup>4</sup>He, with mass fractions of 0.55 and 0.65 for 10% of total mass and for mass above the CO core, respectively. Consequently, the integrated ejected mass of <sup>1</sup>H varies, indicating that these early galaxies may have environments rich in helium. Furthermore, stars with masses less

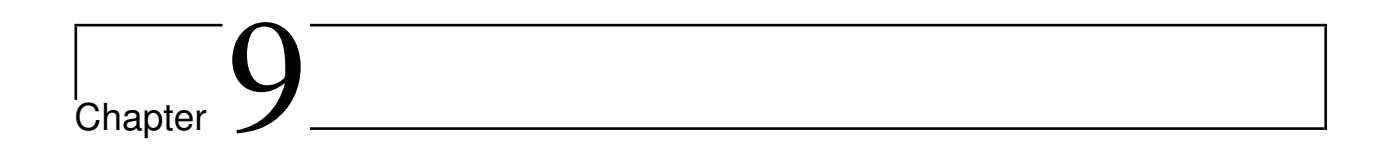
than 2000  $M_{\odot}$  primarily contribute to the  $^{16}O$  enrichment, while stars with higher masses predominantly enrich the ejecta with  $^{14}N$ . After  $^{4}He$  and  $^{1}H$ ,  $^{14}N$  becomes the dominant element in the ejecta of higher mass PopIII stars.

- Matching abundances with GN-z11 and CEERS 1019: When considering mass ejection from all massive PopIII stars, our models closely align with the observed log (N/O), log (C/O), and log (O/H)+12 ratios across a range of dilution factors. The models suggest that nitrogenrich quasars could be a notable signature of prior massive PopIII star formation, potentially originating from the same PopIII stars that initiated the initial nitrogen enrichment.
- The Origin of the High Ne/O Ratio in CEERS 1019: Our models yield a much lower Ne/O ratio (-3.02) compared to the observed ratio in CEERS 1019 (-0.63). In our models, neon predominantly exists as <sup>22</sup>Ne isotopes, originating from the transformation of <sup>14</sup>N during the onset of the core helium-burning phase. This low Ne/O ratio indicates that this process alone is insufficient to match the Ne/O ratios observed in CEERS 1019. Furthermore, our findings show that stars around 3200 with metallicity 10<sup>-6</sup> Z can replicate the observed log<sub>10</sub>(Ne/O) ratio of -0.58. However, the predicted N/O and C/O ratios fall short of the observed values, suggesting the necessity for a more comprehensive analysis of the star formation history to fully understand these observations.
- Abundance Predictions: Our model, focusing on the first generation of extremely massive stars, offers predictions on several abundance ratios. For carbon, the  $\log_{10}$  ( $^{12}$ C/ $^{13}$ C) ratio is found to be 0.87 for the 10% case and 1.47 for the CO core case, reflecting the influence of the CNO cycle. The predicted Ne/O ratio is approximately -3.0 for the halo. These predictions serve as guidelines for future JWST observations, providing targets for empirical validation.
- Impact of 20  $M_{\odot}$  Stars: Including 100 stars of 20  $M_{\odot}$  in the stellar population reveals their limited influence on certain abundance ratios. Specifically, their inclusion results in  $\log_{10}$  (N/O) and  $\log_{10}$  (O/H)+12 values of -0.27 and 11.21, respectively, suggesting that stars of this mass are unlikely to be responsible for high N abundances. However, their addition increases the  $\log_{10}$  (C/O) ratio, improving the fit with observed values from GN-z11 and CEERS 1019.

Our models underscore the likelihood of substantial nitrogen enrichment in the early universe, attributed to massive PopIII stars. This finding aligns with the expectation that if such stars existed and experienced mass ejection, they would significantly contribute to N-enrichment. Additionally, fast-rotating massive stars (8-100  $M_{\odot}$ ) are also known to contribute to nitrogen enrichment,

although their impact differs from the scenario described in our study. Future research should consider the role of these fast-rotating stars in chemical enrichment processes.

Recent JWST observations (JADES, CEERS, UNCOVER) have unveiled massive black holes in the early universe, supporting the hypothesis of a 'heavy seed' formation pathway, likely originating from massive PopIII or SMS stars. Our study reinforces this idea by demonstrating that massive PopIII stars can produce metal abundances in line with these observations. The ongoing exploration of massive PopIII stars' multifaceted nature is crucial in shaping our understanding of early cosmic events and the formation of massive black holes.



# Supermassive stars and general relativistic instability: impact on upper mass limit and luminosity

The discovery of supermassive black holes exceeding  $10^9$  solar masses in the early universe challenges our understanding of their formation, especially within the time constraints imposed by the high redshifts (z > 6) at which they are observed. Traditional models, such as those stemming from the collapse of Population III stars, fail to offer a viable explanation due to the impractical accretion rates required to form such massive entities within the given time frames (Mortlock et al. 2011; Wang et al. 2021; Haemmerlé 2021a).

A more plausible progenitor for these supermassive black holes appears to be 'direct collapse' black holes-massive seeds with initial masses on the order of 10<sup>5</sup> solar masses. These seeds align with the concept of Eddington-limited accretion, a process where the gravitational pull is balanced by the radiation pressure from the accreting material (Volonteri & Begelman 2010; Zhu et al. 2020). The formation of such massive seeds is contingent upon specific environmental conditions within the primordial halos. One critical factor is exposure to a strong Lyman-Werner UV field, which suppresses molecular hydrogen formation, thereby staving off early fragmentation and collapse (Haiman et al. 1997; Dijkstra et al. 2008; Visbal et al. 2014a,c,b; Regan et al. 2017b; Chon et al. 2018).

In the absence of molecular hydrogen, a primordial halo can grow to significant masses (approximately  $10^7$  solar masses) and increase its temperature to about 8000 K. At this juncture, it may undergo isothermal collapse, fostering an environment where accretion rates can range from 0.1 to 10 solar masses per year (Regan & Haehnelt 2009; Latif et al. 2013; Sakurai et al. 2016b; Chon et al. 2018; Grete et al. 2019). While the precise dynamics of the accretion flows that fuel the growth

of central massive objects remain elusive, simulations suggest a tendency towards the formation of a dominant central mass that consumes smaller surrounding clumps (Inayoshi & Haiman 2014; Regan et al. 2014; Hosokawa et al. 2016).

This central object, having formed from primordial gas under optimal conditions, is theorized to be capable of reaching masses between  $10^4$  and  $10^6$  solar masses in under a million years. Such rapid growth assumes accretion rates that are sustained and surpass thresholds of  $10^{-2}$  to 1 solar mass per year (Inayoshi & Haiman 2014; Regan et al. 2014). One of the lingering inquiries in the study of supermassive black hole formation is the persistence of matter inflow and the effects of feedback from radiation on this process. The configuration of the accretionawwhether spherical or disk-likeâhas significant implications. A spherically symmetric infall is known to trigger a UV feedback mechanism that ultimately curtails the accretion, capping the mass of the central object at less than  $10^3$  solar masses (Susa 2013). In contrast, a disk-like accretion process facilitates efficient angular momentum loss and can continue in the absence of strong UV feedback, allowing the central object to amass over 10<sup>5</sup> solar masses (Inayoshi & Haiman 2014). Recent research endeavors have shed light on numerous facets of this astrophysical puzzle, yet the complete picture of how supermassive black holes form in such early epochs remains to be fully depicted. The nuances of accretion geometry and the resulting feedback mechanisms are fundamental in understanding the limits of growth for these cosmic giants. As our computational models and observational capabilities advance, we edge closer to a comprehensive model of supermassive black hole formation, a testament to the remarkable progress in this field.

Determining the factors that define the upper mass limit reached by accretion is pivotal in understanding supermassive black hole formation. Two principal constraints are hypothesized. The first concerns the mass reservoir of the protostellar cloud. Although significant, with atomic hydrogen halos potentially amassing up to  $10^7~{\rm M}_{\odot}$ , this is not deemed to be a stringent limitation (Fowler 1966). The second, more critical, constraint involves the general-relativistic (GR) instability, which is intrinsically tied to the physics of supermassive stars. The GR instability arises from the theoretical understanding that stars composed predominantly of relativistic particles are inherently unstable (Iben 1963; Chandrasekhar 1964b). Supermassive stars, with their radiation-dominated pressure profiles, hint at an approach toward such a state, although they are not comprised solely of relativistic particles. The onset of this instability can occur at various stages in the star's evolution, contingent upon its mass and accretion rate. The formation timescale, a simple ratio of mass to accretion rate  $(M/\dot{M})$ , is juxtaposed against the stellar lifetime. Higher accretion rates abbreviate the formation period, precipitating an earlier encounter with the instability if it occurs (Fuller et al. 1986). The critical mass at which a supermassive object succumbs to GR in-

stability is a topic of interest, as it is anticipated to prescribe the upper limit for black hole mass achievable by consistent accretion rates. Beyond approximately  $10^5 \, \rm M_{\odot}$ , the induced collapse from the GR instability is theorized to be irreversible, leading to direct black hole formation without a supernova and hence without mass loss (Montero et al. 2012). At lower masses, the scenario is more nuanced. While the core hydrogen-burning phase may not trigger the GR instability, subsequent evolutionary phases could, as could other instabilities, such as those induced by electron-positron pair production (Umeda et al. 2016). These latter instabilities may cause explosive events, potentially observable as ultra-long gamma-ray bursts, and are often accompanied by neutrino emissions (Chen et al. 2014; Nagele et al. 2021, 2022).

Extensive research has been dedicated to understanding the upper mass thresholds achievable by supermassive stars before succumbing to general-relativistic (GR) instability. Pioneering works by Iben (1963) and Chandrasekhar (1964b) elucidated that masses in excess of  $10^5$  are a prerequisite for substantial GR effects. Following this foundational research, Fuller et al. (1986) spearheaded the initial simulations tracking the hydrostatic contraction of supermassive stars and their subsequent collapse due to GR instability. Recent advancements in the field have broadened our understanding of the genesis and accretion dynamics of these colossal stars, refining computational methods to gauge the onset of GR instability. Umeda et al. (2012) ventured into previously uncharted territories by examining stars beyond the  $10^5$  threshold, accounting for post-Newtonian corrections. Their work revealed that within accretion rates of 0.1-10 M<sub>☉</sub>/yr, stars could attain masses ranging from  $1-8\times10^5\mathrm{M}_{\odot}$ . Further contributions by Hosokawa et al. (2013b), Woods et al. (2017), and Haemmerlé et al. (2018) concentrated on the evolution of such massive entities up to  $10^5 {\rm M}_{\odot}$  under constant accretion rates associated with atomically cooled haloes. They posited that accretion rates exceeding  $0.1 M_{\odot}$ /yr were essential for sustaining cool protostars that evolve in accordance with the Hayashi limit. Sakurai et al. (2015) were at the forefront in examining the effects of clumpy accretion on the evolutionary trajectory of supermassive Population III stars, concluding that despite intermittent phases of heating, these stars would eventually stabilize and follow the Hayashi track once more. In this chapter, we present the physics behind the models and the GR instability in Sec. 9.2. The evolution, properties, upper mass limit and metallicity of SMS is presented in Sec. 9.3, 9.4, 9.5 and , 9.6. Finally, we present the conclusion in Sec. 9.7

# 9.1 Literature review on accreting models

The formation phase of massive stars is one of the least understood in stellar evolution, primarily due to the scarcity of these stars and the obscured nature of their early evolution. The

process of stellar formation initiates with the dynamic collapse of a molecular cloud, leading to fragmentation (Rees 1976). In the center of these fragments, a hydrostatic stellar core forms and increases in mass. This growth continues until a process such as strong radiative feedback halts the accretion, or until the surrounding material is depleted (Abel et al. 2002). The formation of massive stars through this accretion process is believed to be the most prevalent in the Universe. However other channels have been proposed as those involving stellar mergers (Larson 1981; Sana et al. 2012; Mayer & Bonoli 2019).

Accretion rates change over time, influenced by the evolving nature of the accreting star. As the protostar forms and becomes increasingly luminous, the radiative feedback can slow down or outright halt the accretion process (Chon & Omukai 2020a; Regan et al. 2020a). Additionally, changes in the protostar's surface temperature influence the ionization of surrounding materials, which in turn affects the physical conditions that determine the rate of accretion (Sakurai et al. 2015; Nandal et al. 2023c). Throughout the accretion process, the accreting protostar gains angular momentum. In certain situations, this can lead to the protostar's surface rotation reaching a critical limit where centrifugal acceleration counterbalances gravitational pull at the equator (Maeder & Meynet 2000). At this point, further mass accretion becomes impossible, leading to the formation of an accretion disk (Haemmerlé 2021a). The disk's physics play a crucial role as it can enable infalling matter to lose angular momentum, transferring it to material in the disk's outer part. This disk might also screen the material from radiative and ionizing feedback (Zwick et al. 2023). Consequently, the formation of an accretion disk is often considered a mechanism to overcome the limitations imposed by radiative and angular momentum factors, which may temporarily halt the accretion process. Accretion rates may vary as the star moves through regions of infalling clouds with different densities and sound velocities. This makes the accretion history of a forming star complex, involving the physics of both the cloud and the protostar (Regan et al. 2020b).

Significant uncertainties remain regarding the history of accretion rates. This is largely due to the observational challenges in studying star formation, especially for massive stars (McKee & Tan 2003). These difficulties hinder the ability to obtain clear and quantitative measurements of accretion rates. The challenge is even greater for stars forming in environments with very low or zero metallicity, where direct observations are not available. In such cases, hydrodynamic and magnetohydrodynamic simulations are crucial for shedding light on these poorly understood and constrained phases of stellar evolution (Ohkubo et al. 2009; Haemmerlé et al. 2016). Even in case of such models, one key limitation is the spatial resolution of hydrodynamic simulations, which is still too coarse to accurately capture events near the surface of accreting objects.

In this study, we adopt two assumptions to broadly explore how accretion rates affect key

stellar properties. The first assumption models the history of accretion rates as a constant, time-averaged rate. The second assumption is that the star continues to accrete material until a structural change causes the central regions to collapse. While these assumptions may be somewhat simplistic, they provide a foundation for understanding the maximum mass stars can achieve through accretion and builds on the previous work by Hosokawa et al. (2012); Umeda et al. (2016); Woods et al. (2017); Haemmerlé et al. (2018). This work will also yield insights into how the time-averaged accretion rate influences the final fate of these stars and their potential role in nucleosynthesis. For clarity, throughout this paper, we refer to 'protostars' as accreting objects primarily powered by contraction, and 'accreting stars' as those mainly driven by nuclear reactions.

## 9.2 The models

We have used accretion rates ranging from  $10^{-6}$  to  $10^3$  M $_{\odot}$ /yr, spanning nine orders of magnitude. For lower accretion rates, our results might be more theoretical as they lack support from hydrodynamical simulations. Conversely, such simulations cannot precisely resolve stars, instead providing insights into mass fluxes through surfaces significantly larger than the stars. While these fluxes are likely accurate, it's not certain that all this mass will be incorporated into stars. Therefore, the actual net accretion rates might be lower than those indicated by the simulations. Given the diversity of scenarios likely present in nature, it is reasonable to explore a wide range of accretion rates. In our study, we assume cold accretion, meaning the mass increases at a rate denoted by  $\dot{M}_{\rm accr}$ . This approach does not account for the energy released when mass is accreted at the star's surface, as per the cold accretion scenario.

Our models use net averaged accretion rates and are evolved from the pre-main sequence (pre-MS) phase to the end of core helium burning using the Geneva Stellar Evolution Code () (Eggenberger et al. 2008). These population III (PopIII) models have a homogeneous chemical composition with X = 0.7516, Y = 0.2484, and a metallicity of Z = 0, aligning with the parameters used in Ekström et al. (2012a) and Murphy et al. (2021b). For the models at  $0.1 \text{ M}_{\odot}/\text{yr}$  accretion rates at  $10^{-6}$  and solar metallicity, the chemical composition is similar to Nandal et al. (2023a). Additionally, we include deuterium with a mass fraction of  $X_2 = 5 \times 10^{-5}$ , as in Bernasconi & Maeder (1996); Behrend & Maeder (2001), and Haemmerlé et al. (2018). The equation of states, nuclear reaction rates, opacities are as in Ekström et al. (2012a) and Nandal et al. (2023b). When a convective core is present, we have used a step overshoot of  $\alpha_{ov} = 0.1$ . We have not included rotation in the current models; this will be addressed in a subsequent paper.

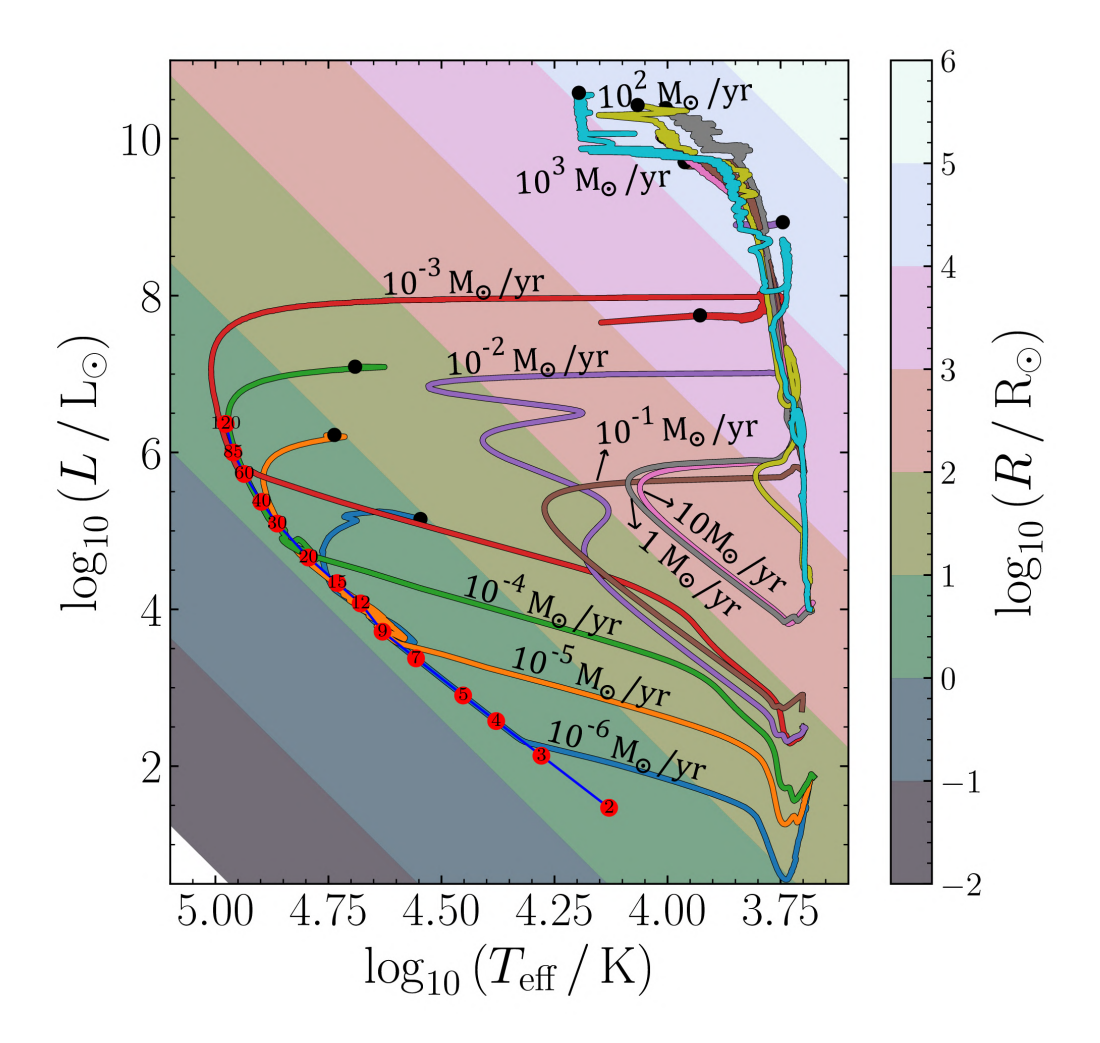


Figure 9.1: An HR diagram of massive and supermassive star models at zero metallicity with accretion rates ranging from  $10^{-6}/\mathrm{yr}$  to  $10^{3}/\mathrm{yr}$ . The background colors indicate the radii in unit of solar radius. The blue line represents the Z=0 ZAMS line with red dots marking the masses in solar units. The tracks are marked by their respective accretion rate in black text. The black dots indicate the end point of computation.

## 9.2.1 Linear adiabatic radial pulsation stability

We can also examine the stability of an SMS model by solving the linear adiabatic pulsational equation. Taking into account the GR effects, Chandrasekhar (1964b) has derived the differential equation for infinitesimal radial displacement  $\xi e^{i\sigma ct}$  as

$$\frac{d}{dr} \left[ e^{3a+b} \frac{\Gamma_1}{r^2} \frac{d}{dr} (e^{-a} r^2 \xi) \right] = e^{2a+b} \xi \left[ \frac{4}{r} \frac{dP}{dr} + \frac{8\pi G}{c^4} e^{2b} P(P + c^2 \rho) - \frac{1}{P + c^2 \rho} \left( \frac{dP}{dr} \right)^2 - \sigma^2 e^{2(b-a)} (P + c^2 \rho) \right]$$
(9.1)

where a and b are the coefficients of the metric as given in Haemmerlé (2020). This is a linear eigenvalue equation with eigenvalue  $\sigma^2$ . The stellar structure is unstable if a pulsation mode has a negative eigenvalue; i.e.,  $\sigma^2 < 0$ .

To solve the second-order differential equations we introduce, similarly to the Newtonian radial pulsations, two non-dimensional variables,

$$Y_1 \equiv \frac{\xi}{r} \quad \text{and} \quad Y_2 \equiv \frac{\Delta P}{P},$$
 (9.2)

where  $\Delta P$  is the Lagrangian perturbation of pressure. Using these variables, Equation 9.1 can be separated into the two first-order differential equations

$$\frac{dY_1}{d\ln r} = -\left(3 + \frac{da}{d\ln r}\right)Y_1 - \frac{1}{\Gamma_1}Y_2,\tag{9.3}$$

and

$$\frac{dY_2}{d\ln r} = \left[4\overline{V} - \frac{d(a+b)}{d\ln r} + \overline{V}\frac{da}{d\ln r} + \omega^2 W e^{2(b-a)}\right] Y_1 + \left[\overline{V} - \frac{d(2a+b)}{d\ln r}\right] Y_2,$$
(9.4)

where  $\overline{V} \equiv -d \ln P/d \ln r$  and  $\omega^2 W \equiv \sigma^2 r^2 (P+c^2 \rho)/P$  with the square of non-dimensional pulsation frequency  $\omega^2 \equiv \sigma^2 c^2 GMR^{-3}$ . The coefficients of metric, a,b can be obtained by using eqs.(33) and (34) in Haemmerlé (2020). The boundary conditions of being finite at the center for  $Y_1$  and at the surface for  $Y_2$  are imposed. In addition, we adopt a normalization,  $Y_1(R)=1$  at the surface. The linear homogeneous differential equations (9.3) and (9.4) with an eigenvalue  $\omega^2$  can be solved by the Henyey-type relaxation method as often used in the analysis for Newtonian stellar pulsations (eg., Unno et al. 1989). We have solved equations (9.3) and (9.4) with eigenvalue  $\omega^2$  for several stellar structures with accretion rates ranging from 0.01 to 10 . The sign of  $\omega^2$  determines the stability of the structure. If  $\omega^2 < 0$ , the GR instability occurs with the growth rate given by

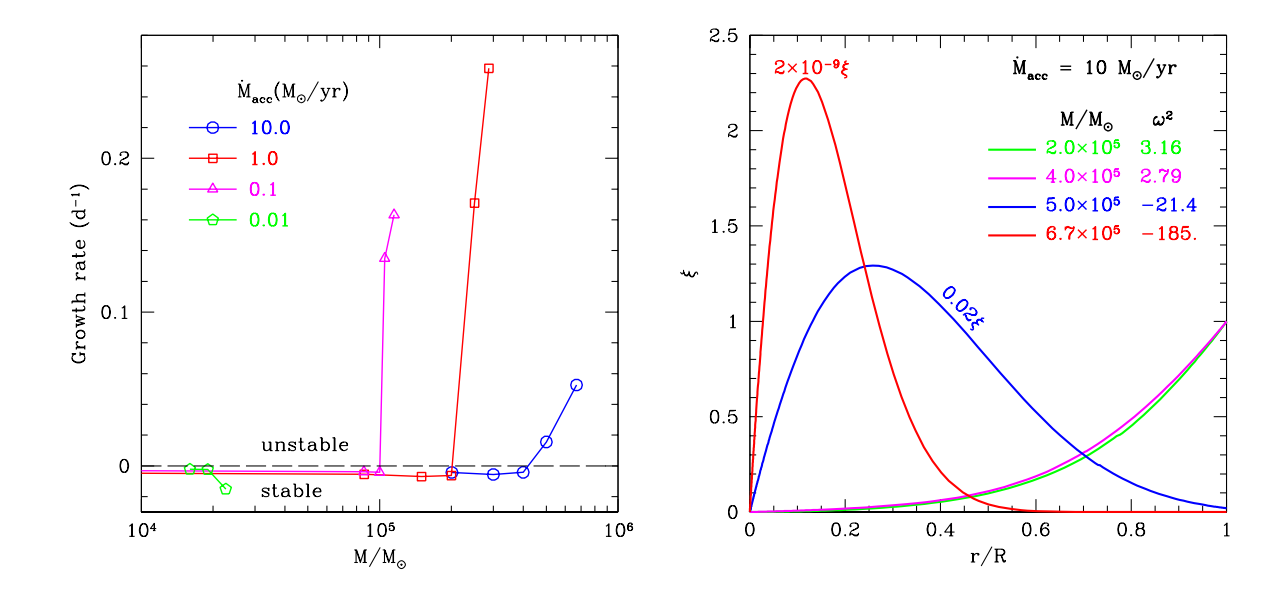


Figure 9.2: Left panel: Growth rate of the GR instability versus stellar mass for each model. The negative part of the vertical axis corresponds to the angular frequency of the stable fundamental pulsation mode. The horizontal dashed line indicates the boundary between stable and unstable regions. A steep increase in the growth rate indicates a strong GR instability occurs as soon as the mass exceeds the critical mass depending on the accretion rate. Right panel: The displacement  $\xi$  of the radial fundamental mode as a function of the distance from the center in some models with an accretion rate of  $10M_{\odot}/\mathrm{yr}$ . The displacement is normalised to  $\xi=1$  at the surface. For unstable modes ( $\omega^2<0$ ),  $\xi$  is scaled by a factor to fit it in the figure.

 $|\omega|\sqrt{GM/R^3}$ , while a positive  $\omega^2$  means the structure to be stable and  $|\omega|\sqrt{GM/R^3}$  corresponds to an angular frequency of adiabatic radial pulsation.

## 9.3 Evolution in the HR diagram

In Fig. 9.1, track of accreting objects for accretion rates varying between  $10^{-6}$  up to  $10^3$  M $_{\odot}$  per year are presented per step of 1 dex. As documented in the works by Hosokawa et al. (2012); ?); Haemmerlé et al. (2018), stellar evolutionary tracks can be broadly classified into two categories: those evolving towards the blue, and those that follow the Hayashi line before igniting hydrogen in their core. The dividing accretion rate between these two behaviors is around  $2.5 \times 10^{-2} M_{\odot}$  (Sakurai et al. 2015; Nandal et al. 2023c).

Focusing on tracks with accretion rates below  $10^{-2}M_{\odot}$  per year, we observe several features: 1) As primarily established through computations at solar metallicity, the higher the accretion rate, the larger the mass  $(M_{\rm J})$  at which the accreting track joins the Zero Age Main Sequence (ZAMS). For instance, Figure 9.1 shows that this mass is around  $3.5M_{\odot}$  for an accretion rate of  $10^{-6}M_{\odot}$  per year, and approximately  $60M_{\odot}$  for  $10^{-3}M_{\odot}$  per year. 2) The core hydrogen burning phase predominantly occurs in the blue region of the HR diagram. However, the birthlines curve rightward, as classical tracks of core H-burning models do. This phase extends over a broader range of effective temperatures as the accretion rate increases. 3) In our models, the most luminous blue stars reach maximum luminosities of about  $10^8 {\rm L}_{\odot}$ . A rough estimate of this mass can be obtained by solving the equation that equates the formation timescale with the Kelvin-Helmholtz timescale. The Kelvin-Helmholtz timescale is estimated using the radius and luminosity of the star at the joining point. This leads to the following equation:

$$\log \frac{M}{M_{\odot}} = -0.1726 + \frac{3}{2} \log \frac{L}{L_{\odot}} - 2 \log T_{\text{eff}} - \log \dot{M}_{\text{acc}}.$$
 (9.5)

In this context, the accretion rate is measured in solar masses per year and the effective temperature in Kelvin. Table 9.1 lists the input values used to estimate  $M_{\rm J}$  from Eq. (5), as well as the values derived from the numerical simulations. It is observed that for an accretion rate of  $10^{-3}M_{\odot}$  per year, there is a significant discrepancy between the analytic and numerical results<sup>1</sup>. This highlights the necessity of numerical simulations for obtaining more realistic estimates in such cases.

We now turn our attention to those tracks evolving along the Hayashi line before the onset of the core hydrogen-burning phase.

1) These tracks transition from blue to red at luminosities that decrease as the accretion rate increases from  $10^{-2}$  to  $10^{-1}M_{\odot}$  per year. For higher accretion rates, the luminosity at the crossing towards the Hayashi line stabilizes between  $10^{5.7}$  and  $10^{6}L_{\odot}$ . 2) The tracks subsequently ascend the Hayashi line, reaching luminosities up to  $10^{10}L_{\odot}$ . 3) Towards the end of the core hydrogen-

<sup>&</sup>lt;sup>1</sup>The actual age when  $M_{\rm J}$  is 60 M<sub>☉</sub> is longer by nearly a factor 2 than the one given by the Kelvin Helmholtz time for a 60 M<sub>☉</sub> star.

Table 9.1: Values of  $M_{\rm J}$  obtained from Eq. 5 and from the numerical simulations.

$\dot{M}_{ m acc}$	$\log L/{ m L}_{\odot}$	$\log T_{ m eff}$	$M_{ m J}/{ m M}_{\odot}$	$M_{ m J}/{ m M}_{\odot}$
$M_{\odot}/y$ .			ana.	num
$10^{-6}$	2.30	4.325	4.24	3.5
$10^{-5}$	3.60	4.610	10.00	8.0
$10^{-4}$	4.75	4.800	22.00	20.0
$10^{-3}$	5.75	4.950	35.68	60.0

burning phase, they evolve to bluer colors. 4) The stars can attain much larger luminosities, up to  $10^{10.5}L_{\odot}$ , for effective temperatures between 4.00 and 4.25.

## 9.4 Some properties of Pop III supermassive stars

#### 9.4.1 Internal structures

In Fig. 9.3, we present the structural evolution of models with three different accretion rates. Several interesting features emerge:

- 1. For all models, there is a point where the total radius increases rapidly (i.e., the radius increases almost vertically on the diagram, indicating a short timescale). This prevents significant mass increase during the same period. This rapid radius expansion occurs at a total mass (logarithmic scale) of approximately 2.5, 1.5, and 1.5 for accretion rates of  $10^{-2}$ , 1 and  $1000~{\rm M}_{\odot}$  per year, respectively.
- 2. An outer convective zone develops, which diminishes in spatial extent as the accretion rate increases.
- 3. The isomass lines reveal that the majority of the star's mass undergoes contraction.
- 4. In the case of the  $1M_{\odot}$  per year accretion rate, as seen in the middle panel, there are two distinct phases with a convective core. The first phase coincides with core deuterium burning and the second phase is driven by hydrogen burning.
- 5. We note that for the very high accretion rate shown in the right panel, the core is nearly fully radiative after the first 100 years of evolution. Conditions are never met for core hydrogen burning.

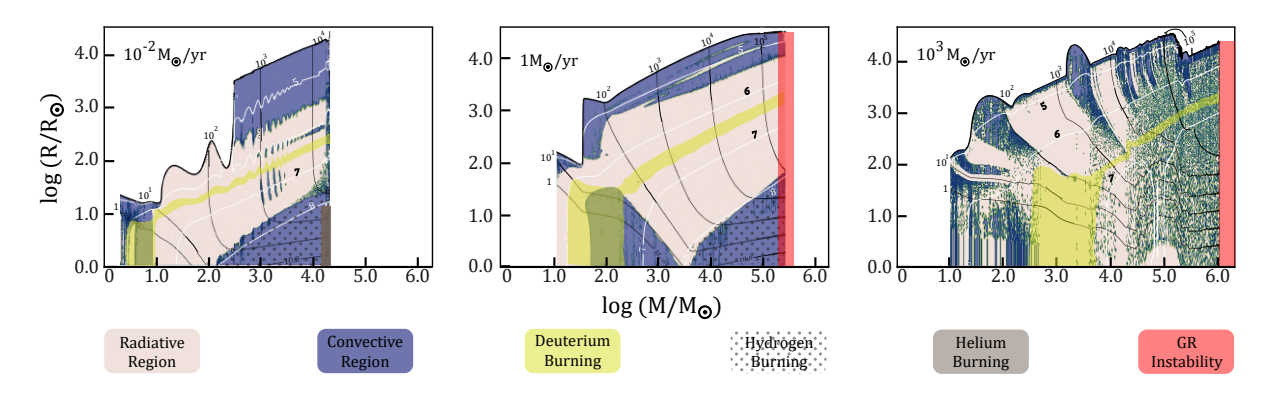


Figure 9.3: Growth of mass versus radius for models with accretion rates of  $10^{-2}/yr$  (left panel), 1/yr (centre panel) and  $10^3/yr$  (right panel) depicted in a Kippenhahn diagram. The coloured regions in the plots correspond to their respective labels in the lower section below the plots.

## 9.4.2 Chemical structure

In Fig. 9.4, the structure of the model with an accretion rate of  $0.1~M_{\odot}$  per year is shown at the end of its evolutionary phase. This phase is characterized by the model encountering GR instability when the central hydrogen mass fraction is at 0.2. Interestingly, this model features a surface region (right panel) where the chemical composition of the primordial material remains intact. As shown in the left panel of the figure, the temperature at the bottom of the outer convective envelope is low enough to prevent the destruction of fragile species such as  $^2H$ ,  $^3He$ , and Li isotopes. At this stage, the star has a luminosity of  $9.6~L_{\odot}$ . In principle, if our models are accurate and if surface abundances can be determined spectroscopically, some of these very massive stars might retain surface abundances of light isotopes identical to those in primordial material. We note also that if at the time of the collapse the star would lose part of its envelope (above the He-core), then most of this mass would be depleted in  $^{12}C$ ,  $^{14}N$  and  $^{16}O$  and enriched in  $^{14}H$  and  $^{4}He$ .

In Nandal et al. (2023a) the chemical feedback from accreting stars ( $10^{-4} - 10^{-3}$ ) with masses in the range of 1000 to 3000  $M_{\odot}$  was examined. This paper will not delve into the specifics but will highlight a few interesting aspects. The studied models do not enoughter general relativistic instability allowing evolution beyond the core hydrogen-burning stage. As they transition into the core helium-burning phase the stars become nearly fully convective. This leads to strong internal mixing and a surface enriched in  $^4$ He, followed by  $^1$ H,  $^{14}$ N and  $^{16}$ O, while being depleted in  $^{12}$ C.

## 9.4.3 Maximum luminosity

Figure 9.1 shows that the highest luminosity reached by an accreting star is around  $10^8 L_{\odot}$  at effective temperatures near 60000 K ( $\lg T_{\rm eff} \sim 4.75$ ). This luminosity increases to over  $10^{10.5} L_{\odot}$  as the effective temperature drops below 18000 K ( $\lg T_{\rm eff} < 4.25$ ). Stars at the extremes of blue and red

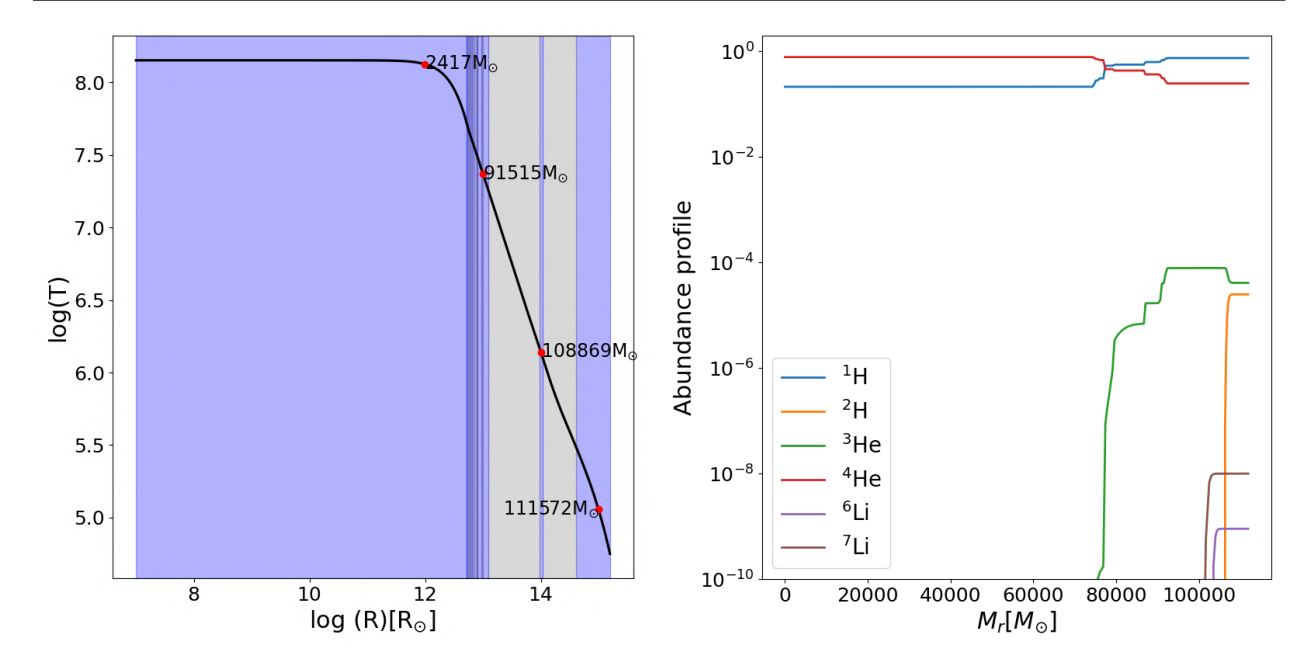


Figure 9.4: *Left panel:* Log T versus log R plot for the 0.1 /yr model at the end of it's evolution upon encountering GR instability. The blue zone indicate convective zones and grey zones correspond to radiative zones. The red indicate the enclosed mass of the interior corresponding to the enclosed radius. A point to note here is that most of the mass(126000) is within a radius of log 13 and only a fraction of mass (still 23000) in in the outer envelope implying the star is extremely bloated. The cyan region represents a convective zone whereas yellow yone is the radiative region. *Right panel:* The plot depicts the change in abundance of various elements inside the 0.1 /yr model at the end of its Hydrogen burning versus the enclosed mass.

side of HR diagram have significantly different structures. Consider a model with a mass of 2072  $M_{\odot}$  at  $\lg T_{\rm eff} = 4.83$ , which is undergoing core hydrogen burning as illustrated in the top panel of Fig. 9.5. The model's central hydrogen mass fraction is 0.30 with the convective core covering about 70% of the total mass. Considering a model of the same luminosity in the HR diagram's redder region, with an accretion rate of  $1M_{\odot}$  per year, it shows a mass similar to its blue counterpart at 2337  $M_{\odot}$ . This model has not started hydrogen burning and its luminosity is primarily from contraction. Inside the star, the ratio  $L_r/L_{\rm tot}$  shows a near-perfect linear relationship with the mass fraction. In regions where the mass fraction ranges from 0.1 to 0.5, the isotope <sup>3</sup>He forms but gets depleted in the core. The model includes an outer convective envelope that is about 10% of its total mass with the majority being radiative as shown in Fig. 9.3's middle panel.

# 9.5 The upper mass limit of stars

Figure 9.6 shows the end states of stars with different maximum masses obtained through accretion. The accretion rate needed for each mass is indicated on the vertical axis. Before we delve into the figure's results, we will first explain how accretion rate affects a star's maximum

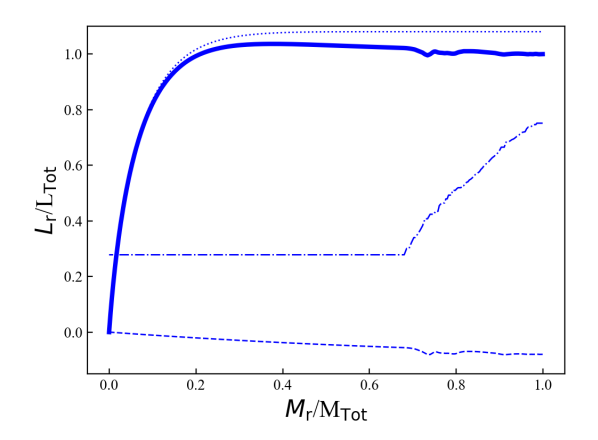
Table 9.2: Some features of the models computed in this work (see text for further details).

$\dot{M}$	End-point	$t_{ m H}$ Myr	$t_{red}/t_{tot.}$	$M_{ m final}$	$X_{ m c,final}$	$M_{\rm core}$
0.000001	End Si-burn	22.5	0.002	22.5	0	5.2
0.00001	End Si-burn	8.40	0.002	86	0	13
0.0001	End Si-burn	4.36	0.002	436	0	121
0.001	End Si-burn	2.796	0.003	3053	0	660
0.010	Mid He-burn $(0.49Y_c)$	2.261	0.998	22600	0	9912
0.050	GR instab. $(0.99Y_c)$	1.680	0.903	82006	0	44792
0.075	GR instab.	1.345	0.826	100972	0.16	62017
0.1	GR instab.	1.040	0.630	112000	0.244	67330
1	GR instab.	0.214	0.230	214100	0.525	60090
10	GR instab.	0.045	0.438	449700	0.619	47560
100	GR instab.	0.007	0.194	697200	0.721	7406
1000	GR instab.	0.001	0.118	1027570	0.751	0

mass. As mentioned, accretion is assumed to occur at a constant rate until instability leads to core collapse and/or explosion. The triggers for core collapse include 1) insufficient exothermic nuclear reactions forming an iron core (nuclear limit), 2) frequent creation of electron-positron pairs from high-energy photons (pair creation limit), and 3) general relativistic instability where photons struggle to support the star against its gravity (General Relativistic limit). These limits are reached at different stages in the evolution of accreting stars. Table 9.2 lists the evolutionary phase during which the core collapses for each accretion rate.

## 9.5.1 The nuclear limit

The nuclear limit occurs at the end of a massive star's nuclear lifespan and is typically reached by stars with maximum masses around 30  $M_{\odot}$ , within the range of massive stars. Models with accretion rates at or below approximately  $2\times 10^{-5}M_{\odot}$  per year typically encounter this limit. These models have been computed until the end of core Silicon burning stage. In the mass range just below the threshold for pair instability supernovae, stars might experience a pulsating phase initiated by pair creation. In non-accreting models, this could lead to mass loss. However, if accretion is ongoing, the impact on the mass evolution of the accreting star is yet to be determined. It is generally believed that when the nuclear limit is reached in this mass range, core collapse may result in the formation of a neutron star or a black hole, possibly accompanied by a supernova event.



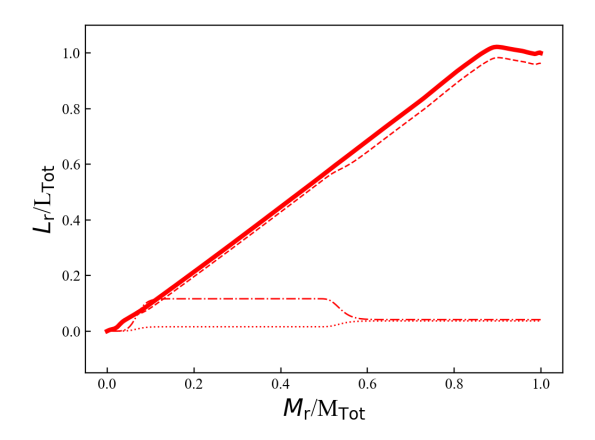


Figure 9.5: top panel: Variation as a function of the mass fraction of the total (continuous line), nuclear (dotted line) and gravitational luminosity (dashed line) for the model computed with an accretion rate of  $10^{-3}~M_{\odot}$  per year when its total luminosity is equal to 6.9  $10^{7}~L_{\odot}$  and the total mass is equal to 2072  $M_{\odot}$ . The dashed line shows the variation inside the model of the hydrogen mass fraction. Bottom panel: Same as for the top panel for the model with an accretion rate of 1.0  $M_{\odot}$  per year when it reaches a luminosity equal to 6.9  $10^{7}~L_{\odot}$  and the total mass is 2337  $M_{\odot}$ . The dashed line shows the variation of the mass fraction of  $^{3}$ He inside the star.

## 9.5.2 The pair creation limit

Pair creation can lead to rapid core collapse in massive stars, potentially resulting in complete stellar disruption. This process is triggered during the later stages of evolution when photon energies exceed 0.51 MeV, corresponding to temperatures of about a billion degrees (REF). Such conditions typically arise post-core helium burning in massive stars. As noted in REF, Population III stars with initial masses between 150 and 250  $M_{\odot}$ , achievable with accretion rates of roughly  $2 \times 10^{-5}$  to  $8 \times 10^{-5} M_{\odot}$  per year, are prone to pair instability supernovae. For higher accretion rates, pair creation destabilizes the core but is unlikely to lead to stellar destruction due to the star's deep gravitational potential well. The fate of stars in this mass range, potentially leading to black hole formation, remains somewhat uncertain. It is unclear whether mass ejection accompanies the black hole formation. Our models suggest that the upper mass limit governed by pair creation is around 3000  $M_{\odot}$ , reached with accretion rates of a few times  $10^{-3} M_{\odot}$  per year, as detailed in the following paragraph.

## 9.5.3 The GR limit

## Pulsational analysis

In the present work, for a few models we performed a pulsation analysis to see when the GR instability will develop. Using the equations discussed in Sect 9.2.1, the stability of the fundamental modes in models with various masses for three various accretion rates is shown in Fig. 9.2. For an accretion rate of  $10^{-1}$  or higher, the fundamental mode becomes unstable when the mass becomes sufficiently large, which is recognized by the steep increase of the growth rate from a negative value. The critical masses for 0.1, 1 and 10 models are 1, 2 and  $4.2 \times 10^5$  at central hydrogen mass fractions = 0.24, 0.52 and 0.62 respectively. Similarly, for models with accretion rates of 100 and 1000(not shown in the plot), the GR instability sets in when = 0.72 and 0.75 respectively. However, in models with the accretion rate  $10^{-2}$   $M_{\odot}$ /yr the central hydrogen is exhausted before the mass is increased enough for the GR instability.

The right-hand panel of Figure 9.2 shows radial displacements  $\xi$  (normalized as unity at the surface) of the fundamental mode as a function of the normalized distance from the center, r/R, for models of different masses accreting at  $10~M_{\odot}/{\rm yr}$ . Models with  $M\lesssim 4\times 10^5 M_{\odot}$  are stable and the displacement  $\xi$  of the fundamental mode is roughly proportional to r, i.e.  $\xi/r\approx {\rm constant}$  irrespective to the stellar mass. Models with  $M\gtrsim 4\times 10^5 M_{\odot}$  are unstable and the displacement  $\xi$  of the fundamental mode ( $\omega^2<0$ ) has a large peak in the interior where the GR effect is strongest. The radial distribution of  $\xi$  indicates that the GR instability leads to a collapse of the central part

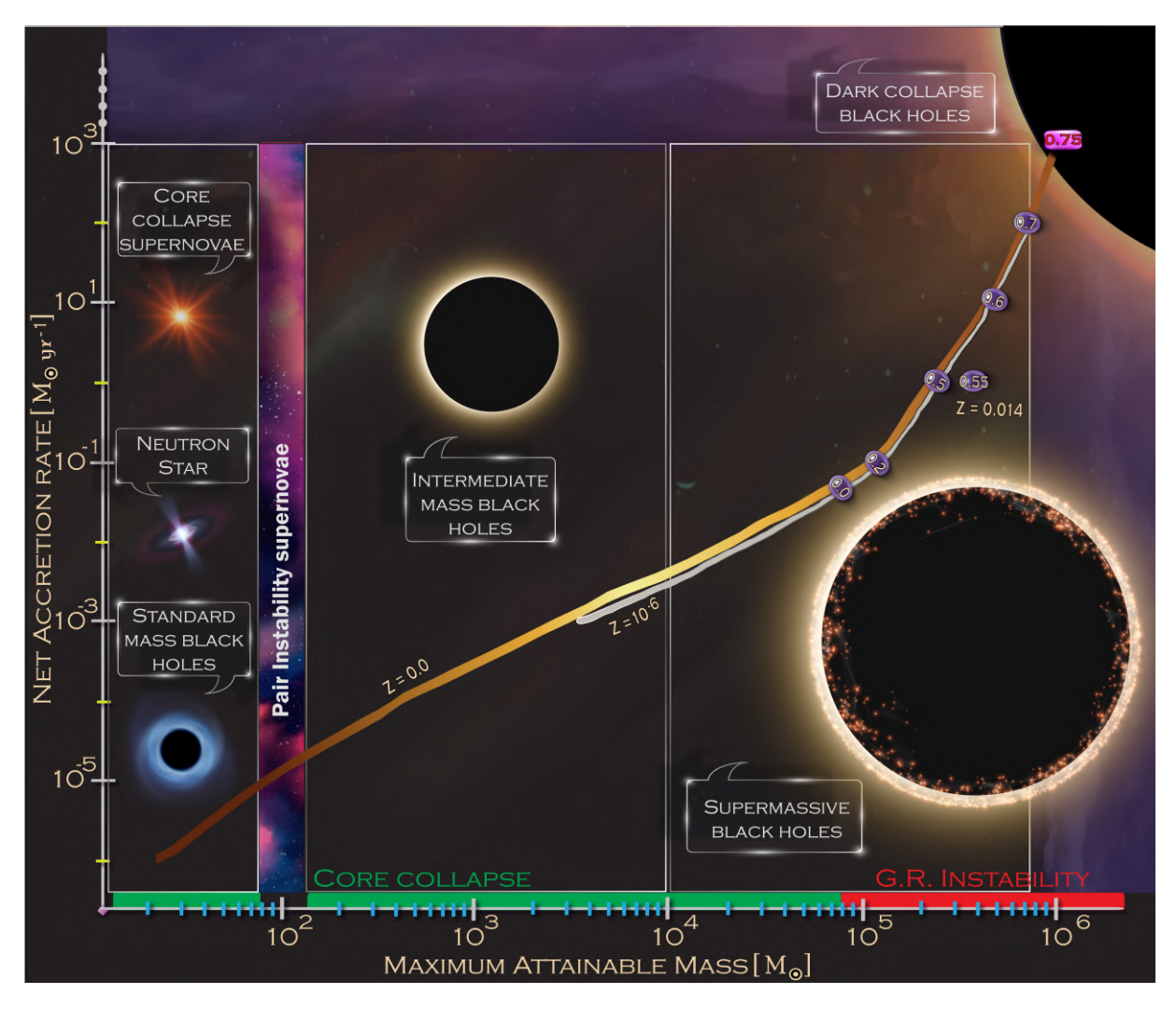


Figure 9.6: An illutration depicting the relation of mass versus the accretion rates for constant accretion rate models ranging from  $10^{-6}/\text{yr}$  to  $10^3/\text{yr}$ . The gold line represents the zero metallicity models, the silver line represents  $Z=10^{-6}$  metallicity and the single dot at 1 /yr shows the solar metallicity model. The green bar on the x-axis indicates the final fate is determined by the core collapse that occurs beyond core silicon burning stage whereas the red bar shows the final premature collapse of a star via the general relativistic instability that occurs during core hydrogen burning. The vertical pair instability strip spans between 150 - 250 . The small black circle on the left of the illustration shows a standard mass black hole that occurs in the mass range of 7 - 150 . The black circle at the center of the image represents an intermediate mass black hole with mass ranging from 250 -  $8 \times 10^4$  and finally the supermassive black holes seeds are depicted by the large black circles with masses in excess of  $10^5$ .

Table 9.3: Final masses (in units of  $10^5 \text{ M}_{\odot}$ ) at the onset of GR instability: comparison between the integral form, the pulsational analysis, and with previous work.

acc		This work				
	Umeda et al. (2016)	Woods et al. (2017)	Haemmerlé et al. (2018)	Haemmerlé (2021b)	Integral form	Puls. analysis
0.1	1.20	1.65	-	-	1.08	1.00
1	3.50	2.60	1.16	2.29	2.04	2.00
10	8.00	3.20	2.61	4.37	4.49	4.20

first.

## The Supermassive star domain

For accretion rates above a few times  $10^{-3}~\rm M_\odot$  per year, the general instability limit is reached at still earlier evolutionary stage when the accretion rate increases. The boundary between stars facing the pair creation and the general relativistic limit depends on their evolutionary sequence. These stars encounter the general relativistic limit before meeting pair creation conditions. Assuming pair creation requires conditions after the core helium burning stage, the critical factor becomes the accretion rate. The lowest accretion rate leading to relativistic instability before the end of core helium burning marks this limit. In our current models, we identified the lowest accretion rate required to reach conditions for the GR instability. This occurs at the end of the core H-burning phase or the beginning of the core He-burning phase. This critical accretion rate is  $5 \times 10^{-2} M_\odot$  per year. It corresponds to a maximum mass of 84600  $M_\odot$ . We regard this mass limit as the transition point between stars facing the pair creation limit and those meeting the GR limit. Past this limit, stars reach the GR instability at progressively earlier stages. In Fig. 9.6, we indicate the central hydrogen mass fraction at points where GR instability occurs. For accretion rates beyond  $100~M_\odot$  per year, GR instability happens before core hydrogen burning begins, leading to what is known as a dark collapse black hole (Mayer & Bonoli 2019).

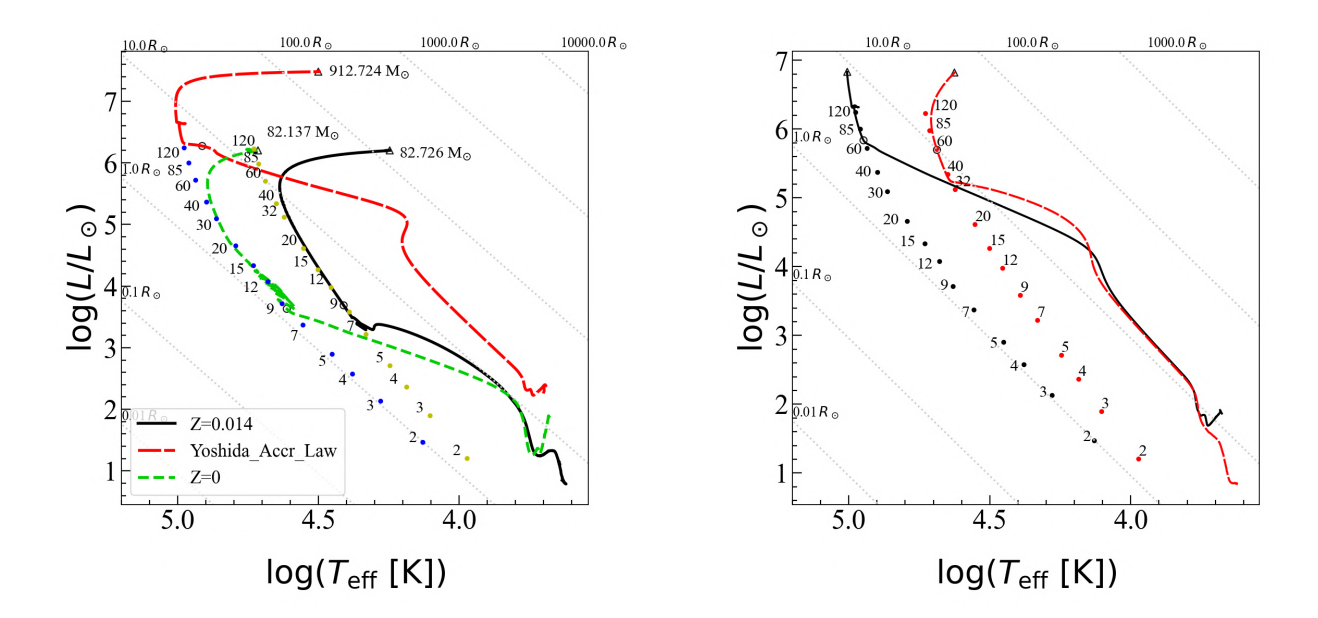


Figure 9.7: Birthlines for different accretion rates and metalicities. The dashed red lines correspond to the variable accretion rate obtained from hydrodynamical simulations by Yoshida et al. 2006 for Pop III stars (see text). The solid black track represents the model at solar metallicity with a constant accretion rate of  $10-5\,\rm M_\odot$  per year. The short dashed green track corresponds to the zero metallicity model with constant accretion rate of  $10-5\,\rm M_\odot$  per year. The black circle on each track marks the beginning of core hydrogen burning and the black triangle marks the end of H burning. Masses at the end of hydrogen burning are indicated in solar masses at the end of each track. The solid blue numbered dots form the ZAMS of Murphy et al. (2020) at zero metallicity and the solid yellow dots are taken from solar metallicity models of Ekström et al. (2012b). The positions of a few initial masses are indicated along the ZAMS. The grey dotted lines are the iso-radii of the indicated radii.

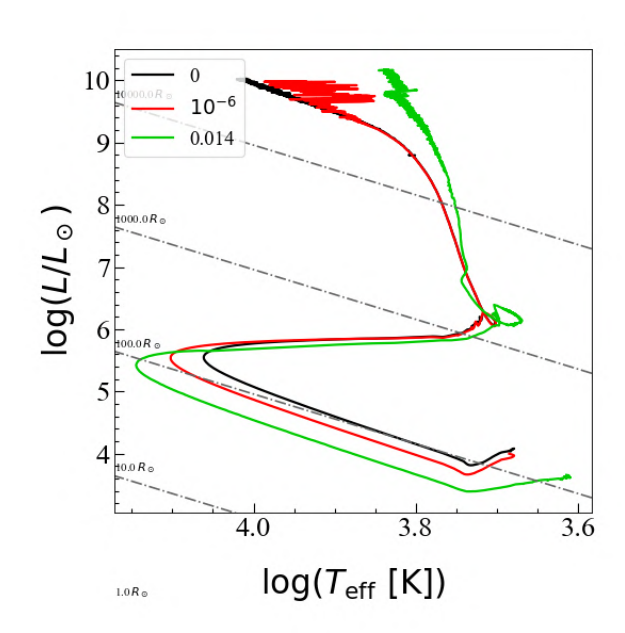


Figure 9.8: HRD of 3 SMS models with accretion rate of 1 /yr at three different metallicities.

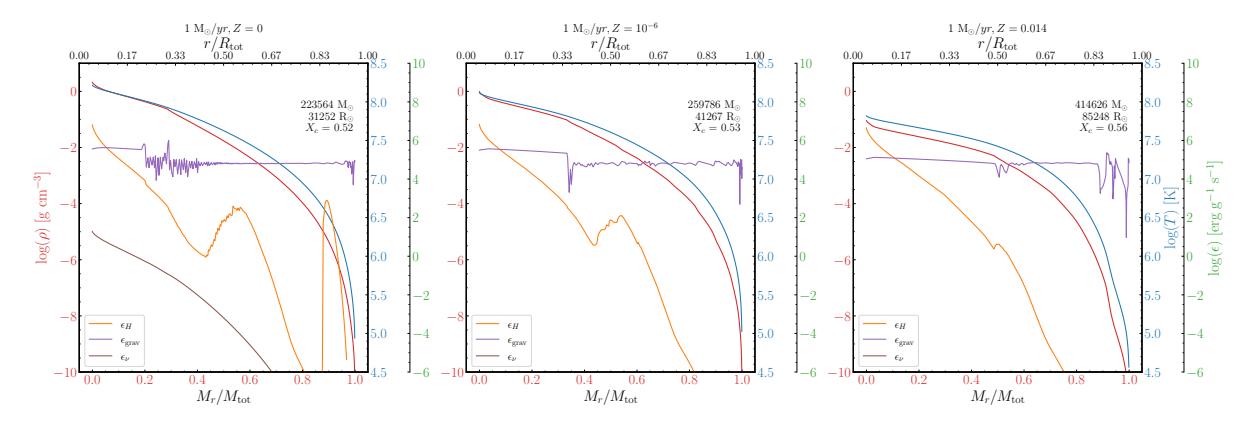


Figure 9.9: The evolution of various physical parameters versus the mass and radius of three models with acretion rate of 1/yr at zero (left panel),  $10^{-6}$  (centre panel) and solar (right panel) metallicities.

# 9.6 Effects of changing the metallicity

## 9.6.1 For classical accretion rates

Figure 9.7 compares birthlines at solar and primordial compositions. The primordial composition birthline is based on accretion rates from hydrodynamical simulations by Yoshida et al. (2006). For solar metallicity, we used a constant accretion rate of  $10^{-5}M_{\odot}$  per year. The comparison between the red and black birthlines in Figure 9.7 offers insights into expected stellar behaviors in primordial mini-haloes versus the solar neighborhood. During the initial evolution phase before contracting to the Zero Age Main Sequence (ZAMS), the track for accreting Population III (Pop III) protostars shifts to lower effective temperatures than those with solar metallicity. This shift is primarily due to the accretion rate rather than metallicity differences. This is evident in the right panel of Figure 9.7, where birthlines for Pop III (black lines) and solar metallicity (red line) with a constant accretion rate of  $10^{-3}M_{\odot}$  per year are shown. Both tracks align up to a luminosity of 4.3 in  $\lg L/L_{\odot}$ , suggesting minimal impact from metallicity changes. Examining the left panel of Fig. 9.7, the birthline with solar metallicity and a lower accretion rate reaches the Zero Age Main Sequence (ZAMS) at about 7  $M_{\odot}$ . In contrast, for the higher accretion rate at Z=0, this occurs at a much higher mass, around 120  $M_{\odot}$ . This difference is attributed to the varying accretion rates, a phenomenon previously discussed in other works Haemmerlé et al. (2016). Essentially, a higher accretion rate leads to a larger mass accreted within a Kelvin-Helmholtz timescale.

The right panel of Fig. 9.7 also shows that the mass at which the birthline reaches the ZAMS is influenced by metallicity. For a given accretion rate, the joining mass at solar metallicity is around  $32\ M_{\odot}$ , compared to  $60\ M_{\odot}$  at Z=0 metallicity. This difference is due to Z=0 stars being more compact, a result of lower opacities and the absence of CNO elements, which are crucial for catalyzing hydrogen burning in the core. The smaller radii, with equal mass and luminosity, lead to longer Kelvin-Helmholtz (KH) timescales, allowing more time for mass accumulation. In the left panel of Fig. 9.7, the birthline for Z=0 metallicity with an accretion rate matching the solar metallicity case is plotted. This reveals that the birthline shapes are quite similar, suggesting the accretion rate plays a more significant role than initial metallicity. Notably, the tracks overlap in the less luminous and redder regions of the HR diagram. Differences start to appear as the star contracts towards the blue part. Furthermore, both birthlines reach the ZAMS at almost the same mass, with the Population III track being slightly larger. The masses achieved at the end of the main sequence phase are also similar in both cases. Finally, the mass achieved at the end of the MS phase varies significantly with the accretion rate. For lower accretion rates, the final mass is around  $83\ M_{\odot}$ , while for higher rates, it exceeds  $900\ M_{\odot}$ .

## 9.6.2 For high accretion rates

Figure 9.9 displays evolutionary tracks for accreting stars at various metallicities with an accretion rate of 1  $M_{\odot}$  per year. Overall, the differences in tracks are relatively minor. For luminosities below  $10^6 L_{\odot}$ , the track shifts towards the blue with increasing metallicity. Conversely, for luminosities above  $10^6 L_{\odot}$ , it shifts towards the red. For stars on the Zero Age Main Sequence (ZAMS), a well-known effect is that higher metallicity shifts the tracks towards the red. This shift occurs because an increase in metallicity raises the star's outer layers, resulting in cooler temperatures at an optical depth of about 2/3. This effect is due to changes in opacity in the outer layers, affecting the star's radius or effective temperature but not its luminosity.

During the initial accreting period, an increase in metallicity actually shifts the tracks towards the blue. This shift arises because the increased opacity affects a larger portion of the star's total mass, which in turn reduces luminosity for a given mass. Therefore, as metallicity increases, the tracks are not only shifted to the right but also towards lower luminosities. The combined effect of these shifts is evident in Fig. 9.9. In the second, more luminous phase of the tracks, stars are undergoing hydrogen burning in their cores. The increased opacities in more metal-rich stars predominantly affect their outer layers. This results in a shift of the track towards the red, similar to what is observed in classical ZAMS stars. Figure 9.8 illustrates various properties of models during the core hydrogen-burning phase at the end of their evolution. These models are compared across different metallicities using an accretion rate of 1  $M_{\odot}$  per year.

Several interesting observations emerge from comparing the plots in these three models:

- 1. The energy released per unit time and mass due to contraction is nearly constant across the interior for all metallicities, averaging around  $10^5$  ergs  $g^{-1}$  s<sup>-1</sup>.
- 2. The total mass at the end of the evolution is higher for greater metallicities. Consequently, the timescales vary with metallicity, being almost twice as long at solar metallicity compared to Population III models.
- 3. Stars have larger sizes at higher metallicities. At the stage shown in Fig. 9.8, the solar metallicity model is more than twice the size of the Population III model.
- 4. There is a notable bump in the rate of nuclear energy production around a mass fraction of 0.6, more pronounced in Population III models than in the solar metallicity model.
- 5. The central temperature is higher in the Population III model, which is a direct result of the absence of CNO elements.

Even during the core hydrogen-burning phase, these stars primarily generate energy through contraction. The longer timescale for the solar metallicity model stems from its larger convective core compared to the Population III counterpart. This larger core extends the core hydrogen-burning phase, providing more time for mass accretion. The increased radius is a result of higher opacities in the outer layers.

## 9.7 Conclusions

In this chapter, we have explored the evolution of accreting objects within the Hertzsprung-Russell diagram, focusing on a range of accretion rates from  $10^{-6}$  to  $10^3 M_{\odot}$  per year. Our findings contribute to a clearer understanding of the impact of these rates on stellar evolutionary paths and highlight the key processes influencing stellar growth and development. The main findings of our study are summarized as follows:

- Stellar evolutionary tracks are broadly divided based on accretion rates, with a critical rate of approximately  $2.5 \times 10^{-2} M_{\odot}$  per year. This rate distinguishes tracks evolving towards the blue from those following the Hayashi line before igniting hydrogen in their cores.
- For accretion rates below  $10^{-2}M_{\odot}$  per year, the mass at which tracks join the Zero Age Main Sequence (ZAMS) increases with the accretion rate. The core hydrogen burning phase predominantly occurs in the blue region of the HR diagram, with luminosities reaching up to  $10^8L_{\odot}$ .
- The study establishes maximum luminosity and mass limits for stars, dictated by Nuclear, Pair Creation, and General Relativistic (GR) Limits. Notably, the upper mass limit for pair creation is around 3000  $M_{\odot}$ , achievable at accretion rates of a few times  $10^{-3}M_{\odot}$  per year. The GR limit becomes significant at an accretion rate of  $5 \times 10^{-2}M_{\odot}$  per year, corresponding to a maximum mass of 84600  $M_{\odot}$ , and potentially leading to a dark collapse black hole.
- Metallicity significantly influences the birthlines of stars, with higher accretion rates leading to larger masses at ZAMS. The evolutionary tracks shift towards the blue at lower luminosities and towards the red at higher luminosities with increasing metallicity. For a constant accretion rate of  $1\,M_\odot$  per year, higher metallicity results in a larger total mass at the end of evolution, increased star sizes, and enhanced nuclear energy production.
- The findings have implications for cosmic reionization processes, indicating that variations
  in accretion rates and metallicity can significantly affect the duration and characteristics of

stars, thereby influencing their role in cosmic events.

This research enhances our understanding of stellar evolution in the context of varying accretion rates and metallicity. These insights lay a foundation for future research in stellar astrophysics and their broader cosmic implications.

This comprehensive research provides an in-depth examination of the formation and evolution of massive stars, particularly focusing on Population III stars. It delves into the complex interplay between accretion processes, metallicity effects, and stellar evolution, while also addressing the broader cosmic context.

- Evolution of Accreting Stars: The study covers accretion rates over nine orders of magnitude, demonstrating how these rates influence the mass growth and evolutionary trajectory of massive stars. Key mass and accretion rate limits are identified for different final fates and characteristics of the stellar remnants.
- Luminosity and Temperature Ranges: We observed that the most luminous accreting stars reach bolometric luminosities up to  $10^8 L_{\odot}$  for higher effective temperatures, and up to  $10^{10.5}$  for lower temperatures.
- Accretion Impact and Instability Conditions: The research explores extreme cases of accretion during a star's lifetime, highlighting that accretion can stop before triggering instabilities, leading to further evolution and impact on the star's surroundings.
- Upper Mass Limit and GR Instability: A significant finding is the identification of the upper mass limit for stars at approximately 1 million  $M_{\odot}$ , beyond which they undergo 'dark collapse' into black holes. The lower mass limit for General Relativistic (GR) instability is identified around 82,000  $M_{\odot}$ , crucial for understanding supermassive star evolution.
- Effect of Initial Metallicity: Changes in initial metallicity have substantial impacts on the
  evolutionary process, with increased metallicity leading to larger star sizes and extended
  core hydrogen-burning phases.
- Considerations and Limitations: The results are influenced by factors such as the choice of FITM, effects of rotation and magnetic fields, and the history of the accretion rate. Observability may also be affected by the optical thickness of the infalling material.
- 1. We have presented the evolution of accreting stars considering accretion rates spanning nine orders of magnitude.

Table 9.4: Mass and accretion rate limits for various final outputs in primordial conditions.

$\dot{M}$	pre-collapse	Type of	BH mass	
	Max. Masses $(M_{\odot})$	limits		
$10^{-6} \sim 10^{-3}$	3000	CC, Pair inst.	660-3000	
$10^{-3} \sim 10^{-1}$	112000	GR	67000-112000	
$10^{-1} \sim 10^1$	449700	GR	112000-449700	
$10^{-3} \sim 10^2$	697200	GR	449700-697200	
$> 10^2$	1027570	GR	697200-1027570	

- 2. We have obtained the following mass and accretion rate limiting values for different final fates and characteristics of the remnant (see Table 9.4)
- 3. The most luminous accreting star have bolometric luminosities up to  $10^8~L_{\odot}$  for effective temperatures larger than NNN, and up to  $10^{10.5}$  for effective temperature below.
- 4. We have shown that SMS might be distinguished from similar luminous objects through a few features that will be difficult to observe but would be signatures of such objects: variability, neutrinos, circumstellar matrials, jets?
- 5. The computations presented here has explored extreme cases of accretions that will occur during the whole lifetime of a star. Accretion can however stops before the conditions for an instablity to be triggerred. In that case the star will continue to evolve and may have impact on their surrondings by mechanical, radiative and chemical feedbacks. We have shown here that...
- 6. Finally we have studied the impact of changing the initial metallicity. We conclude that increasing the metallicity increases the final mass at which the GR instability is reached.

The above results might be different depending on 1) choice of FITM 2) might be impacted by rottaion and magnetic fields 3) the history of the accretion rate 4) Observability may be impacted by the optical thickness of the infalling material.

# Additional work

## 10.1 Final fate of Betelgeuse inferred from its pulsations

Betelgeuse, a red supergiant star in the Orion constellation, is one of the most well-studied stars in the sky due to its size, brightness, and relatively close proximity to Earth. It is a class M star, with a mass estimated to be about 15 to 20 times that of the Sun and a radius that would extend out to the orbit of Mars if placed in our solar system. Betelgeuse is nearing the end of its life; until now, it is expected to explode as a Type II supernova within the next million years, an event that would be visible from Earth even during the day.

The study of Betelgeuse's pulsation periods is of particular interest to astrophysicists because it can provide clues about the internal structure and processes of the star. These pulsations are a form of stellar variability involving the expansion and contraction of the star's outer layers. They are believed to be driven by the same mechanisms that cause Cepheid variables to pulsate, which is understood primarily through the Kappa mechanism or Eddington valve, where radiation gets trapped in ionized layers of the star's atmosphere, leading to increased opacity and outward pressure.

The fundamental equation that describes stellar pulsation is the linear adiabatic oscillation equation:

$$\frac{d}{dr}\left(P_s\frac{d\xi_r}{dr}\right) + \left(\frac{2}{r}\frac{dP_s}{dr} - \frac{Gm\rho}{r^2}\right)\xi_r + \left(\frac{S_l^2\rho}{r^2} - \omega^2\rho\right)\xi_r = 0$$
(10.1)

where  $\xi_r$  is the radial displacement,  $P_s$  is the pressure perturbation,  $\rho$  is the density, G is the gravitational constant, m is the mass within radius r,  $S_l$  is the Lamb frequency, and  $\omega$  is the angular frequency of oscillation.

Betelgeuse's pulsation periods have been observed to change over time, which suggests that the star's internal structure is also changing. This could be due to various factors such as convection, rotation, magnetic fields, and the evolving balance between gravity and radiation pressure in the star's core. By studying these pulsations, astrophysicists can gain insights into the complex processes taking place inside Betelgeuse and other massive stars.

The energy transport in Betelgeuse is believed to be dominated by convection, which can be described by the mixing-length theory. The convective velocity ( $v_{conv}$ ) is given by:

$$v_{\rm conv} = \alpha H_p \left(\frac{L}{L_{\rm edd}}\right)^{1/3} \tag{10.2}$$

where  $\alpha$  is the mixing-length parameter,  $H_p$  is the pressure scale height, L is the luminosity, and  $L_{\rm edd}$  is the Eddington luminosity.

The study of such pulsation periods is critical for testing and refining our models of stellar structure and evolution. It allows us to map the interior of stars like Betelgeuse in a way that would otherwise be impossible, given that we cannot directly observe a star's internal processes. These models are essential not only for understanding the life cycles of individual stars but also for our comprehension of the evolution of galaxies, as massive stars like Betelgeuse play a crucial role in enriching the interstellar medium with heavy elements and in triggering the formation of new stars.

#### 10.1.1 Literature review

Betelgeuse ( $\alpha$  Orionis; HD 39801), a prominent red supergiant star (M1-2 Iab-a) approximately 200 parsecs from the Sun, has an intriguing history. Recent analysis of historical observations by Neuhäuser et al. (2022) indicates that Betelgeuse's surface temperature was significantly warmer two thousand years ago. This star has been known for its semi-regular brightness variations, documented for over a century. These and other phenomena concerning Betelgeuse are thoroughly reviewed in Wheeler & Chatzopoulos (2023).

An unusual drop in Betelgeuse's brightness, termed the 'Great Dimming', occurred from December 2019 to February 2020, with a decrease of approximately 1.2 magnitudes at around a 400-day minimum variation period (Guinan et al. 2019). Triggered by this event, numerous observations and analyses across various wavelengths were conducted. The findings indicate a drop in the effective temperature by roughly 100 K during the dimming (Dharmawardena et al. 2020; Harper et al. 2020; Taniguchi et al. 2022a; Wasatonic 2022; Mittag et al. 2023) and suggest a significant mass ejection (Montargès et al. 2021; Kravchenko et al. 2021; Taniguchi et al. 2022b; Dupree et al. 2022; Jadlovský et al. 2023).

The high luminosity of Betelgeuse and its complex behavior, which may hint at an upcoming

supernova event, have led to extensive research into its evolution (Meynet et al. 2013; Dolan et al. 2016; Wheeler et al. 2017; Nance et al. 2018). Its rapid rotation as a red supergiant, with an equatorial velocity of  $6.5^{+4.1}_{-0.8}$  km/s (Kervella et al. 2018), has prompted theories about its past, including the possibility of a merger with a companion star as a source of angular momentum (Sullivan et al. 2020).

The semi-regular pulsation periods of Betelgeuse provide valuable insights into its current physical parameters and evolutionary stage. Two periods are predominantly acknowledged: 2200 days and 420 days. Historically, the 420-day period was presumed to be the radial fundamental mode (Joyce et al. 2020), while the 2200-day period was thought to arise from a mechanism other than radial pulsations. Contrary to these assumptions, this paper demonstrates that, in a luminous supergiant like Betelgeuse, long-period pulsations are highly nonadiabatic. We argue that the 2200-day period corresponds to the radial fundamental mode, and the 420-day period is better attributed to the first overtone mode.

Supporting our assertion, we extend the period-luminosity (PL) relations for less luminous red giants to include the supergiant range, as depicted in Kiss et al. (2006) and Chatys et al. (2019). Our analysis reveals that the 420-day period, with an absolute magnitude in the K band ( $M_K$ ) of about -10, aligns with the extension of sequence B, identified with the first overtone radial pulsation (Trabucchi et al. 2017). This identification clarifies that the 420-day period is the first overtone mode in Betelgeuse. As pulsation periods for a specific mode are shorter in stars with a smaller radius, assuming the 420-day period as the radial fundamental mode would significantly underestimate Betelgeuse's size.

## **10.1.2** Global Parameters

Determining the global parameters of Betelgeuse has been the focus of various studies. Lobel & Dupree (2000) measured the surface gravity,  $\log g = -0.5$ , and effective temperature,  $T_{\rm eff} = 3500 \pm 100$  K, through the fitting of synthetic profiles to distinct metal absorption lines in near-infrared spectra. Complementary to this, Carr et al. (2000) derived a similar  $T_{\rm eff} = 3540 \pm 260$  K based on CO equivalent widths. More recently, Levesque & Massey (2020) reported  $T_{\rm eff} = 3600 \pm 25$  K from optical spectrophotometry. In light of these spectroscopic determinations, we adopt  $T_{\rm eff} = 3500 \pm 200$  K as a model constraint, aligning with the range used by Dolan et al. (2016).

It is worth noting, as Josselin et al. (2000) highlighted, that the K-magnitude offers a more reliable measure for calculating the bolometric luminosity of red supergiants (RSGs) than the V-magnitude. This preference is due to the K-band bolometric correction's low sensitivity to variations in effective temperature and surface gravity, coupled with its reduced susceptibility to inter-

stellar extinction and pulsation effects. Utilizing data from the 2MASS All-Sky Catalog of Point Sources (Cutri et al. 2003), Betelgeuse's K-magnitude is established at  $-4.378 \pm 0.186$  mag. By applying the distance of  $222^{+48}_{-34}$  pc from the new radio+Hipparcos astrometric solution by Harper et al. (2017), and a K-band bolometric correction of  $2.92 \pm 0.16$  (Levesque et al. 2005) appropriate for  $T_{\rm eff} = 3500 \pm 200$  K, we calculate a bolometric luminosity of  $\log(L/L_{\odot}) = 5.18 \pm 0.11$  for Betelgeuse. This estimate is in close agreement with the value of  $\log(L/L_{\odot}) = 5.10 \pm 0.22$  adopted by Dolan et al. (2016).

#### 10.1.3 Observed Pulsation Periods

The variable luminosity of Betelgeuse is characterized by semi-regular light variations, revealing a spectrum of periodicities from approximately 2200 days to as short as 185 days. This multiperiodicity is evident in the fact that every photometric time series analysis has identified multiple pulsation periods for Betelgeuse (Jadlovský et al. 2023; Ogane et al. 2022; Wasatonic 2022; Granzer et al. 2022; Joyce et al. 2020; Kiss et al. 2006; Stothers & Leung 1971). The most recent determinations of these periods by various researchers are summarized in Table 1. From these findings, we focus on four specific periods, denoted as P1, P2, P3, and P4, which are compiled in the final row of Table 1. The 365-day period noted by Jadlovský et al. (2023) has been dismissed as an annual alias.

In examining these four periods and assuming they result from radial pulsations within Betelgeuse, we have sought stellar evolution models that can excite pulsations of these periods within the observational error margins presented in the Hertzsprung-Russell diagram for this star.

## 10.2 Models

## 10.2.1 Stellar Evolution Models

The evolution of massive stars from the Zero-age main sequence (ZAMS) through to the termination of core-carbon burning, and in some instances to the end of silicon burning, has been simulated utilizing the latest iteration of the Geneva stellar evolution code (GENEC) (Ekström et al. 2012a; Yusof et al. 2022). Consistent with the initial compositions used by Yusof et al. (2022), the models are initiated with hydrogen and heavy element mass fractions of X=0.706 and Z=0.020, respectively. The mixing length parameter for envelope convection has been set to 1.6 times the pressure scale height. The boundaries of the convective core are established following the Schwarzschild criterion, complemented by a step overshooting parameter of  $0.1H_p$ , where  $H_p$  represents the pressure scale height at the core boundary.

## 10.2.2 Rotation and Mixing

Initial rotation velocities ( $v_i$ ) in the models are defined as a fraction of the critical rotation velocity ( $v_{crit}$ ) at ZAMS, considering values of 0.1, 0.2, and 0.4 times  $v_{crit}$ . Although rotation rates in the envelopes of red supergiants are minimal and do not significantly influence radial pulsations, rotational mixing is factored in as it enhances the effective core mass, thereby increasing the luminosity (Ekström et al. 2012a; Yusof et al. 2022). Additionally, the surface abundances of CNO cycle elements are modified depending on the chosen initial rotation rates.

#### 10.2.3 Pulsation Analysis

The periods and stability of radial pulsations across a range of models have been analyzed using the same nonadiabatic linear radial pulsation code as applied by Anderson et al. (2016) for studying Cepheid pulsations. This code, initially outlined in Saio & Wheeler (1983), has been updated to incorporate interactions between pulsation and time-dependent convection. Convective effects are included in line with the methodologies established by Unno (1967) and Grigahcène et al. (2005), which have been instrumental in accurately determining the red-edge of the Cepheid instability strip. A comprehensive description of the pulsation code and its applications is provided in the section.

### Radial pulsations coupled with convection

In this section we derive differential equations to solve radial pulsations taking into account the coupling with convection based on the mixing-length theory. In the beginning we follow Unno (1967) discussion but later we include additional terms to avoid rapid oscillations where the turnover time is longer than the pulsation period (e.g. Grigahcène et al. (2005)). We summarise differential equations of radial pulsations in the last part of this appendix.

#### **Basic Equations**

Equations of motion and mass conservation, including convective motion may be written as

$$(\rho + \rho') \left[ \frac{\partial}{\partial t} + (\mathbf{u} + \mathbf{V}_c) \cdot \nabla \right] (\mathbf{u} + \mathbf{V}_c) = -\nabla (P + P') - (\rho + \rho') \nabla \psi$$
 (10.3)

and

$$\frac{\partial}{\partial t}(\rho + \rho') + \nabla \cdot \left[ (\rho + \rho')(\mathbf{u} + \mathbf{V}_c) \right] = 0, \tag{10.4}$$

where  $\mathbf{u}$  and  $\mathbf{V}_c$  are pulsation and convection velocities, respectively, and a prime ' such as  $\rho'$ , P', T', etc means the convective Eulerian perturbation. We neglect convective perturbation of the gravitational potential  $\psi$ .

Conservation of thermal energy may be written as

$$(\rho + \rho')(T + T') \left[ \frac{\partial}{\partial t} + (\mathbf{u} + \mathbf{V}_c) \cdot \nabla \right] (S + S') = \rho \varepsilon_n + (\rho \varepsilon_n)' - \nabla \cdot (\mathbf{F}_{rad} + \mathbf{F}'_{rad}), \tag{10.5}$$

where S and  $\varepsilon_n$  are the entropy and the nuclear energy generation rate per unit mass, respectively, and  $\mathbf{F}_{rad}$  is the radiative energy flux.

#### Equations for mean fluid

Taking a horizontal average ( $\overline{V_c} = 0$ , (...)' = 0) of equation (10.3), and assuming the Boussinesq approximation for convection motions, we have

$$\frac{d\overline{\rho}}{dt} + \overline{\rho}\overline{V_c} \cdot \overline{V_c} = -\nabla \overline{P} - \overline{\rho}\nabla \psi, \tag{10.6}$$

where the second term on the left-hand-side is the turbulent stress. where we have defined

$$\frac{d}{dt} = \frac{\partial}{\partial t} + \mathbf{u} \cdot \nabla. \tag{10.7}$$

Similarly, taking horizontal averages of equations (10.4) and (10.5) we obtain

$$\frac{d\overline{\rho}}{dt} + \overline{\rho}\mathbf{u} \cdot \mathbf{u} = 0. \tag{10.8}$$

and

$$\overline{\rho}T\frac{d\overline{S}}{dt} + \overline{\rho}T\overline{V_c} \cdot \nabla \overline{S'} = \overline{\rho}\varepsilon_n - \nabla \cdot \mathbf{F}_{\text{rad}}, \tag{10.9}$$

where we have assumed that  $|T'| \ll T$  and  $|\rho'| \ll \rho$ . Since  $\overline{V_c} \cdot \nabla = 0$  (Boussinesq approximation) and hence  $\overline{V_c} \cdot \nabla S' = \nabla \cdot (\overline{V_c} S')$ , we approximately write equation (A7) as

$$\overline{\rho}T\frac{d\overline{S}}{dt} = \overline{\rho}\varepsilon_n - \nabla \cdot \mathbf{F}_{\text{rad}} - \nabla \cdot \mathbf{F}_{\text{con}}, \tag{10.10}$$

with defining the convective flux as

$$F_{\rm con} = \overline{\rho} T \overline{V_c} \nabla T' \tag{10.11}$$

Unno (1967). Considering the pulsational Lagrangian perturbations  $\delta$  and keeping only linear

terms we have

$$\frac{\delta F_{\text{con}}}{F_{\text{con}0}} = \left(\frac{\delta \rho}{\rho} + \frac{\delta T}{T}\right) + \overline{\rho} T \left[ (\delta V_c) \nabla S' + V_c \delta S' \right]. \tag{10.12}$$

In the equilibrium condition the mean convective flux has only radial direction,

$$F_{\text{con0}} = e_r \overline{\rho} T \overline{V_c} S'. \tag{10.13}$$

We can write equation (A10) as

$$\frac{\delta F_{\text{con}}}{F_{\text{con}0}} = \left(\frac{\delta \rho}{\rho} + \frac{\delta T}{T}\right) e_r + \frac{\delta V_c}{V_r} + \frac{V_c \delta S'}{S'}$$
(10.14)

For radial pulsations,  $\mathbf{u} = u_e r$ , we have

$$\frac{\delta F_{\text{con}}}{F_{\text{con}}} = \left(\frac{\delta \rho}{\rho} + \frac{\delta T}{T}\right) + \frac{\delta V_c}{V_r'} + \frac{\delta S'}{S'}$$
(10.15)

Then, we have

$$\delta(\nabla \cdot F_{\text{con}}) = \frac{1}{r^2} \frac{d}{dr} (r^2 \delta F_{\text{con}}) - \frac{d\zeta_r}{dr} \frac{dF_{\text{con}}}{dr} - \frac{2\zeta_r F_{\text{con}}}{r^2}, \tag{10.16}$$

where  $\zeta_r$  stands for the radial displacement of pulsation.

## **Equations for time-dependent convection**

### Mechanical equations

Subtracting equation (10.6) from equation (10.3) and neglecting a non-linear term  $\rho \mathbf{u} \cdot \nabla \mathbf{u}$ , we obtain

$$\rho \frac{d\mathbf{V}_c}{dt} + \rho(\mathbf{V}_c \cdot \nabla \mathbf{V}_c - \mathbf{V}_c \cdot \mathbf{V}_c) + \rho \mathbf{V}_c \cdot \nabla \mathbf{u} = -\nabla P' - \rho' \nabla \psi.$$
 (10.17)

Here we have disregarded  $\rho'$  in the left hand side of equation (10.3), because we are using the Boussinesq approximation for convective motion. Following Unno (1967) conjecture that convection motion would approach to equilibrium in a time scale of the turnover time of convective eddies, we assume that

$$\mathbf{V}_c \cdot \nabla \mathbf{V}_c - \mathbf{V}_c \cdot \mathbf{V}_c = \alpha \left( \frac{1}{\tau} + \sigma_r \right) \mathbf{V}_c, \tag{10.18}$$

where  $\alpha$  is a numerical parameter of order one, and  $\tau$  is the turnover time of convective eddies, which may be written as

$$\tau = \frac{\ell}{v} \tag{10.19}$$

with mixing length  $\ell$  and  $v = |\mathbf{V}_c|$ .

We have included  $\sigma_r$  (the real part of pulsation frequency) in equation 10.18 in addition to Unno (1967) original  $1/\tau$  term, in order to prevent rapid spacial oscillations in pulsation amplitude that occur near the bottom of the convection zone (where  $\tau > 1/\sigma_r$ ) (Gonczi & Osaki 1980; Grigahcène et al. 2005). This modification comes from the conjecture that if the pulsation period is much shorter than the turn-over time  $\tau$  (associated with largest eddies), smaller scale eddies having time-scales of  $\sim 1/\sigma_r$  would be important Saio (1980). Similar assumption was adopted by Grigahcène et al. (2005). Substituting equation 10.18 into equation 10.19 we obtain

$$\rho \frac{d\mathbf{V}_c}{dt} = -\alpha \left(\frac{1}{\tau} + \sigma_r\right) \mathbf{V}_c - \mathbf{V}_c \cdot \nabla \mathbf{u} - \frac{1}{\rho} \nabla P' - \frac{\rho'}{\rho} \nabla \psi. \tag{10.20}$$

For mass conservation of convection motion, we adopt Boussinesq approximation

$$\nabla \cdot \mathbf{V}_c = 0. \tag{10.21}$$

#### Thermal equations

Subtracting equation 10.9 from equation 10.5 we obtain

$$\rho T \left[ \frac{dS'}{dt} + \mathbf{V}_c \cdot \nabla S' \right] + (\rho T)' \frac{dS}{dt} + \rho T \left( \mathbf{V}_c \cdot \nabla S' - \mathbf{V}_c \cdot \nabla S' \right) = (\rho \epsilon_n)' - \nabla \cdot \mathbf{F}'_{\text{rad}}$$
(10.22)

Similarly to equation 10.18, we assume that

$$\mathbf{V}_c \cdot \nabla S' - \mathbf{V}_c \cdot \nabla S' = \beta \left( \frac{1}{\tau} + \sigma_r \right) S', \quad (A21)$$

where  $\beta$  is another numerical parameter of order one. Then we obtain

$$\frac{dS'}{dt} + \mathbf{V}_c \cdot \nabla S' + \left(\frac{T'}{T} + \frac{\rho'}{\rho}\right) \frac{dS}{dt} + \beta \left(\frac{1}{\tau} + \sigma_r\right) S' = -\frac{1}{\rho T} \nabla \cdot \mathbf{F}'_{\text{rad}}.$$
 (10.24)

where we neglected the term  $(\rho \epsilon_n)'$  because we are interested only in the envelope convection. For the last term of the above equation we assume

$$\nabla \cdot \mathbf{F}'_{\text{rad}} \approx -\frac{4acT^3}{3\kappa\rho} \nabla^2 T' \approx \frac{4acT^3}{3\kappa\rho} \frac{T'}{(\ell^2/f)},\tag{10.25}$$

where  $\kappa$  is opacity per unit mass,  $\ell$  mixing length, and f is a numerical factor; its appropriate value will be discussed in the next subsection.

Furthermore, according to the assumptions in the mixing-length theory, we assume  $\rho' \approx 0$  in obtaining convective perturbations of the thermodynamic relations (but  $\rho'$  is retained in the

equation of motion discussed below). Then, we have

$$\frac{T'}{T} \approx \left(\frac{\partial \ln T}{\partial S}\right)_p \frac{S'}{C_p},$$
 (10.26)

and

$$\nabla \cdot \mathbf{F}'_{\text{rad}} \approx \frac{4acT^4}{3\kappa\rho C_p} \frac{S'}{(\ell^2/f)} = \rho T \kappa_{\text{rad}} S', \tag{10.27}$$

with

$$\kappa_{\rm rad} = \frac{4acT^3}{3\kappa\rho C_p(\ell^2/f)}.$$
 (10.28)

Under the same assumption, we can write the density perturbation as

$$\frac{\rho'}{\rho} \approx \left(\frac{\partial \ln \rho}{\partial \ln T}\right)_p \frac{T'}{T} = -\frac{\chi_T T'}{\chi_\rho T} = -\frac{\chi_T S'}{\chi_\rho C_p}.$$
 (10.29)

Then we obtain

$$\rho T' + T\rho' \approx \rho T \left( 1 - \frac{\chi_T}{\chi_\rho} \right) \frac{S'}{C_p},\tag{10.30}$$

where  $\chi_T = \left(\frac{\partial \ln P}{\partial \ln T}\right)_{\rho}$  and  $\chi_{\rho} = -\left(\frac{\partial \ln P}{\partial \ln \rho}\right)_T$ .

$$\frac{dS'}{dt} + \mathbf{V}_c \cdot \nabla S' + \left(1 - \frac{\chi_T}{\chi_\rho}\right) \frac{S'}{C_p} \frac{dS}{dt} \left(\frac{\beta}{\tau} + K_{\text{rad}}\right) S' = 0.$$
 (10.31)

# 10.2.4 Convection in equilibrium

In this subsection we discuss the relation between our formulations and the mixing-length theory to obtain relations among the parameters  $\alpha$ ,  $\beta$  and convective eddy shapes. If there is no pulsation we have steady-state convection, in which  $V_{c0}$  is given from equation 10.30

$$-\frac{V_{c0}}{\tau} = -\frac{1}{\rho} \nabla P' - \frac{1}{\rho} \nabla \Psi. \tag{10.32}$$

Treating the convective motion locally by replacing  $\nabla$  with  $i{\bf k}$ , we obtain the radial component of convection velocity  $V^r_{c0}$ 

$$-\frac{\alpha}{\tau}V_{c0}^{r} = -ik_{r}\left(\frac{\rho'}{\rho}\right)_{0} - g\left(\frac{\rho'}{\rho}\right)_{0}.$$
 (10.33)

and the horizontal component  $V_{c0}^h$ 

$$V_{c0}^{h} = -i\frac{\tau}{\alpha}k_{h}\left(\frac{\rho'}{\rho}\right)_{0}.$$
(10.34)

The continuity equation  $\nabla \cdot \mathbf{V}_{c0} = 0$  can be written as

$$k_r \mathbf{V}_{c0}' + k_h \mathbf{V}_{c0}^h = 0. (10.35)$$

Combining equations 10.31 and 10.35, we obtain

$$ik_r \left(\frac{\rho'}{\rho}\right)_0 = \frac{k_r^2}{k_h^2} \frac{\alpha \mathbf{V}'_{c0}}{\tau}.$$
 (10.36)

Substituting this equation into the first relation in equation 10.32, we obtain

$$\left(\frac{\rho'}{\rho}\right)_0 = -\frac{\alpha}{\tau g} \frac{k^2}{k_b^2} \mathbf{V}'_{c0} \quad \text{or} \quad \left(\frac{S'}{C_p}\right)_0 \frac{\chi T}{\chi p} = \frac{\alpha}{\tau g} \frac{k^2}{k_b^2} \mathbf{V}'_{c0}, \tag{10.37}$$

where  $k^2 = k_r^2 + k_h^2$ .

In the equilibrium state eq. 10.31 can be written as

$$\mathbf{V}'_{c0}\frac{dS_0}{dr} = -\left(\frac{\beta}{\tau} + K_{rad}\right)S'_0. \tag{10.38}$$

Since

$$\frac{dS_0}{dr} = -\frac{C_p}{H_p} (\nabla - \nabla_{ad}),\tag{10.39}$$

equation 10.38 may be written as

$$\left(\frac{\beta}{\tau} + K_{rad}\right) S_0' = v' \frac{C_p}{c_0 H_p} (\nabla - \nabla_{ad}). \tag{10.40}$$

A relation with the mixing length theory is apparent if we have the horizontal average of the absolute value and use the relation

$$\left|\frac{\nabla'v}{c_0}\right| = u = \frac{\ell}{\tau},\tag{10.41}$$

$$\frac{|S_0'|}{C_p} = \frac{|T_0'|}{T} = \frac{1}{\beta \ell + 1} \frac{1}{\tau K_{rad}/\beta} \left(\nabla - \nabla_{ad}\right) \frac{\ell}{H_p}.$$
 (10.42)

In the formulation of MLT by Henyey et al. (1965) the efficiency factor  $\gamma$  defined as

$$\gamma = \frac{\nabla - \nabla'}{\nabla' - \nabla_{ad}} \quad \to \quad \nabla - \nabla' = \frac{\gamma}{\gamma + 1} (\nabla - \nabla_{ad}), \tag{10.43}$$

where  $\nabla'$  is the temperature gradient felt by moving eddies (sometimes called internal temperature gradient). According to eq. 10.38 in Henyey et al. (1965) (their opacity per unit volume is converted to the opacity per unit mass here), for optically thick convective eddies,

$$\frac{1}{\gamma} = \frac{2\alpha cT^3}{C_p \rho^2 \ell^2 y} = \frac{3}{2} \frac{K_{rad} \tau}{yf},\tag{10.44}$$

with  $\gamma = 3/(4\pi^2)$ . If we set  $f = 2\pi^2\beta$ , we have  $\tau K_{rad}/\beta = 1/\gamma$ .

Then equation 10.41 becomes

$$\frac{|T_0'|}{T} = \frac{1}{\gamma} \frac{1}{\beta \gamma + 1} \left( \nabla - \nabla_{ad} \right) \frac{\ell}{H_p} = \frac{1}{\beta} \left( \nabla - \nabla' \right) \frac{\ell}{H_p}. \tag{10.45}$$

This equation can be derived from MLT, where  $\beta=2$  is usually adopted. Using equation 10.44 in equation 10.37 we have

$$\left(\frac{v_r'}{c_0}\right)^2 = -\frac{1}{\beta\alpha} \left(1 - \frac{2}{3}Q\right) gH_p \frac{\chi T}{\chi_\rho} \left(\nabla - \nabla'\right) \left(\frac{\ell}{H_p}\right)^2, \tag{10.46}$$

where Q is defined as  $k_r^2/k^2 = 2Q/3$  meaning Q = 1 for isotropic eddies (?). In MLT,

$$\frac{1}{\beta\alpha}\left(1 - \frac{2}{3}Q\right) = \frac{1}{8}\tag{10.47}$$

is often adopted (e.g., Henyey et al. (1965)), which corresponds to the relation

$$\alpha = \frac{8}{\beta} \left( 1 - \frac{2}{3} Q \right). \tag{10.48}$$

Therefore, we can adopt  $(Q, \alpha, \beta) = (1, 1.3, 2)$  as a standard set of parameters.

# Pulsational perturbation on convection

In this subsection we consider spherical symmetric (radial) linear Lagrangian perturbation  $\delta$  for convective eddies which, as in the previous subsection, are treated locally. We will present  $\delta v^r$  and  $\delta S'$  (convection variables perturbed by pulsation) as functions of regular pulsation variables.

#### Thermal relations

Applying pulsational perturbations to equation 10.31 and using equation 10.38, we obtain

$$\Sigma_{1} \frac{\delta S'}{S'} - K_{\text{rad}} \frac{\delta v^{r}}{v^{r}} = \left(\frac{\beta}{\tau} + K_{\text{rad}}\right) \frac{\delta (dS/dr)}{(dS/dr)} - i\sigma \left(1 - \frac{\chi T}{\chi_{\rho}}\right) \frac{\delta S}{C_{p}} - \delta K_{\text{rad}} + \frac{\beta}{\tau} \left(\frac{\delta H_{p}}{H_{p}}\right), \quad (10.49)$$

where we defined

$$\Sigma_1 = \left(i\sigma + \frac{\beta}{\tau} + \beta\sigma_{\rm r} + K_{\rm rad}\right) \tag{10.50}$$

From the momentum equation 10.20 of convective eddies, we obtain

$$\left(i\omega + \frac{\alpha}{\tau} + \alpha\omega_r\right)\delta\vec{c} = -\frac{\alpha\delta\tau}{\tau}\vec{V_{c0}} - i\omega(\vec{V_{c0}}\cdot\nabla)\xi - ik\delta\left(\frac{P'}{\rho}\right) - \delta\left(\frac{\rho'}{\rho}\right)\nabla\psi - \frac{\rho'}{\rho}\delta(\nabla\psi). \tag{10.51}$$

From equation 10.21 we obtain

$$\vec{k} \cdot \delta \vec{c} = 0. \tag{10.52}$$

Taking the inner product between  $\vec{k}$  and equation 10.51 and using equation 10.52 we have

$$0 = -i\omega \vec{k} \cdot \left[ (\vec{V_{c0}} \cdot \nabla) \vec{\xi} \right] - ik^2 \delta \left( \frac{P'}{\rho} \right) - k_r \delta \left( \frac{\rho'}{\rho} \right) \frac{d\psi}{dr} - k_r \frac{\rho'}{\rho} \delta \left( \frac{d\psi}{dr} \right), \tag{10.53}$$

Substituting above equation into eq. 10.51, we eliminate p',

$$\left(i\sigma + \frac{\alpha}{\tau} + \alpha\sigma_r\right)\delta V_c = i\sigma \begin{bmatrix} \frac{k}{k^2} \cdot (V_{c0} \cdot \nabla)\delta S' - (V_{c0} \cdot \nabla)\delta \xi \\ -\frac{g}{\alpha V_T} \left(\frac{k_r}{k^2} - e_r\right) \frac{\delta S'}{C_p} + \frac{\alpha}{\tau} \left(\frac{\delta H_p}{H_p} - \frac{\delta u}{u}\right) V_{c0} \\ -\frac{\alpha V_T}{c_0^2} \left(\frac{k^2}{k_p^2}\right) \left(\frac{k}{k^2} \cdot \delta(\nabla \psi) - \delta(\nabla \psi)\right), \end{bmatrix}$$
(10.54)

where we used the relations  $\tau = \ell/u$  and  $\ell \propto H_p$ , and the relation between p' and S' (eq. 10.29).

The radial component of equation 10.54 is can be written as

$$\Sigma_{2} \frac{\delta V_{c}'}{V_{c}'} - \frac{\alpha}{\tau} \frac{\delta S'}{S'} = i\sigma \left[ \frac{2}{3} \left( \frac{d\xi}{dr} - \frac{\xi}{r} \right) - \frac{dS}{dr} \right] + \frac{\alpha}{\tau} \frac{\delta H_{p}}{H_{p}} + \frac{\alpha}{\tau g} \delta \left( \frac{d\psi}{dr} \right), \tag{10.55}$$

where we defined

$$\Sigma_2 = i\sigma + \frac{2\alpha}{\tau} + \alpha\sigma_r. \tag{10.56}$$

In deriving equation 10.55, we assumed the relation  $\frac{\delta u}{u} = \frac{\delta V_c'}{V_{c0}'}$  and used the relation between  $S_0'$  and  $V_{c0}'$  given in equation 10.37. We also used the relation

$$\frac{k_r}{k^2} \cdot (\nabla \cdot \delta V_c' \cdot \nabla \xi) = \frac{2}{3} \frac{Q \delta V_{c0}'}{V_{c0}'} \left( \frac{d\xi}{dr} - \frac{\xi}{r} \right), \tag{10.57}$$

which can be derived from the relations  $k \cdot \delta V_{c0} = 0$  (eq. 10.35) and  $\frac{k_r}{k}^2 = \frac{2}{3}$  (eq. 10.45).

From equations 10.48 and 10.55 we can express  $\frac{\delta S'}{S'}$  and  $\frac{\delta V'_c}{V'_c}$  as functions of pulsation variables, which are used in equation 10.64 (below) to obtain the Lagrangian perturbation of convective luminosity,  $\delta L_{conv}$ .

## Equations for linear radial pulsations

Using radial displacement  $\xi$ , the Lagrangian perturbations of pressure  $\delta P$ , and entropy  $\delta S$ , linearised momentum and mass conservation equations can be written as

$$r\frac{d}{dr}\left(\frac{\xi_r}{r}\right) = -3\frac{\xi_r}{r} - \frac{\delta P}{\rho} = -3\frac{\xi_r}{r} - \frac{1}{\Gamma_1 p}\delta P + \frac{\chi_T}{\chi_\rho c_P}\delta S,\tag{10.58}$$

and

$$\frac{d}{d\ln r} \left( \frac{\delta P}{p} \right) = \nu \left( \sigma^2 r^2 + 4 \right) \frac{\xi_r}{r} + \nu \frac{\delta P}{p},\tag{10.59}$$

in which we have neglected turbulent pressure term  $(V_c \cdot \nabla V_c)_r$ .

#### Linearized energy conservation may be written as

$$i\omega T\delta S = \epsilon_n \left( \frac{\delta \rho}{\rho} \epsilon_\rho + \frac{\delta T}{T} \epsilon_T \right) - L_r \frac{d}{dM_r} \left( \frac{\delta L_r}{L_r} \right) - \left( \frac{\delta L_r}{L_r} \right) \frac{dL_r}{dM_r}, \tag{10.60}$$

where  $\epsilon_{\rho} = (\partial \ln \epsilon_n / \partial \ln \rho)_T$  and  $\epsilon_T = (\partial \ln \epsilon_n / \partial \ln T)_{\rho}$ . Luminosity perturbation can be expressed as

$$\frac{\delta L_r}{L_r} = \frac{L_{rad}}{L_r} \frac{\delta L_{rad}}{L_{rad}} + \frac{L_{con}}{L_r} \frac{\delta L_{con}}{L_{conv}}.$$
(10.61)

Radiative luminosity  $L_{rad}$  and its Lagrangian perturbation  $\delta L_{rad}$  are given as

$$L_{rad} = -(4\pi r^2)^2 \frac{4acT^4}{3k} \frac{d\ln T}{dM_r},$$
(10.62)

and

$$\frac{\delta L_{rad}}{L_{rad}} = 4\frac{\xi_r}{r} + 4\frac{\delta T}{T} - \frac{\delta k}{k} + \frac{1}{d\ln T/dM_r} \frac{d}{dM_r} \left(\frac{\delta T}{T}\right). \tag{10.63}$$

For the perturbation of convective luminosity we have from equation 10.15

$$\frac{\delta L_{\text{con}}}{L_{\text{con}}} = 2\frac{\xi_r}{r} + \frac{\delta F_{\text{con}}}{F_{\text{con}}} = 2\frac{\xi_r}{r} + \frac{\delta \rho}{\rho} + \frac{\delta T}{T} + \frac{\delta V'}{V'} + \frac{\delta S'}{S'}.$$
 (10.64)

The convection variables  $\frac{\delta V'}{V'}$  and  $\frac{\delta S'}{S'}$  can be expressed by ordinary pulsation variables using equations 10.48 and 10.55.

A6 Summary of the linear differential equations for radial pulsations

We define non-dimensional variables  $Z_1 \dots Z_4$  as

$$Z_1 = \frac{\delta P}{P}, \quad Z_2 = \frac{\delta S}{C_p}, \quad Z_3 = \frac{\xi_r}{r}, \quad Z_4 = \frac{\delta L_r}{L_r}.$$
 (10.65)

The differential equations may be given as

$$\frac{dZ_1}{d\ln r} = VZ_1 + V\left(c_1\omega^2 + 4\right)Z_3,\tag{10.66}$$

$$\frac{dZ_2}{d\ln r} = b_1 Z_1 + b_2 Z_2 + b_3 Z_3 - b_4 \frac{L_r}{L_{\text{rad}}} Z_4,$$
(10.67)

$$\frac{dZ_3}{d\ln r} = -\frac{1}{\Gamma_1} Z_1 + \frac{\chi_T}{\chi_\rho} Z_2 - 3Z_3,\tag{10.68}$$

$$\frac{dZ_4}{d\ln r} = b_5 Z_1 + b_6 Z_2 - \frac{d\ln L_r}{d\ln r} Z_4,\tag{10.69}$$

where  $V = -\frac{d \ln P}{d \ln r}$ ,  $c_1 = \left(\frac{r}{R}\right)^3 \frac{M}{M_r}$ , and the pulsation angular frequency  $\sigma$  is normalized as  $\omega = \sigma \sqrt{\frac{R^3}{GM}}$ .

$$b_1 = b_4 = (4 - \kappa T) \frac{V_{\text{ad}}}{\Gamma_1} + \frac{\kappa}{\Gamma_1} \frac{V_{\text{ad}}}{V} \left( \frac{d \ln V_{\text{ad}}}{d \ln P} - 1 \right) + f_{CR} \left( \frac{V_{\text{ad}}}{\Gamma_1} + \frac{1}{1 + \alpha \rho} \right), \tag{10.70}$$

$$b_2 = b_4 = \left[4 - \kappa T + \kappa \rho + f_{CR} \left(1 - \frac{\kappa T}{\kappa \rho} + \alpha_s\right)\right], \tag{10.71}$$

$$b_3 = b_4 = \left[4 - \frac{V_{\text{ad}}}{V} \left(c_1 \omega^2 + 4\right) + 2f_{CR} \left(1 + \alpha_r\right)\right],$$
 (10.72)

$$b_4 = \left[ \frac{1}{\sqrt{VV'}} + \frac{f_{CR} \Sigma_{23}}{\Sigma_4} \frac{K_{\text{rad}} + \beta/\tau}{\sqrt{V(V - V_{\text{ad}})}} \right]^{-1}, \tag{10.73}$$

$$b_5 = \frac{4\pi r^3 \rho \epsilon}{L_r} \left( \epsilon T V_{\text{ad}} + \frac{\epsilon \rho}{\Gamma_1} \right), \tag{10.74}$$

$$b_6 = \frac{4\pi r^3 \rho \epsilon}{L_r} \left( \epsilon T - \epsilon \rho \frac{\kappa T}{\kappa \rho} - i\omega \frac{GM}{R^3} \frac{4\pi r^3 T C_p}{L_r} \right), \tag{10.75}$$

where

$$f_{CR} = \frac{L_{\text{conv}}(r)}{L_{\text{rad}}(r)},\tag{10.76}$$

$$a_r = \frac{1}{\Sigma_4} \left[ i\omega \Sigma_5 v_{rr} + \Sigma_{23} \left( 3K_{rad} + \frac{\beta}{\tau} \right) + \frac{1}{\tau} \left( \alpha \Sigma_5 + \beta \Sigma_{23} \right) \right], \tag{10.77}$$

$$a_p = \frac{1}{\Sigma_4} \left[ i\omega \Sigma_5 v_{rp} + \Sigma_{23} s_p + \frac{1}{\tau} \left( \alpha \Sigma_5 + \beta \Sigma_{23} \right) \left( 1 - \frac{1}{\Gamma_1} \right) \right], \tag{10.78}$$

$$a_s = \frac{1}{\Sigma_4} \left[ -i\omega \Sigma_5 v_{rp} + \Sigma_{23} s_s + \frac{1}{\tau} \left( \alpha \Sigma_5 + \beta \Sigma_{23} \right) \frac{\chi T}{\chi_{\rho}} \right], \tag{10.79}$$

$$\Sigma_{23} = \Sigma_2 + \frac{\alpha}{\tau},\tag{10.80}$$

$$\Sigma_4 = \Sigma_1 \Sigma_2 - K_{rad} \frac{\alpha}{\tau},\tag{10.81}$$

$$\Sigma_5 = \Sigma_1 + K_{rad},\tag{10.82}$$

$$v_{rr} = 1 - Q - \frac{\alpha}{i\omega\tau},\tag{10.83}$$

$$v_{rp} = 1 - \frac{2Q}{3},\tag{10.84}$$

$$s_p = \frac{1}{\Gamma_1} \left[ \left( K_{rad} + \frac{\beta}{\tau} \right) - K_{rad} \left( 3 - k\Gamma \right) \upsilon_{ad} - 2 - \frac{k_\rho}{\Gamma_1} \right], \tag{10.85}$$

$$s_{s} = -\left(K_{rad} + \frac{\beta}{\tau}\right) \frac{\chi T}{\chi_{\rho}} \frac{d \ln C_{p}}{d \ln \rho} \left[\nabla - v_{ad}\right] + i\omega \left[\left(\frac{\chi T}{\chi_{\rho}} - 1\right) - K_{rad}\left(3 - k\Gamma + \frac{\chi T}{\chi_{\rho}}\right)\right]. \quad (10.86)$$

## 10.3 Results

#### 10.3.1 Periods of Excited Radial Pulsations

Our non-adiabatic radial pulsation code has been utilized on select evolution models that fall within the error box depicted on the HR diagram (Figure ??). The resulting analysis reveals that models located in the cooler and more luminous section of the error box (Figure ??, right panel) successfully excite four radial pulsation modes. These modes exhibit periods that closely align with the observational data of Betelgeuse. Table ?? provides a list of models where all excited radial pulsation periods are in agreement with the four observed periods for Betelgeuse. These models are at the stage of carbon-burning or nearing its conclusion, with luminosities ranging from  $5.26 < \log(L/L_{\odot}) < 5.28$ . Initially, these stars possessed a mass of  $19 M_{\odot}$ , which has now diminished to approximately  $11-12 M_{\odot}$  during the Betelgeuse phase.

It is important to note that the higher luminosity end of the error bar is favored, particularly because the predicted period of the third overtone mode (P4) shows rapid deviation from the observed value as the luminosity decreases. In contrast, the period P1 exhibits a much slower rate of change with varying luminosity. This behavior of P4 helps to establish the lower limit of luminosity among the models, especially for those with initial rotation velocities ( $v_i$ ) of 0.2 times the critical velocity ( $v_{\rm crit}$ ). Model D, as listed in Table ??, exhibits a luminosity with  $\log(L/L_{\odot}) = 5.265$  and a pulsation period P4 of 181 days, which is at the lower threshold of the observed period range for Betelgeuse at  $185 \pm 4$  days. The core carbon abundance in this model is 0.171, with an expected exhaustion timeline of 260 years. Throughout the evolution from Model D to Model B, which marks carbon exhaustion, the periods of excited pulsation modes correspond with those observed for Betelgeuse. Model C represents an intermediary model between Models B and D.

For models with initial rotation velocities  $v_i = 0.4v_{\rm crit}$ , only Model A is included in Table ??,

although its P4 period of 178 days is marginally shorter than the observed lower limit. This suggests a slightly higher luminosity would be required for an exact match with the observed P4. The central carbon in Model A is nearing depletion, and no significant changes in luminosity and radius are expected until carbon exhaustion is reached.

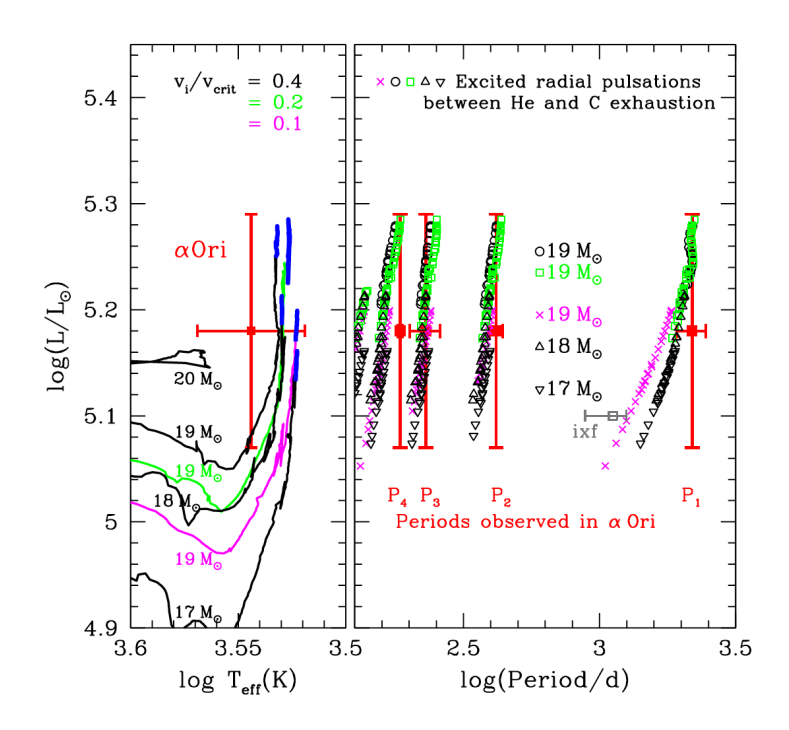


Figure 10.1: Left Panel: The location of Betelgeuse ( $\alpha$  Ori) and various evolutionary tracks on the HR diagram. The blue-coloured sections represent the phase of core-carbon burning. The number along each track indicates the initial mass in solar units. The 20  $M_{\odot}$ -track is taken from Yusof et al. (2022). Right Panel: Period-luminosity diagram showing observed four periods of Betelgeuse with error bars (red lines), and various symbols for excited radial-pulsation periods along the evolutionary tracks from the He exhaustion to the Carbon exhaustion at the stellar center. For comparison, the pulsation period of the RSG progenitor of SN2023ixf (in M101) obtained by Jencson et al. (2023) is shown by the gray horizontal bar labelled as "ixf".

It should be noted that for luminosities below  $\log(L/L_{\odot}) < 5.52$ , an additional pulsation mode eather fourth overtoneas excited as indicated in the right panel of Figure ??. This mode, however, is not detected in Betelgeuse, which supports the hypothesis of its higher luminosity.

Figure 10.2 (top and middle-left panels) illustrates the spatial amplitude variation of each excited mode in Model C. These variations are depicted by solid lines as a function of temperature within the envelope. The linear pulsation modes are computed by solving a set of differential equations where the eigenvalue  $\sigma$  characterizes the temporal variation of radial displacement as  $\delta r \exp(i\sigma t)$ . Here,  $\sigma$  and  $\delta r$  and  $\delta r$  the eigenfunction are complex numbers representing the frequency and spatial function of the pulsation, respectively. The pulsation's physical manifestation is represented by the real part  $[\delta r \exp(i\sigma t)]_r$ , where the imaginary part of  $\delta r$  indicates the deviation from

a pure standing wave in the envelope, meaning that displacement nodes shift during a pulsation cycle. Furthermore, the imaginary component of  $\sigma$ , denoted  $\sigma_i$ , determines the pulsation mode's damping or growth rate. This is in contrast to the nearly adiabatic pulsations seen in classical Cepheids, as the pulsations in supergiants are highly non-adiabatic, making the imaginary components of  $\delta r$  and  $\sigma$  significant in comparison to their real parts.

Table 10.1: Recent period determinations for light and radial-velocity curves of Betelgeuse and the adopted periods in this paper

Authors		Perio	Data		
(lr)2-5	$P_1$	$P_2$	$P_3$	$P_4$	
Jadlovský et al. (2023):	$2190\pm270$	$417\pm17$	$365\pm75$	$230\pm29$	$AAVSO^1$ , $SMEI^2$
Ogane et al. (2022):	2160	405		$202^{a}$	<b>UBVRI</b> photometry
Wasatonic (2022):	$2209\pm183$	$439 \pm 5$			V & NIR photometry
Granzer et al. (2022):	$2169 \pm 6.3$	394.5		216.0	STELLA <sup>3</sup>
Joyce et al. (2020):	$2365\pm10$	$416\pm24$		$185.5\pm0.1$	AAVSO, SMEI
Kiss et al. (2006):	$2050\pm460$	$388 \pm 30$			AAVSO
Adopted in this work:	$2190\pm270$	$417\pm24$	$230\pm29$	$185\pm4$	

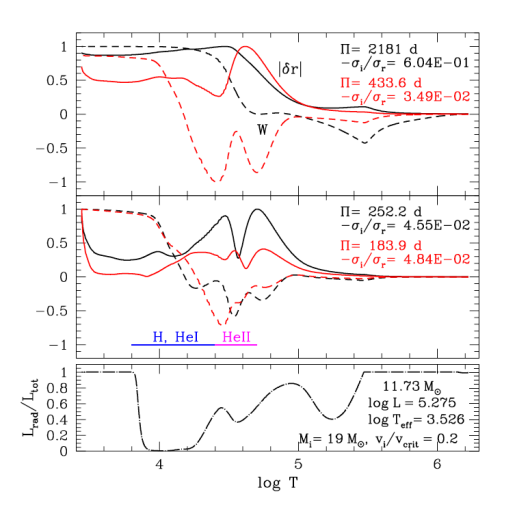
<sup>1)</sup> AAVSO = American Association of Variable Star Observers, 2) SMEI = Solar Mass Ejection Imager, 3) STELLA =  $\tilde{A}$ ©chelle spectrograph

Table 10.2: Model examples which excite pulsations consistent with periods of Betelgeuse

Model	$M^a$	$u_i/v_{crit}$	$P_1[d]$	$P_2[d]$	$P_3[d]$	$P_4[d]$	$M^a$	$\log L/L_{\odot}$	$\log T_{\mathrm{eff}}[K]$	$\log R/R_{\odot}$	$X_c(C)^b$
$\alpha$ Ori			$2190\pm270$	$417\pm24$	$230\pm29$	$185\pm4$		$5.18 \pm 0.11$	$3.544\pm0.025$		
A	19	0.4	2199	418	240	178	11.23	5.279	3.532	3.100	0.0067
В	19	0.2	2186	434	252	184	11.73	5.276	3.526	3.109	0.0048
C	19	0.2	2181	434	252	184	11.73	5.275	3.526	3.109	0.0503
D	19	0.2	2168	428	249	181	11.73	5.265	3.526	3.103	0.1712

In the top left panel of Figure 10.2, the spatial function  $\delta r$  for the longest period mode, P1 (2181 days), is illustrated as nearly uniform in the outermost layers, diminishing gently towards the stellar center. This characteristic flatness is typical of the radial fundamental mode, hence P1 is identified as such, rather than being classified as a Long Secondary Period (LSP). The displacement for P2 (434 days) presents a discernible dip at  $\log T \approx 4.4$ , which corresponds to a nodal point in adiabatic pulsation, designating P2 as the first overtone mode. Due to the highly nonadiabatic nature of the pulsations, clear nodes are not present as the zero points of the real and imaginary components of  $\delta r$  are displaced from each other. In the middle panel, the variations of  $\delta r$  (represented by solid lines) for P3 and P4 are more abrupt, exhibiting several dips. These characteristics lead to the identification of P3 and P4 as the second and third overtones, respectively. It is important to note that all pulsation modes are confined to the envelope, where  $\log T < 6$ . The absolute value of  $\delta r$  for the shorter period modes, specifically P3 and P4, as depicted in the middle left

a) If this periodicity is subtracted from the V-band data as the harmonic of 405 d, additional periods of 237.7 d and 185.8 d are obtained.



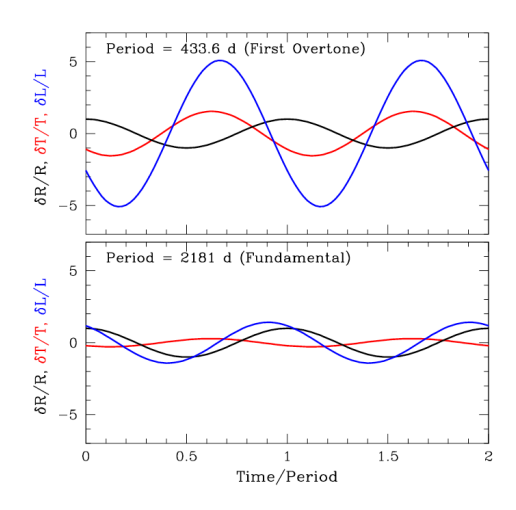


Figure 10.2: *Left Panel*: Characteristics of Mode-Induced Pulsations and Energy Output. This figure illustrates the pulsation attributes of excited modes (in the upper sections) along with the energy output's variation against the logarithmic temperature for model C, as listed in Table 2. The upper and central sections depict the radial displacements' absolute values, normalized to their peak levels, along with the cumulative work curves. A horizontal marker in the central section denotes the H, HeI (blue), and HeII (magenta) ionization areas. Different modes are represented by distinct colors for clarity. The lower section presents the ratio of radiative to total luminosity within the stellar envelope. *Right Panel*: Oscillatory Behavior for Radial and Thermal Variations. Presented here are the cyclic changes in radial displacement (in black), relative temperature fluctuation (in red), and luminosity variation (in blue) at the stellar surface. These are inferred from linear perturbation theory applied to model C's two primary radial modes (refer to Table 10.2 While these models do not account for amplitude growth, they capture the fundamental (P1) and first overtone (P2) modes, resonating over periods of 2181 and 433.6 days, respectively. These amplitudes are normalized, setting the radial displacement ratio to unity at the initial timepoint for both cases.

panel of Figure 10.2, exhibits sharp transitions near the stellar surface. This behavior suggests that pulsation energy from these modes is dissipating at the surface, a phenomenon accounted for by implementing a running-wave outer boundary condition in the eigenvalue problem calculation. Despite this energy dissipation, these pulsations are still found to grow ( $\sigma_i < 0$ ), indicating that the driving forces in the inner envelope surpass the energy losses occurring at the surface.

$$W(r) \propto \int_0^{r'} r^2 P \Im\left(\frac{\delta \rho}{\rho} \frac{\delta P^*}{P}\right) dr',$$
 (10.87)

In Figures ?? and 10.2, represented by a dashed line, the cumulative work integral W for each pulsation mode is displayed. The gradient of this work integral with respect to radial displacement,  $\frac{dW}{dr}$ , provides insight into the local behavior of the pulsation within the stellar layers: a positive gradient ( $\frac{dW}{dr} > 0$ ) signifies driving, whereas a negative gradient ( $\frac{dW}{dr} < 0$ ) indicates damping of the pulsation. The sign of W at the surface of the star denotes the overall excitation (positive W) or damping (negative W) of the pulsation in the stellar model.

The calculation of the cumulative work integral W(r) is derived according to the formula (see,

for instance, Saio (1980):

$$W(r) = \int_0^r \operatorname{Im} \left[ \delta P^* \left( \frac{\delta r}{r} \right) \right] \frac{dP}{P}, \qquad (10.88)$$

where P and  $\rho$  represent the pressure and density, respectively. Here,  $\delta$  indicates the pulsational perturbation of the subsequent quantity, and the notation  $Im[\cdot]$  and (\*) denote the imaginary part and the complex conjugate, respectively.

As depicted in Figure 2, Betelgeuse's fundamental mode  $P_1$  is primarily driven by the helium II ionization zone, located at approximately  $\log T \sim 4.5-4.6$ . In contrast, for the shorter period modes, the driving force is predominant in the hydrogen/helium I ionization zone, where  $4.0 \lesssim \log T \lesssim 4.4$ .

The bottom panel of Figure 10.2 illustrates the ratio of radiative luminosity to total luminosity,  $\frac{L_{\rm rad}}{L_{\rm tot}}$ , which is significantly less than one across a broad range of the envelope. This indicates that a substantial portion of the energy flux within Betelgeuse is transported via convection. The ratio of radiative to convective flux is crucial for both the pulsation period and the driving/damping mechanisms in stars with a high luminosity to mass ratio,  $\frac{L}{M} > 10^4$  (in solar units). Since the thermal timescale can be comparable to or shorter than the dynamical timescale in the envelope of such stars, variations in the energy flux due to pulsation are key to determining the period, as well as to the excitation or damping of the pulsation.

For instance, when convective flux perturbations are excluded (referred to as the frozen convection approximation), model C's pulsation periods (listed in Table 10.2) yield values of 1771, 409, 253, and 192 days. However, when comparing these to the full calculation periods of 2181, 434, 252, and 184 days for model C, it is evident that convective flux perturbations significantly impact the longer-period pulsations in such stars. Notably, if we were to match the observed 2200-day period with the fundamental period calculated without accounting for convection effects, we would deduce an approximately 17% larger stellar radius, because the pulsation period is roughly proportional to  $R^{1.5}$ . Moreover, the predominance of convection effects in the fundamental mode suggests that accurate asteroseismic models could still be achieved without including convection effects in the pulsation calculations, by relying solely on the overtone modes and excluding the fundamental mode.

Right hand panel of Figure 10.2 displays the theoretical periodic changes in fractional radius (black), temperature (red), and luminosity (blue) at the surface for the fundamental radial mode  $P_1$  (2181 days; lower panel) and the first overtone  $P_2$  (433.6 days; upper panel) of model C (refer to Table 10.2). The amplitudes are normalized to  $\delta R/R = 1$  at t = 0 for both pulsations and are adjusted to prevent any potential amplitude increase over time. The variations in luminosity

and temperature for the  $P_1$  mode are considerably less pronounced than those for the  $P_2$  mode. Moreover, the maximum in luminosity for the  $P_1$  mode aligns with the phase of maximum radial displacement  $\delta R/R$ , whereas for the  $P_2$  mode, the luminosity peak coincides with the phase of minimum  $\delta R/R$ , when  $\delta T/T$  is near its maximum. These differences are attributable to the varying degrees of non-adiabatic effects between the long-period  $P_1$  mode and the  $P_2$  mode, with the former being more influenced by non-adiabatic phenomena. The pronounced non-adiabatic effects in Betelgeuse significantly diminish the temperature variation, making the radial displacement effect ( $\delta R/R$ ) more influential on the luminosity variation than the temperature effect. This is the reason the luminosity maximum for the  $P_1$  mode corresponds to the phase of maximum radial displacement. On the other hand, the  $P_2$  mode, which has a shorter period, exhibits a large enough temperature perturbation that outweighs the  $\delta R/R$  effect, resulting in the luminosity peak occurring near the phase of temperature maximum.

#### 10.3.2 Synthesis of Semi-Periodic Variation

Analyses of Betelgeuse's light curves from various authors consistently reveal at least two periods,  $P_1$  and  $P_2$  (refer to Table 1 for examples). This suggests that the fundamental characteristics of Betelgeuse's light variations can be qualitatively described by the combination of these two periodic variations. To verify this, a synthetic semi-periodic variation was created by summing the contributions of the  $P_1$  and  $P_2$  pulsation modes (illustrated in Figure 4). The modes are assumed to begin (at t=0) with equivalent amplitudes. While linear pulsation analysis typically allows amplitudes to grow exponentially as  $\exp(-\sigma_i t)$  – with  $\sigma_i$  being the imaginary part of the eigenfrequency and negative for excited modes – we consider a more gradual increase following  $(1-\sigma_i t)$ , since any rapid growth would be moderated by nonlinear effects at the observable finite amplitudes. The radial velocity (RV) is calculated using the expression  $-\frac{2}{3}\frac{d(\delta R)}{dt}$ , where the  $\frac{2}{3}$  factor accounts for the projection effect from the spherical surface. In the RV variation (top panel), a red shift (signifying contraction) is represented by an upward movement. The luminosity variation is expressed in magnitudes,  $\Delta$ mag  $\equiv -2.5 \log(1+\delta L/L)$ , where  $\delta R/R$  and  $\delta L/L$  are the summations of the contributions from both pulsation modes.

The variations of the 1.2-year ( $P_2$ ; first overtone) mode are influenced by the longer 6.0-year ( $P_1$ ; fundamental) mode pulsation. As the pulsation amplitudes increase over time, so does the modulation amplitude. Notably, the brightness variation (see bottom panel of Fig. 10.3) exhibits a significant minimum at  $t \approx 14.5$  years, reminiscent of Betelgeuse's Great Dimming. To align this minimum in luminosity with the observed Great Dimming event, the luminosity variation has been normalized such that  $\Delta$ mag = 1.2 mag at t = 14.5, by applying a scaling factor to  $\delta L(t)$ .

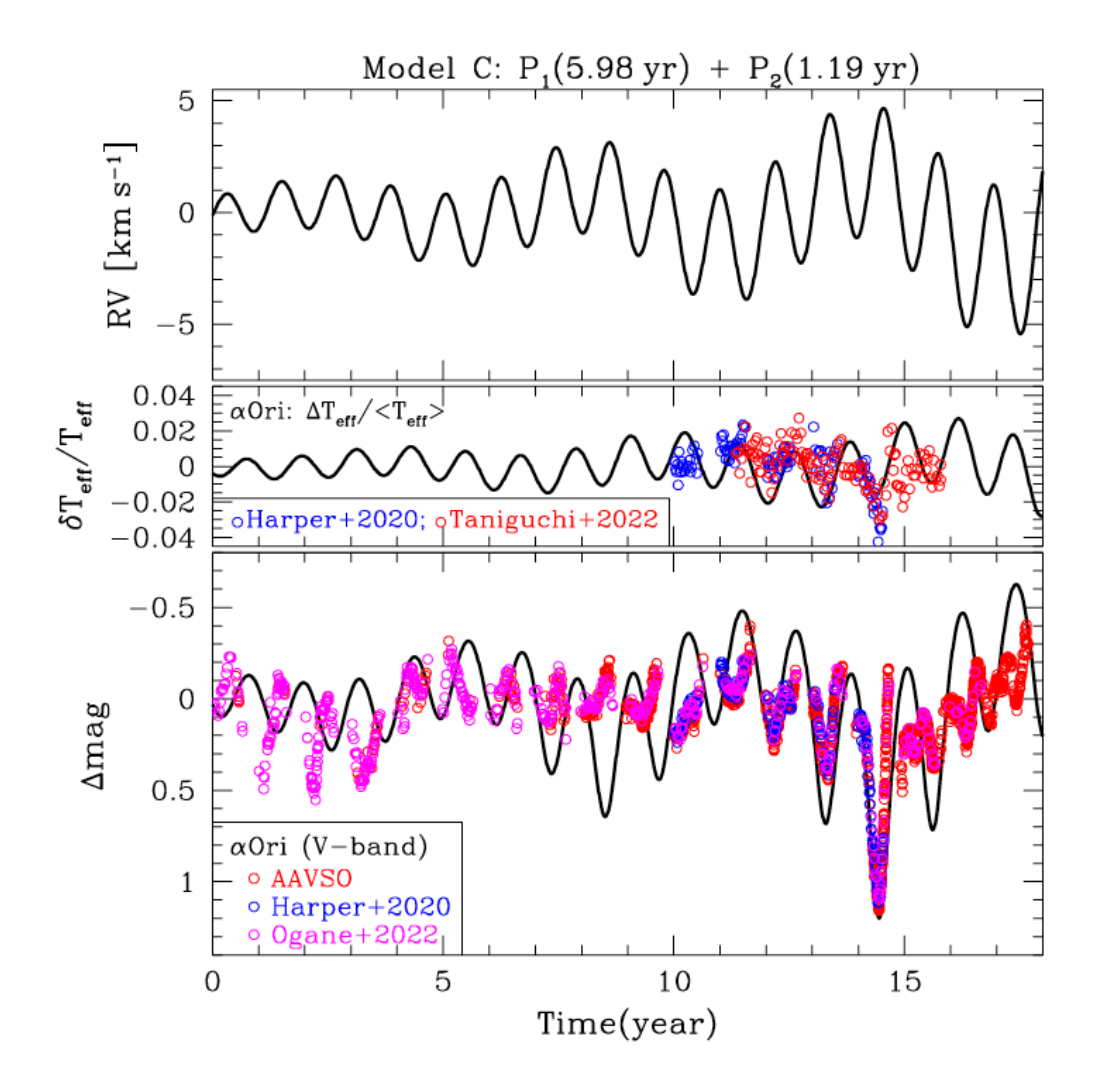


Figure 10.3: Radial velocity (RV;top), Teff variation (middle) and brightness variation (bottom) versus time. The solid line in each panel is obtained by combining the fundamental and the first-overtone radial pulsations excited in model C (Table 10.2). The radial velocity in the top panel is set to be positive for âred-shiftâ. The brightness variations in the bottom panel is normalized such that the maximum magnitude variation in this time range to be 1.2 mag, which also scales the amplitudes of model curves for RV and Teff variations. The V-band magnitudes of Betelgeuse from AAVSO, Harper et al. (2020) and Ogane et al. (2022) are over-plotted, where the mean magnitude is assumed to be 0.5 mag and the observed dates are shifted by â2005.6 yr to fit with the model time. In the middle panel, relative deviations of Teff from the mean âšTeff â© of Betelgeuse obtained by Harper et al. (2020) and Taniguchi et al. (2022a) are also plotted.

Correspondingly, RV(t) and  $\delta T_{\rm eff}(t)$  are adjusted to match the luminosity variation. The synthetic light curve is then augmented with V-band photometry data from various observational sources, adjusted by a shift of -0.5 mag in magnitude and a temporal shift of -2005.6 years to synchronize the theoretical minimum with the Great Dimming in 2020.1.

In the period leading up to the Great Dimming, the synthesized light curve displays increasingly deeper minima that correspond with observational data, suggesting that the dimming could

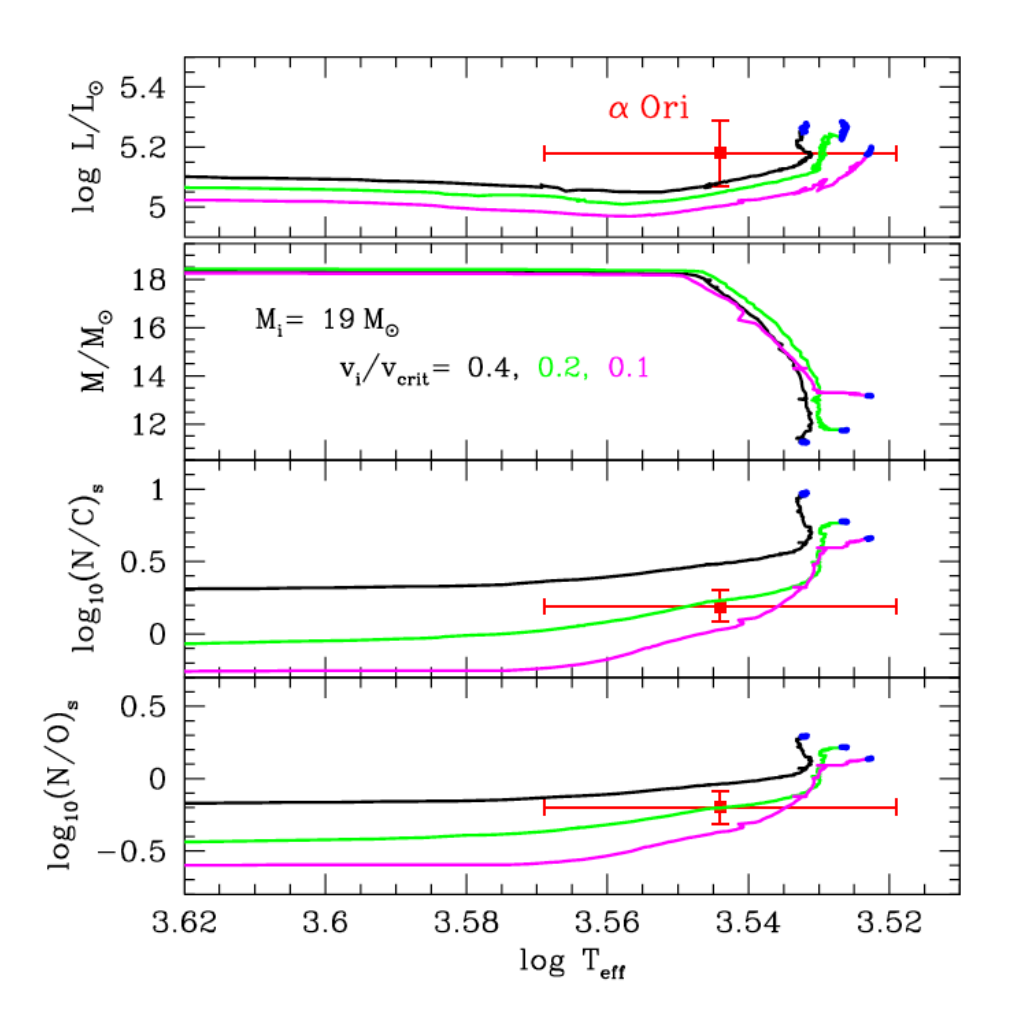


Figure 10.4: Evolutions of luminosity, mass, and surface CNO ratios for an initial mass of  $19 \rm M_{\odot}$  are compared with the observational data of Betelgeuse ( $\alpha$  Ori). Various cases of the initial rotation frequency versus critical one  $v_i/v_{crit}$  are color coded as shown in the second panel from the top. The core carbon burning stage is indicated by blue color. The abundance ratios N/C and N/O stand for the number ratios, while observed ones are adopted from Carr et al. (2000).

be partially attributed to the constructive interference of the fundamental and first overtone pulsations. Despite this, prior to the Great Dimming, the low-amplitude fluctuations attributed to the fundamental mode  $(P_1)$  broadly match the observed light variation's peaks. However, there is a notable deviation in the observed  $P_2$  pulsations from the synthetic curve, which could imply phase modulation within the first overtone pulsation, or that additional shorter-period variations  $(P_3)$  and  $P_4$ , not included in the synthetic curve, might significantly alter the first overtone pulsation. Interestingly, following the Great Dimming, the  $P_2$  (434-day) pulsation ceased to be detectable and was substituted by more modest, shorter-duration (200-day) variations, while the fundamental mode  $(P_1)$  pulsation persisted. This loss of the first-overtone pulsation may be indicative of a substantial mass loss event during the Great Dimming, which could have significantly disrupted the

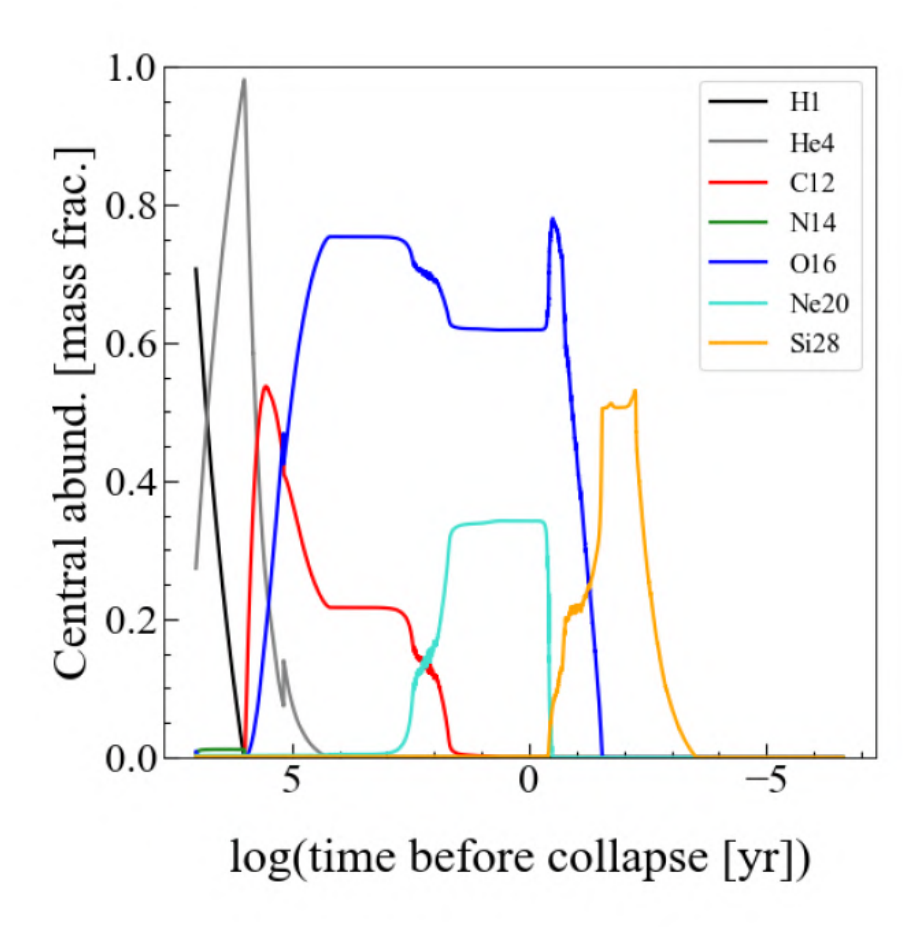


Figure 10.5: Central abundances of various elements versus time (in logarithm of base 10) to collapse for the model of  $M_i = 19M_{\odot}$  with the initial rotation velocity  $v_i = 0.2 \ v_{crit}$ .

 $P_2$  pulsation. Given that the growth time for the first-overtone pulsation is about 5.4 years (refer to left panel of Fig. 10.2), we can anticipate the re-emergence of the 434-day pulsation around the year 2025. In concurrence, MacLeod et al. (2023) predict the return of the 400-day pulsation within a similar timeframe (5â10 years), although they identify it as the fundamental mode.

The effective temperature variation in Betelgeuse, as demonstrated in the middle panel of Figure 10.3, shows minimal modulation with the  $P_1$  period. This is attributed to the significant suppression of temperature variation in the fundamental mode (corresponding to  $P_1$ ) due to the pronounced non-adiabatic effects, as evident in Figure 3. The effective temperature variations observed in Betelgeuse, reported by Harper et al. (2020) and Taniguchi et al. (2022b), are included for comparison. While the observed data exhibit some fluctuations, likely resulting from shorter-period pulsations not accounted for in this model, the range of  $T_{\rm eff}$  variations aligns well with the predictions from the simplified two-mode model. Similar effective temperature variations in

Betelgeuse have also been reported by Wasatonic (2022) and Mittag et al. (2023). During the Great Dimming period, the synthesized radial velocity (RV) curve (top panel of Fig. 4) reaches its maximum (indicating redshift) approximately 0.1 years after the minimum brightness is observed. This phase relation is consistent with observations reported by Dupree et al. (2022) and MacLeod et al. (2023). The two-mode synthesis predicts a maximum RV of 4.5 km/s, aligning with observed values. However, the observed minimum RV of about â6 km/s, which precedes the Great Dimming by approximately 200 days, is less than the predicted value of â1 km/s in our model. This discrepancy could be due to a shock emerging during the expansion phase, as found by Kravchenko et al. (2021) and Dupree et al. (2022), or the breakout of a convective plume, as discussed in MacLeod et al. (2023). While Betelgeuse's RV variations are influenced by several complex phenomena, it is noted that the star's diameter appears to fluctuate by about 5 to 10% on timescales comparable to its pulsation periods, as reported in studies like Townes et al. (2009) and Taniguchi et al. (2022a).

Figure 10.4 in the study presents the evolution of luminosity, mass, and surface CNO abundance ratios in models with varying initial rotation velocities at ZAMS, denoted as  $\frac{v_i}{v_{\rm crit}}$ , for an initial mass of 19  $M_{\odot}$ . The models show that mass loss predominantly occurs in the red-supergiant phase (core helium burning stage), with up to 6  $M_{\odot}$  being lost. This loss is more significant in models with higher initial rotation velocities ( $v_i$ ), due to the increased luminosity linked to larger helium cores formed by extensive rotational mixing around the convective core during the main-sequence stage.

The large mass loss in the red-supergiant stage leads to the emergence of CNO processed matter on the surface, elevating the N/C and N/O ratios. However, the N/C and N/O ratios in the core carbon burning stage of these models, which align well with the observed pulsation periods of Betelgeuse, are higher than the observed values reported by Carr et al. (2000). For instance, the model predicts a N/C ratio approximately 0.5 dex higher than observed. This discrepancy suggests an overestimation of rotational diffusive mixing in the models. The current computations use specific diffusion coefficients for shear turbulence and meridional currents as described in Ekström et al. (2012a), which tend to favor mixing. To explore the effects of these diffusion coefficients, models of 15  $M_{\odot}$  with an initial rotation of 40% of the critical velocity at solar metallicity were computed with different coefficients (Nandal et al.2023 in preparation). Adjusting these coefficients can reduce the N/C ratio at the surface when  $\log T_{\rm eff} = 3.6$  by up to 0.5 dex. Therefore, the issue with the discrepancy in N/C ratio might be resolved by modifying the physics of rotational mixing used in the models. Nonetheless, these changes would not significantly impact the envelope structure during the red supergiant stage, and therefore, the properties of pulsation modes during this phase are not expected to be affected.

#### 10.3.3 Discussion

Our models that successfully excite four radial pulsations, aligning with the observed periods of Betelgeuse, exhibit significantly larger radii exceeding 1200  $R_{\odot}$ . This is in stark contrast with previous seismological estimates which suggested radii in the range of approximately 700 to 900  $R_{\odot}$ , as reported by Dolan et al. (2016) and Joyce et al. (2020). The discrepancy arises from the methodology used in previous studies, which identified the observed period  $P_2$  (around 420 days) as the radial fundamental pulsation, relegating the longer periodicity  $P_1$  (approximately 2200 days) to a non-pulsational origin. In our approach,  $P_1$  is fitted with the fundamental non-adiabatic pulsation period of a core-carbon-burning model with a radius around 1300  $R_{\odot}$  (Table 2). This model not only matches the fundamental mode with  $P_1$  but also successfully excites the first, second, and third overtones, corresponding to observed periods  $P_2$ ,  $P_3$ , and  $P_4$ .

The larger radii of our models find some support in interferometric observations. Haubois et al. (2009) and Neilson et al. (2011) reported an angular diameter for Betelgeuse around  $45.03\pm$ 0.12mas. When combined with the distance of 222+48-34 pc (Harper et al. 2017), this translates to a radius of approximately  $1074+232-165 R_{\odot}$ , aligning with our models. Additionally, Cannon et al. (2023) observed a larger angular diameter of  $59.02 \pm 0.64 mas$  in the 8 to 8.75  $\mu$ m range, corresponding to a radius of about 1409+319 $-229 R_{\odot}$  at the same distance, acknowledging that longer wavelengths tend to yield larger angular diameters. Neilson et al. (2011), employing limb-darkening law in their interferometric observations, deduced a radius to mass ratio (R/M) of 82.17+13.32-11.51  $R_{\odot}/M_{\odot}$ , while our models suggest R/M around 110  $\hat{A}\pm 2R_{\odot}/M_{\odot}$ . This slight discrepancy is not considered critical, as the assumed mass-loss rates in our models may deviate slightly from actual rates. Furthermore, Lobel & Dupree (2000) derived a surface gravity (log g) of -0.5 for Betelgeuse, compared to  $\log g = -0.7$  in our models. We regard this difference as within acceptable margins, given the typical uncertainties in  $\log g$  measurements. Kervella et al. (2018) measured Betelgeuse's equatorial rotation speed as approximately 6.5 km/s, with a potential range between 5.7 and 10.6 km/s. However, this is in contrast with our models of Betelgeuse, which indicate a rotation speed less than  $0.1 \, \text{km/s}$ , even if they were rotating at 40% of the critical value at the Zero-Age Main Sequence (ZAMS) stage. The lack of significant rotation is a common feature in single-star models of Betelgeuse. Wheeler et al. (2017) have suggested a star merger to account for additional angular momentum, aligning with suggestions from Sullivan et al. (2020). Recently, Neuhäuser et al. (2022) presented evidence from pre-telescopic records suggesting that Betelgeuse was a yellow star approximately 2000 years ago. Based on evolution models by Choi et al. (2016), they concluded that Betelgeuse, with an initial mass of approximately  $14 M_{\odot}$ , crossed the Hertzsprung gap a thousand years ago, entering the early stage of Helium burning. This interpretation contrasts with our carbon-burning models. However, we propose an alternative explanation linked to a blue loop from the red supergiant branch. The evolution of supergiants' surface temperature is highly sensitive to internal chemical composition gradients, envelope mass, core mass, and other factors. Blue loops can occur due to subtle differences in these parameters as shown in Georgy et al. (2012) and Meynet et al. (2013, 2015). Observationally, it's noted that progenitors of some Type II supernovae were yellow supergiants (Georgy et al. 2012), suggesting that blue loops occur in late evolutionary stages. Therefore, we interpret Neuhäuser et al. (2022) findings as an indication that Betelgeuse recently returned from such a blue-loop evolution. While our models do not show blue loops, it's conceivable that they might occur in the red supergiant stage with parameter adjustments, a topic for future research.

We have determined that the four periods of photometric variations of Betelgeuse align with the four lowest order radial pulsations in carbon-burning models evolved from an initial mass of  $19\,M_\odot$ . As indicated in Table 10.2, the evolutionary stage of Betelgeuse can be very close to carbon exhaustion, as in models A, B, and C. However, pinpointing the exact evolutionary stage is challenging since surface conditions hardly change in the late stage nearing carbon exhaustion and beyond. The radial pulsation properties depend primarily on the envelope structure. To estimate the time remaining until core-collapse post-carbon exhaustion, we extended the evolution of the model with  $v_{\rm i}=0.2v_{\rm crit}$  to silicon exhaustion. Figure 10.5 shows the model's central elemental abundances versus time to collapse. In model D, central carbon is expected to be exhausted in about 260 years, with the other models in Table 10.2 requiring less time. Post-carbon exhaustion, Figure 10.2 suggests the core will collapse within a few decades. This positions Betelgeuse as a potential candidate for the next Galactic supernova, occurring near Earth.

Interestingly, the recent supernova SN2023ixf in the nearby galaxy M101 (Itagaki et al. 2003) was discovered to have a pulsating red supergiant as its progenitor. Pre-explosion observations archived by Jencson et al. (2023) determined a period of  $1119.4^{+132.4}_{-233.3}$  days and a luminosity of  $\log(L/L_{\odot}) = 5.1 \pm 0.2$ , similar to findings by Soraisam et al. (2023). This period range is depicted in Figure 1 by a horizontal gray line. The position in the Period-Luminosity (PL) relation implies that SN2023ixt's progenitor was slightly less massive compared to Betelgeuse, aligning with Jencson et al. (2023) estimated initial mass of  $17 \pm 4\,M_{\odot}$ .

#### 10.3.4 Conclusion

We have successfully identified carbon-burning models that excite the radial fundamental mode, as well as the first, second, and third overtones. The periods of these excited pulsation

modes are consistent with the observed periods of 2190, 417, 230, and 185 days in Betelgeuse. On the HR diagram, these models fit well within the accepted range of effective temperature and luminosity for Betelgeuse. Originating from a ZAMS mass of  $19 M_{\odot}$  with a rotation velocity between 0.2 and 0.4  $v_{\rm crit}$ , these models undergo significant mass loss, primarily during the core-He burning stage, resulting in a final mass of approximately 11 to 12  $M_{\odot}$  during the core carbon-burning stage.

A notable feature of our models is their large radius, around  $1300~R_{\odot}$ , which is necessary for accommodating the long-period fundamental mode. This large radius is corroborated by some interferometric measurements of Betelgeuse's angular diameter, particularly when combined with its distance of  $222^{+48}_{-34}$  pc (Harper et al. 2017). Based on our seismic and evolutionary models, we conclude that Betelgeuse is likely in a late phase, or nearing the end, of its core carbon-burning stage. The exhaustion of carbon in the core, which is anticipated to occur in less than approximately 300 years, is expected to be followed by a core-collapse leading to a supernova explosion within a few decades.

Chapter 11

# Conclusions and future perspectives

This thesis presents a comprehensive exploration of the formation and evolution of the universe's most massive stars, delving into their dynamics, chemical impacts, and eventual fates. The journey begins with an in-depth examination of standard massive stars in contemporary environments, focusing on those with solar and near-solar metallicity. We then shift our attention to massive, fast-rotating stars at low and zero metallicities, unraveling their pivotal role in the chemical enrichment of the interstellar medium. Further, the study extends to accreting, nonrotating massive stars, with masses spanning a few thousand solar masses, investigating their chemical influence in a similar context. The narrative finishes in an exploration within the atomically cooled halo regime, where we compute the evolution of Supermassive Stars (SMS) exceeding 100,000 solar masses. To achieve this, the Geneva Stellar Evolution Code has been significantly enhanced to model Supermassive Stars. These updates include accurately computing core hydrogen to core-silicon burning, integrating variable accretion rates, and incorporating metallicity aspects. GENEC now simulates metal-enriched SMS models and offers advanced visualization with the UltimateKippenhahn Python script. The 'makeini' module and 'rbin2010' ensure precise initial model generation and compatibility with GENEC. Overall, these enhancements enable GENEC to compute SMS models through their full evolution across a wide range of accretion rates. From the study presented in this work it is possible to draw the following conclusions:

• In Chapter 4, we examined the effects of rotational modifications in GENEC on massive stars, particularly of 15 and  $60~\rm M_{\odot}$ . We found that non-magnetic models, with altered diffusion coefficients like  $D_{\rm shear}$  and  $D_{\rm h}$ , primarily shows different degree of chemical mixing but similar internal angular momentum distribution. These models displayed rapid core rotations after the core He-burning phase, aligning with Georgy et al. (2009). Magnetic models, particularly for 15 and  $60~\rm M_{\odot}$  stars, showed consistent rotation profiles influenced by

magnetic instabilities, as per studies by Heger et al. (2005) and Fuller & Ma (2019). Diffusion coefficient choices in non-magnetic settings significantly affected chemical mixing and evolutionary paths. For instance, varying  $D_{\rm h}$  in a 15  ${\rm M}_{\odot}$  model altered transport near the convective core, leading to different core sizes and luminosity trajectories. Our findings emphasized the onset of the core He-burning phase as a red supergiant, influenced by helium enrichment near the H-burning shell. This phase critically impacts the ratio of blue to red supergiants. This conclusion supports the studies by Maeder & Meynet (2001b) and Farrell et al. (2022b). Furthermore, the 60  ${\rm M}_{\odot}$  model's evolution was found to be highly sensitive to mass losses, overshadowing the impact of diffusion coefficients. Lastly, in non-magnetic models,  $D_{\rm eff}$  emerged as the primary driver for chemical mixing, especially in scenarios with substantial mass loss.

- Chapter 5 delved into the chemical compositions of high-redshift galaxies, focusing on nitrogen enriched galaxies like GN-z11 and CEERS-1019. For this work we have used models computed by GENEC from 9 to  $120\,M_\odot$  across various metallicities with different initial rotation to extract the yields of nitrogen and oxygen. Our findings revealed that fast-rotating Population III stars yields, specifically at  $0.7\,v/v_{\rm crit}$ , closely reproduce with observed abundance ratios, exemplified by  $\log_{10}({\rm N/O}) = -0.37$  and  $\log_{10}({\rm C/O}) = -0.1$  at a dilution factor of f=100. Stars with metallicities  $Z=10^{-5}$  also reproduce the observed abundances whereas stars at Z=0.014 did not replicate these observations. Our models predicted abundance ratios like [He/H] and [ $^{12}{\rm C}/^{13}{\rm C}$ ], with significant variations across different scenarios and metallicities. These predictions will serve as benchmarks for future observational studies. We also noted the impact of stellar mass on elemental production, with lower mass stars focusing on  $^{16}{\rm O}$  and higher mass stars on  $^{14}{\rm N}$  and  $^{12}{\rm C}$ . The study also shed light on the mechanisms of chemical species transport in rotating massive stars and the role of different mass-cuts in determining the ejection of elements at the end of a star's life.
- In Chapter 6, we focused on 3000  $M_{\odot}$  stars, examining their evolution and impact on their surroundings. After core hydrogen burning, our models revealed multiple intermediate convective zones beneath the convective envelope, resulting in intense mixing and helium-rich red supergiants with a surface helium content of 0.74. These stars remain in the red domain of the HRD through subsequent burning stages. A single 3000  $M_{\odot}$  star was found to be significant in primary nitrogen production, with mechanical and radiative feedback comparable to a group of 100, 20  $M_{\odot}$  stars. Our models avoided general relativistic instability, but encountered electron-positron pair production in the core during oxygen combustion. The

maximum mass achievable with a constant accretion rate of  $10^{-3}$  M $_{\odot}$ /year is around 3000 M $_{\odot}$ , limited by the nuclear lifetime. Models with Z=0 and  $Z=10^{-6}$  could significantly enrich the interstellar medium, with potential implications for high redshift galaxies like GN-z11.

- Chapter 7 delved into the evolutionary trajectories of massive Pop III stars under variable accretion rates obtained from cosmological simulations of Regan et al. (2020b). We identified a critical pre-main-sequence (pre-MS) accretion rate ( $\dot{M}_{\rm crit,preMS}$ ) of  $2.5 \times 10^{-2} {\rm M}_{\odot} {\rm yr}^{-1}$ , marking the transition of these stars into the red side of HR diagram. For the hydrogen-burning stage, the critical accretion rate was found to be  $7.0 \times 10^{-3} \rm{M}_{\odot} \, \rm{yr}^{-1}$ . A model underwent a color transition from blue to red during its core hydrogen-burning phase over approximately 17.5 kyr, influenced by the critical main-sequence accretion rate ( $\dot{M}_{\rm crit,MS}$ ) and the global Kelvin-Helmholtz timescale ( $\tau_{KH}$ ). The study reaffirmed the importance of the surface Kelvin-Helmholtz timescale in determining a star's evolution towards the red or blue supergiant phase during the pre-MS period. It was found that the luminosity wave had a minor impact on the initial pre-MS phase, with the accretion rate being a more significant factor in determining the evolutionary trajectory. Fluctuating accretion rates significantly affected Pop III stars' physical properties, including lifespan, time spent in the red phase, and surface helium enrichment. These findings enhance our understanding of primordial star evolution and advocate for a critical accretion rate of  $\dot{M} = 7 \times 10^{-3} \rm M_{\odot} \, yr^{-1}$  in cosmological simulations, and  $\dot{M} = 2.5 \times 10^{-2} \mathrm{M}_{\odot} \, \mathrm{yr}^{-1}$  when modeling is sensitive to pre-MS timescales.
- In Chapter 8, we explored the evolution and impact of massive Population III stars of a few thousand solar masses on early galaxy chemistry. We discovered that the chemical signatures of PopIII stars are highly dependent on their mass. Stars below  $1900\,\mathrm{M}_\odot$  and above  $8900\,\mathrm{M}_\odot$  couldn't match observed N/O ratios in galaxies like GN-z11 and CEERS 1019. The  $1900\,\mathrm{M}_\odot$  to  $8900\,\mathrm{M}_\odot$  mass range proved crucial for aligning with these galaxies' chemical profiles. A small subset of very massive PopIII stars, notably those above 1000, replicated the high nitrogen abundances seen in JWST-observed early galaxies. Lower mass stars diluted this nitrogen-rich pattern, emphasizing the need for a minority of very massive PopIII stars in early galaxies. The study revealed that individual masses of massive PopIII stars dramatically influence halo chemistry. Stars below 2000 enrich environments with  $^{16}\mathrm{O}$ , while higher mass stars contribute significantly to  $^{14}\mathrm{N}$  enrichment. Our models closely matched observed log (N/O), log (C/O), and log (O/H)+12 ratios in GN-z11 and CEERS 1019, suggesting nitrogen-rich quasars might be a remnant of massive PopIII star formation. The

Ne/O ratio in our models was much lower than observed in CEERS 1019, indicating other processes might be at play in achieving the observed ratios. Abundance predictions, such as the  $\log_{10}$  ( $^{12}$ C/ $^{13}$ C) ratio, provided targets for future JWST observations. These findings highlight the potential for massive PopIII stars to significantly influence nitrogen enrichment in the early universe, aligning with the 'heavy seed' formation pathway hypothesis for massive black holes.

- Chapter 9 provided a comprehensive set of models for Population III supermassive stars, focusing on the atomically cooled halo regime  $(10^{-3}-10)$ . The study explored the evolution and internal structures of these stars, emphasizing the pre-collapse stage and their potential to form black holes. For accretion rates at  $10^{-3}$  and  $10^{-2}$ , the models predicted black holes with final masses between  $3.0 \times 10^3$  and  $2.2 \times 10^4$ , undergoing standard nuclear burning stages without experiencing general relativistic (GR) instability until the mid-core helium burning phase. Models with higher accretion rates of 0.1, 1, and 10 showed GR instability during core hydrogen burning, resulting in direct collapse black holes with final masses ranging from  $1.04 \times 10^5$  to  $4.49 \times 10^5$ . The study identified a lower mass limit for GR instability at around  $8.2 \times 10^4$  for accretion rates near  $4.5 \times 10^{-2}$ , expected to occur during core helium burning. Despite evolving along the Hayashi limit as red supergiant protostars, models with high accretion rates showed a departure from this regime towards the end of their evolution, becoming more 'yellow' or 'blue'. Utilizing an updated GR instability criterion (Haemmerlé et al. 2021), the study found final masses for high accretion rates  $(10^{-1}, 1, 10)$  aligning with linear pulsation equation results, reinforcing the predictions.
- In chapter 10, we successfully developed carbon-burning models that resonated with the observed pulsation modes of Betelgeuse. These models, originating from a ZAMS mass of 19  $M_{\odot}$ , matched the observed pulsation periods of 2190, 417, 230, and 185 days. The models, fitting within Betelgeuse's known temperature and luminosity range, predict the star's eventual mass to be around 11 to 12  $M_{\odot}$  during its core carbon-burning stage. This outcome is achieved through significant mass loss, primarily during the core helium-burning phase. The large radius of about 1300  $R_{\odot}$  in these models is crucial for the long-period fundamental mode, aligning with interferometric measurements of Betelgeuse's angular diameter. Based on seismic and evolutionary modeling, Betelgeuse appears to be in a late or nearing the end phase of core carbon-burning, with carbon exhaustion expected in less than 300 years. This phase will likely precede a core-collapse and subsequent supernova event within a few decades.

# 11.0.1 Future perspectives

# 11.0.2 Impact of the Physics of Rotation on Primary Nitrogen Production

We intend to conduct a study on Pop III and very metal-poor stars, utilizing models computed with various rotational mixing physics. Such models at zero and  $1 \times 10^{-8}$  metallicity have already been computed. The goal is to assess the impact of these physics on the production of primary nitrogen. Previous findings indicate that fast-rotating Pop III models can be significant sources of primary nitrogen, albeit these models were derived using a specific set of physics. The robustness of the conclusions drawn from this paper under alternative physics will be a central focus of our upcoming study.

# **Rotating SMS models**

For future work in GENEC, we aim to implement rotation and accretion in Supermassive Stars (SMSs), drawing on pivotal insights from Haemmerlé (2022). The angular momentum challenge is significant. Given the  $\Omega\Gamma$ -limit, SMSs must be slow rotators, with rotation velocities  $\lesssim 10\%~\Omega_K$  and a centrifugal to gravitational forces ratio of  $\sim 1\%$ . Our models will assess the redistribution of angular momentum in SMSs' outer convective envelopes and its implications on rotational dynamics (Haemmerlé 2022). In the convective envelope, we will consider rigid rotation. We will also examine the GR instability in SMSs, pivotal for their collapse into black holes. The adiabatic pulsations' eigenfrequency  $\omega^2$  will be derived from post-Newtonian corrections to radial momentum equations. The GR instability threshold, where  $\omega$  becomes imaginary, will be critical in our models. For non-rotating Pop III SMSs, the GR instability occurs when the stellar mass surpasses  $\sim 10^5~M_{\odot}$ . Implementing rotation in GENEC's SMS models introduces a new dimension. Rotational effects on stability will be examined using the revised equation (Haemmerlé 2021a):

$$\omega^2 I = \int \beta P dV + \frac{4}{9} \int \frac{\Omega^2}{\Omega_K^2} \frac{GM_r}{r} dM_r - \int \left(\frac{2GM_r}{rc^2} + \frac{8P}{3\rho c^2}\right) \frac{GM_r}{r} dM_r$$
 (11.1)

Here,  $\omega$  is the eigenfrequency of adiabatic pulsations, I is the moment of inertia of the star, relevant in the context of rotation,  $\beta$  is the ratio of gas pressure to total pressure within the star. Additionally, P is the pressure within the star, dV is the differential volume element, indicating a small volume change and  $\Omega$  is the angular velocity of the star whereas  $\Omega_K$  is the Keplerian angular velocity, the theoretical orbital speed if gravity were the only force acting. Finally, G is the gravitational constant,  $M_r$  is the mass contained within radius r, r is the radial distance from the center of the star, c is the speed of light in vacuum,  $dM_r$  is the differential mass element, indicating a small

change in mass and  $\rho$  is the mass density of the star. Therefore this equation will be used to determine the conditions under which a supermassive star becomes dynamically unstable, which can lead to gravitational collapse. For supermassive stars, this collapse could result in the formation of a black hole. The terms in the equation combine both Newtonian physics and General Relativity, reflecting the complex interplay of forces within such massive stellar entities. In summary, this will explore how rotation can stabilize SMSs, potentially increasing final stellar masses.

#### Internal magnetic fields and Taylor Spruit dynamo

Exploring the impact of magnetic fields in the evolution of supermassive stars (SMS) is an intriguing research avenue. This idea is rooted in the findings of Eggenberger et al. (2022b) as they (2022) highlighted the need for substantial recalibration of the Tayler-Spruit dynamo in low mass stars. This recalibration involved increasing the damping timescale for the azimuthal field by about 200 times. Such adjustments are intentionally made to reproduce the internal angular velocity profiles deduced from asteroseismic data from red giants. This is in interesting finding and is worth exploring in supermassive stars since their structure is quite similar to red giants.

Additionally, simulations of protostellar environments in the early universe by Hirano et al. (2022) have hinted towards the presence of strong magnetic dynamos in early star formation history. Turbulent dynamos are known to efficiently amplify weak magnetic seed fields in the early universe. These amplified fields can reach up to a few 10% of the kinetic energy density in protostellar accretion disks. This amplification impacts the fragmentation processes and the initial mass function (IMF) of stars. It also affects the rotational dynamics of Population III stars, influencing their lifetimes and overall luminosity.

One of the first massive star models to include the calibrated Taylor-Spruit (TS) dynamo were computed as part of this thesis. Fig. 11.1 depicts the presence of magnetic diffusivity coefficients in the internal profile of 15  $M_{\odot}$  model. These models reveal that magnetic viscosity predominantly governs angular momentum transport. The models also show a significant influence of  $D_{\rm eff}$  on chemical species transport. In the 15  $M_{\odot}$  model, magnetic fields lead to a shift to a red supergiant phase post-main sequence. The  $60~M_{\odot}$  model indicates a retention of an H-rich outer envelope and a slower core rotation by approximately 15% when compared to non magnetic models. However, a wide range of masses above  $60~M_{\odot}$  have yet to be computed, especially in the very massive and extremely massive star ranges. For the SMS mass regime, the importance of rotating models has been made clear in the previous section. The next step will be the impact of magnetic fields in determining the GR instability, core size and upper mass limit for supermassive stars. Another magnetic instability that may actually be more efficient in transporting the angular momentum

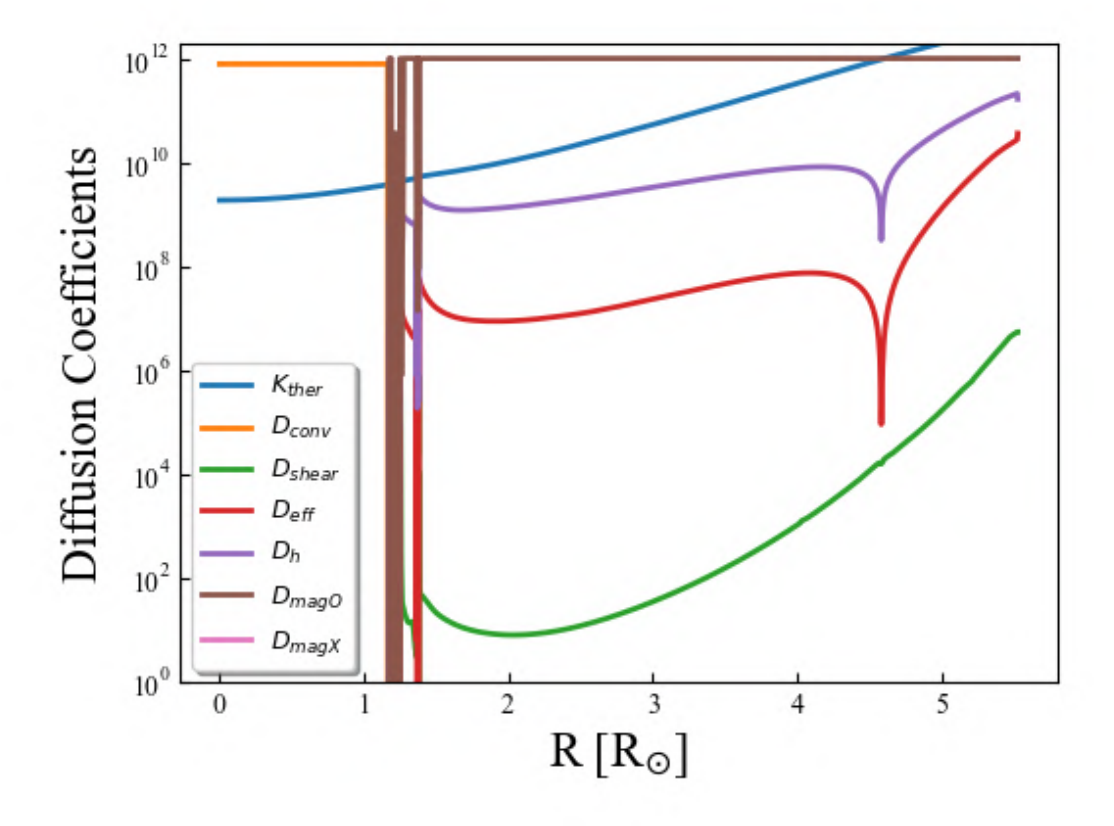


Figure 11.1: The profile of various diffusion coefficients inside the 15  $M_{\odot}$  at  $X_c$  = 0.35. The magnetic diffusivity coefficient is denoted by  $D_{magO}$  and impacts the transport of angular momentum inside the star.

during the pre-MS phase is the magneto-rotational instability (see e.g. the study by Griffiths et al. (2022)). We plan also to study the impact of that instability in future models.

#### WIMP annihilation in SMS

Exploring the role of Weakly Interacting Massive Particles (WIMPs) in supermassive star formation is a notable field for future investigation. Research has indicated that WIMP dark matter annihilation could significantly impact the formation of Population III.1 stars (Tan 2007; Natarajan et al. 2009; Singh et al. 2023). This influence arises from the alteration of the dark matter density profile due to adiabatic contraction in the baryon-dominated core. In scenarios where dark matter density follows a self-similar power-law structure, the resultant heating could dominate cooling in all considered halos. This effect occurs at scales inside approximately  $3\times10^5$  pc. The formation of equilibrium halos, with constant density cores for both baryons and dark matter, would lead to luminosities of around  $103 \ L_{\odot}$ . The core sizes in such halos could range from 1 to 40 AU. The im-

pact of this additional heating on protostellar structure, and its subsequent influence on the mass scale of Pop III.1 stars, is yet to be fully understood. It's conceivable that this mechanism could elevate the mass scale to levels significant for supermassive black hole formation. Future research, incorporating self-consistent cosmological simulations that account for WIMP annihilation heating, is crucial to elucidate these effects and their implications for the evolution of early universe stars.

Building on this foundation, this thesis has advanced our understanding by implementing a WIMP annihilation subroutine within the Geneva stellar evolution code (GENEC). This innovative feature explores WIMP-powered stellar models, using parameters like WIMP mass in GeV and density. Due to uncertainties in WIMP physics, these values vary, offering a range of scenarios. Our models, starting from a 2  $M_{\odot}$  seed, show that WIMP annihilation's influence on energy production in SMSs depends on WIMP parameters and the accretion rate. When WIMP annihilation exceeds a certain threshold, it dominates energy production, 'freezing' nuclear reactions (see Fig. 11.2). These 'frozen' stars, sustained by WIMP annihilation, could exist for extended periods, contrasting with typical stellar lifecycles (Taoso et al. 2008; Freese et al. 2009). Conversely, if WIMP annihilation is below this threshold, stars evolve normally through standard nuclear burning stages.

Yet to be addressed is how the presence of WIMPS can affect the upper mass limit of accreting stars. This upper mass limit is determined by the General Relativistic (GR) instability and therefore, the ancillary study would explore the time at which these WIMP-powered models encounter the GR instability. The internal structure of stars, particularly those with halted nuclear reactions due to WIMP annihilation, requires detailed investigation. Future research will aim to integrate GR instability effects and examine the internal makeup of these unique stellar entities. Such studies will not only deepen our understanding of SMSs in the presence of WIMP dark matter but also potentially influence theories on supermassive black hole formation. This new research avenue promises to shed light on the intricate relationship between dark matter and stellar evolution.

#### Observable traces of SMS

Investigating supermassive star formation using variable accretion rates from cosmological simulations is a vital area for future astrophysical research. Recent studies, like Regan et al. (2020b); Hirano et al. (2022), have shown that these rates significantly affect SMS formation in the early universe. They highlight how the turbulent nature of star-forming environments influences the mass and evolution of these stars. In this thesis, a significant step was taken by incorporating these variable accretion rates into the Geneva stellar evolution code (GENEC). This development

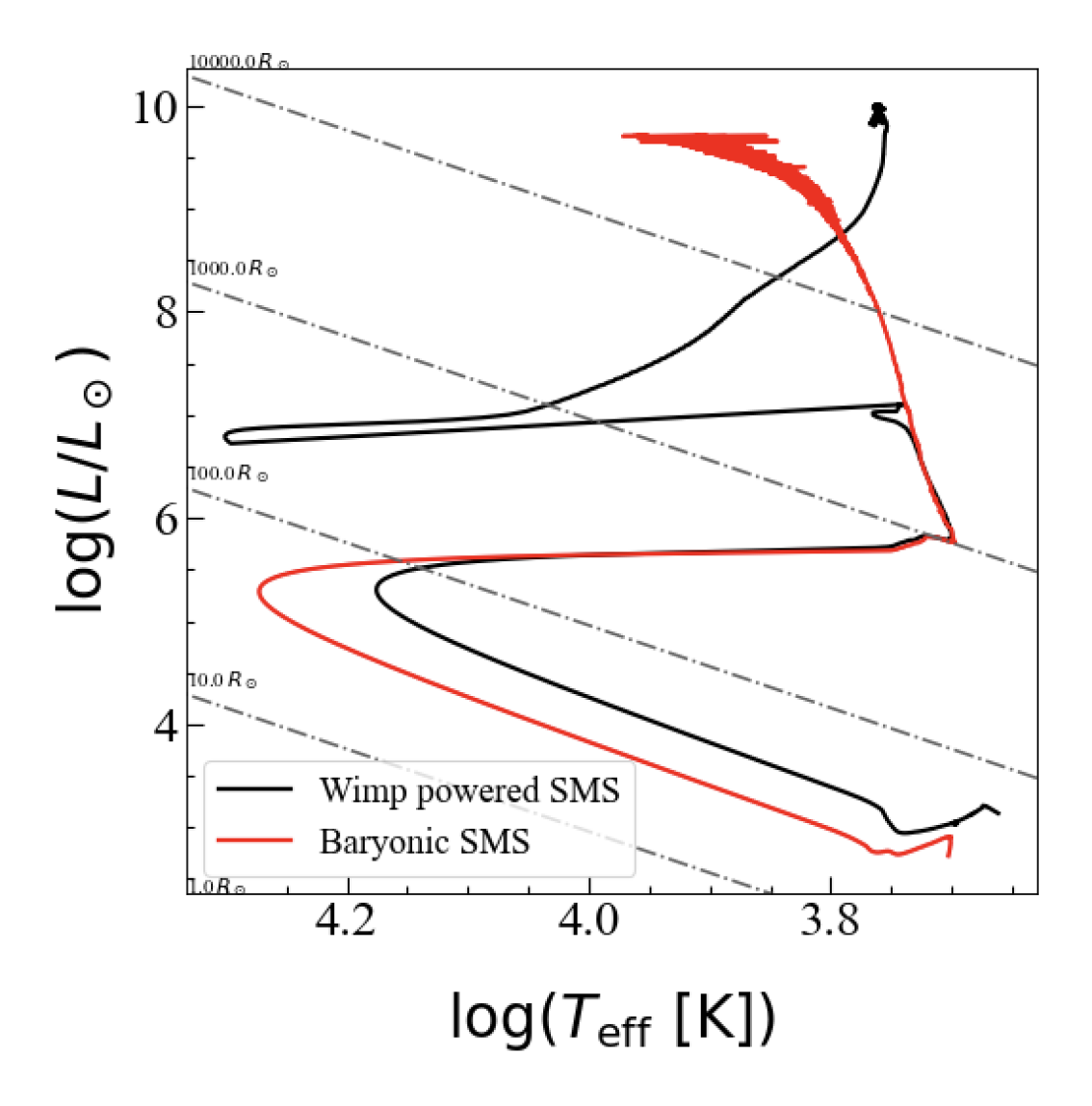


Figure 11.2: The evoltuion of accreting SMS stars at a constant accretion rate of  $0.1~M_{\odot}/yr$ . The black line represents the WIMP powered SMS and the red line shows the standard baryonic SMS. The evolution of both model is quite identical until the energy production from WIMP changes the structure of the star and leads to a contraction towards blue. After this short excursion, the star migrates to red and is solely powered by WIMP annihilation. The consequence of such an evolution is the difference in final fate of these two models; baryonic SMS underwent GR instability at  $104000~M_{\odot}$  whereas WIMP powered SMS has yet to encounter the instability.

allowed for the creation of realistic SMS models that were evolved until the end of their evolution. These models have successfully replicated chemical signatures such as N/O, C/O, and O/H ratios observed in high-redshift galaxies like GN-z11 and CEERS 1019.

The next step involves utilizing the observational data from James Webb Space Telescope, especially its NIRSpec and NIRCam. The goal is to match the chemical and spectroscopic signatures JWST observes in future targets with predictions from GENEC models. This approach aims to confirm the presence of supermassive stars in the early universe and understand their impact on galaxy formation. Future research will continue to refine these models, integrating more data from cosmological simulations and JWST observations. This work is essential for understanding the formation and evolution of supermassive stars and their potential transition into massive black holes.

# **Published Papers**

- Nandal, D., Meynet, G., Ekstrom, S., Moyano, F., Eggenberger, P., Choplin, A., Georgy, C., Farrell, E., Maeder, A. "Impact of different approaches for computing rotating stellar models I. The solar metallicity case." Accepted in *Astronomy and Astrophysics*.
- 2. Nandal, D., Regan, J., Woods, T.E., Farrell, E., Meynet, G., Ekstrom, S. "Explaining the high nitrogen abundances observed in high-z galaxies via PopIII stars of a few thousand solar masses." Accepted in *Astronomy and Astrophysics*.
- 3. H. Saio, D. Nandal, G. Meynet, S. Ekström, "The evolutionary stage of Betelgeuse inferred from its pulsation periods," *Monthly Notices of the Royal Astronomical Society*, vol. 526, pp. 2765â2775, 2023. DOI: 10.1093/mnras/stad2949
- 4. D. Nandal, E. Farrell, G. Buldgen, G. Meynet, S. Ekstrom, "The evolution and impact of 3000  $M_{\odot}$  stars in the early Universe," *arXiv e-prints*, 2023. DOI: 10.48550/arXiv.2309.04435
- D. Nandal, J. A. Regan, T. E. Woods, E. Farrell, S. Ekström, G. Meynet, "Critical accretion rates for rapidly growing massive Population III stars," *Astronomy and Astrophysics*, vol. 677, 2023. DOI: 10.1051/0004-6361/202346938
- 6. S. Martinet et al., "Very massive star winds as sources of the short-lived radioactive isotope <sup>26</sup>Al," *Astronomy and Astrophysics*, vol. 664, 2022. DOI: 10.1051/0004-6361/202243474
- 7. P. Eggenberger et al., "Grids of stellar models with rotation. VI. Models from 0.8 to 120  $M_{\odot}$  at a metallicity Z=0.006," *Astronomy and Astrophysics*, vol. 652, 2021. DOI: 10.1051/0004-6361/202141222
- 8. Nandal, D., Tsiatsiou, S., Sibony, Y. "Explaining the High Nitrogen Abundances Observed in high-z Galaxies via Fast Rotating PopIII Stars." Submitted to *Astronomy and Astrophysics*.

# **Submitted Manuscripts**

- 1. Nandal, D., Meynet, G., Ekstrom, S., Moyano, F., Eggenberger, P., Tsiatsiou, S., Georgy, C., Maeder, A. "Impact of different approaches for computing rotating stellar models II. The low metallicity case." Submitted to *Astronomy and Astrophysics*.
- 2. Nandal, D., Saio, H., Regan, J., Woods, T.E., Mayer, L., Meynet, G., Ekstrom, S. "Models for accreting supermassive stars: maximum mass, luminosities, effects of metallicity." Submitted to *Astronomy and Astrophysics*.

	268	

# Bibliography

Abel, T., Bryan, G. L., & Norman, M. L. 2002, Science, 295, 93

Alvarez, M. A., Wise, J. H., & Abel, T. 2009, ApJL, 701, L133

Anderson, R. I., Saio, H., Ekström, S., Georgy, C., & Meynet, G. 2016, A&A, 591, A8

Angulo, C., Arnould, M., Rayet, M., et al. 1999, Nucl. Phys. A, 656, 3

Appenzeller, I. & Fricke, K. 1972, A&A, 21, 285

Arnett, W. D. & Moravveji, E. 2017, ApJL, 836, L19

Asplund, M., Grevesse, N., Sauval, A. J., Allende Prieto, C., & Kiselman, D. 2004, A&A, 417, 751

Asplund, M., Grevesse, N., Sauval, A. J., & Scott, P. 2009, ARA&A, 47, 481

Bañados, E., Venemans, B. P., Mazzucchelli, C., et al. 2018, Nature, 553, 473

Banerjee, P., Heger, A., & Qian, Y.-Z. 2019, ApJ, 887, 187

Barkana, R. & Loeb, A. 2001, Phys. Rep., 349, 125

Baugh, C. M., Lacey, C. G., Frenk, C. S., et al. 2005, MNRAS, 356, 1191

Baumgarte, T. W. & Shapiro, S. L. 1999a, ApJ, 526, 941

Baumgarte, T. W. & Shapiro, S. L. 1999b, ApJ, 526, 937

Beck, R. 1996, Nachr. Akad. Wiss. Göttingen II, 1996, 262

Beckmann, R. S., Dubois, Y., Volonteri, M., et al. 2022, arXiv e-prints, arXiv:2211.13301

Begelman, M. C. 2010, MNRAS, 402, 673

Begelman, M. C. & Rees, M. J. 1978, MNRAS, 185, 847

Begelman, M. C., Volonteri, M., & Rees, M. J. 2006, MNRAS, 370, 289

Behrend, R. & Maeder, A. 2001, A&A, 373, 190

Bellovary, J. M., Governato, F., Quinn, T. R., et al. 2010, ApJL, 721, L148

Berg, D. A., Erb, D. K., Henry, R. B. C., Skillman, E. D., & McQuinn, K. B. W. 2019, ApJ, 874, 93

Bernasconi, P. A. & Maeder, A. 1996, A&A, 307, 829

Bertone, G., Zentner, A. R., & Silk, J. 2005, Phys. Rev. D, 72, 103517

Biermann, L. 1950, Zeitschrift Naturforschung Teil A, 5, 65

Bisnovatyi-Kogan, G. S., Zel'dovich, Y. B., & Novikov, I. D. 1967, , 11, 419

Blumenthal, G. R., Faber, S. M., Flores, R., & Primack, J. R. 1986, ApJ, 301, 27

Bodenheimer, P. 1995, ARA&A, 33, 199

Bogovalov, S. V., Petrov, M. A., & Timofeev, V. A. 2021, MNRAS, 502, 2409

Böhm, K. H. 1958, Zeitschrift fÅr Astrophysik, 46, 245

Brinkman, H. E., den Hartogh, J. W., Doherty, C. L., Pignatari, M., & Lugaro, M. 2021, ApJ, 923, 47

Brinkman, H. E., Doherty, C., Pignatari, M., Pols, O., & Lugaro, M. 2023, ApJ, 951, 110

Bromm, V., Coppi, P. S., & Larson, R. B. 1999, ApJL, 527, L5

Bromm, V., Coppi, P. S., & Larson, R. B. 2002, ApJ, 564, 23

Bromm, V. & Loeb, A. 2003, ApJ, 596, 34

Brott, I., de Mink, S. E., Cantiello, M., et al. 2011, A&A, 530, A115

Brummel-Smith, C., Bryan, G., Butsky, I., et al. 2019, The Journal of Open Source Software, 4, 1636

Bryan, G. L., Norman, M. L., O'Shea, B. W., et al. 2014, ApJS, 211, 19

Bullock, J. S. & Boylan-Kolchin, M. 2017, ARA&A, 55, 343

Bunker, A. J., Saxena, A., Cameron, A. J., et al. 2023, arXiv e-prints, arXiv:2302.07256

Cameron, A. J., Katz, H., Rey, M. P., & Saxena, A. 2023, MNRAS

Carr, J. S., Sellgren, K., & Balachandran, S. C. 2000, ApJ, 530, 307

Cescutti, G., Chiappini, C., Hirschi, R., Meynet, G., & Frischknecht, U. 2013, A&A, 553, A51

Chaboyer, B. & Zahn, J. P. 1992, A&A, 253, 173

Chabrier, G. 2003, PASP, 115, 763

Chandrasekhar, S. 1933, MNRAS, 93, 390

Chandrasekhar, S. 1939, ApJ, 90, 1

Chandrasekhar, S. 1961, Hydrodynamic and hydromagnetic stability

Chandrasekhar, S. 1964a, ApJ, 140, 417

Chandrasekhar, S. 1964b, ApJ, 140, 417

Charbonnel, C., Schaerer, D., Prantzos, N., et al. 2023, A&A, 673, L7

Chatys, F. W., Bedding, T. R., Murphy, S. J., et al. 2019, MNRAS, 487, 4832

Chatzopoulos, E. & Wheeler, J. C. 2012, ApJ, 748, 42

Chen, P., Wise, J. H., Norman, M. L., Xu, H., & O'Shea, B. W. 2014, ApJ, 795, 144

Chiaki, G. & Yoshida, N. 2022, MNRAS, 510, 5199

Chiappini, C., Hirschi, R., Meynet, G., et al. 2006a, A&A, 449, L27

Chiappini, C., Hirschi, R., Meynet, G., et al. 2006b, A&A, 449, L27

Chiappini, C., Matteucci, F., & Meynet, G. 2003, A&A, 410, 257

Choi, J., Dotter, A., Conroy, C., et al. 2016, ApJ, 823, 102

Chon, S., Hosokawa, T., & Yoshida, N. 2018, MNRAS, 475, 4104

Chon, S. & Omukai, K. 2020a, MNRAS, 494, 2851

Chon, S. & Omukai, K. 2020b, MNRAS, 494, 2851

Choplin, A., Hirschi, R., Meynet, G., et al. 2018, A&A, 618, A133

Clark, P. C., Glover, S. C. O., Smith, R. J., et al. 2011, Science, 331, 1040

Collet, R., Asplund, M., & Trampedach, R. 2006, ApJL, 644, L121

Cristini, A. 2017, PhD thesis, Keele University, UK

Cuesta, A. J., Illana, J. I., & Masip, M. 2023, arXiv e-prints, arXiv:2305.16838

Cutri, R. M., Skrutskie, M. F., van Dyk, S., et al. 2003, VizieR Online Data Catalog, II/246

Däppen, W. 1998, Space Sci. Rev., 85, 49

de Mink, S. E. & Mandel, I. 2016, MNRAS, 460, 3545

Denissenkov, P. A. & Hartwick, F. D. A. 2014, MNRAS, 437, L21

Dharmawardena, T. E., Mairs, S., Scicluna, P., et al. 2020, ApJL, 897, L9

Dijkstra, M., Haiman, Z., Mesinger, A., & Wyithe, J. S. B. 2008, MNRAS, 391, 1961

Dolan, M. M., Mathews, G. J., Lam, D. D., et al. 2016, ApJ, 819, 7

Dupree, A. K., Strassmeier, K. G., Calderwood, T., et al. 2022, ApJ, 936, 18

Eggenberger, P., Buldgen, G., & Salmon, S. J. A. J. 2019, A&A, 626, L1

Eggenberger, P., Buldgen, G., Salmon, S. J. A. J., et al. 2022a, Nature Astronomy, 6, 788

Eggenberger, P., Ekström, S., Georgy, C., et al. 2021, A&A, 652, A137

Eggenberger, P., Meynet, G., Maeder, A., et al. 2008, Ap&SS, 316, 43

Eggenberger, P., Moyano, F. D., & den Hartogh, J. W. 2022b, A&A, 664, L16

Eisenstein, D. J. & Loeb, A. 1995, ApJ, 443, 11

Ekström, S., Georgy, C., Eggenberger, P., et al. 2012a, A&A, 537, A146

Ekström, S., Georgy, C., Eggenberger, P., et al. 2012b, A&A, 537, A146

Ekström, S., Georgy, C., Eggenberger, P., et al. 2012c, A&A, 537, A146

Ekström, S., Meynet, G., & Maeder, A. 2006, in Astronomical Society of the Pacific ConferenceSeries, Vol. 353, Stellar Evolution at Low Metallicity: Mass Loss, Explosions, Cosmology, ed.H. J. G. L. M. Lamers, N. Langer, T. Nugis, & K. Annuk, 141

Elmegreen, B. G. 2002, ApJ, 577, 206

Endal, A. S. & Sofia, S. 1976, ApJ, 210, 184

Endal, A. S. & Sofia, S. 1981, ApJ, 243, 625

Ertl, T., Janka, H. T., Woosley, S. E., Sukhbold, T., & Ugliano, M. 2016, ApJ, 818, 124

Ertl, T., Woosley, S. E., Sukhbold, T., & Janka, H. T. 2020, ApJ, 890, 51

Espinosa Lara, F. & Rieutord, M. 2011, A&A, 533, A43

Farmer, R., Renzo, M., de Mink, S. E., Marchant, P., & Justham, S. 2019, ApJ, 887, 53

Farrell, E., Groh, J. H., Meynet, G., & Eldridge, J. J. 2022a, MNRAS, 512, 4116

Farrell, E., Groh, J. H., Meynet, G., & Eldridge, J. J. 2022b, MNRAS, 512, 4116

Faulkner, J., Roxburgh, I. W., & Strittmatter, P. A. 1968, ApJ, 151, 203

Federrath, C., Chabrier, G., Schober, J., et al. 2011, , 107, 114504

Ferguson, A. & et al. 1994, in Panchromatic View of Galaxies. Their Evolutionary Puzzle, ed. G. Hensler, C. Theis, & J. S. Gallagher, 329

Fernandez, R., Bryan, G. L., Haiman, Z., & Li, M. 2014, MNRAS, 439, 3798

Fialkov, A., Barkana, R., Tseliakhovich, D., & Hirata, C. M. 2012, MNRAS, 424, 1335

Fields, C. E. 2022, ApJL, 924, L15

Finkelstein, S. L., Dickinson, M., Ferguson, H. C., et al. 2017, The Cosmic Evolution Early Release Science (CEERS) Survey, JWST Proposal ID 1345. Cycle 0 Early Release Science

Fliegner, J., Langer, N., & Venn, K. A. 1996, A&A, 308, L13

Fosbury, R. A. E., Villar-Martín, M., Humphrey, A., et al. 2003, ApJ, 596, 797

Fowler, W. A. 1966, ApJ, 144, 180

Fowler, W. A. & Hoyle, F. 1964, ApJS, 9, 201

Freese, K., Bodenheimer, P., Gondolo, P., & Spolyar, D. 2009, New Journal of Physics, 11, 105014

Freese, K., Spolyar, D., & Aguirre, A. 2008, , 2008, 014

Fricke, K. J. 1973, ApJ, 183, 941

Frischknecht, U., Hirschi, R., Meynet, G., et al. 2010, A&A, 522, A39

Frischknecht, U., Hirschi, R., Pignatari, M., et al. 2016, MNRAS, 456, 1803

Fuller, G. M., Woosley, S. E., & Weaver, T. A. 1986, ApJ, 307, 675

Fuller, J. & Lu, W. 2022, MNRAS, 511, 3951

Fuller, J. & Ma, L. 2019, ApJL, 881, L1

Fuller, J., Piro, A. L., & Jermyn, A. S. 2019, MNRAS, 485, 3661

Gammie, C. F. 2001, ApJ, 553, 174

Gehan, C., Mosser, B., Michel, E., Samadi, R., & Kallinger, T. 2018, A&A, 616, A24

Georgy, C. 2010, PhD thesis, University of Geneva, Switzerland

Georgy, C., Ekström, S., Eggenberger, P., et al. 2013a, A&A, 558, A103

Georgy, C., Ekström, S., Meynet, G., et al. 2012, A&A, 542, A29

Georgy, C., Meynet, G., Walder, R., Folini, D., & Maeder, A. 2009, A&A, 502, 611

Georgy, C., Walder, R., Folini, D., et al. 2013b, A&A, 559, A69

Gieles, M., Charbonnel, C., Krause, M. G. H., et al. 2018, MNRAS, 478, 2461

Girichidis, P., Federrath, C., Banerjee, R., & Klessen, R. S. 2011, MNRAS, 413, 2741

Glover, S. 2013, in Astrophysics and Space Science Library, Vol. 396, The First Galaxies, ed. T. Wiklind, B. Mobasher, & V. Bromm, 103

Gonczi, G. & Osaki, Y. 1980, A&A, 84, 304

Granzer, T., Weber, M., Strassmeier, K. G., & Dupree, A. 2022, in Cambridge Workshop on Cool Stars, Stellar Systems, and the Sun, Cambridge Workshop on Cool Stars, Stellar Systems, and the Sun, 185

Grasso, D. & Rubinstein, H. R. 2001, Phys. Rep., 348, 163

Gratton, R., Bragaglia, A., Carretta, E., et al. 2019, A&A Rev., 27, 8

Greif, T. H. 2015, Computational Astrophysics and Cosmology, 2, 3

Greif, T. H., Bromm, V., Clark, P. C., et al. 2012, MNRAS, 424, 399

Greif, T. H., Springel, V., White, S. D. M., et al. 2011, ApJ, 737, 75

Grete, P., Latif, M. A., Schleicher, D. R. G., & Schmidt, W. 2019, MNRAS, 487, 4525

Griffiths, A., Eggenberger, P., Meynet, G., Moyano, F., & Aloy, M.-Á. 2022, A&A, 665, A147

Grigahcène, A., Dupret, M. A., Gabriel, M., Garrido, R., & Scuflaire, R. 2005, A&A, 434, 1055

Groh, J. H., Ekström, S., Georgy, C., et al. 2019, A&A, 627, A24

Guinan, E. F., Wasatonic, R. J., & Calderwood, T. J. 2019, The Astronomer's Telegram, 13341, 1

Haemmerlé, L. 2014, PhD thesis, University of Geneva

Haemmerlé, L. 2020, A&A, 644, A154

Haemmerlé, L. 2021a, A&A, 650, A204

Haemmerlé, L. 2021b, A&A, 650, A204

Haemmerlé, L. 2022, arXiv e-prints, arXiv:2209.02790

Haemmerlé, L., Eggenberger, P., Meynet, G., Maeder, A., & Charbonnel, C. 2013, A&A, 557, A112

Haemmerlé, L., Eggenberger, P., Meynet, G., Maeder, A., & Charbonnel, C. 2016, A&A, 585, A65

Haemmerlé, L., Eggenberger, P., Meynet, G., et al. 2017, Mem. S. A. It., 88, 785

Haemmerlé, L., Klessen, R. S., Mayer, L., & Zwick, L. 2021, A&A, 652, L7

Haemmerlé, L., Mayer, L., Klessen, R. S., et al. 2020, Space Sci. Rev., 216, 48

Haemmerlé, L., Meynet, G., Mayer, L., et al. 2019, A&A, 632, L2

Haemmerlé, L., Woods, T. E., Klessen, R. S., Heger, A., & Whalen, D. J. 2018, MNRAS, 474, 2757

Haiman, Z. 2006, New Astronomy Review, 50, 672

Haiman, Z. & Loeb, A. 2001, ApJ, 552, 459

Haiman, Z., Rees, M. J., & Loeb, A. 1997, ApJ, 476, 458

Harikane, Y., Nakajima, K., Ouchi, M., et al. 2023a, arXiv e-prints, arXiv:2304.06658

Harikane, Y., Zhang, Y., Nakajima, K., et al. 2023b, arXiv e-prints, arXiv:2303.11946

Harper, G. M., DeWitt, C., Richter, M. J., et al. 2017, ApJ, 836, 22

Harper, G. M., DeWitt, C. N., Richter, M. J., et al. 2020, ApJL, 893, L23

Haubois, X., Perrin, G., Lacour, S., et al. 2009, A&A, 508, 923

Hayashi, C. 1961, PASJ, 13, 450

Heger, A., Langer, N., & Woosley, S. E. 2000, ApJ, 528, 368

Heger, A., Woosley, S., Baraffe, I., & Abel, T. 2002, in Lighthouses of the Universe: The Most Luminous Celestial Objects and Their Use for Cosmology, ed. M. Gilfanov, R. Sunyeav, & E. Churazov, 369

Heger, A. & Woosley, S. E. 2010, ApJ, 724, 341

Heger, A., Woosley, S. E., & Spruit, H. C. 2005, ApJ, 626, 350

Henyey, L., Vardya, M. S., & Bodenheimer, P. 1965, ApJ, 142, 841

Henyey, L. G., Lelevier, R., & Levée, R. D. 1955, PASP, 67, 154

Hillebrandt, W., Thielemann, F.-K., & Langer, N. 1987a, in Nuclear Astrophysics, ed. W. Hillebrandt, R. Kuhfuss, E. Mueller, & J. W. Truran, Vol. 287, 233

Hillebrandt, W., Thielemann, F.-K., & Langer, N. 1987b, ApJ, 321, 761

Hillebrandt, W., Thielemann, F.-K., & Langer, N. 1987c, ApJ, 321, 761

Hirano, S., Hosokawa, T., Yoshida, N., & Kuiper, R. 2017, Science, 357, 1375

Hirano, S., Hosokawa, T., Yoshida, N., et al. 2014a, ApJ, 781, 60

Hirano, S., Hosokawa, T., Yoshida, N., et al. 2014b, ApJ, 781, 60

Hirano, S., Machida, M. N., & Basu, S. 2022, arXiv e-prints, arXiv:2209.03574

Hirschi, R., Meynet, G., & Maeder, A. 2004, A&A, 425, 649

Hirschi, R., Meynet, G., & Maeder, A. 2005a, A&A, 443, 581

Hirschi, R., Meynet, G., & Maeder, A. 2005b, A&A, 433, 1013

Hosokawa, T., Hirano, S., Kuiper, R., et al. 2016, ApJ, 824, 119

Hosokawa, T. & Omukai, K. 2009, ApJ, 691, 823

Hosokawa, T., Omukai, K., & Yorke, H. W. 2012, The Astrophysical Journal, 756, 93

Hosokawa, T., Omukai, K., Yoshida, N., & Yorke, H. W. 2011, Science, 334, 1250

Hosokawa, T., Yorke, H. W., Inayoshi, K., Omukai, K., & Yoshida, N. 2013a, The Astrophysical Journal, 778, 178

Hosokawa, T., Yorke, H. W., Inayoshi, K., Omukai, K., & Yoshida, N. 2013b, The Astrophysical Journal, 778, 178

Hosokawa, T., Yorke, H. W., & Omukai, K. 2010a, ApJ, 721, 478

Hosokawa, T., Yorke, H. W., & Omukai, K. 2010b, ApJ, 721, 478

Hoyle, F. & Fowler, W. A. 1963, MNRAS, 125, 169

Hoyle, F. & Tayler, R. J. 1964, Nature, 203, 1108

Iben, Icko, J. 1963, ApJ, 138, 1090

Iglesias, C. A. & Rogers, F. J. 1993, ApJ, 412, 752

Inayoshi, K. & Haiman, Z. 2014, Monthly Notices of the Royal Astronomical Society, 445, 1549

Inayoshi, K., Visbal, E., & Haiman, Z. 2020, ARA&A, 58, 27

Iocco, F., Mangano, G., Miele, G., Pisanti, O., & Serpico, P. D. 2007, Phys. Rev. D, 75, 087304

Itagaki, K., Nakano, S., Beutler, B., & Li, W. 2003, , 8230, 2

Jadlovský, D., Krtička, J., Paunzen, E., & Štefl, V. 2023, , 99, 101962

Jencson, J. E., Pearson, J., Beasor, E. R., et al. 2023, ApJL, 952, L30

Jeon, M., Pawlik, A. H., Greif, T. H., et al. 2012, ApJ, 754, 34

Josselin, E., Blommaert, J. A. D. L., Groenewegen, M. A. T., Omont, A., & Li, F. L. 2000, A&A, 357, 225

Joyce, M., Leung, S.-C., Molnár, L., et al. 2020, ApJ, 902, 63

Jungman, G., Kamionkowski, M., & Griest, K. 1996, Phys. Rep., 267, 195

Kazantsev, A. P. 1968, Soviet Journal of Experimental and Theoretical Physics, 26, 1031

Kervella, P., Decin, L., Richards, A. M. S., et al. 2018, A&A, 609, A67

Keszthelyi, Z., Meynet, G., Shultz, M. E., et al. 2020, MNRAS, 493, 518

Keto, E. 2007, ApJ, 666, 976

Kippenhahn, R., Meyer-Hofmeister, E., & Thomas, H. C. 1970, A&A, 5, 155

Kippenhahn, R. & Thomas, H. C. 1970, in IAU Colloq. 4: Stellar Rotation, ed. A. Slettebak, 20

Kippenhahn, R. & Weigert, A. 1990, Stellar Structure and Evolution

Kiss, L. L., Szabó, G. M., & Bedding, T. R. 2006, MNRAS, 372, 1721

Klessen, R. S. & Glover, S. C. O. 2016, in Saas-Fee Advanced Course, Vol. 43, Saas-Fee Advanced Course, ed. Y. Revaz, P. Jablonka, R. Teyssier, & L. Mayer, 85

Klessen, R. S. & Glover, S. C. O. 2023, arXiv e-prints, arXiv:2303.12500

Kobayashi, C. & Ferrara, A. 2023, arXiv e-prints, arXiv:2308.15583

Kong, D., Zhang, K., & Schubert, G. 2015, MNRAS, 448, 456

Kratter, K. & Lodato, G. 2016, ARA&A, 54, 271

Kravchenko, K., Jorissen, A., Van Eck, S., et al. 2021, A&A, 650, L17

Kroupa, P. 2001, MNRAS, 322, 231

Krtička, J., Owocki, S. P., & Meynet, G. 2011, A&A, 527, A84

Kuiper, R., Klahr, H., Beuther, H., & Henning, T. 2010, ApJ, 722, 1556

Kulkarni, M., Visbal, E., & Bryan, G. L. 2021, ApJ, 917, 40

Lada, C. J. & Lada, E. A. 2003, ARA&A, 41, 57

Larson, R. B. 1969, MNRAS, 145, 271

Larson, R. B. 1972, MNRAS, 157, 121

Larson, R. B. 1981, MNRAS, 194, 809

Larson, R. B. 2000, in ESA Special Publication, Vol. 445, Star Formation from the Small to the Large Scale, ed. F. Favata, A. Kaas, & A. Wilson, 13

Larson, R. L., Finkelstein, S. L., Kocevski, D. D., et al. 2023, ApJL, 953, L29

Latif, M. A., Niemeyer, J. C., & Schleicher, D. R. G. 2014a, MNRAS, 440, 2969

Latif, M. A., Schleicher, D. R. G., Bovino, S., Grassi, T., & Spaans, M. 2014b, ApJ, 792, 78

Latif, M. A., Schleicher, D. R. G., & Hartwig, T. 2016, MNRAS, 458, 233

Latif, M. A., Schleicher, D. R. G., Schmidt, W., & Niemeyer, J. C. 2013, MNRAS, 436, 2989

Latif, M. A., Whalen, D. J., Khochfar, S., Herrington, N. P., & Woods, T. E. 2022, Nature, 607, 48

Lazar, M., Schlickeiser, R., Wielebinski, R., & Poedts, S. 2009, ApJ, 693, 1133

Ledoux, P., Noels, A., & Boury, A. 1982, A&A, 108, 49

Lee, H. & Yoon, S.-C. 2016, ApJ, 820, 135

Levesque, E. M. & Massey, P. 2020, ApJL, 891, L37

Levesque, E. M., Massey, P., Olsen, K. A. G., et al. 2005, ApJ, 628, 973

Limongi, M. & Chieffi, A. 2018, VizieR Online Data Catalog, J/ApJS/237/13

Liu, B., Sibony, Y., Meynet, G., & Bromm, V. 2021, MNRAS, 506, 5247

Lobel, A. & Dupree, A. K. 2000, ApJ, 545, 454

Lupi, A., Haiman, Z., & Volonteri, M. 2021, MNRAS, 503, 5046

Machida, M. N. & Doi, K. 2013, MNRAS, 435, 3283

Machida, M. N., Matsumoto, T., & Inutsuka, S.-i. 2008a, ApJ, 685, 690

Machida, M. N., Matsumoto, T., & Inutsuka, S.-i. 2008b, ApJ, 685, 690

MacLeod, M., Antoni, A., Huang, C. D., Dupree, A., & Loeb, A. 2023, ApJ, 956, 27

Madau, P., Weisz, D. R., & Conroy, C. 2014, ApJL, 790, L17

Maeder, A. 1987, A&A, 178, 159

Maeder, A. 1992, A&A, 264, 105

Maeder, A. 1997, A&A, 321, 134

Maeder, A. 1999, A&A, 347, 185

Maeder, A. 2002, A&A, 392, 575

Maeder, A. 2003, A&A, 399, 263

Maeder, A. 2009, Physics, Formation and Evolution of Rotating Stars

Maeder, A. & Meynet, G. 1987, A&A, 182, 243

Maeder, A. & Meynet, G. 2000, ARA&A, 38, 143

Maeder, A. & Meynet, G. 2001a, A&A, 373, 555

Maeder, A. & Meynet, G. 2001b, A&A, 373, 555

Maeder, A. & Meynet, G. 2005, A&A, 440, 1041

Maeder, A. & Meynet, G. 2012, Reviews of Modern Physics, 84, 25

Maeder, A. & Zahn, J.-P. 1998, A&A, 334, 1000

Mandel, I. & de Mink, S. E. 2016, MNRAS, 458, 2634

Marchant, P. & Moriya, T. J. 2020, A&A, 640, L18

Marques-Chaves, R., Schaerer, D., Kuruvanthodi, A., et al. 2023, arXiv e-prints, arXiv:2307.04234

Martinet, S., Meynet, G., Nandal, D., et al. 2022, A&A, 664, A181

Mathis, S., Palacios, A., & Zahn, J. P. 2004, A&A, 425, 243

Mayer, L. & Bonoli, S. 2019, Reports on Progress in Physics, 82, 016901

Mayer, L., Capelo, P. R., Zwick, L., & Di Matteo, T. 2023, arXiv e-prints, arXiv:2304.02066

Mayer, L., Kazantzidis, S., Escala, A., & Callegari, S. 2010a, Nature, 466, 1082

Mayer, L., Kazantzidis, S., Escala, A., & Callegari, S. 2010b, Nature, 466, 1082

McKee, C. F. & Ostriker, E. C. 2007, ARA&A, 45, 565

McKee, C. F. & Tan, J. C. 2003, ApJ, 585, 850

Medvedev, M. V. & Silva, L. O. 2004, in APS Meeting Abstracts, Vol. 46, APS Division of Plasma Physics Meeting Abstracts, BO3.008

Mendel, J. T., Venn, K. A., Proffitt, C. R., Brooks, A. M., & Lambert, D. L. 2006, ApJ, 640, 1039

Meynet, G., Chomienne, V., Ekström, S., et al. 2015, A&A, 575, A60

Meynet, G., Eggenberger, P., & Maeder, A. 2011, A&A, 525, L11

Meynet, G., Ekstrom, S., Maeder, A., et al. 2013, in Lecture Notes in Physics, Berlin Springer Verlag, ed. M. Goupil, K. Belkacem, C. Neiner, F. Lignières, & J. J. Green, Vol. 865, 3

Meynet, G. & Maeder, A. 1997a, A&A, 321, 465

Meynet, G. & Maeder, A. 1997b, A&A, 321, 465

Meynet, G. & Maeder, A. 2002, A&A, 381, L25

Meynet, G. & Maeder, A. 2005, A&A, 429, 581

Meynet, G. & Maeder, A. 2006, in Astronomical Society of the Pacific Conference Series, Vol. 355, Stars with the B[e] Phenomenon, ed. M. Kraus & A. S. Miroshnichenko, 27

Mihalas, D. 1998, in Saas-Fee Advanced Course 27: Computational Methods for Astrophysical Fluid Flow., ed. O. Steiner & A. Gautschy, 161

Milosavljević, M., Couch, S. M., & Bromm, V. 2009, ApJL, 696, L146

Mishra, A. & Basu, D. N. 2011, arXiv e-prints, arXiv:1106.2972

Mittag, M., Schröder, K. P., Perdelwitz, V., Jack, D., & Schmitt, J. H. M. M. 2023, A&A, 669, A9

Montargès, M., Cannon, E., Lagadec, E., et al. 2021, Nature, 594, 365

Montero, P. J., Janka, H.-T., & Müller, E. 2012, ApJ, 749, 37

Montero, P. J., Janka, H.-T., & MÃŒller, E. 2012, The Astrophysical Journal, 749, 37

Moriya, T. J., Chen, K.-J., Nakajima, K., Tominaga, N., & Blinnikov, S. I. 2021, MNRAS, 503, 1206

Mortlock, D. J., Warren, S. J., Venemans, B. P., et al. 2011, Nature, 474, 616

Müller, P. E. & Vink, J. S. 2014, A&A, 564, A57

Murphy, L. J., Groh, J. H., Ekström, S., et al. 2020, MNRAS

Murphy, L. J., Groh, J. H., Ekström, S., et al. 2021a, MNRAS, 501, 2745

Murphy, L. J., Groh, J. H., Farrell, E., et al. 2021b, MNRAS, 506, 5731

Nagakura, T. & Omukai, K. 2005, MNRAS, 364, 1378

Nagele, C. & Umeda, H. 2023, ApJL, 949, L16

Nagele, C., Umeda, H., Takahashi, K., Yoshida, T., & Sumiyoshi, K. 2021, MNRAS, 508, 828

Nagele, C., Umeda, H., Takahashi, K., Yoshida, T., & Sumiyoshi, K. 2022, MNRAS, 517, 1584

Nakamura, F. & Umemura, M. 2001, ApJ, 548, 19

Nance, S., Sullivan, J. M., Diaz, M., & Wheeler, J. C. 2018, MNRAS, 479, 251

Nandal, D., Farrell, E., Buldgen, G., Meynet, G., & Ekstrom, S. 2023a, arXiv e-prints, arXiv:2309.04435

Nandal, D., Meynet, G., Ekström, S., et al. 2023b, arXiv e-prints, arXiv:2312.13340

Nandal, D., Regan, J. A., Woods, T. E., et al. 2023c, arXiv e-prints, arXiv:2306.17223

Natarajan, A., Tan, J. C., & O'Shea, B. W. 2009, ApJ, 692, 574

Natarajan, P., Pacucci, F., Ricarte, A., et al. 2023, arXiv e-prints, arXiv:2308.02654

Nayfonov, A., Däppen, W., Hummer, D. G., & Mihalas, D. 1999, ApJ, 526, 451

Neilson, H. R., Lester, J. B., & Haubois, X. 2011, in Astronomical Society of the Pacific Conference Series, Vol. 451, 9th Pacific Rim Conference on Stellar Astrophysics, ed. S. Qain, K. Leung, L. Zhu, & S. Kwok, 117

Neuhäuser, R., Torres, G., Mugrauer, M., et al. 2022, MNRAS, 516, 693

Nguyen, C. T., Costa, G., Girardi, L., et al. 2022, A&A, 665, A126

Noels, A. & Grevesse, N. 1993, in Astronomical Society of the Pacific Conference Series, Vol. 40, IAU Colloq. 137: Inside the Stars, ed. W. W. Weiss & A. Baglin, 410–425

Nomoto, K., Tominaga, N., Umeda, H., Kobayashi, C., & Maeda, K. 2006, Nucl. Phys. A, 777, 424

Oesch, P. A., Brammer, G., van Dokkum, P. G., et al. 2016, ApJ, 819, 129

Ogane, Y., Ohshima, O., Taniguchi, D., & Takanashi, N. 2022, Open European Journal on Variable Stars, 233, 1

Oh, S. P. & Haiman, Z. 2002, ApJ, 569, 558

Ohkubo, T., Nomoto, K., Umeda, H., Yoshida, N., & Tsuruta, S. 2009, ApJ, 706, 1184

Omukai, K. 2007, PASJ, 59, 589

Omukai, K. & Palla, F. 2001, ApJL, 561, L55

Omukai, K. & Palla, F. 2003, ApJ, 589, 677

Omukai, K., Schneider, R., & Haiman, Z. 2008, ApJ, 686, 801

O'Shea, B. W. & Norman, M. L. 2007, ApJ, 654, 66

O'Shea, B. W., Wise, J. H., Xu, H., & Norman, M. L. 2015, ApJL, 807, L12

Palacios, A., Meynet, G., Vuissoz, C., et al. 2005, A&A, 429, 613

Palla, F. & Stahler, S. W. 1992, ApJ, 392, 667

Patrício, V., Richard, J., Verhamme, A., et al. 2016, MNRAS, 456, 4191

Patton, R. A. & Sukhbold, T. 2020, MNRAS, 499, 2803

Pauli, D., Langer, N., Aguilera-Dena, D. R., Wang, C., & Marchant, P. 2022, A&A, 667, A58

Peebles, P. J. E. 1993, Principles of Physical Cosmology

Perivolaropoulos, L. & Skara, F. 2022, , 95, 101659

Peters, T., Schleicher, D. R. G., Smith, R. J., Schmidt, W., & Klessen, R. S. 2014, MNRAS, 442, 3112

Pfister, H., Volonteri, M., Dubois, Y., Dotti, M., & Colpi, M. 2019, MNRAS, 486, 101

Piau, L., Beers, T. C., Balsara, D. S., et al. 2006, ApJ, 653, 300

Pignatari, M., Gallino, R., Meynet, G., et al. 2008, ApJL, 687, L95

Pitts, E. & Tayler, R. J. 1985, MNRAS, 216, 139

Planck Collaboration, Ade, P. A. R., Aghanim, N., et al. 2016, A&A, 594, A13

Planck Collaboration, Aghanim, N., Akrami, Y., et al. 2020, A&A, 641, A1

Prat, V., Guilet, J., Viallet, M., & Müller, E. 2016, A&A, 592, A59

Proffitt, C. R., Jönsson, P., Litzén, U., Pickering, J. C., & Wahlgren, G. M. 1999, ApJ, 516, 342

Proffitt, C. R., Lennon, D. J., Langer, N., & Brott, I. 2016, ApJ, 824, 3

Proffitt, C. R. & Quigley, M. F. 2001, ApJ, 548, 429

Prole, L. R., Clark, P. C., Klessen, R. S., & Glover, S. C. O. 2022, MNRAS, 510, 4019

Rees, M. J. 1976, MNRAS, 176, 483

Rees, M. J. 1978, , 17, 193

Rees, M. J. 1984, ARA&A, 22, 471

Regan, J. 2022, arXiv e-prints, arXiv:2210.04899

Regan, J. A. & Haehnelt, M. G. 2009, MNRAS, 393, 858

Regan, J. A., Johansson, P. H., & Haehnelt, M. G. 2014, Monthly Notices of the Royal Astronomical Society, 439, 1160

Regan, J. A., Visbal, E., Wise, J. H., et al. 2017a, Nature Astronomy, 1, 0075

Regan, J. A., Visbal, E., Wise, J. H., et al. 2017b, Nature Astronomy, 1, 0075

Regan, J. A., Wise, J. H., O'Shea, B. W., & Norman, M. L. 2020a, MNRAS, 492, 3021

Regan, J. A., Wise, J. H., Woods, T. E., et al. 2020b, The Open Journal of Astrophysics, 3, 15

Renzo, M. & Götberg, Y. 2021, ApJ, 923, 277

Renzo, M., Ott, C. D., Shore, S. N., & de Mink, S. E. 2017, A&A, 603, A118

Renzo, M., Zapartas, E., Justham, S., et al. 2023, ApJL, 942, L32

Ripamonti, E., Iocco, F., Bressan, A., et al. 2009, arXiv e-prints, arXiv:0903.0346

Rogers, J. H., Leblanc, B., Majeski, R., et al. 1996, in APS Division of Plasma Physics Meeting Abstracts, APS Meeting Abstracts, 4F.09

Romeo, A. B. & Falstad, N. 2013, MNRAS, 433, 1389

Sabhahit, G. N., Vink, J. S., Sander, A. A. C., & Higgins, E. R. 2023, MNRAS, 524, 1529

Saijo, M., Baumgarte, T. W., Shapiro, S. L., & Shibata, M. 2002, ApJ, 569, 349

Saio, H. 1980, Highlights of Astronomy, 5, 461

Saio, H. & Wheeler, J. C. 1983, ApJL, 272, L25

Sakurai, Y., Hosokawa, T., Yoshida, N., & Yorke, H. W. 2015, MNRAS, 452, 755

Sakurai, Y., Vorobyov, E. I., Hosokawa, T., et al. 2016a, MNRAS, 459, 1137

Sakurai, Y., Vorobyov, E. I., Hosokawa, T., et al. 2016b, MNRAS, 459, 1137

Salpeter, E. E. 1954, in Liege International Astrophysical Colloquia, Vol. 5, Liege International Astrophysical Colloquia, 116

Sana, H., de Mink, S. E., de Koter, A., et al. 2012, Science, 337, 444

Santoliquido, F., Mapelli, M., Giacobbo, N., Bouffanais, Y., & Artale, M. C. 2021, MNRAS, 502, 4877

Schaller, G., Schaerer, D., Meynet, G., & Maeder, A. 1992, A&AS, 96, 269

Schauer, A. T. P., Glover, S. C. O., Klessen, R. S., & Clark, P. 2021a, MNRAS, 507, 1775

Schauer, A. T. P., Glover, S. C. O., Klessen, R. S., & Clark, P. 2021b, MNRAS, 507, 1775

Schauer, A. T. P., Regan, J., Glover, S. C. O., & Klessen, R. S. 2017, MNRAS, 471, 4878

Schauer, A. T. P., Whalen, D. J., Glover, S. C. O., & Klessen, R. S. 2015, MNRAS, 454, 2441

Schleicher, D. R. G., Palla, F., Ferrara, A., Galli, D., & Latif, M. 2013, A&A, 558, A59

Schlickeiser, R. & Shukla, P. K. 2003, ApJL, 599, L57

Schober, J., Schleicher, D. R. G., & Klessen, R. S. 2015, MNRAS, 446, 2

Senchyna, P., Plat, A., Stark, D. P., & Rudie, G. C. 2023, arXiv e-prints, arXiv:2303.04179

Shakura, N. I. 1973, , 16, 756

Shang, C., Bryan, G. L., & Haiman, Z. 2010, MNRAS, 402, 1249

Shibata, M., Uchida, H., & Sekiguchi, Y.-i. 2016, ApJ, 818, 157

Sibony, Y., Liu, B., Simmonds, C., Meynet, G., & Bromm, V. 2022, A&A, 666, A199

Sigl, G., Olinto, A. V., & Jedamzik, K. 1997, Phys. Rev. D, 55, 4582

Silk, J. 1986, , 72, 582

Singh, V., Bhowmick, D., & Basu, D. N. 2023, arXiv e-prints, arXiv:2304.08032

Smith, B. D., Regan, J. A., Downes, T. P., et al. 2018, MNRAS, 480, 3762

Song, H. F., Meynet, G., Maeder, A., Ekström, S., & Eggenberger, P. 2016, A&A, 585, A120

Soraisam, M., Matheson, T., Andrews, J., et al. 2023, Transient Name Server AstroNote, 139, 1

Spitzer, Lyman, J. 1978, , 72, 349

Spitzer, L. 1956, Physics of Fully Ionized Gases

Spolyar, D., Freese, K., & Gondolo, P. 2008, , 100, 051101

Spruit, H. C. 2002, A&A, 381, 923

Stacy, A. & Bromm, V. 2013, MNRAS, 433, 1094

Stacy, A., Greif, T. H., & Bromm, V. 2010, MNRAS, 403, 45

Stacy, A., Greif, T. H., & Bromm, V. 2012, in American Institute of Physics Conference Series, Vol. 1480, First Stars IV - from Hayashi to the Future -, ed. M. Umemura & K. Omukai, 97–100

Stacy, A., Pawlik, A. H., Bromm, V., & Loeb, A. 2014, MNRAS, 441, 822

Stahler, S. W., Palla, F., & Salpeter, E. E. 1986, ApJ, 302, 590

Stothers, R. & Leung, K. C. 1971, A&A, 10, 290

Subramanian, K. & Barrow, J. D. 1998, , 81, 3575

Sugimura, K., Hosokawa, T., Yajima, H., Inayoshi, K., & Omukai, K. 2018, MNRAS, 478, 3961

Sugimura, K., Matsumoto, T., Hosokawa, T., Hirano, S., & Omukai, K. 2020, ApJL, 892, L14

Sullivan, J. M., Nance, S., & Wheeler, J. C. 2020, ApJ, 905, 128

Sunyaev, R. A. & Zeldovich, Y. B. 1970, Ap&SS, 9, 368

Susa, H. 2013, ApJ, 773, 185

Susa, H. 2019, ApJ, 877, 99

Talon, S. & Zahn, J. P. 1997, A&A, 317, 749

Tan, J. C. 2007, in Revista Mexicana de Astronomia y Astrofisica Conference Series, Vol. 29, Revista Mexicana de Astronomia y Astrofisica Conference Series, ed. R. Guzmán, 66–68

Tanaka, K. E. I., Tan, J. C., & Zhang, Y. 2017, ApJ, 835, 32

Tanaka, T. & Haiman, Z. 2009, ApJ, 696, 1798

Tanaka, T. L. & Li, M. 2014, MNRAS, 439, 1092

Tang, M., Stark, D. P., Chen, Z., et al. 2023, arXiv e-prints, arXiv:2301.07072

Taniguchi, D., Yamazaki, K., & Uno, S. 2022a, in Cambridge Workshop on Cool Stars, Stellar Systems, and the Sun, Cambridge Workshop on Cool Stars, Stellar Systems, and the Sun, 174

Taniguchi, D., Yamazaki, K., & Uno, S. 2022b, Nature Astronomy, 6, 930

Taoso, M., Bertone, G., Meynet, G., & Ekström, S. 2008, Phys. Rev. D, 78, 123510

Tayler, R. J. 1973, MNRAS, 161, 365

Toomre, A. 1964, ApJ, 139, 1217

Townes, C. H., Wishnow, E. H., Hale, D. D. S., & Walp, B. 2009, ApJL, 697, L127

Trabucchi, M., Wood, P. R., Montalbán, J., et al. 2017, ApJ, 847, 139

Tremmel, M., Governato, F., Volonteri, M., Pontzen, A., & Quinn, T. R. 2018, ApJL, 857, L22

Trinca, A., Schneider, R., Valiante, R., et al. 2023, arXiv e-prints, arXiv:2305.04944

Tseliakhovich, D., Barkana, R., & Hirata, C. M. 2011, MNRAS, 418, 906

Tseliakhovich, D. & Hirata, C. 2010a, Phys. Rev. D, 82, 083520

Tseliakhovich, D. & Hirata, C. 2010b, Phys. Rev. D, 82, 083520

Turk, M. 2011, in APS Meeting Abstracts, Vol. 2011, APS April Meeting Abstracts, E4.003

Turk, M. J., Abel, T., & O'Shea, B. 2009, Science, 325, 601

Umeda, H., Hosokawa, T., Omukai, K., & Yoshida, N. 2016, ApJL, 830, L34

Umeda, H., Yoshida, T., & Takahashi, K. 2012, Progress of Theoretical and Experimental Physics, 2012, 01A302

Unno, W. 1967, PASJ, 19, 140

Unno, W. 1971, PASJ, 23, 123

Unno, W., Osaki, Y., Ando, H., Saio, H., & Shibahashi, H. 1989, Nonradial oscillations of stars (Univ. Tokyo Press, Tokyo)

Venn, K. A., Brooks, A. M., Lambert, D. L., et al. 2002, ApJ, 565, 571

Vincenzo, F., Belfiore, F., Maiolino, R., Matteucci, F., & Ventura, P. 2016, MNRAS, 458, 3466

Visbal, E., Haiman, Z., & Bryan, G. L. 2014a, MNRAS, 442, L100

Visbal, E., Haiman, Z., & Bryan, G. L. 2014b, MNRAS, 445, 1056

Visbal, E., Haiman, Z., Terrazas, B., Bryan, G. L., & Barkana, R. 2014c, MNRAS, 445, 107

Visbal, E., Loeb, A., & Hernquist, L. 2012, arXiv e-prints, arXiv:1206.5852

Volonteri, M. & Begelman, M. C. 2010, MNRAS, 409, 1022

von Zeipel, H. 1924, MNRAS, 84, 665

Vorobyov, E. I., DeSouza, A. L., & Basu, S. 2013, ApJ, 768, 131

Wang, F., Yang, J., Fan, X., et al. 2021, arXiv e-prints, arXiv:2101.03179

Wasatonic, R. 2022, , 50, 205

Weaver, T. A., Zimmerman, G. B., & Woosley, S. E. 1978, ApJ, 225, 1021

Weinberg, S. 1972, Gravitation and Cosmology: Principles and Applications of the General Theory of Relativity

Wheeler, J. C. & Chatzopoulos, E. 2023, Astronomy and Geophysics, 64, 3.11

Wheeler, J. C., Nance, S., Diaz, M., et al. 2017, MNRAS, 465, 2654

Willott, C. J., Delorme, P., Reylé, C., et al. 2010, AJ, 139, 906

Wise, J. H., Regan, J. A., O'Shea, B. W., et al. 2019, Nature, 566, 85

Woods, T. E., Agarwal, B., Bromm, V., et al. 2019, PASA, 36, e027

Woods, T. E., Heger, A., & Haemmerlé, L. 2020, MNRAS, 494, 2236

Woods, T. E., Heger, A., Whalen, D. J., Haemmerlé, L., & Klessen, R. S. 2017, ApJL, 842, L6

Woods, T. E., Willott, C. J., Regan, J. A., et al. 2021, ApJL, 920, L22

Xu, H., Norman, M. L., O'Shea, B. W., & Wise, J. H. 2016, ApJ, 823, 140

Yoon, S. C., Langer, N., & Norman, C. 2006, A&A, 460, 199

Yorke, H. W. & Bodenheimer, P. 2008, in Astronomical Society of the Pacific Conference Series, Vol. 387, Massive Star Formation: Observations Confront Theory, ed. H. Beuther, H. Linz, & T. Henning, 189

Yorke, H. W. & Sonnhalter, C. 2002, ApJ, 569, 846

Yoshida, N., Abel, T., Hernquist, L., & Sugiyama, N. 2003, ApJ, 592, 645

Yoshida, N., Omukai, K., & Hernquist, L. 2007, ApJL, 667, L117

Yoshida, N., Omukai, K., Hernquist, L., & Abel, T. 2006, ApJ, 652, 6

Yusof, N., Hirschi, R., Eggenberger, P., et al. 2022, MNRAS, 511, 2814

Zahn, J. P. 1992, A&A, 265, 115

Zhu, Q., Li, Y., Li, Y., et al. 2020, arXiv e-prints, arXiv:2012.01458

Zinnecker, H. & Yorke, H. W. 2007, ARA&A, 45, 481

Zwick, L., Mayer, L., Haemmerlé, L., & Klessen, R. S. 2023, MNRAS, 518, 2076